Multi-messenger & multi-wavelength signatures of compact object transients

Cooper, A.J.

Publication date
2022
Document Version
Final published version

Citation for published version (APA):
Cooper, A. J. (2022). *Multi-messenger & multi-wavelength signatures of compact object transients*. [Thesis, fully internal, Universiteit van Amsterdam].

Multi-messenger and multi-wavelength signatures of compact object transients

Multi-messenger and multi-wavelength signatures of compact object transients

A. J. Cooper

Multi-messenger & multi-wavelength signatures of compact object transients

A. J. Cooper

Multi-messenger and multi-wavelength signatures of compact object transients, Anton Pannekoek Institute, Universiteit van Amsterdam

UNIVERSITY OF AMSTERDAM

ANTON PANNEKOEK
INSTITUTE

Multi-messenger & multi-wavelength signatures of compact object transients

ACADEMISCH PROEFSCHRIFT

ter verkrijging van de graad van doctor
aan de Universiteit van Amsterdam
op gezag van de Rector Magnificus
prof. dr. ir. P.P.C.C. Verbeek
ten overstaan van een door het College voor Promoties ingestelde
commissie, in het openbaar te verdedigen in de Aula der Universiteit
op 16 december 2022, te 11.00 uur

door

A. J. Cooper

geboren te High Wycombe

Promotiecommissie:

Promotor(es):	Prof. dr. R. A. M. J. Wijers	Universiteit van Amsterdam
Copromotor(es):	dr. B. A. Rowlinson	Universiteit van Amsterdam
Overige leden:	prof. dr. R. Fender	University of Oxford
	prof. dr. S. B. Markoff	Universiteit van Amsterdam
	prof. dr. J.W.T. Hessels	ASTRON/Universiteit van Amsterdam
	dr. S. Nissanke	Universiteit van Amsterdam
	dr. P. Moesta	Universiteit van Amsterdam

Faculteit der Natuurwetenschappen, Wiskunde en Informatica

In memory of Kieran Strudwick

Contents

Chapter 1

Introduction

With the naked eye, we observe the same night's sky as our ancient ancestors that shared our hemisphere, with the exception of local comets and meteors. The unchanging nature of the stars informed the first cosmological theories, involving an eternal and unchanging Universe surrounded by celestial spheres of fixed stars. We now know that the Universe is extremely dynamic, but often on timescales much longer than the human lifetime, or even the lifetimes of human civilisations. Transient or time-domain astronomy is the study of those astrophysical sources that vary in nature on human timescales. Often, these astrophysical transients involve the strange behaviour of matter close to dense, compact objects.

The first recorded observations of astrophysical transients outside of our solar system were conducted by ancient Chinese astronomers, who noted so-called 'guest stars' appearing in the sky where no star was previously present. Modern astronomers interpret these guest stars as novae or supernovae, and the compact objects left behind by these explosions can be identified with specific guest stars to this day (SN135; Thorsett 1992). As technology has advanced over the centuries new ways in which to observe the Universe have been uncovered. In almost all cases when we hunt for dynamic astronomical activity using new techniques or messengers, we find something.

A brief history of astrophysical messengers

Until the 20th century, astronomy was a 4 dimensional problem[1]: we observe photons at different energies, at different times, across the sky; a 2 dimensional solid angle. Until 1933, when Karl Jansky invented the radio telescope (Jansky 1933; Fig. 1.1b), all observations of the Universe were performed in the small range of photon wavelengths ($\delta\lambda \approx 300$nm) observable to the human eye. Jansky's radio source in the constellation Sagittarius would be imaged almost 90 years later by a worldwide network of radio telescopes, resulting in the first image of the supermassive black hole at the centre of our Galaxy (Akiyama et al., 2022). The range of photon energies accessible to humans grew immensely as a result of the space

---

[1]Parallax distances measurements represent an exception to this general statement (Bessel, 1838).

1

race, with Soviet and US space-borne satellites carrying X-ray and gamma-ray detectors, allowing us to observe high-energy photons that cannot penetrate our atmosphere. We now have access to over 20 orders of magnitude of wavelengths, from the lowest frequencies that our ionosphere allows through undisturbed at roughly 10^7 Hz (van Haarlem et al., 2013), to the highest energy photons the universe allows through undisturbed at approximately 10^{29} Hz (Cao et al., 2019). Moreover, in the past century new astrophysical messengers other than light have been identified. Each of these new messengers present novel challenges that must be overcome for astronomers to utilize them to learn about the Universe.

In 1912 Victor Hess (Hess 1928; Fig. 1.1a) discovered cosmic rays, astrophysically accelerated atomic nuclei. The origin of cosmic rays, where and how they are accelerated, is a century-old mystery that has led to leaps forward in our understanding of particle acceleration. The locally observed spectrum extends over nearly 20 orders of magnitude, and the highest energy cosmic rays are powered by the most extreme particle accelerators in the Universe. Unlike photons, cosmic rays have charge, meaning that their path is deflected in Galactic and intergalactic magnetic fields. This means they do not point back to their sources which limits their astronomical use. Cosmic ray detectors range from small-scale space-based instruments like AMS-02 onboard the International Space Station (Aguilar et al., 2013) which measures the most common, low-energy ($\sim 1-100$ GeV) cosmic rays & accelerated leptons; to enormous ground-based observatories such as the Pierre Auger Observatory which covers 3000 km^2. This detector measures the enormous showers of particles & light initiated by the highest energy ($\geq 10^{18}$ eV) and rarest (1 particle km^{-2} yr^{-1}) cosmic rays.

Neutrinos are extremely weakly interacting particles, first predicted in 1930 by Wolfgang Pauli [2], which are produced through a variety of nuclear and hadronic channels. Their weak interaction necessitate the construction of huge, shielded detectors. Neutrinos were detected in a terrestrial experiment in 1956 (Cowan et al., 1956), using a tank of water close to a nuclear reactor. The first experiments to detect solar neutrinos were performed in the 1960s (Davis et al., 1968) making use of giant underground tanks of cleaning fluid to observe interactions of electron neutrinos and Chlorine-37 (Fig. 1.1c). Their work and the subsequent discrepancy between the predicted and observed solar neutrino flux eventually led to the discovery of neutrino oscillations. The current state-of-the-art neutrino detectors are IceCube and ANTARES, consisting of kilometre-long strings of photon multiplier tubes embedded in the Antarctic ice and Mediterranean sea respectively. These experiments target the neutrinos expected to be produced when cosmic rays are accelerated to very high energies, and a TeV-PeV flux of astrophysical neutrinos have now been confirmed (Aartsen et al., 2014). Associating observed neutrinos with astrophysical transients temporally and spatially can provide insight to the extreme inner engines of these sources that are otherwise opaque to even the highest energy photons due to absorption (e.g. Murase et al. 2014). The first neutrinos from an astrophysical transient were discovered in association with a supernovae SN1987a in the Large Magellanic Cloud (Hirata et al., 1987; Bionta et al., 1987). With IceCube, such associations have been reported during a blazar flare (IceCube Collaboration et al., 2018a)

---

[2]For a translation of Pauli's original letter positing the existence of the neutrino see: https://icecube.wisc.edu/neutrino-history/1931/01/1931-pauli-presents-hypothetical-neutron-particle/.

and a tidal disruption event (Stein et al., 2021), possibly indicating high-energy cosmic ray acceleration in these sources.

Gravitational waves, the newest cosmic messenger, are ripples in the fabric space-time, produced by the quadrapole moment of an object's mass (Einstein, 1916). These perturbations can propagate across the Universe, and their amplitude decreases linearly as a function of distance. Any massive body with angular momentum that is not rotationally or spherically symmetric will radiate gravitational waves, including binary stars, asymmetric rotating bodies, and the planets and moons of our own solar system. However, the amplitude of these waves and their effect on the local space-time on Earth is usually so small as to be imperceptible. The first claim of the detection of gravitational waves came in 1969 (Weber, 1969), using mechanical bars that could resonate with gravitational waves, but was soon discredited. The possibility of directly detecting gravitational waves was spurred on by the first indirect detection: a measurement of the decreasing separation of a radio pulsar in a binary orbit (Taylor & Weisberg, 1982). The first direct detection of gravitational waves came in 2015, when the Laser Interferometer Gravitational-Wave Observatory (LIGO; 1.1d) detected the merger of two ~ 30 solar mass black holes from 500 Mpc away (Abbott et al., 2016). Despite radiating over 10^{56} ergs of energy as gravitational waves during the inspiral, the measured gravitational wave strain on Earth (i.e. the fraction by which lengths are stretched and compressed) was just one part in 10^{-21}. The gravitational wave detection of compact object inspirals and mergers can allow observations of these events across the electromagnetic spectrum on key discovery timescales. Furthermore, gravitational radiation can also 'shine' from astrophysical sources from which we do not expected observable electromagnetic emission, such as rotating (slightly aspherical) neutron stars (Lasky, 2015), double white dwarf binaries, and the mergers of supermassive black holes. The latter two of which are key targets for the planned space-based gravitational wave detector, the Laser Interferometer Space Antenna (LISA; Amaro-Seoane et al. 2017)

1.1 Particle acceleration & radiation

Most of the signatures we observe from the Universe are due to the motion of charged particles, of which there are two varieties: thermal and non-thermal. Thermal emission is electromagnetic radiation that is produced from all bodies of matter with a non-zero temperature T, due the random motion of particles converting thermal energy to radiation. The luminosity scales as $L_{\text{therm}} \propto T^4$, and the nature of this emission is relatively well understood after centuries of research. The content of this thesis is focused on non-thermal particle acceleration and radiation, which often powers the most extreme astrophysical transients. Non-thermal particle acceleration in shocks or electric fields leads to the production of photons, neutrinos and cosmic rays; the study of which can inform us about the nature of the particle acceleration mechanism itself. In the following, we discuss the mechanisms by which particles are accelerated and astrophysical messengers are produced.

1

(a)

(b)

(c)

(d)
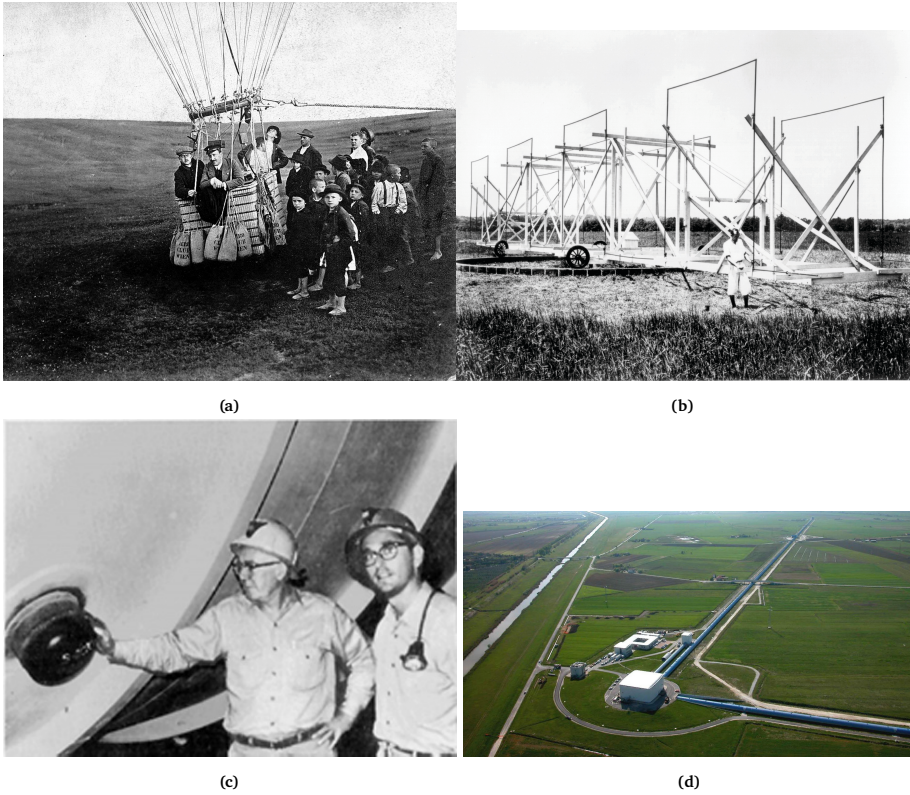
Figure 1.1: Pioneers of new astrophysical messengers. (a) 1911: Victor Hess departs from Vienna in his balloon (b) 1933: Karl Jansky with the first radio telescope (c) 1966: Davis and Bahcall with the Homestake solar neutrino experiment, (d) 2016: LIGO gravitational wave detector

1.1.1   Shock acceleration

In jetted or exploding astrophysical transients such as gamma-ray bursts (GRBs), active galactic nuclei (AGN), supernovae (SNe) and X-ray binaries (XRBs), particles are accelerated in shocks. Enrico Fermi paved the way for modern theories of particle acceleration in his attempt to explain the observed cosmic ray spectrum (Fermi, 1949). He suggested that particles could be accelerated or decelerated by way of reflection on magnetic clouds in the interstellar medium, which he referred to as 'magnetic mirrors'. On average, Fermi found that particles gain energy. This mechanism is now known as second-order acceleration, as a charged particles' mean energy gain is proportional to the square of the cloud's velocity.

In 1977 & 1978, theorists independently demonstrated a subset of (first-order) Fermi acceleration known as diffusive shock acceleration (DSA), is particularly efficient and can explain the power-law nature of the cosmic ray spectrum. In this version, stochastic diffusion across the shock front occurs via scattering from magnetic turbulence generated by the particles themselves (Krymskii 1977; Axford et al. 1977; Bell 1978a,b; Blandford & Ostriker 1978; Drury & Voelk 1981). DSA is now the canonical mechanism for high-energy particle acceleration in a range of astrophysical sources. In the following, I provide a brief explanation of the simplest version of shock acceleration.

Let us assume a charged particle with energy E undergoes n shock crossings and increases its energy by $\Delta E = \chi E$ after each crossing. The particle energy after n crossings is:

$$E_n = E_0(1 + \chi)^n \tag{1.1}$$

Rearranging Eq. 1.1, the number of shock crossings to reach a particular energy E_1 can be expressed as:

$$n = \ln\left(\frac{E_1}{E_0}\right) / \ln\left(1 + \chi\right) \tag{1.2}$$

If the probability of a particle escaping the acceleration region after each shock crossing is constant, then the probability a particle remains after n shocks is $P_{\mathrm{remain}} = (1 - P_{\mathrm{esc}})^n$. The number of particles with an energy less than E_1 can be found by considering how many remain long enough to achieve E_1:

$$N(\le E_1) = \sum_0^n P_{\mathrm{remain}} = \frac{(1 - P_{\mathrm{esc}})^n}{P_{\mathrm{esc}}} \tag{1.3}$$

Substituting for Eq. 1.2, we find that the $N_p(\le E_1) \propto \left(\frac{E_1}{E_0}\right)^{-p}$ where the value of the power-law index p depends on P_{esc} and χ. The values of these parameters depend on the specifics of the shock acceleration, but observations of cosmic rays (see Section 1.1.2) and theoretical simulations (Malkov, 1997; Bednarz & Ostrowski, 1998; Achterberg et al., 2001; Spitkovsky, 2008; Sironi et al., 2013) suggest values of $p \approx 1.8 - 2.4$.

1

1.1.2 Cosmic rays

Cosmic rays (CRs) are not rays, and most are not cosmic. They are accelerated atomic nuclei, and their discovery in the early 20th century (Hess, 1928) led to much of the theoretical research related to shock acceleration in the above subsection. We observe CRs with space and ground based detectors that utilize a variety of techniques, but because CRs are charged particles they are perturbed by the interstellar and intergalactic magnetic field. This means that observations lose not only the direction from which CRs are produced, but also the time at which they were produced: high-energy CR astronomy is (almost[3]) fully described by the observed CR flux at different energies, of CRs with different compositions.

The spectrum of CRs is observed as a powerlaw with $p \approx 2.7$ (e.g. Ryan et al. 1972) over almost 11 decades of energy, with the highest energy particles carrying roughly the same amount of energy as a 100 kilometre per hour baseball, despite being sub-atomic. In Fig. 1.2 I show the cosmic ray spectrum where the flux is scaled by a factor $E^{2.7}$, such that small deviations to the powerlaw are visible. This energy-weighted flux allows us to see the features of the spectrum: the 'knee', a softening of the spectra at around 3×10^{15} eV; the 'second knee', a further softening at around 2×10^{17} eV; and the 'ankle', a hardening of the spectrum occurring at roughly 4×10^{18} eV. These 3 features are crucial nuggets of information, and understanding their origin is an ongoing debate among cosmic ray theorists.

Cosmic ray acceleration is thought to primarily occur in astrophysical shocks (Sect. 1.1.1). By considering the fact that particles must stay confined within the shock to cross many times and be accelerated to high energies, Hillas (1984) was able to put generic constraints on the type of astrophysical systems that may accelerated CRs to observed energies. For an astrophysical source with magnetic field strength B and size L, one can quantify the Larmor radius, which is the radius of the projected motion of the particle perpendicular to the field:

$$r_L = \frac{m v_\perp}{|q| B} \tag{1.4}$$

For continuous re-acceleration in shocks, r_L should at least be smaller than the source size L, leading to the Hillas criterion, which states that the maximum energy attained by a shock accelerated atomic nuclei with Z protons is the product of the sources' magnetic field and size:

$$E_{\mathrm{PeV}} < \frac{Z}{2} \left(\frac{B}{\mu \mathrm{G}} \right) \left(\frac{L}{\mathrm{pc}} \right) \tag{1.5}$$

The average interstellar magnetic field strength is approximately $B_{\mathrm{MW}} \sim 3 \mu G$, and the Milky Way has a typical scale height of $H \sim 30$ pc. By substituting H for the Larmor radius, we can find the maximum energy of a cosmic ray that is expected to be confined within the Galaxy: $E_{\max} \sim 10^{17}$ eV. This value falls in between the 'knee' and 'second knee' breaks in the cosmic ray spectrum, and therefore it is widely accepted that around this region a transition from Galactic to extra-Galactic CRs occurs.

---

[3] It is possible to trace the highest energy CRs back to their sources, as they are deflected least in magnetic fields (e.g. (Takeda et al., 1999; Pierre Auger Collaboration et al., 2007, 2017)). It may also be possible to detect changes to the CR spectrum as a function of time, e.g. if nearby transient sources contribute significantly to the local observed spectrum.
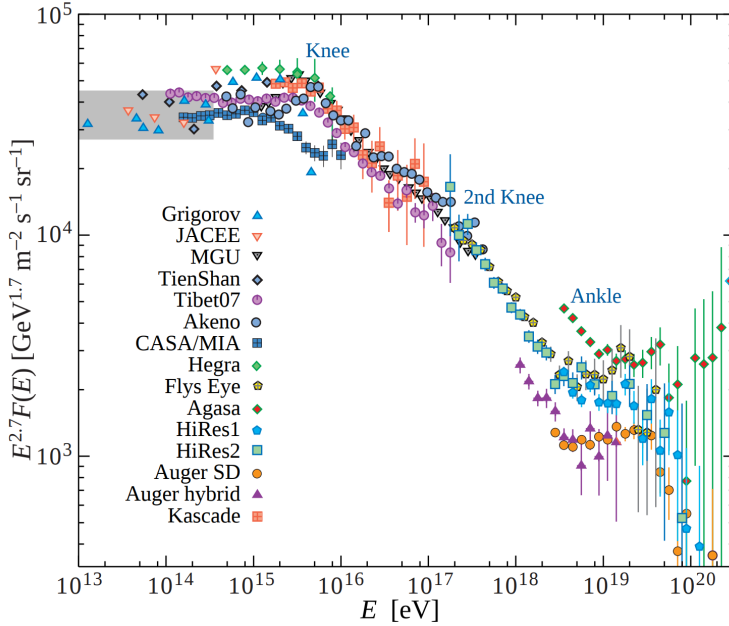
Figure 1.2: The energy-weighted Cosmic Ray Spectrum (Amsler et al., 2008). The spectrum is weighted by a factor $E^{2.7}$, such that observed breaks are very clear, which are thought to represent composition changes or transitions to new source populations.

To explain the sources of CRs, one must in general be able to explain the required luminosity, as well as the maximum possible energy. It is widely agreed that Galactic supernova remnants (SNRs) are responsible for accelerating a large fraction of CRs below the knee in the spectrum. Firstly, one can crudely estimate the SNR-accelerated CR luminosity assuming reasonable Galactic supernova rate of 1-3 per century[4] and an CR acceleration efficiency of $1-10\%$. The total Galactic CR luminosity of approximately 5×10^{40} erg s^{-1} appears to be consistent with estimated SNR-CR energy budget (Baade & Zwicky, 1934). Furthermore, recent gamma-ray observations have found smoking gun evidence for PeV acceleration of hadrons within SNR shocks (Ackermann et al., 2013). Identifying the sources of extra-Galactic CRs at the very highest energies is more difficult, primarily because the energy budget is much less constrained.

1.1.2.1 Neutrino production

Neutrinos are charge neutral particles, with a non-zero but extremely small mass (Aker et al., 2021). They are produced during radioactive decay (e.g. in terrestrial nuclear reactors) and during the fusion processes powering stars. Our Sun is a prolific neutrino producer: the solar

---

[4]Despite this estimate, the most recent supernova in the Milky Way was Kepler's supernova in 1604.

neutrino flux on Earth is approximately $10^{11}\,\mathrm{cm}^{-2}\,\mathrm{s}^{-1}$ but the interaction cross-section is so small that the vast majority propagate straight through the Earth.

Neutrinos are also produced during proton-proton and proton-photon interactions, meaning their detection can be used to trace hadronic processes in astrophysical sources. As cosmic rays do not point back to their sources (Section 1.1.2), the detection of a high-energy ($\geq \mathrm{TeV}$) neutrino from a point source represents a smoking gun signal for PeV CR acceleration[5]. The primary neutrino production channel of interest involves the interaction between a cosmic ray and an ambient proton, which produces unstable charged pions. These pions further decay to produce (anti-)muons and muon (anti-)neutrinos, where the neutrinos inherit roughly 5% of the initial cosmic ray's energy (Mannheim & Schlickeiser, 1994).

$$p_{\mathrm{CR}} + p \rightarrow p + p + \pi_+ + \pi_- \tag{1.6}$$

$$\begin{aligned} \pi_+ &\rightarrow \mu_+ + \nu_\mu \\ \pi_- &\rightarrow \mu_- + \bar{\nu}_\mu \end{aligned} \tag{1.7}$$

Multi-messenger neutrino astronomy is still in its infancy. Nevertheless, the first associations with astrophysical transients (a blazar TXS 0506+056; IceCube Collaboration et al. 2018a & a radio-loud TDE AT2019dsg; Stein et al. 2021) and the detection of an astrophysical flux of PeV neutrinos (Aartsen et al., 2013) are encouraging signs. The planned upgrade of IceCube to the second generation (Aartsen et al., 2021) promises an order-of magnitude sensitivity increase over the previous generation. This means the theoretically predicted neutrino flux of luminous gamma-ray bursts (GRBs) and tidal disruption events (TDEs) will be verifiable, as will high-energy cosmic ray accelerators within our Galaxy. Furthermore, the predicted 10 arcminute localization of PeV neutrinos will enable multi-wavelength follow-up campaigns to probe (new) classes of transients capable of high-energy cosmic ray acceleration.

1.1.3 Synchrotron radiation

The acceleration of charged particles produces an electric field, and the resulting electromagnetic waves are observable as emitted photons. For relativistic particles, it can be shown that the radiated power depends on whether acceleration is perpendicular or parallel to the motion of the particle. For a particle of charge q propagating with a Lorentz factor γ, the total radiated power is:

$$P = \frac{2q^2}{3c^3}\gamma^2(a_\perp^2 + \gamma^2 a_\parallel^2) \tag{1.8}$$

Where $a_\perp$ and $a_\parallel$ are the particle's acceleration perpendicular and parallel to its motion respectively. One way in which a particle can undergo acceleration, is by interaction with a magnetic field **B**. This radiation is known as cyclotron or synchrotron radiation in the non-

---

[5]Electromagnetic signatures of decaying pions produced during the same interaction have been observed in supernova remnants (Ackermann et al., 2013).

relativistic and relativistic cases respectively. The equation of motion of a particle with mass m, velocity $\mathbf{v}$ and charge q in an electromagnetic field is (Rybicki & Lightman, 1986):

$$\frac{d(\gamma m \mathbf{v})}{dt} = \frac{q\mathbf{v}}{c} \times \mathbf{B}$$
$$\frac{d(\gamma m c^2)}{dt} = q\mathbf{v} \cdot \mathbf{E} \tag{1.9}$$

If γ is constant, $v_\perp$, the component of particle velocity perpendicular to $\mathbf{B}$ is:

$$\frac{d(\mathbf{v}_\perp)}{dt} = \frac{q}{\gamma m c} \mathbf{v}_\perp \times \mathbf{B} \tag{1.10}$$

The solution is uniform circular motion about the magnetic field line $\mathbf{B}$, or helical motion if $v_\parallel =$ constant, with a frequency of gyration:

$$\omega_B = \frac{qB}{\gamma m c} \tag{1.11}$$

The associated acceleration is $a_\perp = \omega_B v_\perp$, and substituting this into Eq. 1.8 we find that the power emitted by a relativistic charged particle gyrating in a magnetic field with magnitude B is:

$$P_{\text{sync}} = \frac{2q^4 \beta^2 B^2 \gamma^2 \sin(\alpha)^2}{3c^3 m^2} \tag{1.12}$$

Where $\beta = v/c$ and $\alpha = v_\perp/v_{\text{total}}$ is the pitch angle subtended between the particles velocity and the magnetic field. By averaging over all pitch angles, if the astrophysical source has disorganised magnetic fields, we find that:

$$P_{\text{sync}} = \frac{4}{3} \sigma_T c \beta^2 \gamma^2 u_B \tag{1.13}$$

Here σ_T is the Thompson cross section and u_B is the magnetic energy density.

As particles move at relativistic velocities on helical paths, emission is beamed into a small cone $\delta\theta = 2/\gamma$, and in the particle's frame the pulses are separated by a time $\delta t \approx \frac{2}{\gamma \omega_B \sin(\alpha)}$. For an observer, this time is shorter by a factor $1 - \beta \approx \frac{1}{2\gamma^2}$, such that $\delta t_{\text{obs}} \approx \left(\gamma^3 \omega_B \sin(\alpha)\right)^{-1}$. This defines the critical frequency at which synchrotron emission is observed:

$$\nu_{\text{crit}} = \frac{3}{4\pi} \gamma^3 \omega_B \sin(\alpha) \tag{1.14}$$

By further consideration of the beaming effects in the highly relativistic regime (Sections 6.2 & 6.4 of Rybicki & Lightman 1986), it can be shown that the emitted power per particle per unit frequency is:

$$P(\nu) = \frac{\sqrt{3}q^3 B \sin(\alpha)}{2\pi m c^2} F\left(\frac{\nu}{\nu_{\text{crit}}}\right) \tag{1.15}$$

In two regimes above and below ν_{crit} the emission can be approximated as:

$$P_\nu \propto \begin{cases} \left(\frac{\nu}{2\nu_{\text{crit}}}\right)^{1/3} & \nu \ll \nu_{\text{crit}} \\ \exp(-\frac{\nu}{\nu_{\text{crit}}})\left(\frac{\nu}{\nu_{\text{crit}}}\right)^{1/2} & \nu \gg \nu_{\text{crit}} \end{cases} \tag{1.16}$$

1

1.1.3.1 Populations of particles

As discussed in Sect. 1.1.1, in cosmic explosions and astrophysical jets particles are often accelerated into a power-law distribution such that:

$$N(E)dE = KE^{-p}dE \qquad (1.17)$$

Where K is a normalization factor that depends on the number density of particles and can vary with the pitch angle α of the electrons. To understand the total synchrotron power spectra emitted by this distribution of particles, we can integrate Eq. 1.15 over a range of energies:

$$P_{\text{total}}(\nu) = K \int_{E_0}^{E_1} P(\nu)E^{-p}dE \propto \int_{E_0}^{E_1} F\left(\frac{\nu}{\nu_{\text{crit}}}\right)E^{-p}dE \qquad (1.18)$$

Let $x \equiv \frac{\nu}{\nu_{\text{crit}}}$, and recalling that $\nu_c \propto \gamma^2 \propto E^2$:

$$P_{\text{total}}(\nu) \propto \nu^{-(p-1)/2} \int_{x_1}^{x_0} F(x)x^{(p-3)/2}$$
$$\propto \nu^{-(p-1)/2} \qquad (1.19)$$

Where in the second line we have used the fact that the integral is approximately unity if $x_0 \approx 0$ and $x_1 \approx \infty$.

Incoherent transients where synchrotron radiation from shock accelerated particle populations dominate observed emission (i.e. some sources in the blue region of Fig. 1.3) can be described by the above equations. For exploding or expanding sources synchrotron self-absorption results in a characteristic evolution in which higher frequency radiation peaks first, followed by lower-frequency emission (van der Laan, 1966). Variations of this basic model of radio transients have been invoked to explain GRBs (e.g. Paczyński & Rhoads 1993; Sari et al. 1998), active galactic nuclei (Begelman et al., 1984), supernovae (Chevalier, 1998), X-ray binary jets (Mirabel & Rodríguez, 1999), and FRB afterglows (Metzger et al., 2019), with appropriate adaptations to account for relativistic motion, particle composition and other source specific effects.

Comment on the brightness temperature limit

The brightness temperature of an astrophysical source is defined in the Rayleigh-Jeans limit ($h\nu \ll kT$) as:

$$T_B = \frac{\lambda^2 F_\nu}{2k\Omega} \qquad (1.20)$$

Where $\Omega = \frac{4\pi r^2}{D^2}$ is the solid angle of the source. A limit to the brightness temperature of sources was first observed by Kellermann & Pauliny-Toth (1969), who studied some thirty radio sources between 30 MHz to 30 GHz. They inferred maximum brightness temperatures of between 10^{11} and 10^{12} K, a result which has become canonical in radio astronomy ever

since. Their original explanation[6] was inverse-Compton scattering, which effectively cools electrons in sources with high brightness temperatures. Relativistic electrons interact with the synchrotron photons they produce in a process known as synchrotron self-Compton scattering. The particle energy loss rate due to inverse-Compton scattering (Rybicki & Lightman, 1986) is:

$$P_{IC} = \frac{4}{3}\sigma_T c u_\gamma \left(\frac{v}{c}\right)^2 \gamma^2 \tag{1.21}$$

Where u_γ is the energy density of the synchrotron photons. Noting the similarity to Eq. 1.13, we can define $\eta = P_{IC}/P_{sync} = u_\gamma/u_B$ as the ratio of the synchrotron and inverse-Compton energy loss rates. The resulting upscattered photons provide a further photon field with which electrons may interact such that the total electron losses can be quantified in the following divergent geometric series (Melrose, 2002; Longair, 2011):

$$P_{sync+IC} = \frac{4}{3}\sigma_T c u_B \left(\frac{v}{c}\right)^2 \gamma^2 \left(1 + \eta + \eta^2 + ...\right) \tag{1.22}$$

This equation tells us that if $\eta > 1$, electrons undergo catastrophe radiation losses. The first term represents electron loss due to synchrotron radiation, the second from synchrotron self-Compton scattering, and higher order terms from electron scattering with next generation of upscattered photons[7]. The photon energy density of a source can be expressed in terms of its brightness temperature $u_\gamma \propto T_b \nu^3$ such that the brightness temperature as a function of η is:

$$T_b = \frac{4k\nu^3}{\eta c^3 B^2} \tag{1.23}$$

Assuming self-absorption, $T_b \approx \frac{\gamma m_e c^2}{3k}$ and recalling Eq. 1.13, we can rewrite B in terms of ν and T_b such that we can express the brightness temperature in terms of only the observing frequency to find that when $\eta = 1$:

$$T_{b,max} \approx 10^{12} \text{ K } \nu_{GHz}^{-1/5} \tag{1.24}$$

The brightness temperature limit can be violated by relativistic motion (Rees & Simon, 1968). For this reason relativistic sources like AGN & GRBs have brightness temperatures above the limit[8] in Fig. 1.3). Proton synchrotron radiation (Kardashev, 2000) and transient particle acceleration (Slysh, 1992) have also been suggested as ways in which a source may overcome the brightness temperature limit. These violations to $T_{B,max}$ are usually small, therefore the limit is generally used to distinguish between incoherent and coherent radiation mechanisms (e.g. Fig. 1.3), the latter of which is not bound by the constraint.

---

[6]Alternative explanations for the observed $T_{B,max}$ exist, such as the equipartion of energy (Readhead, 1994).

[7]We note this series is applicable when the photon energy in the frame of the electron is less than the electron mass energy, after which the Klein-Nishina cross-section and energy transfer suppress scattering probability and photon energy gain respectively.

[8]Relativistic sources can exceed $T_{B,max}$ by $\approx \Gamma^2$ where Γ is the bulk Lorentz factor, or by Γ^3 if the light-crossing timescale of variability is used to estimate source size.
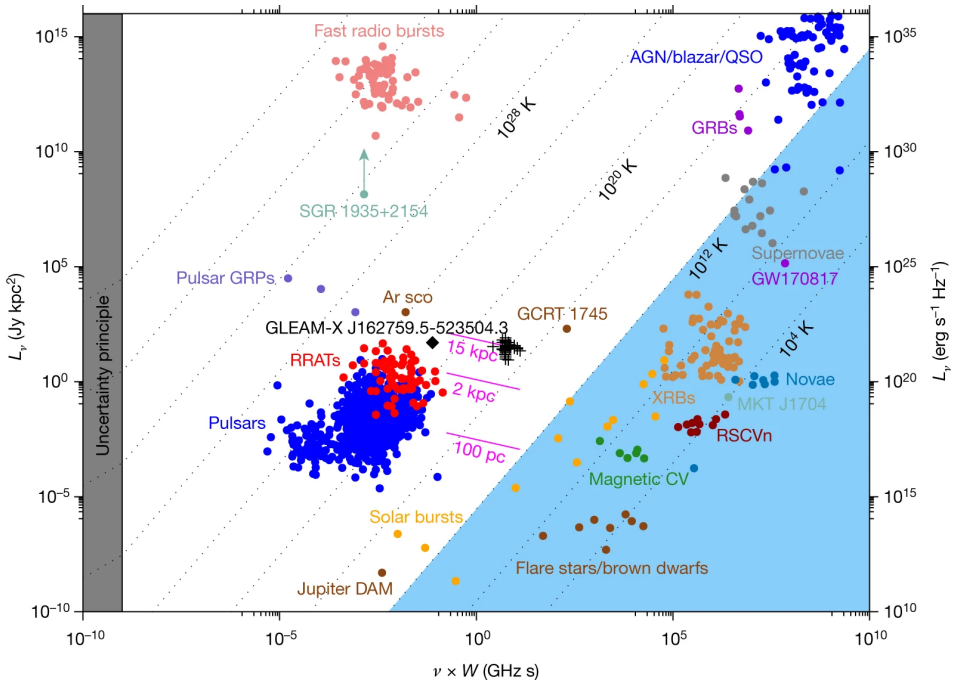
Figure 1.3: The radio transient phase space from Hurley-Walker et al. (2022), adapted from Pietka et al. (2015). The brightness temperature limit separating incoherent and coherent transients is denoted in blue, where relativistic sources GRBs and AGN violate the limit.

1.1.4 Curvature radiation

Particle acceleration occurs differently for astrophysical systems that have strong, organised magnetic fields. In this regime one cannot simply average over a pitch angle α in order to calculate the luminosity of a set of particles. Furthermore, if the magnetic field is strong enough, accelerated particles can be confined to stream along field lines. We can understand this by considering the characteristic timescale in which a particle with a pitch angle α to the magnetic field line radiates all of its energy:

$$\tau_{\rm rad} = \frac{E_{\rm particle}}{P_{\rm sync}} = \frac{3 m_e c^2}{4 \sigma_T c \sin(\alpha)^2 \beta^2 \gamma u_B}$$
$$= 10^{-18} \, B_{12}^{-2} \, \gamma_2^{-1} \, \sin(\alpha)_0^{-2} \text{ seconds} \tag{1.25}$$

We find that in strong magnetic fields particles rapidly radiate their entire energy if $\alpha \neq 0$. Therefore accelerated particles radiate away any momentum perpendicular to the field lines, and stream along pulsars magnetic field lines (i.e. $v \times B = 0$). In this case, particles can be accelerated by electric fields to very high energies. Recall that the force a particle experiences in an electric field is $F = qE$. The resultant increase in the particles' Lorentz factor is large and neglecting radiation losses can be estimated as:

$$\dot{\gamma} \approx \frac{qE}{m_e c} \approx 10^{15} \text{ s}^{-1} \, E_8 \tag{1.26}$$

The magnetic field lines along which particles propagate are usually curved. For example, pulsars and magnetars are thought to possess a dipole magnetic field, in addition to more complex multi-polar components (Sect. 1.2.1). As the particles follow these curved magnetic fields, they are accelerated in such a way that they do not deviate from the field line, and thus will radiate. In this simple definition, we define each curved field line in terms of the radius of the circle it traces out locally, known as the curvature radius $\rho_{\rm c}$. For neutron star magnetospheres, typical values range between $10^5 < \rho_{\rm c} < 10^9$ cm. Returning to Eq. 1.8, we can find the radiated power for particles accelerated along these curved trajectories. As in circular motion, $a_\perp = v^2/r$, which for a relativistic particle travelling along a field line with a curvature radius $\rho_{\rm c}$ is $a_\perp = \beta^2 c^2 \rho_{\rm c}^{-1}$ such that:

$$P_{\rm curv} = \frac{2 q^2 a_\perp^2 \gamma^4}{3 c^3} = \frac{2 q^2 c \gamma^4}{3 \rho_{\rm c}^2} \tag{1.27}$$

We can define the gyrofrequency as $\omega_{\rm curv} = \frac{v\gamma}{2\pi\rho_{\rm c}}$, and recall from Sect. 1.1.3 that the critical frequency of observed radiation is higher by a factor γ^2 such that:

$$\nu_{\rm crit,curv} \approx \frac{\gamma^3 c}{2\pi\rho_{\rm c}} \tag{1.28}$$

For particles of the same energy, curvature radiation produces much less energetic photons than synchrotron radiation. The primary reason for this is that the curvature radius of the particles' path is macroscopic and therefore emitted photons have much larger wavelengths. Accelerated particles can in general achieve very large Lorentz factors in organised magnetic

fields, which can be seen by equating the acceleration and radiation timescales to find a stable Lorentz factor in the radiation reaction regime:

$$P_{\text{acc}} = P_{\text{curv}}$$

$$qE_{\text{parallel}}c = \frac{2q^2c\gamma^4}{3\rho_{\text{c}}^2}$$

$$\gamma \approx \left(\frac{3E_{\text{parallel}}\rho_{\text{c}}^2}{2q}\right)^{1/4} \tag{1.29}$$

$$\gamma \approx 7 \times 10^7 \, E_{\text{parallel},8}^{1/4} \, \rho_{\text{c},7}^{1/2}$$

This states that an electron accelerated by an electric field while radiating curvature emission will attain nearly 100 million times its rest mass energy. Furthermore, using Eq. 1.28 one can show that each emitted photon will have an energy of approximately $E_{\text{ph}} \approx 500$ GeV $E_{\parallel,8}^{1/4}$, or nearly a million times the rest energy of an electron. As we will show in Section 1.2.1, the fact that such high energy photons can be produced via curvature radiation is a crucial component to our theoretical understanding of the pulsar magnetosphere: curvature photons' interactions with the magnetic field forms the bedrock of many theories of radio pulsar emission (Sturrock, 1971; Ruderman & Sutherland, 1975; Timokhin & Arons, 2013).

Coherent curvature radiation

It is thought that curvature radiation can also be coherent. Coherent curvature radiation is classified as an 'antenna' mechanism for coherent emission, meaning it relies on the spatial proximity of particles to invoke coherence between particles. In essence, if particles' momenta are well aligned and they are confined within one emission wavelength of each other, the electromagnetic waves which constitute their radiation can constructively interfere. This type of coherent emission means that the power of the radiation is greater than the sum of the parts. The luminosity of N coherently emitting particles is $P_{\text{coh}} = N^2 P_{\text{incoh}}$, where P_{incoh} refers to the power each particle would radiate in the absence of any coherence. In other words, N particles with charge q that are coherently emitting essentially act like one a single particle with charge $Q = qN$. It is important (and not always obvious) to note that the power radiated per particle is also higher by a factor N for coherent emission: $P_{\text{indiv,coh}} = P_{\text{total,coh}}/N \approx N P_{\text{indiv,incoh}}$. The idea of coherent curvature radiation dates back to the early theoretical attempts to explain coherent emission from pulsars (Lerche, 1970; Goldreich & Keeley, 1971; Benford & Buschauer, 1977), and more recently has been invoked to explain very high brightness temperature FRBs (Kumar et al., 2017; Katz, 2018). However, the theory relies on the existence of a mechanism by which particles can bunch together such that coherence requirements can be attained. Many suggested bunching mechanisms have come under heavy theoretical criticism (e.g. Melrose 2017; Melrose et al. 2021 and references therein).

1.2 Compact Objects

Compact objects are the remnants of massive, dead stars. When a massive star reaches the end of its life it explodes in a supernova, and the core of the star leaves behind a remnant. The mass of the remnant depends on the mass and metallicity of the progenitor. If the resulting object is more massive than approximately 1.4 solar masses, gravitational forces overcome the electron degeneracy pressure that stabilizes white dwarfs, a compact object forms (Chandrasekhar, 1931). If the mass is less than approximately 2-3 solar masses[9] a neutron star forms; larger than this and gravitational forces overwhelm the degeneracy pressure of neutrons to form a black hole (BH) (Oppenheimer & Volkoff, 1939; Bombaci, 1996).

Neutron stars, the study of much of this thesis, are extreme in almost every sense of the word. They have the highest known densities (apart from BHs), packing in roughly 1-2 solar masses within a sphere with a radius of just 12km, as well as the largest known magnetic fields (more so than the next magnetic astrophysical object by a factor 10^6). For these reasons, they give rise to a range of interesting pulses, bursts and explosions across the electromagnetic spectrum and beyond. Neutron stars are extraordinary astrophysical laboratories, with which one can probe not only macroscopic processes such as general relativistic gravitational lensing, but also the microscopic through exotic quantum electrodynamic processes only present in the strongest magnetic fields. It is thought that there are billions of black holes and neutron stars in the Milky Way alone, but only a few of the youngest are detectable on Earth, as older isolated compact objects tend not to emit radiation. In the following subsections, I briefly discuss the different categories of observable compact object that are the study of this thesis.

1.2.1 Pulsars

Isolated, rotating neutron stars with strong surface magnetic fields are observable as radio pulsars, first discovered in 1968 by Jocelyn Bell-Burnell (Hewish et al., 1968). These objects are named for the observed pulses of radio emission modulated by the spin period of the star, which are only visible when the radio beam is directed towards us. Precise timing of radio pulses over long time spans allow for measurements of the spin period of the neutron star P, but also the spin period derivative $\dot{P}$ and the double derivative $\ddot{P}$. These measurements of how a pulsar spin is changing over time allows us to crudely estimate properties such as the characteristic age and surface magnetic field of the pulsar [10]:

$$\tau_c \equiv \frac{P}{2\dot{P}} = 15.8 \text{ Myr } P_0 \, \dot{P}_{-15}^{-1}$$

$$B_s \approx \sqrt{\frac{3c^3 I P \dot{P}}{8\pi^2 R_{\text{NS}}^6} \sin(\alpha)^2} = 10^{12} \text{ G } P_0^{1/2} \, \dot{P}_{-15}^{1/2} \, R_{\text{NS},6}^{-3} \, I_{45}^{1/2} \tag{1.30}$$

---

[9]This threshold is uncertain as it depends on the specific behaviour and equation of state of extremely dense matter.

[10]Throughout this thesis, we make use of the convenient notation $X_n \equiv X/10^n$, and use centimetre-gram-second units, unless otherwise stated.

Where I is the moment of inertia, R_{NS} is the radius of the neutron star and α is the angle between the rotation axis and the magnetic moment, where we assume $\sin(\alpha) \sim 1$ in this simple example. The magnetic field estimate relies on the assumption that the pulsar is spun-down due to energy losses related to the luminosity of the dipole radiation: $L_{\mathrm{dipole}} = \frac{2}{c} \mathbf{m}^2 \Omega^4 \sin(\alpha)^2$. Pulsar emission is broadband, and some pulsars are observable across the electromagnetic spectrum to the gamma-ray wavelength (Abdo et al., 2009, 2013).

Pulsars are extremely strong magnets and are surrounded by a dipole[11] magnetic field which co-rotates with the spin of the neutron star. As electromagnetic forces are much stronger than gravitational forces surrounding a pulsar, one can model them as highly magnetised, rotating superconducting spheres. In their seminal model of the pulsar magnetosphere, Goldreich & Julian (1969) found that the magnetosphere must be densely populated with charged particles commensurate with the local magnetic field divided by the spin period. Inside the neutron star, an electric field develops that must satisfy:

$$E + \frac{\Omega \times r}{c} \times B = 0 \tag{1.31}$$

Where Ω is the angular velocity of the neutron star. A $B \times v$ electric field also exists outside the star, however the boundary condition from the surface to the magnetosphere requires $B \cdot E = 0$ outside the star. This can be satisfied by a current of charged particles that screens the electric field at all points, which can be expressed as the Goldreich-Julian number density:

$$n_{\mathrm{GJ}} = \frac{\Omega B_s}{2\pi c q} = \frac{B}{cqP}\left(\frac{R_{\mathrm{NS}}}{R}\right) \tag{1.32}$$

The co-rotation of the external magnetic field with the rotating neutron star occurs until a distance known as the light cylinder, which is the radius at which co-rotation would require the field lines to move faster than the speed of light:

$$R_{\mathrm{LC}} = \frac{cP}{2\pi} = 5 \times 10^7 \text{ cm } P_0 \tag{1.33}$$

Beyond this distance, field lines cannot be viewed as static rotating structures, and are instead considered as propagating electromagnetic waves (Fig. 1.5). Magnetic field lines can be classified in terms of whether they extend beyond R_{LC} (open field lines), or if they are completely contained within R_{LC} (closed field lines).

Despite decades of theoretical study and observation, the nature of the emission mechanism behind radio pulsars is poorly understood (see e.g. Melrose 2017). The emission is too bright to be the sum of individual particle radiation and thus coherence between particles must be invoked. Two types of pulsars are generally observable as strong radio emitters (Fig. 1.4). Recycled or millisecond pulsars are old neutron stars that have been spun up and reactivated by accretion, typically characterised by short periods of $1 - 10$ milliseconds and estimated surface magnetic fields of $B_s \approx 10^9$ G. Isolated radio pulsars are younger

---

[11]In reality, we see indications of multi-polar magnetic field components close to the surface (Bilous et al., 2019; Riley et al., 2019). As higher multipole moments drop decay more rapidly with distance from the neutron star, these components are often neglected for simplicity.
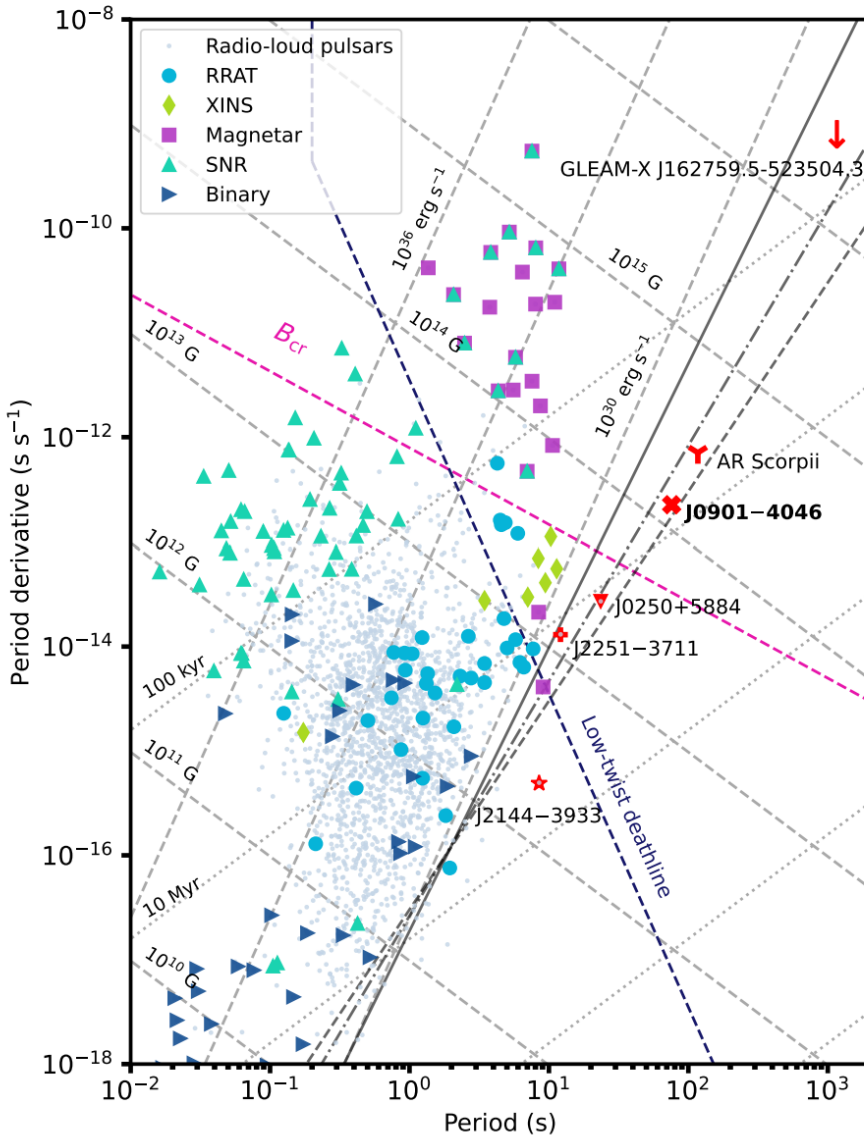
Figure 1.4: The $P - \dot{P}$ diagram of neutron stars, with magnetars in the top centre. Millisecond pulsars are shown as blue triangles in the bottom left, and isolated radio pulsars as faint blue dots clustered $10^{-1} < P < 10$s. Also shown are various formulations of the pulsar death line (e.g. Chen & Ruderman 1993), as well as the low-twist death line (Wadiasingh & Timokhin, 2019) and long period sources (e.g. Caleb et al. 2022; Hurley-Walker et al. 2022) in red.

first-time emitters, with periods of $0.1 - 1$ seconds and surface magnetic fields $B_s \approx 10^{12}$ G. These two populations are thought to be active due to a threshold value of the rotation powered electric field $E \propto \frac{B}{P}$ (e.g. Chen & Ruderman 1993) that powers the pulsar emission mechanism.
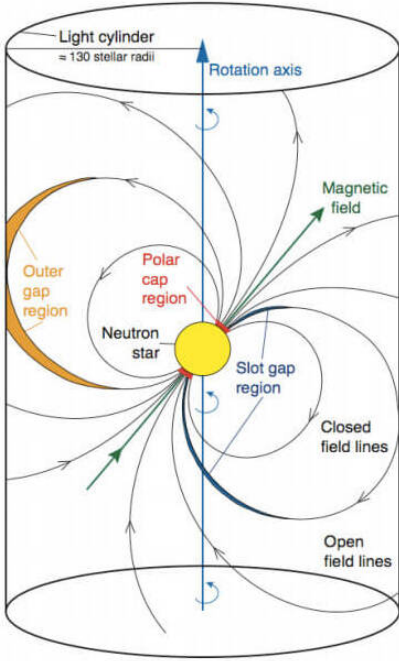
Figure 1.5: Pulsar schematic showing the external magnetic field, offset magnetic and rotational axis and the light cylinder. Highlighted are possible particle acceleration regions, namely the polar gap, slot gap and outer gap.

Coherent radio emission within the magnetosphere requires a local departure from the stable Goldreich-Julian model, which can be achieved through particle acceleration and pair cascades (Sturrock, 1971). If there exists a region in the magnetosphere where $B \cdot E \neq 0$, a component to the electric field will be parallel to the magnetic field lines $E_\parallel$ and may freely accelerate particles along the magnetic field lines. The strong magnetic fields mean that curvature radiation will be produced (see Section. 1.1.4), which results in high-energy gamma-ray photons[12] (Eqs. 1.28 & 1.28). In strong magnetic fields, photons can interact with the magnetic field to produce pairs. The mean free path of a photon with energy $E_\gamma > 2m_e c^2$ is (Erber, 1966):

$$l_\gamma = \frac{4.4\hbar^2}{m_e q^2} \frac{B_{\mathrm{QED}}}{B_\perp} \exp\left(\frac{4}{3\chi}\right) \qquad (1.34)$$

Where:

$$\chi \equiv \frac{h\nu}{2m_e c^2} \frac{B_\perp}{B_{\mathrm{QED}}} \qquad (1.35)$$

Where $E_\gamma = h\nu$ is the photon energy expressed in terms of its frequency ν, $B_{\mathrm{QED}} = \frac{m_e^2 c^3}{q\hbar}$ is the quantum critical magnetic field and $B_\perp$ is the component of the magnetic field perpendicular to the motion of the photon. Initially, curvature radiation is directed along the magnetic field lines such that $B_\perp = 0$, and pair production cannot occur. However photons traverse approximately straight paths, while the magnetic field lines diverge with a curvature radius ρ_c, meaning $B_\perp$ can be approximated as $B_\perp \approx \frac{l_\gamma B}{\rho_\mathrm{c}}$, where l_γ is the distance traversed by the high-energy curvature photon.

Pair production begins after a distance $h = l_\gamma + l_\mathrm{acc}$ where l_acc is the short length scale associated with the acceleration of pairs to energies at which they begin to emit curvature

---

[12]Note that alternative origins of gamma rays capable of pair production have been suggested e.g. inverse-Compton scattering (Daugherty & Harding, 1986).

photons with energies greater than $2m_ec^2$, i.e. capable of pair production. Ruderman & Sutherland (1975) show that in the polar gap model, the gap height, h, is approximately:

$$h \approx 5 \times 10^3 \text{ cm } \rho_{c,6}^{2/7} \, P_0^{3/7} \, B_{s,12}^{-4/7} \qquad (1.36)$$

After this distance h, pair production cascades occur, with the produced secondary pairs outnumbering the local Goldreich-Julian density by factors of $10 - 10^6$ (Harding & Muslimov, 2011; Timokhin & Harding, 2015, 2019), resulting in a high number density region with conditions conductive to coherent radiation. The exact coherent radiation mechanism is still under debate, but it is thought that non-stationary pair plasma discharges of the gap can launch superluminal electromagnetic waves, which result in the observed broadband coherent radiation (Timokhin & Arons, 2013; Philippov et al., 2020).

Two canonical regions in the magnetosphere are thought to be candidates for this gap acceleration region. First, the polar gap, defined by the open field line region at the magnetic poles of the neutron star, where a charge separated outflow might form (Sturrock, 1971; Ruderman & Sutherland, 1975). Since the magnetic field emanating from this region penetrates the light cylinder, the circuit defined by the closed field lines is incomplete and the region of $E_\parallel \neq 0$ can accelerate charges. The second possibility is the outer gap region near the light cylinder where $\Omega \cdot B = 0$. This region separates charges of different signs (Holloway, 1973), and if charges flow from this region they are not replenished, resulting in an unscreened electric field. This gap is thought to be chiefly responsible for higher energy X-ray and gamma-ray emission observed from pulsars such as the Crab (Cheng et al., 1986; Hirotani et al., 2003).

1.2.2 Magnetars

Magnetars, also historically divided in subclasses known as soft gamma repeaters (SGRs) & anomalous X-ray pulsars (AXPs), are isolated, highly magnetized neutron stars ($B_s > 10^{13}$G) that are observable primarily in the X-ray band (see Kaspi & Beloborodov 2017 for a recent magnetar review). Approximately 30 magnetars are known to exist in the Galaxy [13] (Olausen & Kaspi, 2014), and they have typical spin periods and spin period derivatives of $P = 2 - 12$ seconds and $\dot{P} = 10^{-10} - 10^{-12}$. The relatively large $\dot{P}$ is a consequence of their extreme magnetic fields and therefore large energy dissipation. Although some magnetars are persistant X-ray and radio sources (Rea et al., 2012), they are often identified during active periods in which stochastic X-ray bursts are observed. These bursts are broadly categorized by their energy as short ($E_X \approx 10^{40-41}$ erg), intermediate ($E_X \approx 10^{41-43}$ erg) or giant flares ($E_X \approx 10^{44-46}$ erg), the latter of which are very rare and have only been seen on a handful of occasions.

On the 5th of March 1979[14], two Soviet space probes (Venera 11 & 12) were blasted with an unprecedented flux of high-energy gamma-rays from SGR 0526-66 (Mazets et al., 1979).

---

[13] http://www.physics.mcgill.ca/~pulsar/magnetar/main.html. Note that some GRBs are in fact magnetar giant flares from other Galaxies e.g. Burns et al. (2021), which are not counted here.

[14] For more on the history of magnetars see: https://solomon.as.utexas.edu/magnetar.html.

The Konus gamma-ray detectors on board jumped from 100 to 4×10^5 counts per second in a millisecond. 11 seconds later the expanding sphere of gamma-rays impacted the American solar probe Helios 2 in orbit around our Sun, and then a Venus probe Pioneer, where gamma-ray detectors were saturated in both cases. Finally, 7 seconds later, it reached Earth, detected by all gamma-ray instruments in orbit. It would be 20 years later, on the 27th of August 1998 that this record gamma-ray flux would be surpassed, by a new source SGR 1900+14 (Hurley et al., 1999). This flare impacted the Pacific Ocean in the middle of the night which such intensity that the Earth's outer atmosphere was ionized, detectable in US Navy's long-wavelength radio communications (Tanaka et al., 2008). On the 27th December 2004, a third giant flare was observed from SGR 1806-20, exceeding the total energy of the previous two by a factor of 100 (Palmer et al., 2005). In all three cases, the intense flash of prompt gamma-rays was followed by a decaying tail, oscillating with a regular period of 8.0, 5.1 and 7.6 seconds respectively, attributed to a confined fireball magnetically trapped on the surface of the neutron star observable as the star spins (Thompson & Duncan, 1995).

The large values of $\dot{P}$ of the observed Galactic magnetars imply they have large magnetic fields (Kouveliotou et al., 1998) and are relatively young, which in some cases can be confirmed by observations of the supernova remnant that still surrounds them (Kothes et al., 2018). The large magnetic field possessed by magnetars is likely formed when the newly-born neutron star is rapidly rotating. Heat is dissipated from the dense, conductive inner neutron fluid through convection. If the star is born rotating very rapidly, magnetic field lines are swept up by convective motion and a dynamo action occurs. This can greatly increase the stars overall magnetic field strength in the first tens of seconds of a neutron stars life (Duncan & Thompson, 1992). For the first 10^4 years of their life, as a supernova remnant expands around them, highly magnetized neutron stars are extremely active. Persistent thermal emission is observed as charged particles stream along closed magnetic field lines and collide with the crust, heating it with such voracity that it glows in X-rays (Thompson & Duncan, 1996). Transient X-ray outbursts are also emitted, triggered by stresses or fractures in the crust that perturb magnetic field lines threaded through to the inner core (Thompson & Duncan, 1995). Occasionally, the magnetic field becomes unstable and undergoes an extreme reconfiguration of the global magnetosphere, leading to giant flares as observed in the March 5th, August 27th & December 27th events (Thompson & Duncan, 1995).

The least energetic short X-rays bursts are naturally the most common and have been studied in the most detail. These bursts last approximately 0.1 seconds on average, and their spectra can be modelled, often as a two thermal blackbodies categorized by their temperature T and area A (van der Horst et al., 2012). The distribution of time one must wait having just seen a burst to observe another is well described by a lognormal with a mean of approximately 100 seconds, and the burst energy distribution is a power law (Göğüş et al., 1999; Göğüş et al., 2000). These statistical properties are shared not only with FRBs (Gourdji et al., 2019; Hewitt et al., 2021), but also with earthquakes (Cheng et al., 1996), providing support that starquakes power magnetar bursts. This may also indicate a common origin of FRBs and magnetar bursts, describing both as self-organized critical systems (Bak et al., 1987), where the magnetar exists in a critical state with an instability threshold that dissipates energy

non-linearly. Incidentally, this model can describe a diverse range of astrophysical transients, including solar flares.

After a magnetars short active lifespan its periods decays, spinning slow enough such that no significant magnetic dissipation occurs. Many millions of dead, (ultra-)long period magnetars may be drifting through the Galaxy (or escaping it, if the kick imparted by the supernova is large enough), possibly waiting to be detected once again as slowly pulsating (Hurley-Walker et al., 2022; Caleb et al., 2022) or FRB-emitting (Beniamini et al., 2020) radio sources.

1.2.3 X-ray binaries

Most stars are born in binaries (Duchêne & Kraus, 2013), and a portion of these may stay together when the more massive, shorter-lived of the pair goes supernova (van den Heuvel, 1977). If this is the case an X-ray binary can form, a system with a compact object (either a black hole or a neutron star) and a donor star that transfers matter to the compact object. This accretion occurs either by Roche-lobe overflow, where the star swells to the inner Lagrange point separating the stars (typically from low-mass donor stars); or strong stellar winds (typically from massive stars). As the matter is gravitationally attracted towards the compact object, it is circularised due to the conservation of angular momentum, and thus an accretion disk forms (Shakura & Sunyaev, 1976).

X-ray binaries are named for the bright thermal X-rays which shine from their disks, and the observed variability across the electromagnetic spectrum is understood in terms of disk instabilities. During their outbursts, these systems trace out characteristic patterns in their evolving X-ray spectra and luminosity. Associated changes in the accretion disks drive the production of either steady, compact radio jets (Blandford & Königl, 1979) (known as the 'hard state') or transient ejecta (known as the 'soft state') which can appear superluminal (Mirabel & Rodríguez, 1994). Understanding whether and how the accretion disk (Blandford & Payne, 1982) and/or the compact object spin (Blandford & Znajek, 1977) power the jet is an open question. This disk-jet connection can be probed by multi-wavelength/messenger studies of XRB jets or their large-scale analogues AGN jets, where scale-invariant similarities are quantifiable (Heinz & Sunyaev, 2003; Merloni et al., 2003; Falcke et al., 2004a; McHardy et al., 2006a).

The jets of X-ray binaries have a flat, broadband spectrum that is attributable to shock accelerated particles. Different regions of the jet have differing plasma conditions and therefore the self-absorption peaks of the synchrotron spectrum occur at different frequencies. We observe the sum of emission from all jet regions, resulting in a flat spectrum (Blandford & Königl, 1979). It is still uncertain as to whether jet emission is powered only by accelerated leptons (Markoff et al., 2001) or if hadrons contribute (Bosch-Ramon et al., 2005; Kantzas et al., 2021), but we know at least some jets have hadronic components (Migliari et al., 2002; Díaz Trigo et al., 2013).

1

1.2.4   Neutron star mergers

Once both stars in a binary system have undergone a supernova explosion, a compact object binary may remain intact. If the stars are massive enough, these remnants will be black holes and neutron stars.

In 1974, just a few years after the discovery of the first pulsar, the first pulsar in a binary was discovered (Hulse & Taylor, 1975). Gravitational waves are emitted as the stars orbit around each other and subsequent energy loss results in orbital decay. Taylor & Weisberg (1982) found that the orbital decay of the binary pulsar was in perfect agreement with theoretical prediction of Einstein's theory of general relativity, if the binary companion is a neutron star. Despite the fact that the merger timescale before a compact object merger could occur is extremely long (10^8 years for the Hulse-Taylor binary), it was realised that some systems will merge within a Hubble time (Lattimer & Schramm, 1976; Clark & Eardley, 1977). These findings motivated the development of gravitational wave detectors, and in 2015 the first detection of a compact object merger was announced by the Laser Interferometer Gravitational-Wave Observatory (LIGO; Abramovici et al. 1992) collaboration (Abbott et al., 2016), providing the first glimpse of black holes utilizing this new messenger.

The total energy involved in the collision of two compact objects is enormous, and since the discovery of the double neutron star system many theoretical predictions related to compact object mergers have been made. Contemporaneously with the discovery of the double neutron star system, Lattimer & Schramm (1974) realised that r-process elements (that were known to be formed by neutron capture; Burbidge et al. 1957) could be synthesised in a merger event, and that the result would be consistent with observed abundances. Symbalisty & Schramm (1982) made the specific connection to NS-NS mergers, and the first models of what we now know of as kilonovae was formulated by Li & Paczyński (1998)[15]. In addition, Lattimer & Schramm (1976) & later Eichler et al. (1989) realised that some of the associated energy could be released as neutrinos, gravitational waves and gamma-rays, the latter of which was associated to the also recently discovered GRBs (Paczyński 1986; see also Section 1.2.5).

After much theoretical study, many of these long-awaited predictions were confirmed in 2017 when the LIGO collaboration reported the discovery of the first NS-NS merger (Abbott et al., 2017b). In a watershed moment for high-energy astrophysics, a gamma-ray burst was also observed 1.8 seconds later (Abbott et al., 2017c; Goldstein et al., 2017), followed by a kilonovae (Abbott et al., 2017d; Kasen et al., 2017) and subsequent multi-wavelength afterglow (Hallinan et al., 2017; Abbott et al., 2017d). The event was ground-breaking for a multitude of fields providing: an independent measurement of the mass and radius of the merging neutron stars (Abbott et al., 2018), stringent tests of the theory of general relativity (Abbott et al., 2019), the exclusion of classes of dark energy models (Ezquiaga & Zumalacárregui, 2017), and an independent standard siren measurement of the local expansion rate of the Universe, the Hubble constant (Abbott et al., 2017e).

---

[15]For a recent review on the current status of kilonovae research see: Metzger (2019)

We are at the beginning of the gravitational-wave multi-messenger revolution. The next observing runs will see new detectors KAGRA (Kagra Collaboration et al., 2019) and LIGO-India (Abbott et al., 2020) coming online to aid in the detection and localization of these gravitational wave events to enable multi-wavelength and multi-messenger follow-up. Other sources of gravitational waves at lower frequencies will be probed by the planned space-borne interferometer LISA (Amaro-Seoane et al., 2017) and pulsar-timing arrays (e.g. Lentati et al. 2015; Arzoumanian et al. 2020). The third generation of terrestrial gravitational wave detectors such as the Einstein Telescope (Punturo et al., 2010) and Cosmic Explorer (Abbott et al., 2017a) promise to localize thousands of compact object binaries, allowing population studies of multi-messenger transients.

1.2.5   Fast radio bursts (and gamma-ray bursts)

The transiently emitting compact objects discussed in the previous subsections involve known astronomical sources, where emission mechanisms can be studied theoretically by considering the properties of the objects themselves. However, when a new type of transient is discovered without a strong theoretical prediction beforehand, we must find new ways to infer the properties and mechanisms of the sources. In the late 1960s, the Vela satellites, designed to enforce the Cold War era ban on nuclear tests in space, discovered flashes of extraterrestrial gamma-rays (Klebesadel et al., 1973). The isotropic distribution of the GRBs on the sky suggested they may be cosmological, implying energies of in excess of 10^{52} ergs. Additional observations by purpose built instruments confirmed their isotropic distribution (Meegan et al., 1992), and sub-populations of long and short GRBs (Kouveliotou et al., 1993b), and soft gamma repeaters (Kouveliotou et al., 1993a). Later, observational identification of these different sub-populations with supernovae (Galama et al., 1998), neutron star mergers (Gehrels et al., 2005; Goldstein et al., 2017) and magnetars (Duncan & Thompson, 1992) respectively confirmed the progenitors of these gamma-ray events. Finally, the discovery of afterglows allowed precise localization (van Paradijs et al., 1997) and characterization of the GRB jet parameters within simple models (Wijers & Galama, 1999).

Since their discovery in 2007 (Lorimer et al., 2007), FRBs have traced a similar discovery path at an accelerated pace (Table 1.1). First, their extra-Galactic nature was confirmed through large dispersion measure (DM[16]; Thornton et al. 2013) and eventual localization (Chatterjee et al., 2017). Two flavours of FRBs were identified with the discovery of a repeating source FRB 121102 (Spitler et al., 2016) and apparently one-off bursts (The CHIME/FRB Collaboration et al., 2021a). Theorists had already identified magnetized neutron stars as likely sources of FRBs (Popov & Postnov, 2013; Lyubarsky, 2014; Katz, 2016; Beloborodov, 2017), before the discovery of a low-luminosity FRB from a Galactic magnetar SGR 1935+2154 (The Chime/Frb Collaboration et al., 2020; Bochenek et al., 2020b). For recent reviews of the state of FRB research, see Zhang (2020) & Petroff et al. (2022).

---

[16]a measurement of the column density of free electrons along the line of sight, the radio waves interact with in a characteristic frequency-dependent manner.

1

Table 1.1: A comparison between FRB and GRB discovery timelines, adapted from Zhang (2020).

	GRBs	FRBs
Are they real?	1967: Discovery 1973: Published	2007: Discovery 2013: Confirmation 2015: Microwaves ruled out
More than one type?	1979: Magnetar flares 1992: Long vs. short GRBs	2016: Some sources repeat 2019: Do all sources repeat?
Where are they?	1979: Galactic magnetars 1997: GRBs cosmological	2016: Extra-Galactic 2020: At least one Galactic
What are the progenitors?	1998: Magnetar flares 1998: lGRBs from core collapse 2005 (2017): sGRBs from NS-NS	2020: SGR 1935+2154 2022: Other FRB sources?

As of the time of writing, over 1000 FRBs have been observed (The CHIME/FRB Collaboration et al., 2021a) partially consisting of 25 repeating sources that have been identified. Around 20 FRBs have now been localized to a host galaxy[17] (e.g. Bhandari et al. 2018). FRBs are bright, millisecond-duration radio bursts, typically observed with narrow spectral bandwidths, although properties differ between repeaters and non-repeaters (Pleunis et al., 2021a) which may suggest different progenitors or emission mechanisms. After dispersion delay has been corrected for, FRBs have distinct spectro-temporal properties inclusive of scattering tails at lower frequencies and a characteristic downward drift in frequency as a function of time (e.g. Hessels et al. 2019). Approximately 90% of CHIME-observed FRBs consist of a single peak, with about 5% having two peaks and 5% having more complex morphology involving many peaks (The CHIME/FRB Collaboration et al., 2021a), or possible quasi-periodic structure (The CHIME/FRB Collaboration et al., 2021b; Pastor-Marazuela et al., 2022). Longer term periodicity has also been identified in at least one repeating FRB source, (Chime/Frb Collaboration et al., 2020) and the activity window appear to be frequency-dependent (Pastor-Marazuela et al., 2021). The aforementioned low-luminosity FRB 200428 from a Galactic magnetar constituted a leap forward in our understanding of FRBs. The burst occurred during an intense period of X-ray activity (Younes et al., 2020; Cai et al., 2022b) and a simultaneous hard X-ray burst was observed (Mereghetti et al., 2020; Li et al., 2021; Tavani et al., 2021; Ridnaia et al., 2021). This was the first observation of a multi-wavelength counterpart to an FRB, challenging and constraining our best theories of how FRBs are powered (Lu et al., 2020; Margalit et al., 2020a).

The challenge for theorists is two-fold: to explain the sources of FRBs and the radiation mechanism that powers them. The enormous true (beaming-corrected) energy of GRBs is roughly 10^{52} erg, which meant that the energy alone requires extreme events involving a decent fraction of the rest-mass energy of stellar objects. Comparatively, FRBs are energetically cheap ($\approx 10^{40}$ erg), meaning that theorists had the freedom to invent a myriad of possible FRB

---

[17]https://frbhosts.org/.
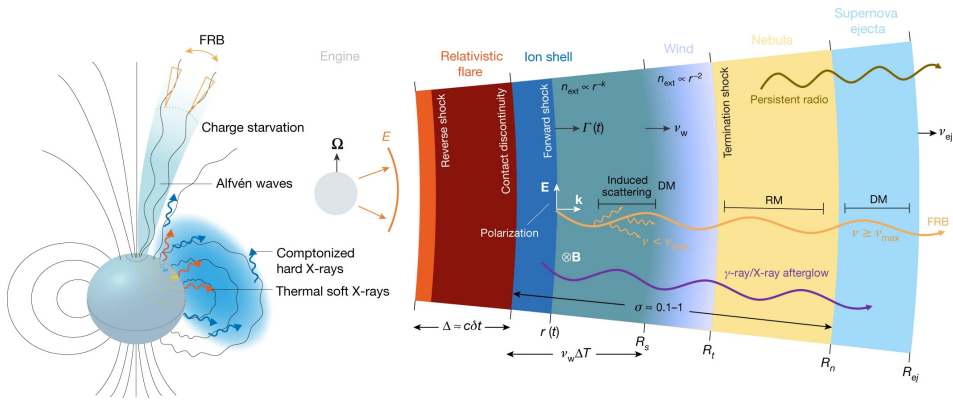
Figure 1.6: Schematic from Zhang (2020) (adapted from Metzger et al. 2019; Lu et al. 2020) showing the coherent curvature radiation model (left) and the synchrotron maser shock model (right) of FRBs from magnetized compact objects.

sources (see e.g. Platts et al. 2019), ranging from superconducting quantum strings (Vachaspati, 2008) to Schwinger pair sparks (Lieu, 2017). Fortunately, there are some obvious candidate progenitors, namely magnetars. Firstly, all known luminous ($L_\nu > 10^{15} \, \mathrm{erg\,s^{-1}Hz^{-1}}$) coherent transients are powered by neutron stars. FRBs, as the most extreme example of coherent radiation, are likely powered by magnetars which are the most extreme example of neutron stars. Furthermore, as mentioned in Section 1.2.2, the global wait-time distribution and luminosity function of the much higher energy X-ray magnetar burst population appear to be shared with the repeating FRB population.

There are two broad classes of theories at the forefront of our theoretical understanding of the FRB radiation mechanism, both primarily invoking magnetars as the most likely progenitors. These classes of current models are referred to as the 'far-off' and 'magnetospheric' models (see Fig. 1.6 for schematic examples of each) and are deeply rooted in GRB and pulsar theory respectively. In both models, an event on the crust of the neutron star dissipates magnetic energy in a manner similar to that which is thought to power magnetar flares (Thompson & Duncan, 1995). In the 'far-off' models, the resultant flare is relativistic and leads to magnetized shocks. In this scenario a simulated emission process known as a synchrotron maser forms, emitting bright coherent millisecond radiation behind the shock front at large distances from the central compact object (Lyubarsky, 2014). This kind of coherent maser emission has been shown to emit FRB-like radiation in 1D (Plotnikov & Sironi, 2019) and 3D (Sironi et al., 2021) particle-in-cell (PIC) simulations of relativistic, magnetized shocks; a finding that was predicted long before the discovery of FRBs (Langdon et al., 1988; Hoshino et al., 1992; Gallant et al., 1992; Usov & Katz, 2000). It has been suggested that this model can explain the prolific first repeater FRB 121102 (Beloborodov, 2017; Margalit & Metzger, 2018), as well as the Galactic FRB 200428 (Margalit et al., 2020a) from SGR 1935+2154. The synchrotron maser shock model also predicts a multi-wavelength afterglow (Metzger et al., 2019) similar to GRBs (Sari et al., 1999) but at lower energies and

with inefficient particle acceleration. Such an afterglow may provide observational paths to verify (or falsify) the theory if the afterglow is bright enough and our telescopes are fast enough.

Magnetospheric models of FRBs often require an transient acceleration region of unscreened electric field within the magnetosphere, similar to polar gaps in pulsars. One plausible method is to invoke the dissipation of magnetic energy stemming from a spontaneous crustal or magnetospheric event. This magnetic energy propagates away from the magnetar in the form of Alfvén waves into regions of lower charge density, where the current required to screen the associated electric field is not sufficient (Kumar & Bošnjak, 2020). Due to this charge starvation, an $E_{\parallel}$ field develops which results in the acceleration of charged particles along magnetic field lines. If the particles' spatial distribution is inhomogenous (through e.g. radiation reaction or two-stream instability; Lu & Kumar 2018), bunches of particles necessary for coherent curvature radiation can form. The nature of how particles can bunch up, and whether this is physical, is as hotly debated now (Melrose et al., 2021; Lyubarsky, 2021; Lyutikov, 2021) as it was when the theory was first proposed to explain pulsars (Melrose, 1981; Larroche & Pellat, 1987). Despite this, magnetospheric theories of FRB radiation can more easily explain the peculiar aspects of observed FRBs including downwards drift in frequency and time (Wang et al., 2019), coincident high-energy emission (Yang & Zhang, 2021; Cooper & Wijers, 2021), nanosecond variability (Nimmo et al., 2021) and closely separated but distinct sub-bursts (Lu et al., 2020).

It is unlikely that either of these theories are completely correct and can describe the behaviour of all FRBs, chiefly as it appears today that could be many different FRB progenitors. No theory of prompt GRB emission or radio pulsar emission has yet to convincingly explain either phenomenon, and it may be the case that decades pass before FRB radiation is understood. Although new instruments such as DSA-2000 (Hallinan et al., 2019) and CHORD (Vanderlinde et al., 2019) promise to discover more FRBs than ever before, conclusive answers to open questions could come from elsewhere. For example, multi-wavelength observations of localized sources; either sensitive measurements of extra-Galactic repeaters or rapid follow-up of nearby one-off FRBs may detect predicted (or unanticipated) counterparts. Other answers could come from somewhere unexpected, such as multi-messenger observations of neutrino and gravitational wave transients, or interdisciplinary theoretical advances.

1.3   This Thesis

In this thesis, I have sought to understand how particles behave and emit close to black holes and neutron stars. One of the unifying themes of this thesis is to predict multi-wavelength and multi-messenger counterparts to transient phenomena which will enable a better fundamental understanding of particle acceleration.

In Chapter 2, we examine the Galactic population of black hole X-ray binaries (BH-XRBs). Our aim is to understand whether their jets could accelerate hadronic particles to high energies, which are be observable on Earth as CRs. We estimate the total CR energy budget

of BH-XRB jets within the Milky Way, making use of the fundamental plane radio/X-ray BH activity, in addition to recent population estimates from X-ray observations and population synthesis simulations. Using the *DRAGON* CR propagation code, we find the expected contribution to the CR and diffuse neutrino spectra given various model parameters, constrained by local CR measurements and Galactic centre observations. We find that XRB jets can be responsible for a fraction (1-10%) of observed high-energy CRs. Moreover, we suggest that it is plausible that XRB jets could accelerate particles above the knee in the spectrum, and the second knee break could be attributed to the XRB accelerated CR cut-off. We further find that any significant second Galactic CR component above 1 PeV will be verifiable by a break in the diffuse Galactic neutrino spectrum observable by IceCube in the coming years.

In Chapter 3, we investigate the coherent curvature radiation emission mechanism as invoked to explain transient pulsar emission and FRBs. We find that the necessary conditions that constrain the spatial & momentum properties of a set of coherently radiating particles can be used to understand the extent to which individual particles' paths are perturbed. We find that individual particles propagate on helical paths, a departure from the previous assumption that particles' propagate directly along the curved magnetic field lines of neutron stars. By considering when coherence conditions break down, we can express a maximum coherent bunch luminosity in terms of the spin and magnetic field strength of the emitting neutron star. Furthermore, we predict a weak high-energy component to coherent radio emission that is nominally emitted in the X-ray and gamma-ray bands. We apply our results to the most extreme known coherent radiation, namely the nanoshots observed from the Crab pulsar and the FRB-like burst from SGR 1935+2154. We find that in the former case, the origin of the nanoshot must be very close to the NS surface. In the latter case, the coincident X-ray burst could plausibly be explained by our predicted high-energy component, and thus could be a test of whether the emission is indeed powered by coherent curvature radiation.

Chapter 4 is focused on the prospects for detecting coherent pre-merger emission from compact object mergers, where one component is a high magnetic field neutron star. We adapt and correct a literature model of the electrodynamics of the inspiral to map the particle acceleration regions where coherent radiation could be produced. We consider two possible coherent emission mechanisms: a pulsar-inspired model of particle acceleration and radiation, as well as a curvature radiation alternative. We estimate the radio luminosity using the power of the primary accelerated particles as a proxy, and make viewing-angle dependent light curves based on the temporal evolution of the electrodynamic model. We find that coherent radio emission is directly along locally deflected magnetic field lines and has a characteristic temporal morphology which depends on the observer's inclination angle and the magnetic obliquity of the system. The pre-merger radio luminosity depends strongly on the surface magnetic field of the magnetized neutron star and the efficiency of the conversion of primary particles' energy to coherent radio emission. In the second half of the chapter we provide a comprehensive overview of the ways in which pre-merger coherent radio emission could be detected by current and future observatories. Specifically we look at detection prospects in blind FRB searches and rapid triggered observations of gravitational-wave

events or gamma-ray bursts with low-frequency radio observatories. We find that current and planned wide-field FRB searches could detect such emission particularly if magnetar-strength neutron stars merge, which we consider plausible given recent observations of long period magnetars and theoretical evolutionary channels. We further find that triggered observations of short GRBs have already probed optimistic models of the predicted radio emission and that upgraded low-frequency radio telescopes could detect the emission in the next gravitational-wave observing runs. Finally, we discuss whether multi-wavelength follow-up could confirm a merger-origin of a sub-population of FRBs. We consider models of both radio afterglows and kilonovae and advocate for multi-wavelength follow-up of nearby, localized one-off FRBs expected from the next-generation of FRB instruments.

In Chapter 5 of this thesis, we present LOFAR imaging observations taken during the April/-May 2020 active phase of SGR 1935+2154, after the Galactic FRB 200428. We report the non-detection of both persistent and transient low-frequency emission from the source in the hours and months following the FRB. Our observations coincided with one X-ray burst, for which we place limits on the fluence ratio between radio and X-ray emission. We suggest that similar observations could be used to constrain both the Lorentz factor of the emission region in magnetospheric models of FRBs, and the radio afterglow in maser-shock models of FRBs. For the latter, we analyse the predicted multi-wavelength afterglow expected in the synchrotron maser interpretation of FRB 200428. We find that early optical limits rule out simple versions of the afterglow in a constant external density medium case, but adaptations to the model may mitigate these constraints. We also suggest further adaptations to the model, including non-thermal particle acceleration at late-times. We conclude with a discussion on the outlook of the verifying the maser-shock model through follow-up observations of Galactic and nearby extra-galactic FRBs.

Chapter **2**

High-energy cosmic ray production in X-ray binary jets

A. J. Cooper, D. Gaggero, S. Markoff, S. Zhang

Abstract

As smaller analogs of Active Galactic Nuclei (AGN), X-ray Binaries (XRBs) are also capable of launching jets that accelerate particles to high energies. In this work, we reexamine XRB jets as potential sources of high-energy cosmic rays (CRs) and explore whether they could provide a significant second Galactic component to the CR spectrum. In the most intriguing scenario, XRB-CRs could dominate the observed spectrum above the so-called "knee" feature at $\sim 3 \times 10^{15}$ eV, offering an explanation for several key issues in this transition zone from Galactic to extragalactic CRs. We discuss how such a scenario could be probed in the near future via multi-messenger observations of XRB jets, as well as diffuse Galactic neutrino flux measurements.

2.1   Introduction

The origin of Cosmic Rays (CRs), high-energy particles from beyond the solar system, is a century-old puzzle (Ginzburg & Syrovatskii, 1964; Berezinsky et al., 1990; Blasi, 2013). We are yet to firmly identify classes of astrophysical sources able to accelerate hadronic cosmic particles up to extremely high energies; much larger than those accessible by terrestrial accelerators.

Spectral features in the locally observed all-particle CR spectrum can shed light on this mystery. The observed spectrum follows a power law with an index of $p \approx -2.7$ over many decades of energy. However, over years of observation, small deviations with respect to the power law have been identified as follows: *the knee*, a softening of the spectra at 3×10^{15} eV; the *second knee*, a further softening at around 2×10^{17} eV, and *the ankle*, a hardening of the spectrum occurring at roughly 4×10^{18} eV (Blasi, 2013).

It is commonly thought that Galactic sources are able to accelerate hadrons up to the knee, with Supernova Remnant (SNR) shocks as the prime candidates, yet many aspects of this picture are far from clear. CR paths are deflected in the Galactic magnetic field and therefore we cannot directly trace them back to their source. To this end, indirect "smoking gun" signals, including characteristic TeV γ-ray spectra from pion decay channels, can be observed to verify CR acceleration sites. Although observations of X-ray filaments (Vink & Laming, 2003) and γ-ray spectra from old SNRs (Ackermann et al., 2013) suggest that protons are efficiently accelerated at these sources, it is not clear whether SNRs can universally attain the crucial PeV energies required to explain the softening at the knee (see e.g. the recent discussion in Gabici et al. 2016; Ahnen et al. 2017b and references therein). In the context of the SNR hypothesis, one of the key ideas to explain the knee and second knee features is rigidity-dependent diffusive shock acceleration (DSA), in which the maximum possible energy of a given CR species depends on its atomic number Z such that $E_{max}(Z) = Z * E_{max}(1)$. This has had success in explaining the second knee feature in terms of the cut-off of accelerated iron nuclei, as extensively discussed in the literature for many decades (see e.g. the early discussion in Peters 1961).

Besides the nature of the knee, we are still left with many open issues regarding the potential Galactic CR component. In particular, the origin of CRs between second knee and ankle, and the location of the transition from Galactic to extragalactic CRs remains unclear. One possibility is that the extragalactic component is dominant all the way down to 10^{17} eV, requiring the ankle feature to be a peculiar extragalactic propagation effect. However, alternative models also exist, mostly based on the assumption of energy-dependent leakage of high-energy cosmic rays from the Galaxy (see, for instance, Giacinti et al. 2015), which look to negate the need for an extragalactic CR component to dominate down to the second knee. Another option that has been put forward is the existence of a second Galactic component that "fills the gap" (see Fig. 2.1). Taking this additional component into account, as discussed e.g. in Hillas (2005) and Gaisser et al. (2013), it is possible to provide a complete and consistent description of all the features from the knee to the ankle. Possible candidates for such high-energy Galactic components include strong Galactic winds (Jokipii & Morfill,

1987), newborn pulsars (Fang et al., 2013), Galactic γ-ray bursts (Levinson & Eichler, 1993), Wolf-Rayet star supernovae (Thoudam et al., 2016) and many others.

Recently, this idea of a second Galactic CR component has been bolstered by new composition measurements that favour a strong light composition at around 10^{17} eV. For instance, in Buitink et al. (2016), a novel dataset based on 150 days of radio observations of CR-induced extensive air showers (EAS) made with the Low Frequency Array (LOFAR) implies a significant light-mass component in the $10^{17} - 10^{17.5}$ eV range. The authors suggest this composition dip likely necessitates a primarily proton-dominated Galactic component which can reach approximately these energies. Measurements from different types of surface detectors including HiRes, Auger, Telescope Array, and KASCADE-Grande data (Pierre Auger Collaboration 2014; Hanlon 2019; reviewed in e.g. Kampert & Unger 2012), are compatible with these recent findings, and clearly outline a decrease of the average mass of cosmic rays towards the ankle.

In this paper we follow this line of inquiry and explore whether X-ray binary (XRB) jets, given the expected total overall power and maximum energy cut-off, could be viable candidates for the second Galactic source of CRs. Cosmic ray acceleration in XRB jets has been previously explored by Heinz & Sunyaev (2002) and later by Fender et al. (2005), yet largely neglected since. In light of increasingly detailed multi-wavelength studies of many more XRB jets (Tetarenko et al., 2016a; Corral-Santana et al., 2016), which help constrain population statistics, as well as in anticipation of the next-generation of VHE γ-ray, neutrino and CR observatories, we revisit the possibility of CR production in XRB systems. We focus on the energy budget available for CR acceleration in all Galactic XRB jets and the maximum energy these XRB-CRs could attain, as these are the crucial inputs to determine a potential CR contribution. As mentioned, CRs are deflected in Galactic magnetic field and thus do not point back to their sources. To this end, we also investigate multi-messenger possibilities of verifying or falsifying XRB jets as a significant source of CRs.

2.2   X-ray Binary jets as cosmic ray accelerators

Active Galactic Nuclei (AGN), also powered by accreting black holes, are a natural analogues to XRB jets and their similarities are starting to be quantifiable (Merloni et al., 2003; Falcke et al., 2004a; McHardy et al., 2006b; Plotkin et al., 2012). These systems have the theoretical capability to accelerate ultra high-energy CRs (Hillas, 1984; Matthews et al., 2019), and we are beginning to see multi-messenger hints of extreme particle acceleration occurring either in the jets of AGN or at the termination shock sites (Pierre Auger Collaboration et al., 2008; HESS Collaboration et al., 2016; IceCube Collaboration et al., 2018b). AGN jets are some of the prime candidates of the ultra high-energy extragalactic CRs and it is plausible that in the scaled down XRB jets we might expect similar CR production at lower energies, assuming similar physical processes occur across mass and luminosity scales.

Since their discovery as superluminal sources (Mirabel & Rodríguez, 1994) XRB jets have been shown to accelerate leptons to very high energies in the jet-dominated hard state, where high-energy radiation is associated with extremely energetic electrons up to 100s TeV.

2
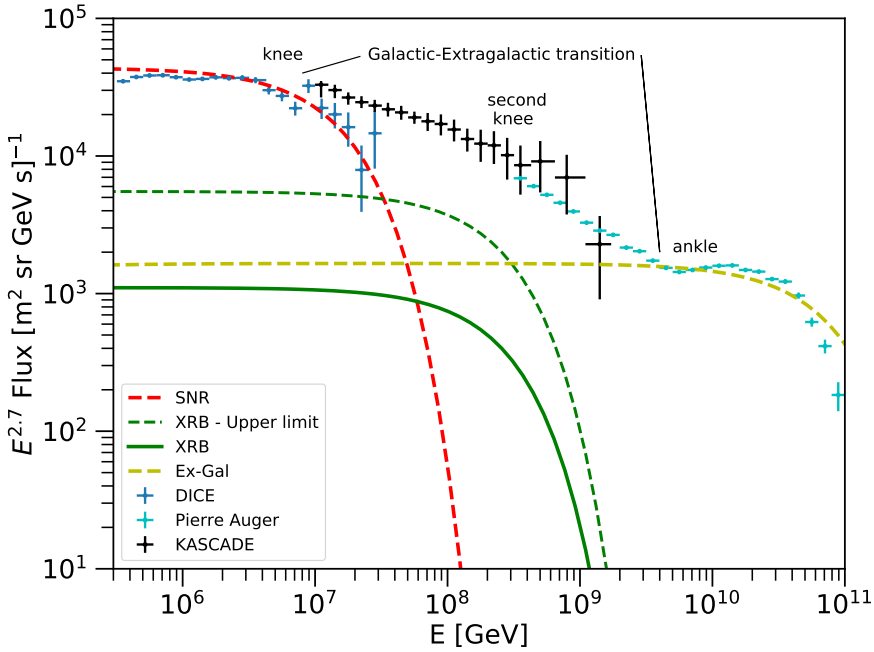
Figure 2.1: Schematic of a 3 source component all-particle cosmic ray spectrum. The components are SNR-CRs (red), XRB-CRs (this work; green) and a canonical extragalactic component (yellow). The green line reflects an XRB-CR contribution with a total power of approximately 10^{38} erg/s, using the reasonable parameters in the middle column of Table 2.1. The dashed green line represents the upper limit of the allowed XRB-CR power as discussed in Section 3, using the upper parameters in Table 2.1. Such a contribution is dominant around 10^{16-17} eV, and could be probed via composition measurements. Here we have assumed all sources share the same powerlaw index of accelerated CRs. Allowing a slightly harder spectra for XRB-CRs mean they could explain the entire CR flux at the second knee without violating energetic constraints.

The most characteristic examples are Cygnus X-1 (Zanin et al., 2016), Cygnus X-3 (Tavani et al., 2009) and recently SS 433, which was resolved in the TeV range (HAWC Collaboration et al., 2018; Sudoh et al., 2019). Models of jet emission therefore require very high-energy electrons as sources of X-ray and γ-ray emission (e.g Markoff et al. 2005; Bosch-Ramon et al. 2006; Zdziarski et al. 2014). Shocks propagating in the jet likely accelerate charged particles to very high energies in a process known as diffusive shock acceleration (DSA) (Krymskii, 1977; Bell, 1978b), although other acceleration mechanisms such as magnetic reconnection could play a role (Sironi et al., 2015b). Such particle acceleration may occur at any point along the jets, and the signature flat/inverted radio spectra suggests that continuous re-acceleration of radiating particles is required throughout the jet to combat adiabatic losses (Blandford & Königl, 1979; Malzac, 2014; Péault et al., 2019). Some authors have proposed specific zones offset from the black hole where this continuous acceleration initiates, such as near the base of the jet, or in a termination shock at jet-ISM working surface (Heinz & Sunyaev, 2002; Fender et al., 2004; Markoff et al., 2005; Bordas et al., 2009; Russell et al., 2014; Zdziarski et al., 2014).

Although leptonic processes such as inverse-Compton scattering might be the dominant mechanism for such high-energy emission, hadronic particles may also significantly contribute. XRB jets are fed from accretion disks and stellar winds, presumably hadron-rich environments, yet the composition of XRB jets is still unclear. Observational evidence of Doppler shifted atomic line emission at relativistic velocities (Margon et al., 1979; Migliari et al., 2002; Díaz Trigo et al., 2013; Díaz Trigo et al., 2014) suggests that at least some Galactic XRB jets have hadronic components, but whether this is ubiquitous is unknown. Protons/ions present in the jets will also undergo shock acceleration and in fact would attain much higher energies than electrons due their lower cooling efficiency compared to leptonic counterparts. Some authors suggest proton energies above 10^{15-16} eV are achievable in XRB jets, considering loss-limited acceleration due to radiative and adiabatic processes (Romero & Vila, 2008; Vila & Romero, 2011; Pepe et al., 2015). If efficient particle acceleration occurs in jets and a hadronic component is present, then a high-energy population of accelerated protons and ions is likely, making XRB jets promising candidate cosmic ray sources.

2.3   Population and CR power of Galactic XRBs

The most important factors when considering generic CR sources are the total available CR power and the maximum attainable CR energy that the source can generate. The former relies on understanding the population and energetics of typical systems. While the latter cannot be directly determined at this time, recent improvements in the modeling of multi-wavelength data of XRBs is providing more realistic constraints on cooling rates, and thus potential CR energies. We consider a model for the entire Galactic XRB population, and try to understand the potential total ensemble power. By considering the global energetics and estimating the proportion of power available for CR acceleration, we can estimate the CR flux and evaluate whether XRBs could reasonably account for a significant Galactic CR contribution.

XRBs come in four varieties, categorized by the compact object (either a black hole; BH, or neutron star; NS), and the companion star (low-mass; LM, or high-mass; HM). The outflows of each category of system depend strongly on the nature of their accretion. X-ray binaries with LM secondaries accrete via Roche lobe overflow, and thus undergo frequently recurring transient outbursts. Thermal-viscous instabilities developing within the accretion disk give rise to outburst cycles (e.g., Lasota, 2001). When observed in the X-ray waveband, a LM-XRB will evolve through a number of distinct accretion states defined by the source spectrum and luminosity (Remillard & McClintock, 2006). Comparatively, XRBs with HM secondaries tend to persistently accrete matter via strong stellar winds (with some notable exceptions; see e.g., Tetarenko et al. 2016a) and thus have somewhat more continuous outflows. The initial mass function (IMF; Salpeter 1955; Kroupa 2001) states that low-mass stars are far more common than high-mass stars. Therefore BHs, which generally require more massive progenitors, are less common than NSs. Thus we expect many more NS-XRBs than BH-XRBs, as well as more systems with LM companions than HM companions. These distributions are encapsulated in population synthesis codes (e.g. Belczynski et al. 2008; Paxton et al. 2011; Spera et al. 2015), which use the IMF, stellar evolution and binary interaction models to predict Galactic population statistics for each type of XRB.

This being said, Fender et al. (2005) suggest that BH-LMXRB may actually dominate XRB-CR production despite the fact that they are less numerous in the Galaxy. The reason for this stems from the fact that their primarily due to their powerful radio jets implying large amounts of energy available. However, the number of BH-LMXRBs in the Milky Way is poorly constrained, with population synthesis predictions ranging from 10^2 to 10^5 (e.g. Pfahl et al. 2003; Kiel & Hurley 2006; Yungelson et al. 2006; Sadowski et al. 2008). Unfortunately the large range of estimates is due to the uncertainties associated with modelling stellar evolution, particularly common envelope and SNe kick phases.

The most recent population synthesis results from Olejak et al. (2019) suggest 1.2×10^5 binaries involving a BH and main sequence star exist in the disk of the Milky Way. However, it is not immediately clear how many of these systems are actively transferring mass and could therefore be classed as XRBs. To understand this, we used the synthetic black hole catalog database provided by Olejak et al. (2019) [1] to look at all binary systems containing a main sequence star and a black hole. For each of these systems, we looked up the binary separation, a, and approximated the radius of the main-sequence star from its mass. We estimate the proportion of the binaries which are actively transferring mass via Roche Lobe overflow by counting only those systems in which the radius of the main sequence star extends beyond the first Lagrangian point, L_1, of the system. We make use of the fitted formula of Plavec & Kratochvil (1964) for the distance b_1 between L_1 and the centre of the primary:

$$\frac{b_1}{a} = 0.5 - 0.227 \log(q) \tag{2.1}$$

Where q is the binary mass ratio. Given this criteria, we find 5531 XRBs in the model A datasets, and 5501 in the model B datasets, where the models differ slightly in the treatment

---

[1] available at: https://bhc.syntheticuniverse.org/

of the common envelope phase. The vast majority of the XRBs are found in the Galactic disk. All the XRBs found in the datasets had main sequence stars of less than $10M_\odot$ and so can be in general considered BH-LMXRBs.

Recent observations suggest many more such systems may exist in the Galaxy than previously thought (Corral-Santana et al., 2016; Tetarenko et al., 2016b; Hailey et al., 2018). In particular, based on recent *NuSTAR* observations, Hailey et al. (2018) suggest that $300 - 1000$ BH-LMXRB might exist in just the central parsec of the Milky Way, and as such lower estimates from population synthesis simulations may be disfavoured. Given our population synthesis analysis, the density cusp in the Galactic centre and the uncertainties involved, we suggest 10^4 is a reasonable upper limit for the Galactic XRB population, as reflected in Table 2.1. While we take 10^3 as a conservative lower estimate for the total number of Galactic BH-LMXRB in this work, we note that only ~ 60 BH-XRBs have been (observationally) confirmed to exist in the Galaxy [2]. Thus the true Galactic BH-LMXRB population remains a major source of uncertainty in our calculations. Furthermore, XRB outburst durations are typically on the order of months (Tetarenko et al., 2016a), yet CRs take Myrs to propagate through the Galaxy. Therefore predictions made based on current observations make the implicit assumption that the Galactic XRB population has not changed significantly in that time frame.

The fraction of an XRB jet's total power transferred to CR acceleration, the CR luminosity L_{CR}, also involves many parameters lacking strict uncertainties. To estimate the realistic range of values of L_{CR}, we use plausible ranges for each parameter. We adopt the method used in Fender et al. (2005), using an outburst-oriented approach to incorporate advances in recent population studies, particularly the Watchdog database[3] (Tetarenko et al., 2016a). We simplify our calculations by only considering CR acceleration for BH-LMXRB systems in the hard, compact jet state[4]; as this is when we expect steady, particle accelerating outflows. By considering only the hard, compact jet state, we can obtain a conservative lower limit of L_{CR}. Realistically, particle acceleration is also expected in other accretion states. In particular, the higher luminosity intermediate state, where transient jets and ejections are observed (e.g. Miller-Jones et al. 2012; Tetarenko et al. 2017; Russell et al. 2019), will likely contribute to L_{CR}. However, given the comparatively short lifetime of the intermediate compared to hard accretion states in BH-LMXRBs (i.e., $t_{IMS} \sim 1 - 10$ days, $t_{HS} \sim 20 - 50$ days; Tetarenko et al. 2016a), we do not believe the inclusion of the intermediate states will significantly alter our estimate of L_{CR}.

The following equation gives us an estimated total power of CRs, in units of the Eddington luminosity, from a set of N similar BH-XRB systems where $M_{BH} = 10M_\odot$:

$$L_{CR} = \frac{1}{2} \cdot \eta \cdot \delta t \cdot A \cdot \left(\frac{L_X}{L_{edd}} \right)^{\frac{1}{2}} \cdot N \tag{2.2}$$

---

[2]BlackCat BH-XRB catalog: http://www.astro.puc.cl/BlackCAT/

[3]available at: http://astro.physics.ualberta.ca/WATCHDOG/

[4]Note that in Tetarenko et al. (2016a), the hard, compact jet state is referred to as the "Hard (Comptonized) State" (HCS).

2
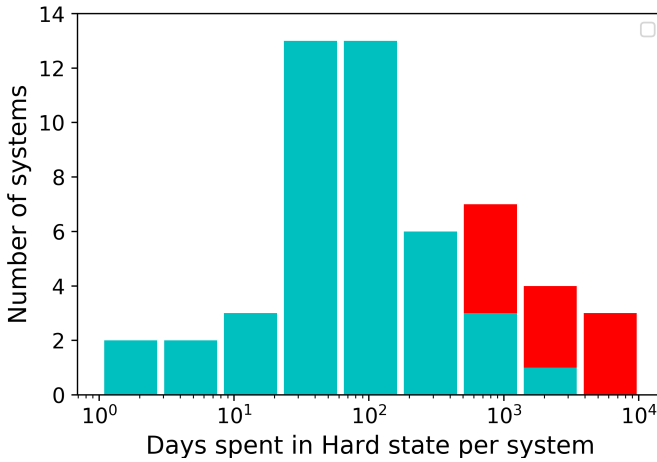
Figure 2.2: Histogram showing the number of days spent in the hard state for all known BH-XRBs over the entire 19 year period; in blue transient systems and in red persistent systems (Tetarenko et al., 2016a).

Here, the factor of $\frac{1}{2}$ comes from the fact that we naively assume an equipartition between particles and magnetic fields, as well as sharing of the energy budget between leptons and hadrons. This gives us $\frac{1}{4}$ of the available power for hadronic acceleration, multiplied by two as there are two similar jets in each system. η is the acceleration efficiency, i.e. how much of the jet power is transferred to high-energy particles via acceleration mechanisms, for which we take a canonical value of 0.1 as supported by simulations (Caprioli & Spitkovsky, 2014). As our model is based on outbursts, δt represents the hard state duty cycle of the systems. This factor is the average amount of time an BH-XRB spends in the hard state; the state in which we expect steady, compact jets which efficiently accelerate particles.

To estimate δt, we utilize the data collected in Tetarenko et al. (2016a), in which the authors catalogued X-ray observations of all known BH-XRB over the last 19 years. In Table 15 of Tetarenko et al. (2016a), we find detailed outburst statistics for 52 systems; 42 classed by the authors as transient, 10 as persistent. Most pertinent for our study, we find the number of days each system has spent in the hard, compact jet state, which is invaluable to constrain the hard state duty cycle. It is important to note that although almost 25% of all BH-XRBs seem to be persistent accretors with high-mass companions, this is likely inflated due to observational bias due to their persistent and thus more reliably detected emission. As discussed high-mass companions are rarer and live shorter lives, and likely make up a minority of BH-XRB systems.

Of the transient systems, we find a mean and median number of days spent in the hard state of 183 and 66 days respectively. Taking the mean and median number of days divided by the total time in which the data was collected (19 years) as the duty cycle of these systems, we compute hard state duty cycles of 2.6% and 1.0% respectively. While this data set is the

Table 2.1: Parameter limits for quantifying cosmic ray power of low-mass companion, black hole X-ray binary systems

Parameter	Upper	Middle	Lower
A	0.3	0.1	6×10^{-3}
$\dfrac{L_{\mathrm{X}}}{L_{\mathrm{edd}}}$	0.05	0.03	0.01
N	10^4	3×10^3	10^3

most complete to date with respect to XRB duty cycles, the mean duty cycle derived has to be considered as an upper limit, by virtue of the fact that only systems that have gone into outburst at least once are counted. Furthermore, the average outburst duration (months to years) is still somewhat comparable to the 19 year total on-time, which makes rigorous statistical statements difficult.

Lastly, we use the A-parameter normalization prescription, as presented in Fender et al. (2005), to evaluate the XRB jet power from X-ray observations. The A factor depends on both the type of XRB system and accretion state, and the values of A considered in Table 2.1 are chosen due to the discussion in Fender et al. (2005). By combining (i) the relationship between jet power and radio luminosity motivated by models of steady, conical jets ($L_{\mathrm{radio}} \propto L_J^{\sim 1.4}$; Blandford & Königl 1979; Falcke & Biermann 1995) and (ii) the observed relation between X-ray and radio luminosity for accreting BH systems ($L_{\mathrm{radio}} \propto L_X^{0.7}$; Corbel et al. 2000; Merloni et al. 2003; Falcke et al. 2004b), Fender et al. (2005) was able to show that jet power (L_J) depends on the X-ray luminosity, according to:

$$L_J = A L_X^{0.5} \tag{2.3}$$

Using an X-ray luminosity of jets varying between 1-5% L_{edd} (Maccarone, 2003; Miller-Jones et al., 2012; Curran et al., 2014; Russell et al., 2019), the A-parameter normalization estimated by Fender et al. (2005) in this relation (see Table 2.1), and a mean δ_t estimated from the WATCHDOG catalogue as discussed above, we are able to compute an L_{CR} estimate via Equation 2.2.

All together, we find a total XRB-CR power in the Milky Way of between approximately 10^{36} to 2×10^{39} erg/s for the lower and upper bound parameters respectively, where each XRB provides an average CR power of 10^{33-36} erg/s depending on parameter choices. For the reasonable parameter values in the middle column of Table 2.1, we find $L_{\mathrm{CR}} \approx 10^{38}$ erg/s; approximately 1% of the total estimated Galactic CR power. The actual XRB-CR power output is likely to be significantly higher as we neglect three important additional populations: persistently accreting BH-HMXRB systems, quiescent systems which are thought to behave much like jet-dominated hard state systems (Plotkin et al., 2013), as well as all NS-XRB systems, many of which have powerful jets (Tudose et al., 2006; Migliari & Fender, 2006) which may accelerate CRs.

2.3.1   Constraints from Galactic centre observations

Galactic CRs propagate from their sources interacting with interstellar gas to produce γ-rays and neutrinos. The observation of diffuse γ-ray emission in a region can therefore tell us about the density of both the ambient medium and high-energy CRs in that region. Furthermore, low-energy CRs interact with molecular clouds to produce X-rays. Observations of such clouds can be used to constrain the low-energy CR flux in the surrounding region. In the following, we look to the inner 200 parsecs of the Galaxy to constrain the power of Galactic XRB jets as CR sources.

2.3.1.1   High-energy constraints on the CR power

The recent *NuSTAR* observation by Hailey et al. (2018) suggests the existence of a density cusp of BH-XRBs in the inner parsec of the Galactic centre. If this population of BH-XRBs is similar to the broader Galactic population in their potential to accelerate CRs, we expect to see γ-ray signatures of this in the region. Comparing the expected emission from CR-accelerating XRBs in the Galactic centre to the observed emission, we can constrain the CR power of these systems, and thus by extrapolation gain an additional constraint on the Galactic population as a whole. We use the very-high-energy γ-ray spectra observed by HESS Collaboration et al. (2016), and assume that CRs accelerated in the jets of the *NuSTAR* population of XRBs is responsible for all of the observed γ-rays. This is a very conservative constraint, as we assume all of the γ-ray emission is due to XRB-CR interactions with ambient protons. In reality, it is likely that many sources of CRs, including Sgr A* (HESS Collaboration et al., 2016) and SNe in the region (Jouvin et al., 2017), and possibly other γ-ray production channels, contribute to the observed H.E.S.S. flux. In order to estimate the γ-ray emission from a population of cosmic particles injected by a cusp of XRBs located in the inner Galaxy, we perform both an analytical estimate and a numerical simulation.

For the analytical order-of-magnitude estimate, we follow the approach described in detail in Jouvin et al. (2017). The authors consider the well-understood problem of a steady-state injection of hadrons at the GC from GeV all the way up to PeV energies with a single power-law energy spectrum, and their subsequent energy-dependent diffusive escape from a box with a Central Molecular Zone (CMZ) size H. They derive the following expression for the γ-ray luminosity associated to this hadronic population:

$$L_\gamma(> 200\,\mathrm{GeV}) = 3.2 \times 10^{35} \left(\frac{H}{50\,\mathrm{pc}} \right)^2 \left(\frac{L_{\mathrm{CR}}}{1.6 \times 10^{39}\,\mathrm{erg/s}} \right) \times$$
$$\left(\frac{n}{100\,\mathrm{cm}^3} \right) \, \mathrm{erg/s}$$

where L_{CR} is the total power associated to the CR flux. Given the average gas density in the CMZ and a typical size of the region $H \simeq 100$ pc we get:

$$L_\gamma(> 200\text{GeV}) \;=\; 1.2 \times 10^{36}\,\text{erg/s}\,\left(\frac{L_{\text{CR}}}{1.6 \times 10^{39}\,\text{erg/s}}\right) \tag{2.4}$$

Given the γ-ray luminosity of the Galactic Ridge in $L_\gamma \simeq 3.5 \times 10^{35}$erg/s as reported in HESS Collaboration et al. (2016), it is straightforward to compute the maximum allowed power associated with the CR acceleration and injection in the ISM due to the population of the XRBs at the Galactic centre, that is still compatible with the H.E.S.S. measurement. The conservative upper limit on this quantity is $L_{\text{CR}} \sim 10^{38}\,\text{erg/s}$. For more details regarding the analytical estimate, we refer to Section 2 in Jouvin et al. (2017).

In order to validate this estimate by means of a numerical simulation, we use the public codes DRAGON (Evoli et al., 2017) and GammaSky. Using these codes we are able to propagate CRs from any given source distribution and, adopting detailed models for the gas and interstellar radiation in the Galaxy, compute the γ-ray/neutrino flux associated to the CR population under consideration. We set up the DRAGON code to inject CRs with a Gaussian source term centered on the Galactic centre with a 1 pc width, consistent with the Hailey et al. (2018) population. We set a hard injection spectrum described by a single power law $Q = Q_0(E/E_0)^{-\alpha}$ with $\alpha = 2.2$ and $E_{\min} = 1$ GeV, and let the particles propagate through the CMZ and diffuse out of the Galaxy.

After the equilibrium distribution of CRs is obtained, we compute the hadronic γ-ray flux from the Galactic Ridge region with the GammaSky code, adopting the same model for the gas distribution in the CMZ as in Gaggero et al. (2017). For a CR injected power $L_{\text{CR}}(> 1\text{GeV}) \simeq 10^{38}\,\text{erg/s}$, we obtain an average flux from the Galactic Ridge region $\mathrm{d}\Phi/\mathrm{d}E_\gamma = 2 \times 10^{-11}\,\text{GeV}^{-1}\text{cm}^{-2}\text{s}^{-1}\text{sr}^{-1}$ at 1 TeV (cfr. Aharonian et al. 2006). Furthermore, we obtain an integrated flux of $\mathrm{d}\Phi/\mathrm{d}E_\gamma \simeq 2 \times 10^{-12}\,\text{TeV}^{-1}\text{cm}^{-2}\text{s}^{-1}$ at 1 TeV from the inner annulus centered on Sgr A* as considered in HESS Collaboration et al. (2016). Such γ-ray flux clearly saturates the γ-ray emission reported by the H.E.S.S. Collaboration (see Fig. 2.3): thus we confirm the analytical order-of-magnitude estimate for the upper limit on the power injected in CRs at the GC from a XRB population.

Hailey et al. (2018) suggest that between 300-1000 BH-XRBs exist in the Galactic centre. Although these systems currently seem to be mostly in quiescence, they could have been more active in the past. If we conservatively assume CR acceleration in the jets of these systems is responsible for all of the observed γ-ray flux in HESS Collaboration et al. (2016), we can constrain the maximum CR power per system to be: $10^{34} \lesssim L_{\text{CR}} \lesssim 3 \times 10^{35}$ erg/s. Extrapolating this to the wider Galactic population of $10^3 - 10^4$ systems, we find a total XRB-CR power of $10^{37} - 3 \times 10^{39}$ erg/s. This range of values falls within our estimates for the total XRB-CR power as found above; representing 0.1% to 10% of the total Galactic CR power. This is consistent with our total XRB-CR power derived earlier in this section. We stress that this is an upper limit based on the entire γ-ray flux as observed by HESS Collaboration et al. (2016) to originate from CRs accelerated in jets of the density cusp of XRBs in the Galactic

2
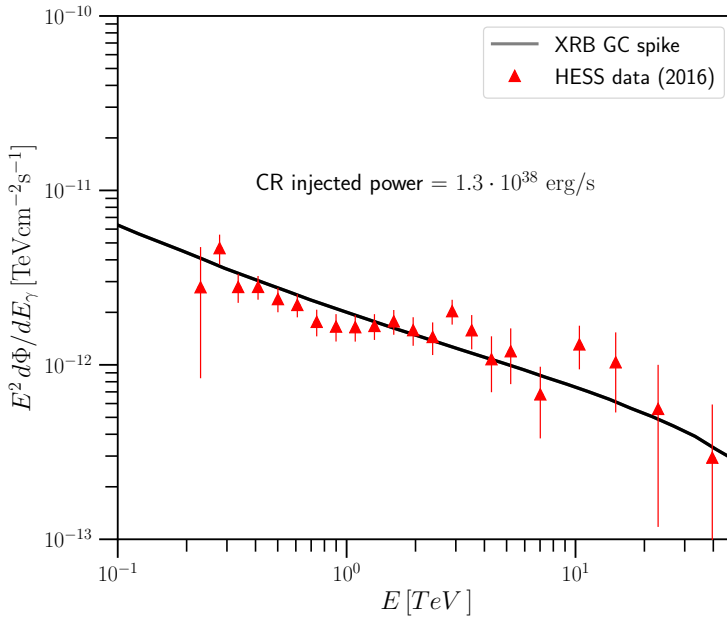
Figure 2.3: Gamma-ray spectral energy distribution associated to the population of CRs accelerated by XRBs located at the GC. We have assumed a CR injected power $L_{\mathrm{CR}}(> 1\mathrm{GeV}) = 1.3 \times 10^{38}\,\mathrm{erg/s}$. The γ-ray flux is integrated over the region of interest defined in HESS Collaboration et al. (2016) (Figs 1 and 3); the H.E.S.S. data are shown as red triangles.

centre, and is primarily used as a sanity check to ensure our assumptions do not violate observational limits.

2.3.1.2 Low-energy constraints on the CR power

An additional constraint on the CR power in the Galactic centre region comes from X-ray observations of the giant molecular clouds in the Central Molecular Zone (CMZ). Once again, this is an upper limit as we assume XRB-CRs from the Hailey et al. (2018) population are the only sources of CRs that contribute to the X-ray illumination.

GeV CR protons/ions bombarding giant molecular clouds produce X-ray emission through collisional ionization and bremssthalung. The Galactic centre molecular cloud Sgr B2's X-ray emission has been decaying over the last two decades, which is primarily due to X-ray echo of past activities of Sgr A* (Inui et al., 2009; Terrier et al., 2010; Dogiel et al., 2011). However, in the recent years, as the X-ray echo component further faded away, Sgr B2's X-ray emission seemed to enter a constant low flux stage, which is intepreted as GeV CR illumination. Observations of the Sgr B2 molecular cloud using *NuSTAR* in 2013 have shown that, after more than ten years of flux decaying, the remaining X-ray emission from Sgr B2 is consistent with the GeV CR illumination scenario (Zhang et al., 2015). Assuming that all the Sgr B2 X-ray emission comes from CR illumination, Zhang et al. (2015) derived a CR proton spectral index of $\alpha = 1.9^{+0.8}_{-0.7}$, and a required GeV proton power of $L_{\mathrm{CR}} = (0.4-2.3) \times 10^{39}$ erg/s. We note that the GeV proton power derived from this method shall be taken as an upper limit, since the X-ray emission from Sgr B2 in 2013 can come partly from CR illumination, and partly from X-ray echoes. Future Sgr B2 X-ray observations will put a tighter constraints on the required CR proton power in the CMZ. This CR power upper limit from X-ray observation of Sgr B2 is consistent with the new estimate of XRB-CR power of the Hailey et al. (2018) population derived in this work.

2.3.1.3 Consistency of constraints

As we have both low-energy and high-energy constraints on the CR power in the region, we can check whether they are compatible by assuming our XRB-CR injection spectral index of $\alpha = 2.2$ holds across the entire energy range. The total low-energy CR power upper limit of $(0.4-2.3) \times 10^{39}$ erg/s applies to CR energies between the $E_{\min} = 1-100$ MeV and $E_{\max} = 1$ GeV, i.e. the model parameters used by Zhang et al. (2015). Using this, we extrapolate to find an allowed high-energy XRB-CR power due to the Hailey et al. (2018) population of $L_{\mathrm{CR}}(> 1\mathrm{GeV}) \leq (1.3-39) \times 10^{38}$ erg/s, where the range of values reflects the allowed ranges of both the $E_{\min}$ parameter and low-energy CR power constraints described in Section 3.1.2. As the analytical and numerical analysis of the H.E.S.S. data suggests an upper limit of $L_{\mathrm{CR}}(> 1\mathrm{GeV}) \sim 10^{38}$ erg/s, we find that the H.E.S.S. γ-ray measurements better constrain the CR power in the region, assuming $\alpha = 2.2$. However, a softer CR injection spectra or alternative contributions to the observed γ-rays in region would mean the low-energy constraints are more stringent limits.

2
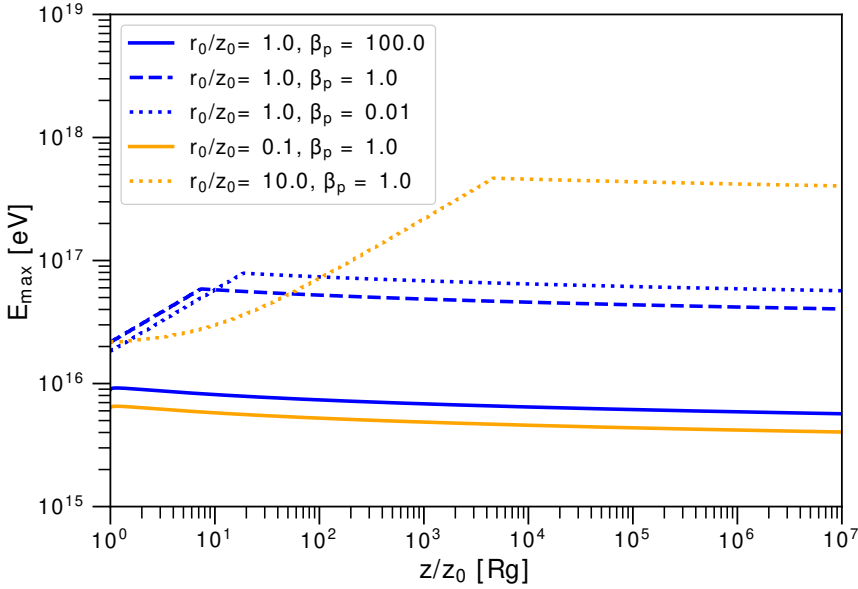
Figure 2.4: Maximum proton energy as a function of distance from the base of the jets for a quasi-isothermal jet model, where we use $\eta = 0.1$. We vary 2 important parameters: initial aspect ratio $\frac{r_0}{z_0}$ in orange and plasma $\beta_p = \frac{U_{e+p}}{U_B}$ in blue. The higher the initial aspect ratio, the wider the jet and thus the particles are confined more easily at high jet heights; the smaller β_p, the higher the magnetic field strength which results in smaller Larmor radii, aiding confinement, but producing larger synchrotron losses. In general, the maximum energy is limited by radiative losses at lower jet height due to strong magnetic fields, and is confinement-limited at large z.

2.4   Maximum Energy of XRB-CRs

We have shown that BH-XRBs can viably contribute a significant fraction of the total Galactic CR power without violating constraints in the Galactic centre, so we now consider the maximum energy attainable by XRB-CRs.

The maximum energy of accelerated CRs in jets is limited either by energy losses (synchrotron, inverse-Compton and adiabatic losses are the primary channels) or by the Hillas criteria for confinement (Hillas, 1984). This is to say that accelerated CRs must stay confined within the accelerating medium in order to undergo re-acceleration, which we can quantify using the Larmor radius. The importance of the radiative losses can be quantified by comparing the timescales of the loss channels and the timescale of the acceleration mechanism. We compute the maximum energy as a function of jet height, $E_{\max}(z)$, such that it satisfies both of these constraints. Here we neglect proton-photon interactions. These interactions are expected to be sub-dominant at these extreme energies and magnetic field strengths even in photon-rich XRB systems (Romero & Vila, 2008; Pepe et al., 2015; Sudoh et al., 2019). This

is especially true for BH-LMXRB systems where the low-mass companions are expected to have a relatively modest photon field contributions.

2.4.1 Jet Model

We calculate the maximum energy of accelerated protons for the 3 different dynamical jet models (isothermal, adiabatic and quasi-isothermal *agnjet* variant) outlined in Crumley et al. (2017). In the Appendix of this paper, we provide an overview of the different jet models and the parameters involved in computing the maximum CR energy. In Fig. 2.4, we focus on the quasi-isothermal model as used in the *agnjet* model, due to its ability to fit the flat jet spectrum we see in multi-wavelength XRB data (Markoff et al., 2001, 2005).

In general, models of jets are based on the jet-disk symbiosis ansatz laid out in Falcke & Biermann (1995). The jet is fed by the disk and the power of the jet at a height z is given by:

$$L_j(z) = \Gamma_j^2 \beta_j c \omega \pi z^2 \sin^2(\theta) \tag{2.5}$$

where $\Gamma_j(z)$ is the lorentz factor of the bulk jet flow, z is the height of the jet above the black hole (z_0 is the height of the jet base) and $\omega(z)$ is the enthalpy. For a jet with a co-moving particle number density, $n(z)$, the enthalpy can be written as:

$$\omega(z) = nmc^2 + U_j + P_j \tag{2.6}$$

Here, U_j and P_j are the energy density and the pressure of the jet respectively. We can approximate to:

$$\omega(z) = nm_p c^2 + \Gamma_{\text{adi}} U_j \tag{2.7}$$

where we have assumed the jet can be treated as an ideal gas with adiabatic index, Γ_{adi}, as in Falcke & Biermann (1995). These equations are valid for all jet models considered in the Appendix.

To compute radiative losses and confinement of accelerated CRs in the jet, the most important parameters are the jet radius, $R(z)$, and the magnetic field strength, $B(z)$. In all models, we define the magnetic field strength of the jet as:

$$B(z) = \sqrt{\frac{8\pi U_j(z)}{\beta_p + 1}} \tag{2.8}$$

where:

$$\beta_p = \frac{U_{e+p}}{U_B} \tag{2.9}$$

β_p is an important free parameter which sets how energy is distributed amongst particles and magnetic fields, and we show how different values of β_p affect the maximum CR energy in Fig. 2.4.

The prescription of $U_j(z)$ depends on the choice of jet model as shown in the Appendix. From Equations 2.5 - 2.7, we see that the value of $L_j(z_0)$, the power at the base of the jet, depends on $n(z_0)$ and $U_j(z_0)$, the number density and internal energy density at the base of

the jet. In this analysis, we normalize $L_j(z_0)$ to the hard state jet power expected from the discussion in the previous section: $\sim 1 - 5\%$ of the Eddington luminosity of a $10M_\odot$ black hole. This results in a jet base magnetic field strength, $B(z_0)$ of $(5-10) \times 10^6$ G, in line with other models (Romero & Vila, 2008; Pepe et al., 2015).

To compute the radius of the jet, we follow (Crumley et al., 2017). For the isothermal and adiabatic jet models, we use a simple conical jet model in which:

$$r_{\text{cone}}(z) = r_0 + (z - z_0)\sin(\theta) \tag{2.10}$$

Here θ is the opening angle of the jet. This means that r_0 is an important free geometric parameter, which sets the initial radius of the jet. It directly influences the extent to which high-energy CRs can be confined, resulting in further acceleration. The quasi-isothermal *agnjet* model used in Fig. 2.4 is not a conical model but instead considers self-collimation. This results in a slightly different jet radius profile:

$$r_{\text{coll}}(z) = r_0 + (z - z_0)\frac{\gamma_0\beta_0}{\gamma_j\beta_j} \tag{2.11}$$

This gives us a slightly narrower jet for larger values of z.

When we calculate the maximum energy of accelerated CRs in the jet, we vary both r_0 and β_p. This helps us understand the parameter space available for a generic XRB population, and the different maximum CR energies attainable. As the magnetic field strength depends strongly upon the internal energy density of the jet, U_j, the maximum CR energy increases significantly for higher jet powers. This is to say that the most powerful XRB jets may be capable of producing higher energy CRs than outlined here. For more on the jet models please see the Appendix.

2.4.2   Calculating Maximum Energy

The timescales of interest in computing the maximum energy are as follows:

$$t_{\text{acc}}^{-1} = \frac{\eta ecB}{E} \tag{2.12}$$

$$t_{\text{sync}}^{-1} = \frac{4}{3}\left(\frac{m_e}{m_p}\right)^3 \frac{c\,\sigma_T\,U_B}{m_e c^2}\frac{E}{m_p c^2} \tag{2.13}$$

$$t_{\text{adi}}^{-1} = \frac{2}{3}\frac{\beta}{z} \tag{2.14}$$

The maximum CR energy, as limited by radiation losses, is given by the condition:

$$t_{\text{acc}}(E,z)^{-1} > t_{\text{adi}}(E,z)^{-1} + t_{\text{sync}}(E,z)^{-1} \tag{2.15}$$

The condition for confinement can be rewritten from Hillas' seminal paper (Hillas, 1984) as:

$$\text{E}_{\text{CR}}(z) < \frac{B(z)}{\mu G} \times \frac{R(z)}{pc} \times \frac{\beta}{0.5} \times 10^{15}\text{ eV} \tag{2.16}$$

Equations 2.15 and 2.16 provide us with the constraints with which we compute the maximum jet power for all models. Specifically, we compute the maximum CR energy limited by each of these constraints, and take the minimum of these two values. In Fig. 2.4 we show our results for how the maximum possible energy varies as a function of the jet height for the quasi-isothermal jet model (that provides the best description of flat spectra jets; Crumley et al. 2017), for different values of the initial aspect ratio, $\frac{r_0}{z_0}$, and β_p of the jet.

Radiative losses dominate near the black hole, as the high magnetic field strength close to the base of the jet results in large synchrotron losses. Most models then show a flattening when a lack of confinement of the particles limits the maximum energy of XRB-CR higher up in the jet. One can assume that in the confinement-limited region, accelerated CRs which exceed the critical energy at which the particle stays confined escape the jet to propagate through the ISM.

We find that the maximum attainable CR energy depends strongly on geometry, jet model and acceleration region; but in general protons can reach energies of 10^{16-17} eV if accelerated with a canonical efficiency of $\eta = 0.1$ (Caprioli & Spitkovsky, 2014). We note that varying η scales the maximum energy linearly in the radiative loss dominated regime at small z. These calculations assume protons (i.e. $Z = 1$), but if more massive CR ions are present in the jet they would attain greater energies as the maximum CR energy scales with rigidity. Lastly, we note that in specific geometries and acceleration regions CR energies higher than 10^{17} eV could be reached, but this might only be plausible in atypical systems such as very powerful, wide or highly magnetized jets.

2.5 Multi-messenger tests of the XRB-CR scenario

Any source class contribution to the CR spectrum can only be directly probed by CR observatories if those sources dominate the spectrum at specific energies. Although XRB-CRs might dominate the parts of the CR spectrum, this is highly dependent on the total CR power, maximum energy of individual CRs and the acceleration powerlaw index. Given our results, we suggest that in the most optimistic case XRB-CRs might dominate (or contribute significantly to) the spectrum close to 10^{17} eV, near the second knee, where a light-mass component has been detected (Pierre Auger Collaboration, 2014; Buitink et al., 2016; Hanlon, 2019; Yushkov, 2019).

The latest results from CR instruments seem to only strengthen the evidence for a light-mass component above 10^{17} eV (Kang, 2019; Yushkov, 2019), and upgrades of such instruments (e.g. Mulrey et al. 2019; The Pierre Auger Collaboration et al. 2016) will be crucial to understand the composition of the transitional energy region between Galactic and extragalactic CRs. While this observed lighter mass component could be interpreted as the start of the extragalactic component, this would require the ankle to be a propagation effect. Thus any Galactic CR accelerator able to reach these energies is of great interest. However, the allowed range of XRB-CR power found in this work means that the contribution could be subdominant at all energy ranges, and thus any confirmation of CR acceleration in XRB jets might only be found via indirect measurements of γ-rays or neutrinos. In Fig. 2.1, we show

a schematic of the all-particle CR spectrum, with a range of allowed contributions from the XRB-CR component calculated in this work. In particular, we show (green dashed line) the maximum allowed contribution, which is calculated by taking the upper parameters in Table 2.1. Such a contribution would make up a significant fraction of the CRs in the energy range between second knee and ankle, where the role of a second Galactic component is currently under debate.

2.5.1 γ-rays

Several XRB jets are now known to emit γ-rays (Tavani et al., 2009; Bordas et al., 2015; Zanin et al., 2016; HAWC Collaboration et al., 2018), although some observations have reported non-detections (Bodaghee et al., 2013; Ahnen et al., 2017a; MAGIC Collaboration et al., 2018). Given the transient nature of some of these sources (and especially the complex environment of the SS 433 system), we do not necessarily expect CR acceleration and subsequent γ-ray emission continuously from XRB systems. Furthermore, although the observation of such high-energy radiation is a clear signature of particle acceleration, it is not trivial to pin down the origin of observed γ-rays which could be leptonic, hadronic or a combination. The upcoming, next generation Cherenkov Telescope Array (CTA; Cherenkov Telescope Array Consortium et al. 2019) will have an order of magnitude better sensitivity compared to current facilities, and up to 4-5 orders of magnitude better sensitivity than *Fermi* in the 100 GeV range for fast transients. CTA will thus likely be able to detect and identify the Galactic PeVatron sources in the near future (Kantzas et al. in prep).

As a consistency check, we again used the DRAGON code to look at the expected diffuse Galactic γ-ray emission due to the XRB population. However, as this population is subdominant to the (SNR) low-energy CR sources below 10^{16} eV, it is impossible to distinguish the sources in currently observable γ-ray wavelengths. Therefore, we suggest point source γ-ray observations of the most powerful XRB jets will pave the way for identifying CRs from XRBs through traditional electromagnetic observations.

2.5.2   Neutrinos

Neutrinos are also produced through CR interactions with protons or photons, and XRB jets have long been predicted as a sources of neutrinos (Levinson & Waxman, 2001; Distefano et al., 2002). As neutrino astronomy is still in its infancy, observations of Galactic-origin neutrinos thus far have been compatible with background (Albert et al., 2017). However, the current limits from a joint analysis of ANTARES and IceCube data (Albert et al., 2018) are now getting close to the most optimistic predictions regarding the expected Galactic neutrino flux. Therefore, the clear detection of a component associated to the Galactic plane may be round the corner (see for instance a recent 2σ hint reported in Aartsen et al. 2019), and diffuse Galactic searches could provide indeed a novel approach towards identifying a second source of Galactic CRs. Neutrino observations probe higher energies than γ-ray facilities and therefore high-energy breaks in the diffuse Galactic neutrino spectra (Aartsen

et al., 2017; Albert et al., 2018) could be interpreted as separate contributions from different CR source classes.

Using the DRAGON code, we compute the expected diffuse neutrino emission due to CRs propagating from two different components: the dominant low-energy (SNR) component and a higher energy (XRB) component. We assume a low-energy component that saturates the observed CR spectrum below the knee, as expected by the dominant Galactic CR source. The subdominant, higher maximum energy component has approximately 10% of the power of the low-energy source, in agreement with most optimistic findings of total XRB-CR power in Section 3. For the source distributions, we have assumed a Lorimer pulsar distribution (Lorimer et al., 2006) for both source populations, as this is a good approximate tracer of compact objects and therefore of SNRs and XRBs. In Fig. 2.5, we see the resulting diffuse neutrino spectra due to these two components, where we assume the low-energy and higher energy components are due to SNR and XRB sources respectively. We plot a different maximum energy cut-offs, as the maximum CR energy for each source is not well-known. Unlike cosmic rays, neutrinos trace back to their sources and thus confirming a break/hardening in the spectrum towards the Milky Way could verify the Galactic origin of high-energy CRs. The current upper limits on the Galactic contribution to the astrophysical neutrino flux by IceCube and ANTARES are also shown in the figure.

As the next-generation of neutrino observatories come online (Icecube-Gen2, IceCube-Gen2 Collaboration et al. 2014; KM3-NET (2.0), Adrián-Martínez et al. 2016), we can probe PeV energy ranges in order to verify whether there are two clear populations of high-energy CR sources within our Galaxy. As diffuse neutrino limits are already encroaching on best models of neutrino emission from Galactic CRs, the ten-fold detector volume increase specified for IceCube-Gen2 will probe our predictions of a break in the Galactic neutrino spectrum due to a high-energy Galactic component. Furthermore, KM3-NET upgrades over the next decade will increase the angular resolution of detections to $< 0.1°$ at PeV energies. Coupled with greater sensitivities, point source neutrino astronomy will soon be at the forefront of identifying CR sources within our Galaxy. Once these upgrades are realised, XRB systems such as Cygnus X-1 will be key targets for neutrino observatories to test whether XRB jets are important CR accelerators.

2.6   Conclusion

We have suggested that XRB jets could accelerate protons to high energies, similar to their larger counterparts in AGN. Within the uncertainties allowed by current population models, jet composition and Galactic centre observational constraints, a total XRB-CR power of between 10^{36-39} erg/s is possible. The most likely allowed value of around 10^{38} erg/s means XRB-CRs could contribute a few percent of the dominant SNR-CR component, representing a non-negligible contribution to the observed CR spectrum. The maximum energy of XRB-CR is relatively high compared to other Galactic sources of CRs, with models suggesting protons could be accelerated to 10^{16-17} eV in some systems. Together these two results indicate that XRB-CRs could even dominate the total CR spectrum in part of the transition region be-

2
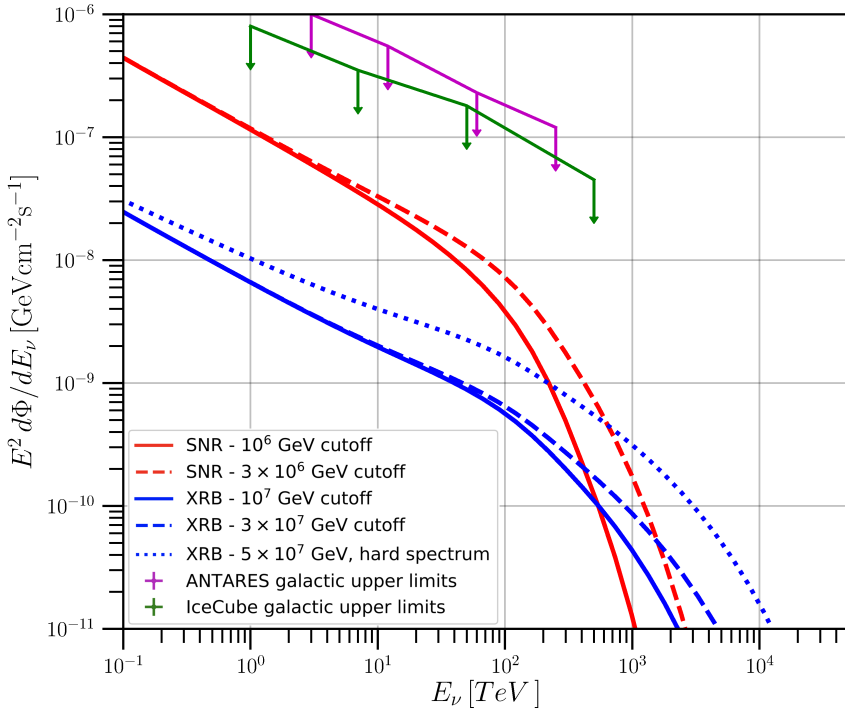
Figure 2.5: The predicted diffuse Galactic neutrino spectrum from SNR-CRs and XRB-CRs with joint upper limits from ANTARES and IceCube (Aartsen et al., 2017) using the DRAGON code. Specifically, we note that breaks in the spectra are predicted in the total spectrum at model-dependent sensitivities even with very conservative maximum energy cut-offs.

tween SNR-CR and extragalactic CR components, above the knee and below the ankle, in broad agreement with recent mass composition results. Lastly, we suggest multi-messenger possibilities to confirm XRB-CR (or generic second Galactic components) through diffuse neutrino and γ-ray measurements of our Galaxy, as well as point source observations.

Acknowledgements

2

Appendices

2.A Jet models

In Section 4, we looked at dynamical jet models in order to estimate the maximum attainable CR energy as a function of jet height. We rely heavily on Crumley et al. (2017), in which the equations governing the different jet models are derived. Here we give a quick overview of each jet model, and show how the maximum CR energy depends on the jet model. As mentioned in Section 4 we believe that for XRB jets, the quasi-isothermal jet model is the most appropriate.

From this starting point, assumptions about the physics of the jet lead to different models. The most important difference is that in the adiabatic jet model, adiabatic losses are not compensated for. In all other models, losses are compensated for by e.g. continuous reacceleration of particles. In the isothermal model adiabatic losses are fully compensated for; whereas in the quasi-isothermal models only longitudinal (z-direction) losses are compensated for. These assumptions lead to different internal energy profiles, and different Euler equations from which the Lorentz profile of the jet is derived. In each case, we briefly explain the assumptions and list the Euler equation for the model. For a more thorough explanation, we suggest the reader refers to Crumley et al. (2017).

2.A.1 Adiabatic jets

In the adiabatic jet model, the jet conserves energy such that it obeys the relativistic Bernoulli equation: $\gamma_j \frac{\omega}{n} = \mathrm{const}$. This means that $T_j \propto n^{\Gamma_{\mathrm{adi}}-1}$. The internal energy density profile is:

$$U_j(z) = \zeta n_0 m_p c^2 \left(\frac{\gamma_j \beta_j}{\gamma_0 \beta_0} \right)^{-\Gamma_{\mathrm{adi}}} \left(\frac{z}{z_0} \right)^{-2\Gamma_{\mathrm{adi}}} \tag{2.17}$$

The Euler equation then is:

$$\left(\gamma_j \beta_j \frac{\Gamma_{\mathrm{adi}} + \xi}{\Gamma_{\mathrm{adi}} - 1} - \Gamma_{\mathrm{adi}} \gamma_j \beta_j - \frac{\Gamma_{\mathrm{adi}}}{\gamma_j \beta_j} \right) \frac{\partial \gamma_j \beta_j}{\partial z} = \frac{2}{z} \tag{2.18}$$

$$\xi = \frac{1}{\zeta} \left(\gamma_j \beta_j \sqrt{\frac{1 + 2\zeta \Gamma_{\mathrm{adi}} - \zeta \Gamma_{\mathrm{adi}}^2}{\zeta \Gamma_{\mathrm{adi}} (\Gamma_{\mathrm{adi}} - 1)}} \right)^{\Gamma_{\mathrm{adi}}-1} \left(\frac{z}{z_0} \right)^{2(\Gamma_{\mathrm{adi}}-1)} \tag{2.19}$$
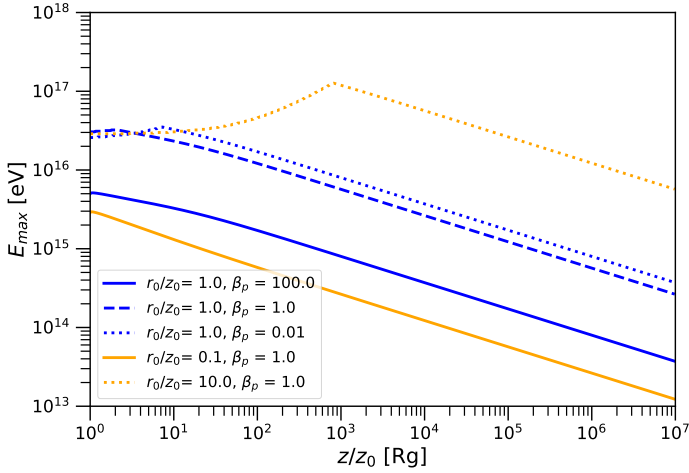
Figure 2.6: Maximum CR energy as a function of jet height z for the adiabatic Jet model.

In terms of CR acceleration, adiabatic jets generally attain lower CR energies compared to other jet models, espcially at large z. This is because the internal energy density and thus magnetic field strength decreases rapidly as z increases, as no reacceleration occurs. We stress that the adiabatic jet model cannot fit the flat spectra we see in XRB jets, and is presented primarily for comparison.

2.A.2   Isothermal jets

In the isothermal jet model, all adiabatic losses are recompensated for and thus T_j is constant. This means that $U_p \propto n$, and energy is not conserved.

$$U_j(z) = \zeta n_0 m_p c^2 \left(\frac{\gamma_j \beta_j}{\gamma_0 \beta_0} \right)^{-\Gamma_{\mathrm{adi}}} \left(\frac{z}{z_0} \right)^{-2} \tag{2.20}$$

The Euler equation is:

$$\left(\gamma_j \beta_j \frac{\Gamma_{\mathrm{adi}} + 1}{\Gamma_{\mathrm{adi}} - 1} - \Gamma_{\mathrm{adi}} \gamma_j \beta_j - \frac{\Gamma_{\mathrm{adi}}}{\gamma_j \beta_j} \right) \frac{\partial \gamma_j \beta_j}{\partial z} = \frac{2}{z} \tag{2.21}$$

2.A.3   Quasi-Isothermal jets (*agnjet*)

In the quasi-isothermal model, the gas in the jet can only do work in the z-direction, meaning that $T_j \propto (\gamma_j \beta_j)^{1-\Gamma_{\mathrm{adi}}}$. A key difference here is that we include self-collimation, and so the
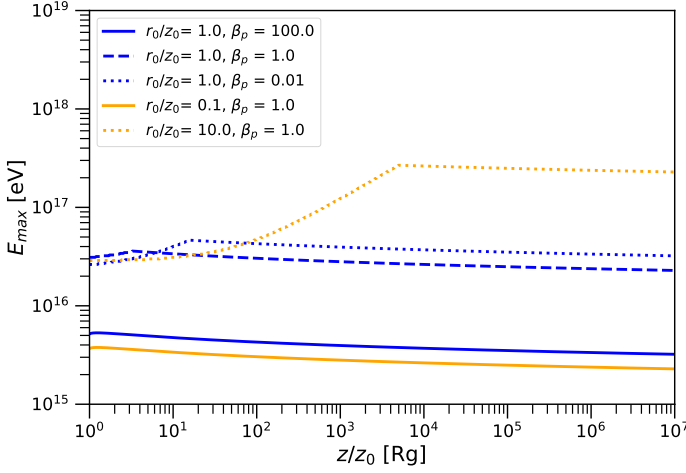
Figure 2.7: Maximum CR energy as a function of jet height z for the isothermal Jet model.

radius of the jet as a function of jet height z is given by Equation 2.11. The internal energy density profile is the similar to the isothermal case:

$$U_j(z) = \zeta n_0 m_p c^2 \left(\frac{\gamma_j \beta_j}{\gamma_0 \beta_0} \right)^{-\Gamma_{\mathrm{adi}}} \left(\frac{r_{\mathrm{coll}}}{r_0} \right)^{-2} \tag{2.22}$$

Here, we use the collimated radius from Equation 2.11. The Euler equation, however includes an additional factor:

$$\left(\gamma_j \beta_j \frac{\Gamma_{\mathrm{adi}} + \xi}{\Gamma_{\mathrm{adi}} - 1} - \Gamma_{\mathrm{adi}} \gamma_j \beta_j - \frac{\Gamma_{\mathrm{adi}}}{\gamma_j \beta_j} \right) \frac{\partial \gamma_j \beta_j}{\partial z} = \frac{2}{z} \tag{2.23}$$

$$\xi = \frac{1}{\zeta} \left(\frac{\gamma_j \beta_j}{\gamma_0 \beta_0} \right)^{\Gamma_{\mathrm{adi}} - 1} \tag{2.24}$$

The figure for this jet model is found in Section 4, Fig. 2.4. We note that $U_j(z)$ is very similar for the isothermal and quasi-isothermal models, as only the dependence on the radius is different. For this reason, their maximum CR energies are very similar.

Chapter **3**

Coherent curvature radiation: maximum luminosity and high-energy emission

A. J. Cooper & R. A. M. J. Wijers

Abstract

High brightness temperature radio transients such as pulsars and fast radio bursts require the coherent radiation of particles. The antenna class of coherent radiation models require a large number of charged particles radiating in phase, therefore the particles must be spatially confined and have well-aligned velocities. Given these necessary conditions, we look at the magnetic field induced by the currents associated with coherently emitting accelerated particles and consider the interaction between the radiating particles and the induced magnetic field. We find a maximum luminosity of coherent curvature radiation that depends on source parameters such as surface magnetic field and neutron star spin period. We find that coherent radio emission across all luminosities can be explained by coherent curvature radiation and suggest it could be universally responsible for both FRBs and extreme galactic sources. Using the Crab Pulsar as an example, we constrain the emission parameters and origin of the most extreme nanoshots to within 60km of the pulsar surface assuming coherent curvature radiation. In agreement with recent observations, we also predict simultaneous X-ray emission from small-scale particle gyration due to the induced field.

3.1   Introduction

Coherent radiation is required for luminous, short duration radio transients, where the high brightness temperature cannot be explained by relativistic beaming alone (Pietka et al., 2015; Melrose, 2017). The two primary examples of these very high brightness temperature astrophysical sources are pulsars and Fast Radio Bursts (FRBs). Coherent emission can be broadly classified into either maser emission or antenna emission which requires spatial clustering of particles (Zhang, 2020). Coherent curvature radiation is a model of the latter and here we examine limits of this radiation model.

Coherent curvature radiation has been used to explain high brightness temperature emission from pulsars (Sturrock, 1971; Ruderman & Sutherland, 1975; Yang & Zhang, 2018). More recently, this model has become one of the front-running radiation models of FRBs, where the conditions for the coherent emission of a large number of particles are found in the inner magnetospheres of highly-magnetized neutron stars known as magnetars (Katz, 2016; Cordes & Wasserman, 2016; Kumar et al., 2017; Ghisellini & Locatelli, 2018). In general, these models suggest that acceleration gaps of unscreened electric field parallel to the magnetic field lines, $E_\parallel$, accelerate particles along magnetic field lines producing curvature radiation. However, there are many open questions in terms of how these particles radiate in phase (Lyubarsky, 2021); for example what are the sufficient conditions for particles to act coherently in this manner. In this Letter we focus on two basic, necessary properties of coherent radiation and look at the electrodynamic interactions between radiating particles.

Firstly, we use the fact that coherently emitting particles must do so from a region no bigger than a comoving size $R_{\rm coh} < \gamma\lambda$ where λ is the wavelength of observed emission. Secondly, we assume that the particles' velocities must not be misaligned by more than a factor of γ^{-1}, i.e. $\frac{\delta \boldsymbol{p}}{|p|} < 1/\gamma$. This limit is used in the coherent curvature radiation model of Kumar et al. (2017), where authors suggest the induced perpendicular field due to the current of accelerated particles $B_\perp$ must be smaller than the local field B along which the electrons stream by a factor of γ:

$$B \geq \gamma B_\perp \tag{3.1}$$

For magnetic fields approaching $B_c = \dfrac{m_{\rm e}^2 c^3}{e\hbar} = 4.4 \times 10^{13}$ G, the excitation energy of the first electron Landau level becomes comparable to the electron rest mass. In Kumar et al. (2017), the authors suggest that the local magnetic field in which bright FRBs radiate must be $\gtrsim 10^{14}$G such that particles are not dislodged from the ground state despite perturbation, and coherence is maintained.

In Section 3.2 we look at the magnetic field induced by accelerated particles and re-derive Eq. 3.1 by considering the perturbation of particles' momenta. In Section 3.3 we look at the constraints due to this perturbation, and find an upper limit of the lorentz factor of the coherently radiating particles. In Section 3.4 we find an upper limit for radio luminosity of coherent curvature radiation for sub-critical magnetic fields, in agreement with the luminosity gap between extreme galactic pulsar emission (Hankins et al., 2003; Kuiack et al., 2020) and extra-galactic FRBs (Petroff et al., 2019; Zhang, 2020). We apply these constraints to

the giant pulses observed from the Crab Pulsar and constrain the emission to within 60km of the NS surface. Furthermore, the most extreme crab nanoshots (Hankins & Eilek, 2007) must originate on the surface of the star if produced by coherent curvature emission. We also look at high-energy emission due to the small-scale perturbations of particles' motion, and suggest this could explain the recent detection of enhanced X-ray activity emission associated with giant radio pulses (Enoto et al., 2021). We conclude with a short discussion in Section 3.5. We use convenient notation $X_{\mathrm{n}} \equiv X/10^n$ throughout.

3.2   Induced magnetic field

Consider a bunch of electrons or positrons that are spontaneously accelerated along curved magnetic field lines B by an strong electric field parallel to the magnetic field lines $E_{\parallel}$, where $E < B$. The origin of the accelerating electric field or charge creation event is not discussed here, but could be for example a magnetic reconnection event. The acceleration length scale $l_{\mathrm{acc}} = \gamma m_{\mathrm{e}} c^2/qE_{\parallel} \approx 10^{-2}\,\mathrm{cm}\ \gamma_3\,E_{\parallel,8}^{-1}$ is assumed to be smaller than the spatial scale of the radiation patch throughout. To observe coherent radiation at a wavelength λ the particles must at least obey the following conditions:

$$R_{\mathrm{coh}} \leq \gamma\lambda = \gamma c \nu^{-1} \tag{3.2}$$

$$\frac{\delta\boldsymbol{p}}{|p|} < \frac{1}{\gamma} \tag{3.3}$$

These two equations tell us that the particles' positions and momenta respectively must be well confined in order to radiate coherently. Eq. 3.2 applies to the source's longitudinal extent, but the transverse coherent region can be larger than $\gamma\lambda$ by a factor $\eta^{1/2}$ due to photon arrival delay which depends on the distance to the source's trigger l_t (Kumar et al., 2017). We take $\eta = 1$ for simplicity and because our results depend very weakly on this parameter, such that the total comoving volume is $V' = \eta\gamma^3\lambda^3$. We further assume that the bunch has propagated a distance l_t from the trigger such that coherent region is transversely causally connected: $R_{\mathrm{coh}} < \dfrac{l_t}{\gamma^2}$, or $l_t > \gamma^3\lambda$. Multiple longitudinal patches of coherent radiation $N_{\mathrm{p,l}}$ may be consecutively observed as discussed in Section 3.3.4.

Particles streaming along the guiding magnetic field line B induce a current which in turn induces a magnetic field. This secondary field $B_{\perp}$ can perturb the particles, limiting coherent emission. We consider a bunch of N particles confined in a space with a co-moving radius R_{coh} moving at γ, where the $E_{\parallel}$ acceleration balances radiation losses. These particles produce a current density J such that:

$$J = 2n_{\mathrm{e}}ce = 2\gamma n_{\mathrm{e}}'ce \tag{3.4}$$

The co-moving electron density $n_{\mathrm{e}}' = n_{\mathrm{e}}/\gamma$ where n_{e} is in the lab frame, and we have assumed that the particles are accelerated to approximately $v = c$. Assuming this current is

steady on short time scales, it induces a magnetic field perpendicular to the current (Kumar et al., 2017):

$$\nabla \times B \approx \frac{B_\perp}{R_{\mathrm{coh}}} = \frac{4\pi J}{c} \tag{3.5}$$

$$B_\perp = \frac{4\pi R J}{c} = 8\pi R_{\mathrm{coh}} e n_{\mathrm{e}} = 8\pi e n_{\mathrm{e}} \gamma c \nu^{-1} \tag{3.6}$$

3.2.1   Particle motion

Consider the motion of these particles due to the induced field. We define $B = B_z$, $B_\perp = B_{\perp,\phi}$, $E_\parallel = E_{\parallel,z}$, such that the z-axis is locally tangent to the curved dipole magnetic field lines. Particles follow the total field line $B_z + B_\perp$ resulting in helical motion about B_z with a pitch angle $\alpha = v_\phi/c = B_\perp/B_z$, where we have assumed $v_z \approx c$ due to the strong $E_\parallel$. Given this, we can see how the momenta condition in Eq. 3.3 is the same as the condition in Eq. 3.1. The particle acceleration and gyroradius are:

$$a_r = \frac{v_\phi^2}{r} = -\frac{q v_\phi B_z}{\gamma m_{\mathrm{e}}} - \frac{q v_z B_\perp}{\gamma m_{\mathrm{e}}} = -\frac{2qc B_\perp}{\gamma m_{\mathrm{e}}} \tag{3.7}$$

$$r_g = r = \frac{\gamma m_{\mathrm{e}} c B_\perp}{2q B_z^2} = \frac{\gamma m_{\mathrm{e}} c \alpha}{2q B_z} = \frac{\gamma m_{\mathrm{e}} v_\phi}{2q B_z} \tag{3.8}$$

In Section 3.4.2 we will suggest this particle acceleration along field lines, which is the equivalent motion as synchrotron gyration about B_z, results in high-energy radiation. It is possible for accelerated particles to emit coherently for a short period of time $t < \delta t$ before the force due to the induced field $B_\perp$ has imparted sufficient momentum to destroy coherence, however this timescale is extremely short: $dt < \frac{2\pi r_g}{v_\phi} = 10^{-26}$ s $\gamma_3 B_{11}^{-1}$.

3.3   Limits of coherent curvature radiation

3.3.1   Constraint due to spatial confinement and absorption

For coherent radiation we require that particles are spatially confined via Eq. 3.2, therefore we should also require that $r_g < R_{\mathrm{coh}}$:

$$\frac{\gamma m_{\mathrm{e}} c B_\perp}{2q B^2} < \frac{\gamma c}{\nu}$$

$$n_{\mathrm{e}} \gamma < \frac{B^2}{4\pi m_{\mathrm{e}} c} \approx 2 \times 10^{37} \ B_{11}^2 \tag{3.9}$$

Where we have used the lab frame number density and Eq. 3.2, and B is the local magnetic field strength of B_z. We find that the gyration radius r_g is small compared to the coherent

emission radius R_{coh}, and therefore this does not meaningfully constrain the emission. In fact, the particle gyroradius derived in Eq. 3.8 could help explain why coherently emitting particles can stay confined spatially for the duration of emission despite electrostatic repulsion. The coherent curvature radiation will have a X-mode component transverse to both the local magnetic field $\vec{B}$ and the wave-vector $\vec{k}$ (Kumar et al., 2017). This component easily escapes even high particle density sources as it may propagate in a magnetized plasma if: $\omega > \omega_p^2/\omega_B > 10^{-11} B_{11}^{-1} n_{\mathrm{e},12} \gamma_3^{-1}$ Hz when $\omega_B > \omega_p$ (Arons & Barnard, 1986).

3.3.2   Constraint due to particle gyration cooling

The particles follow the total $B_z + B_\perp$ field lines along a helical path with pitch angle $\alpha = B_\perp/B_z$. The particles' path is identical to synchro-curvature radiation (Cheng & Zhang, 1996; Kelner et al., 2015) despite following the total field line, and this gyration leads to additional incoherent cooling. For particles in the coherent region, we must compare incoherent synchrotron radiation due to gyration to the large scale coherent curvature radiation to find the dominant cooling mechanism:

$$P_{\mathrm{sync}} > P_{\mathrm{curv}}$$
$$\frac{1}{4} N \pi c \sigma_T B^2 \gamma^2 \alpha^2 > \frac{2(Ne)^2 c \gamma^4}{3\rho^2} \tag{3.10}$$
$$\gamma < \left(\frac{24 \rho^2 \pi \sigma_T \nu n_{\mathrm{e}}}{c} \right)^{1/3} \approx 5 \, \rho_7^{2/3} \, \nu_9^{1/3} \, n_{\mathrm{e},12}^{1/3}$$

Where we have used Eq. 3.6. We find that synchrotron radiation is almost always subdominant, and does not constrain coherent curvature radiation. The small scale gyration leads to simultaneous high-energy radiation, especially outside of the coherent region where the gyration will dominate particle cooling. We estimate and discuss such emission in Section 3.4.2.

3.3.3   Constraint due to momentum misalignment

For the radiation to be coherent, given the constraint in Eq. 3.1, we require that:

$$B > \gamma B_\perp = 8\pi e n_{\mathrm{e}} \gamma^2 c \nu^{-1}$$
$$\gamma < \left(\frac{B\nu}{8\pi e n_{\mathrm{e}} c} \right)^{1/2} \tag{3.11}$$
$$\gamma_{\mathrm{max}} \approx 500 \, B_{11}^{1/2} \, \nu_9^{1/2} \, n_{\mathrm{e},12}^{-1/2}$$

Here we have used Eqs. 3.6 and typical magnetized neutron star (NS) parameters, and find that particle bunches with large lorentz factors induce a magnetic field which destroys coherence. In most situations from which we expect coherent radiation, it is thought the

number density of particles scales with the magnetic field B (Goldreich & Julian, 1969) as approximately:

$$n_e = \xi n_{GJ} = \frac{2\xi B_s R_{\mathrm{NS}}^3}{ecPR^3} = 1.4 \times 10^{12} \, B_{s,11} \, P_{-1}^{1/2} \, \xi_1 \, R_6^{-3} \, \mathrm{cm}^{-3} \tag{3.12}$$

Where P is the NS period, $R_{\mathrm{NS}} = 10^6$ cm is the NS radius, $R \geq R_{\mathrm{NS}}$ is the distance from the NS centre, B_s is the dipole surface magnetic field and $\xi > 1$ is the pair multiplicity due to photon-magnetic field interactions producing pairs. We assume the leptons originate from pair creation, so there is charge neutrality. We can rewrite Eq. 3.11 explicitly in terms of the NS parameters:

$$\gamma_{\mathrm{max}} = \left(\frac{P\nu}{16\pi\xi} \right)^{1/2} = 500 \, P_{-1}^{1/2} \, \nu_9^{1/2} \, \xi_1^{-1/2} \tag{3.13}$$

To obey Eq. 3.3, we should also require that all field lines occupied by the coherent patch be well aligned. Assuming a dipole field, and that the transverse source size extends from R above the polar cap to $(R, \delta\theta)$, we find that this could further limit emission close to the NS surface:

$$\frac{1}{\gamma} > \frac{\sin(\delta\theta) R_{\mathrm{NS}}^3}{R^3} \approx \frac{R_{\mathrm{coh}} R_{\mathrm{NS}}^3}{R^4}$$
$$\gamma < \left(\frac{R^4 \nu}{R_{\mathrm{NS}}^3 c} \right)^{1/2} \approx 180 \, R_6^2 \, \nu_9^{1/2} \tag{3.14}$$

However, a source with a transverse size less than R_{coh} can have higher lorentz factors.

3.3.4   Constraints on duration

If the decay timescale of the accelerating electric field is large, we expect many patches of coherent emission $N_{\mathrm{p,l}}$ to extend along the observer's line of sight. The observed duration of coherent curvature radiation is then limited by either the observer frame light crossing time of the patches: $\frac{N_{\mathrm{p,l}} R_{\mathrm{coh}}}{\gamma c} = N_{\mathrm{p,l}}/\nu$, the sweep of the radiation beam: $\frac{N_{\mathrm{p,l}}\rho}{\gamma c}$, or the movement of particles along field lines into regions of lower field strength such that coherence cannot be supported via Eq. 3.11. In all cases, bursts that originate closer to the NS surface are expected to be shorter in duration due to smaller spatial scales, tighter field lines (Bilous et al., 2019) and more rapidly decreasing magnetic field strength.

3.4 Predictions

3.4.1 Maximum luminosity of coherent curvature radiation

Given the condition in Eq. 3.13, we can derive a maximum emitted luminosity of coherent curvature radiation given source parameters:

$$L_{\mathrm{coh,max}} = \frac{2N_{\mathrm{p}}(Ne)^2 c\gamma_{\mathrm{max}}^4}{3\rho^2} = N_{\mathrm{p}} n_{\mathrm{e}}^2 R_{\mathrm{coh}}^6 \frac{2e^2 c\gamma_{\mathrm{max}}^4}{3\rho^2}$$
$$= 2 \times 10^{37}\, B_{s,11}^2\, P_{-1}^3\, \rho_7^{-2}\, \nu_9^{-1}\, \xi_1^{-3}\, N_{\mathrm{p}}\, R_6^{-6}\ \mathrm{erg\,s^{-1}} \qquad (3.15)$$

Where we have used Eqs. 3.2 and 3.13, ρ is the magnetic field line curvature radius and N_{p} is the number of coherent patches that add to the luminosity incoherently. The maximum observed spectral luminosity is approximately $L_{\nu,\mathrm{obs}} = \gamma^2 L/\nu_c$ where $\nu_c = 3c\gamma^3/4\pi\rho$ and the γ^2 factor is due to beaming of emission into a small observable solid angle (Lyutikov, 2021):

$$L_{\nu,\mathrm{max}}^{\mathrm{obs}} = 6 \times 10^{31}\, B_{s,11}^2\, P_{-1}^{5/2}\, \rho_7^{-1}\, \nu_9^{-3/2}\, \xi_1^{-5/2}\, N_{\mathrm{p}}\, R_6^{-6}\ \mathrm{erg\,s^{-1}\,Hz^{-1}}$$
$$T_{\mathrm{B,max}}^{\mathrm{obs}} = \frac{2c^2 L_{\nu}^{\mathrm{obs}}}{k_B \nu^2 R_{\mathrm{coh}}^2} \qquad (3.16)$$
$$= 4 \times 10^{42}\, B_{s,11}^2\, P_{-1}^{3/2}\, \rho_7^{-1}\, \nu_9^{-5/2}\, \xi_1^{-3/2}\, N_{\mathrm{p}}\, R_6^{-6}\ \mathrm{K}$$

This upper limit to the spectral luminosity fits well with the observed maximum spectral luminosity from extreme galactic coherent sources as shown in Fig. 3.1. Except for FRBs, these pulses represent the brightest coherent radio emission observed, suggesting a common coherent curvature mechanism for giant pulses and FRBs (Keane et al., 2012; Cordes & Wasserman, 2016). Eq. 3.16 refers to the $\gamma = \gamma_{\mathrm{max}}$ maximal case, for non-maximal bursts with $\gamma < \gamma_{\mathrm{max}}$ the luminosity drops rapidly: $L_{\nu}^{\mathrm{obs}} \propto R_{\mathrm{coh}}^6 \gamma^3 \propto \gamma^9$.

3.4.2 Coincident incoherent high-energy emission

There is growing evidence that the mechanism responsible for coherent radio emission is also powers emission at higher energies (Younes et al., 2021; Enoto et al., 2021; HAWC Collaboration et al., 2021). In Section 3.3.2 we discussed the possibility of a subdominant radiation mechanism due to small-scale gyrations caused by the induced field. We can look at the power and critical frequency of the emission, assuming it manifests as incoherent synchrotron radiation about B with an angle $\alpha = B_\perp/B$ as discussed in Section 3.2.1:

$$L_{\mathrm{sync}} = N_{\mathrm{p}} n_{\mathrm{e}} P_{\mathrm{sync}} = 16\pi\zeta^5 c^6 \sigma_T n_{\mathrm{e}}^3 e^2 N_{\mathrm{p}} \gamma_{\mathrm{max}}^7 \nu^{-5}$$
$$= 5 \times 10^{31}\, B_{s,11}^3\, P_{-1}^{1/2}\, \nu_9^{-3/2}\, \xi_1^{-1/2}\, \zeta^5\, N_{\mathrm{p}}\, R_6^{-9}\ \mathrm{erg\,s^{-1}} \qquad (3.17)$$

The total transverse particle acceleration region may be larger than R_{coh} by a factor of ζ, as long as the total size does not exceed $\approx R_{\mathrm{NS}}$. Accelerated particles outside of the coherent region will follow helical field lines and radiate incoherently, so the radio is much suppressed relative to the high-energy emission. The larger transverse size means these particles have

a larger pitch angle and a large emission volume such that the incoherent luminosity scales as ζ^5. We have assumed particles outside of the incoherent region will have approximately the same lorentz factor as the coherent particles, which may not be the case. Furthermore, we note sometimes only field lines outside of the coherent region point towards the observer such that only the high-energy radiation is visible. The critical frequency of this emission is:

$$
\begin{aligned}
\nu_{c,sync} &= \frac{3}{2}\gamma_{max}^3 \omega_B \sin(\alpha) \\
&\approx 10^{21}\, P_{-1}^{1/2}\, \nu_9^{1/2}\, B_{s,11}\, \xi_1^{-1/2}\, \zeta\, R_6^{-3}\ \text{Hz}
\end{aligned}
\tag{3.18}
$$

Or approximately $E_{ph} = 5\,\text{MeV}$. We note that the observed cut-off will be below this critical frequency in high-field sources, due to photo-magnetic processes of photon splitting and pair production (Daugherty & Harding, 1983). Observations of a high-energy cut-off are usually dominated by one photon pair production, and could be used as a diagnostic of the local magnetic field B. Assuming $\mathcal{X} \ll 1$, which holds for the low-energy cut-off in non-critical fields, the photon attenuation factor is approximately (Harding et al., 1997):

$$
T_{pp} \approx \frac{0.3\alpha m_e c}{\hbar}\frac{B}{B_c}\exp\left(\frac{-4}{3\mathcal{X}}\right) \quad \text{where } \mathcal{X} = \frac{E_{ph}}{2m_e c^2}\frac{B}{B_c}
\tag{3.19}
$$

Where we have made simplifying assumptions that photons propagate a distance comparable to the curvature radius ρ such that $\sin(\theta_{kB}) \approx 1$, and that the drop in B is negligible across this distance. If photons are attenuated if $T_{pp} > 1$, we find an approximate maximum energy cut-off of a few MeV for $B = 10^{13}$ G and around 10 GeV for $B = 10^9$ G. The emission spectrum of this incoherent emission is expected to follow a synchrotron spectrum and thus for $\nu < \nu_c$, we estimate the observed spectral luminosity as:

$$
\begin{aligned}
L_{\nu,sync}^{obs} &= \frac{4\gamma^2 L_{sync}}{3\nu_{c,sync}}\left(\frac{\nu_x}{\nu_{c,sync}}\right)^{1/3} \\
&= 8\times10^{14}\, B_{s,11}^{5/3}\, P_{-1}^{5/6}\, \nu_{x,18}^{1/3}\, \xi_1^{-5/6}\, \nu_9^{-7/6}\, \zeta^{11/3}\, N_p\, R_6^{-5}\ \text{erg s}^{-1}\,\text{Hz}^{-1}
\end{aligned}
\tag{3.20}
$$

Using Eqs. 3.16 & 3.20 we can estimate the ratio of radio/X-ray flux in representative bands by assuming luminosity across a bandwidth $\delta\nu$ centred on ν is approximately $L_\nu \delta\nu$, where $\delta\nu \approx \nu$:

$$
\frac{F_{0.1-1\text{GHz}}}{F_{1-10\text{keV}}} \approx 7\times10^7\, B_{s,11}^{1/3}\, P_{-1}^{5/3}\, \rho_7^{-1}\, \nu_{x,18}^{-4/3}\, \xi_1^{-5/3}\, \nu_9^{2/3}\, \zeta^{-11/3}\, R_6^{-1}
\tag{3.21}
$$

3.4.3   Crab Pulsar

The Crab Pulsar produces kilo-Jansky flux giant pulses at GHz frequencies (Lundgren et al., 1995), which represents a spectral luminosity of approximately $L_\nu \approx 5\times10^{24}\ \text{erg s}^{-1}\,\text{Hz}^{-1}$, thought to come from high altitudes close to the light cylinder (Eilek & Hankins, 2016). We can place limits on emission parameters using source parameters for the Crab ($B_s = 7\times10^{12}$G, $P = 0.033$s; Lyne et al. 1993) and Eq. 3.16 to solve for R, assuming coherent
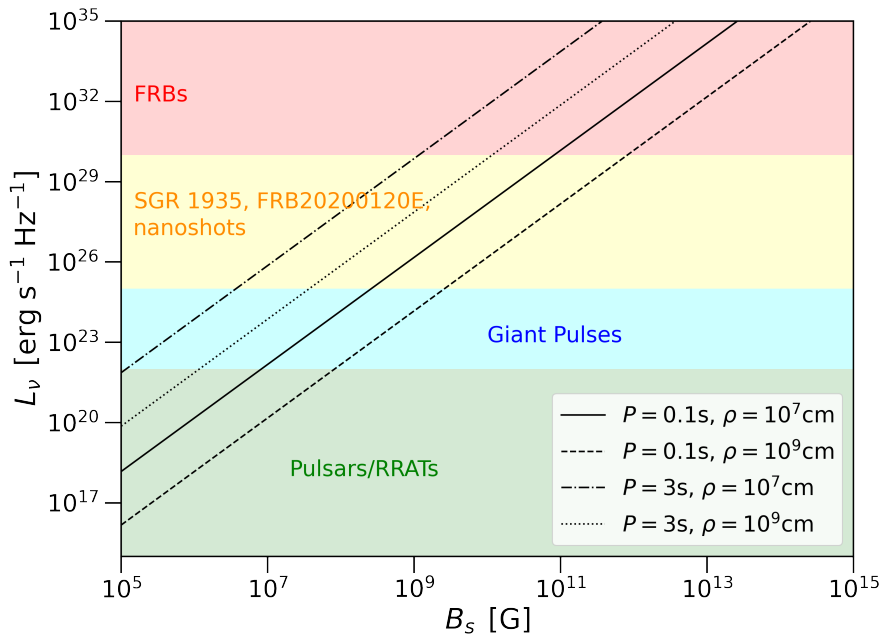
Figure 3.1: We plot the maximum spectral luminosity for two reasonable limiting source parameters using Eq 3.16. We fix $\xi = 10$, $N_{\mathrm{p}} = 1$, $\nu = 10^9$ and $R = 2 \times 10^6$ cm. In the background we show typical spectral luminosities of coherent radio sources (Pietka et al., 2015), noting in particular the sources in yellow that bridge the gap between extra-galactic and galactic sources (Hankins & Eilek, 2007; Bochenek et al., 2020b; Nimmo et al., 2021).

curvature radiation. We further assume a pure dipole magnetic field, $\rho = 10^7$ and $\xi = 10$. We find the origin of a kJy burst must be less than 400km from the surface of the NS. The inferred limits on parameters of the emission are: $B \geq 10^8$G and $20 < \gamma \leq 250$ depending on $\frac{R}{R_{\mathrm{NS}}}$, but emission closer to the NS with modest lorentz factors is preferred due to causality arguments in Section 3.2.

The most extreme Crab nanoshot had a 9 GHz flux of 2 Mega-Jansky ($L_\nu \approx 10^{28} \, \mathrm{erg \, s^{-1} \, Hz^{-1}}$; Hankins & Eilek 2007). Again via Eq. 3.16, we find that these brightest nanoshots must originate from less than 60km from the neutron star surface, assuming fiducial parameters. Despite the uncertainties involved in estimates of B_s and ξ, the dependence of R^{-6} in Eq. 3.16 means this result is very constraining even for large uncertainties in the source parameters. The short duration of these bursts is also consistent with discussion in Section 3.3.4 given how close to the NS the emission originates.

Recently Enoto et al. (2021) observed for the first time a 3% increase in the 0.2-12 keV X-ray flux associated with Crab giant pulses ($\nu = 2$ GHz), detecting a flux increase of $\delta F \approx 8 \times 10^{-10} \, \mathrm{erg \, s^{-1} \, cm^{-2}}$. We can estimate the 0.2-12 keV flux associated with the brightest giant pulses ($\approx$ 10kJy) observed by Enoto et al. (2021) via Eq. 3.21, assuming B_s and P as before. We find that fiducial parameters can explain both fluxes simultaneously at a distance for maximal bursts originating $\approx$ 200 km from the NS surface if $\zeta \approx 30$. The implied coherent and incoherent emission regions have transverse sizes of 5×10^3 cm and 1.5×10^5 cm respectively. We therefore suggest that small-scale particle gyration due to the induced field could plausibly explain the X-ray flux observed by Enoto et al. (2021), and the X-ray/radio flux ratio could be used to constrain the location of giant pulse emission. Non-detections of higher energy emission by other observatories, particularly the stringent upper limit reported in MAGIC Collaboration et al. (2020), is line with predictions of emission from close to the NS surface as higher energy photons are attenuated as discussed in Sect. 3.4.2. We note that in Enoto et al. (2021), the authors discuss possible origins of the increased X-ray flux during giant pulses which are not related to the coherently emitting particles themselves.

3.4.4   SGR 1935+2154

On 27th April 2020 a bright radio burst was observed from SGR 1935 with a 1.4 GHz spectral luminosity of $L_\nu = 1.6 \times 10^{26} \, \mathrm{erg \, s^{-1} \, Hz^{-1}}$ (Bochenek et al., 2020b). Assuming $B_s = 2.2 \times 10^{14}$ G and $P = 3.24$ s (Younes et al., 2021), Eq. 3.16 suggests the maximum distance of approximately 4000 km from the magnetar's surface assuming fiducial parameters. Furthermore, a coincident X-ray burst was observed with an 100 keV luminosity of approximately $10^{39} \, \mathrm{erg \, s^{-1}}$ (Mereghetti et al., 2020; Li et al., 2021; Ridnaia et al., 2021), with a harder spectrum than other magnetar bursts from the source (Younes et al., 2021). We find that both fluxes can be explained simultaneously for a maximal burst only if we allow non-fiducial parameters e.g. $\rho \approx 10^{10}$cm and $\zeta \approx 100$. Nevertheless, the prediction of high-energy emission with the same beaming factor as the coherent emission can explain the peculiar spectra of the X-ray burst temporally coincident with the radio burst. We sug-

gest coherent curvature radiation could be a universal feature of magnetar X-ray bursts, but observable only for a small fraction of cases due to the beaming restriction, whereas the thermal quasi-isotropic X-ray emission is observed more often.

3.4.5   Caveats and FRBs

There are a few caveats to the luminosity upper limit in Eq. 3.15. Firstly, we have assumed an approximately spherical source. A coherent source with longitudinal size R_l and transverse size R_t where $R_\mathrm{coh} > R_\mathrm{l} > R_\mathrm{t}$ would induce a smaller current and therefore allow luminosities up to a factor of $R_\mathrm{l}/R_\mathrm{t}$ larger. Furthermore, we have not considered in detail sources with $N_\mathrm{p} > 1$, where the number and geometry of the patches affects both the luminosity and duration of the observed radiation. We also note it is possible that some essential property of coherent curvature radiation prevents the emission of simultaneous high-energy radiation as predicted in Section 3.4.2.

The limitations described here still apply in quantum critical magnetic fields as was outlined in Kumar et al. (2017), where the authors suggest that FRBs must occur very close to the surface of magnetars in fields $B > 10^{14}$G. If particles confined to the ground state follow the total $B+B_\perp$ field, they should still gyrate as described in Section 3.2.1 and thus we might expect high-energy emission. Using Eq. 3.17 we predict X-ray emission of $\approx 10^{44}\,\mathrm{erg\,s}^{-1}$ below 1 MeV to accompany maximal magnetar ($B_s = 10^{15}\,$G) bursts. We can compare our prediction to the X-ray limits of Scholz et al. (2017) using Eq. 3.21 and assuming a 1 millisecond burst duration. We find a $0.5 - 10\,$keV fluence of approximately $10^{-26}\,\mathrm{erg\,cm}^{-2}$ to accompany radio bursts of 0.5 Jy, well below the constraints. We note that isotropic magnetar burst emission may dominate, depending on the parameters.

3.5   Conclusion

In this Letter we have considered electrodynamic interactions between coherently radiating particles. We have shown in Section 3.3 & 3.4 that there is an upper limit to the radio luminosity of coherent curvature radiation which depends on the source parameters. This limit suggests that if the giant pulses are powered by coherent curvature radiation, they must originate in the inner magnetosphere very close to the NS surface. Furthermore, small scale particle gyration could mean that coherent curvature radio pulses are universally associated with high-energy counterparts. A common coherent curvature radiation origin of giant pulses and FRBs can be falsified by observations of emission from a known source more luminous than allowed by the limits in Fig. 3.1. Future work includes investigating the quantitative effect of multiple coherent patches, the frequency and polarization predictions of coherent curvature emission taking into account individual particle gyration on small scales and modelling giant pulse & FRB populations.

Acknowledgements

Data Availability

A Python notebook from which the results and figures of this Letter can be reproduced will be made available at DOI:10.5281/zenodo.5211149

3

Chapter **4**

Pulsar revival in neutron star mergers: multi-messenger prospects for the discovery of pre-merger coherent radio emission

A. J. Cooper, O. Gupta, R.A.M.J. Wijers, Z. Wadiasingh, O. M. Boersma, I. Andreoni, A. Rowlinson, K. Gourdji

Abstract

We investigate pre-merger coherent radio emission from neutron star mergers arising due to the magnetospheric interaction between compact objects. We consider two plausible radiation mechanisms, and show that if one neutron star has a surface magnetic field $B_\mathrm{s} \geq 10^{12}$G, coherent millisecond radio bursts with characteristic temporal morphology and inclination angle dependence are observable to Gpc distances with next-generation radio facilities. We explore multi-messenger and multi-wavelength methods of identification of a NS merger origin of radio bursts, such as in fast radio burst surveys, triggered observations of gamma-ray bursts and gravitational wave events, and optical/radio follow-up of fast radio bursts in search of kilonova and radio afterglow emission. We present our findings for current and future observing facilities, and make recommendations for verifying or constraining the model.

4.1   Introduction

Compact object mergers involving black holes (BH) and neutron stars (NS) have long been hypothesized to power a range of high-energy, multi-messenger astrophysical phenomena (Lattimer & Schramm, 1974; Clark & Eardley, 1977; Blinnikov et al., 1984; Eichler et al., 1989; Li & Paczyński, 1998). Many of these predictions were confirmed by the discovery of an electromagnetic counterpart to gravitational wave event GW170817, which provided direct evidence of a common origin of gravitational waves from a NS-NS merger (Abbott et al., 2017b), short gamma-ray bursts (sGRBs) powered by bipolar jets (Abbott et al., 2017c; Goldstein et al., 2017), kilonovae (Abbott et al., 2017d; Tanvir et al., 2017; Kasen et al., 2017; Pian et al., 2017) and late-time afterglow emission (e.g. Alexander et al. 2017; Hallinan et al. 2017; Abbott et al. 2017d; Lazzati et al. 2018; Mooley et al. 2018; Dobie et al. 2018; Ghirlanda et al. 2019). Prompt radio observations of the localisation region began 30 minutes post-merger (Callister et al., 2017), therefore radio emission mechanisms related to the inspiral or merger itself were not probed.

Two-body electromagnetic interactions are thought to be the sources of coherent radio emission since the seminal work by Goldreich & Lynden-Bell (1969) investigating the Jupiter-Io system. The inspiral phase that precedes coalescence during NS-NS mergers has been hypothesised to give rise to pre-merger electromagnetic emission due to the strong surface magnetic fields present in known pulsars and magnetars. A range of mechanisms have been considered as candidates to power precursor electromagnetic emission during NS mergers including: the unipolar inductor model (Hansen & Lyutikov, 2001; Lai, 2012; Piro, 2012), resonant NS crust shattering (Tsang et al., 2012; Suvorov & Kokkotas, 2020), magnetohydrodynamic plasma excited by gravitational waves (Moortgat & Kuijpers, 2006) nuclear decay of tidal tails (Roberts et al., 2011), the formation of a optically thick fireball (Vietri, 1996; Metzger & Berger, 2012; Beloborodov, 2021), wind-driven shocks (Medvedev & Loeb, 2013; Sridhar et al., 2021) and particle acceleration through the revival of pulsar-like emission during inspiral (Lipunov & Panchenko, 1996; Lyutikov, 2019). Numerical studies of force-free electromagnetic interaction between magnetized NS-NS binaries support the conclusion that flares may be observed before the merger (Palenzuela et al., 2013; Most & Philippov, 2020, 2022).

High-energy precursor emission has previously been observed in sGRBs, and may be a powerful tool to either infer properties of the merging compact objects (see Section. 4.3.6), or enable targeted observations of the merger event by automated or rapid slew. Troja et al. (2010) found that 8-10% of *Swift* detected sGRBs display precursor emission in the *Swift* bandwidth, compared to around 20% of long GRBs (lGRBs) detected by Burst and Transient Source Experiment (*BATSE*; Lazzati 2005). Furthermore, Coppin et al. (2020) find that lGRBs observed by *Fermi* are 10 times more likely to display precursor gamma-ray emission before the main burst, as compared to sGRBs. However, we note that apparent precursor emission may be merely a manifestation of variable prompt gamma-ray burst emission: Charisi et al. (2015) show that precursor and post-cursor emission are statistically similar, and may share a common origin. The recent claim of a quasi-periodic precursor emission to coincident with a kilonovae-associated lGRB further implies that precursor emission could

be used to infer the nature of the progenitor (e.g. probing crust shattering events at small separation; Suvorov et al. 2022), as well as the resultant post-merger compact object (Xiao et al., 2022).

Predictions of pre-merger emission are particularly relevant in light of new observational techniques with which theoretical predictions can be tested. For example, automatic triggered observations in response to high-energy alerts, particularly by software interferometers such as the LOw Frequency ARray (LOFAR van Haarlem et al. 2013) & the Murchison Widefield Array (MWA; Tingay et al. 2013) where physical repointing is not necessary, enable rapid observations on source within $\approx$ 4 minutes and $\approx$ 10 seconds, respectively. Observations triggered by GRB or gravitational wave (GW) alerts (e.g. Anderson et al. 2021b; Rowlinson et al. 2021; Tian et al. 2022) also benefit from dispersion delay of low-frequency emission during propagation, which at LOFAR frequencies of 144 MHz corresponds to approximately 3 minutes of delay between gamma-ray and radio signals for a redshift of $z \sim 1$ (corresponding to a dispersion measure of $\sim$800 pc cm^{-3}). Furthermore, these techniques are enhanced if raw data is saved using transient buffers enabling negative latency triggers (e.g. ter Veen et al. 2019), or making use of early time alerts from gravitational wave detectors (James et al., 2019). Rapid radio observations of sGRBs can test theories of coherent radiation after the merger (Rowlinson et al., 2019) predicted in shocks (Usov & Katz, 2000; Sagiv & Waxman, 2002), or from a short-lived magnetar remnant (Rowlinson et al., 2013). The constraints set by past observations of kind are discussed with respect to the model presented here in Section. 4.4.2.

Theoretically, interest in the electromagnetic interaction between coalescing compact objects has recently been revived to explain a subset of fast radio bursts (FRBs) (Lorimer et al., 2007; Thornton et al., 2013; Spitler et al., 2014; Petroff et al., 2016, 2022) which do not appear to repeat (Totani, 2013; Zhang, 2014; Wang et al., 2016; Gourdji et al., 2020). This was further bolstered by the tentative association of FRB 150418 with a fading radio source, which was originally thought to be consistent with a short gamma-ray burst afterglow (Keane et al., 2016); however the association was later ruled out as unrelated transient activity from an active galactic nucleus (AGN) (Williams & Berger, 2016). Recent estimates of the rates of NS-NS mergers (see Andreoni et al. 2021a; Mandel & Broekgaarden 2021 and references therein) suggest a local volumetric NS-NS merger rate not more than $\approx 10^3$ Gpc^{-3} yr^{-1}, which appears to fall short of the volumetric FRB rate (Luo et al., 2020). Comparing the volumetric rates of FRBs and plausible cataclysmic progenitors, Ravi (2019) demonstrates that most apparently one-off FRBs likely repeat albeit with a low repetition rate, and thus NS mergers may power a fraction of truly non-repeating FRBs. It is an open question as to whether sub-populations of FRBs evolve differently as a function of redshift; Hashimoto et al. (2020a) suggest that an older stellar population underlies one-off FRBs, which may support e.g. merger progenitors, although this is disputed by James et al. (2022). Interactions between magnetized neutron stars and other objects such as black holes (Zhang, 2016) or asteroids (Dai et al., 2016; Voisin et al., 2021) could also induce magnetospheric interactions resulting in coherent emission observable to cosmological distances. This is discussed

further in Section 4.5, and many of the results of Sect. 4.3 are relevant for NS interactions with other conducting bodies.

In this work, we take a detailed look at the plausible emission due to the magnetospheric interaction between merging neutron stars, adapting and extending the work of Lyutikov (2019). We implement plausible radiation mechanisms, and make robust predictions of the temporal evolution and observer inclination angle dependence of pre-merger coherent radiation emission. The paper is organised as follows. In Section 4.2, we present the electrodynamic model of the NS-NS merger originally suggested by Lyutikov (2019), and present adaptations to the model with a full derivation available in Appendix 4.A. In Section 4.3 we discuss plausible particle acceleration and radiation mechanisms that result in coherent pre-merger emission, and estimate the radio luminosity. In Section 4.4 we discuss prospects of detecting such emission in FRB surveys, through triggered observations of gravitational wave and gamma-ray burst detected mergers and confirming a NS-NS merger origin after the fact through observations of kilonovae or radio afterglow emission. Each subsection is devoted to a separate observing strategy, in which we discuss prospects for current and future instrumentation. We conclude with a discussion in Section 4.5 and present our primary findings in Section. 5.6.

4.2   Model: Conductor in NS magnetosphere

In Lyutikov (2019), the authors consider electromagnetic interaction between two neutron stars in a binary system. In the first case (denoted in Lyutikov (2019) as the 1M-DNS scenario) which we focus on, it is assumed that one NS is highly magnetized (henceforth the primary NS) such that the other neutron star (henceforth the secondary NS, or the conductor) acts as a perfect, spherical conductor due to negligible magnetization. This is a natural scenario expected from evolutionary considerations, as the first-to-form, older secondary NS may be partially recycled, burying its field, while the younger primary NS will retain higher magnetization. It is also in concordance with the double pulsar system (Lyne et al., 2004), where one pulsar is partially recycled. During orbital motion, the secondary NS moves through the magnetosphere of the primary, expunging magnetic field field lines and inducing an electric field outside the surface of the secondary NS, with a significant component parallel to the magnetic field lines, $E_\parallel$. We also note that the results in this work will also be applicable to pre-merger emission from double white dwarf (WD) binaries that Laser Interferometer Space Antenna (LISA; Amaro-Seoane et al. 2017) will observe in our Milky Way. Although they will emit at a much lower luminosity, their proximity may mean that incoherent higher frequency nonthermal emission is within the horizon of optical or X-ray instruments, similar to AR Scorpii (Marsh et al., 2016).

To estimate particle acceleration and the pre-merger emission signature, we derive the parallel electric field component due to the motion of the secondary neutron star. We use a spherical coordinate system (r, θ, ϕ) centred on the conductor unless otherwise stated, where r is the radial distance, θ is the polar angle and ϕ the azimuthal angle. $B = B(r, \theta, \phi)$ is the magnetic field strength at the location of the secondary due to the primary, and $\beta = v/c$
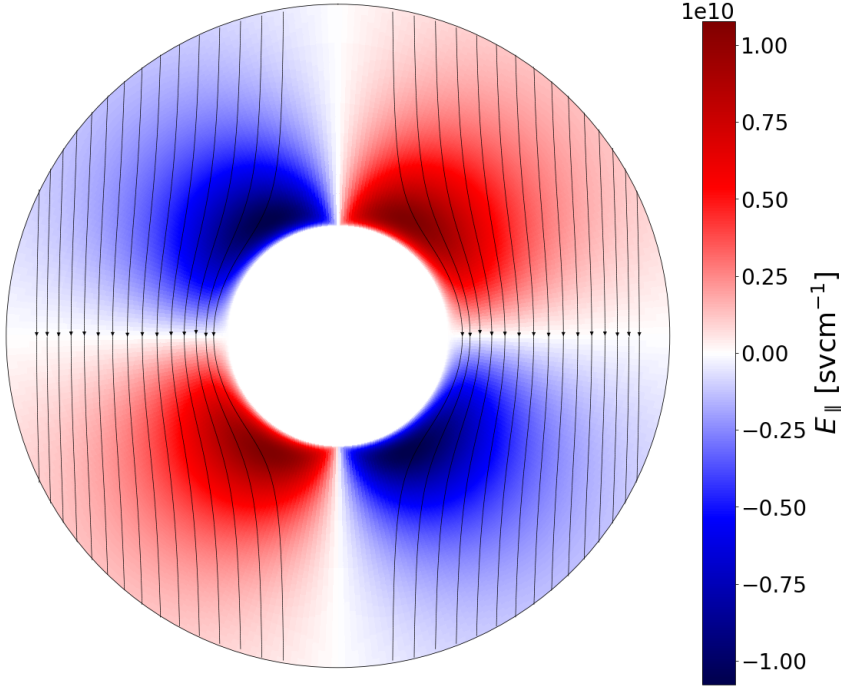
Figure 4.1: A map of the electric field parallel to the magnetic field lines $E_\parallel$ surrounding the conductor in the $x - z$ plane for representative values of $B = 10^{11}\,$G and $\beta = 0.5$. The induced $E_\parallel$ field has a quadrupole structure, meaning coherent radiation is preferentially emitted in solid angles perturbed from the primary NS' magnetic axis.

where v is the relative velocity of the conductor through the magnetosphere. For the purpose of this simple electromagnetic model, the direction of the magnetic field of the primary NS dipole is assumed to be uniform at the position of the secondary NS (as in Lyutikov 2019), as would be the case for large binary separations. The parallel magnetic field approximation holds reasonably well despite the fact that the conducting secondary and the primary are close together, as the regions with large values of $E_\parallel$ are close to the conducting NS surface where expunged magnetic field lines are tangential (see Fig. 4.1). This means that even for small binary separations the emission region and direction are dominated by the motion of the conductor and not by the primary's field topology. We use a separation-dependent magnetic field strength in Section 4.2.2.

In Appendix 4.A, we present a full derivation of the electric field that develops. We find a small correction to the $E_\parallel(r, \theta, \phi)$ derived in Lyutikov (2019) (given by Eqs. (4.1) & (4.2)). The correction is made by first finding the electric field vector in a frame co-moving with the secondary NS. It is in this frame that the electromagnetic interface conditions are solved for, following which a Lorentz transformation to the primary NS frame gives the electric field for an observer stationary with respect to the primary's magnetosphere. The electromagnetic

response of the secondary establishes a surface current and a surface charge, which are responsible for eliminating the magnetic field and the electric field respectively from within the secondary unmagnetized NS. While the magnetic field is tangential at the surface in both frames when ignoring second order terms of velocity originating from relativistic correction, the stipulation that the electric field is perpendicular to the conductor's surface is valid only in the co-moving frame, but not in the primary's frame. The parallel component of the electric field is calculated by taking the dot product with the unit vector in the direction of the magnetic field. It becomes evident from Eq. (4.2) that the region of maximum parallel electric field is not at the surface of the conductor, but approximately $0.23 R_{\mathrm{NS}}$ away from the surface (see Figure 4.1).

$$E_{\parallel,\mathrm{L19}} = -\frac{3}{2\sqrt{2}} \frac{\sin(\theta)\cos(\theta)\cos(\phi)\left(6 - \frac{R_{\mathrm{NS}}^3}{r^3}\right)}{\sqrt{8\left(1 - \frac{R_{\mathrm{NS}}^3}{r^3}\right)^2 + 6\left(4 - \frac{R_{\mathrm{NS}}^3}{r^3}\right)\frac{R_{\mathrm{NS}}^3}{r^3}\sin^2(\theta)}} B\beta \frac{R_{\mathrm{NS}}^3}{r^3} \tag{4.1}$$

$$E_{\parallel,\mathrm{this\ work}} = \frac{3\sin(\theta)\cos(\theta)\cos(\phi)\left(1 - \frac{R_{\mathrm{NS}}^3}{r^3}\right)}{\sqrt{4\cos^2\theta\left(1 - \frac{R_{\mathrm{NS}}^3}{r^3}\right)^2 + \sin^2(\theta)\left(2 + \frac{R_{\mathrm{NS}}^3}{r^3}\right)^2}} B\beta \frac{R_{\mathrm{NS}}^3}{r^3} \tag{4.2}$$

4.2.1   Inspiral phase

Using the post-Newtonian approximation by Peters (1964), we can write down the binary separation a, of two identical spherical objects of mass M, as a function of time t, due to gravitational radiation:

$$\frac{1}{a}\frac{da}{dt} = -\frac{128}{5}\frac{G^3 M^3}{c^5 a^4} \tag{4.3}$$

As in Metzger & Zivancev (2016), the merger time until $a = 0$ is:

$$t_{\mathrm{m}} = \frac{5}{512}\frac{c^5 a^4}{G^3 M^3} \tag{4.4}$$

This equation is valid only until the disruption of the conductor at a_{min}. We can put a lower limit on a_{min} by considering how the Roche lobe of the conductor evolves as the binary separation decreases (Eggleton, 1983). Assuming two identical $1.4 M_\odot$ NSs ($q = 1$), we find that $a_{\mathrm{min}} = 26.4$km, however depending on the equation of state of the NS, tidal disruption may occur sooner. We note that the secondary NS will always move through the magnetosphere of the primary neutron star as the stars will not be tidally locked, but that neglecting tidal forces may effect dynamics and therefore lightcurve morphology (Sect. 4.3.6) during the final few orbital periods (Bildsten & Cutler, 1992).

Solving Eq. (4.3) we find:

$$a(t) = \left(a_0^4\left(1 - \frac{t}{t_{\mathrm{m},0}}\right)\right)^{1/4} \tag{4.5}$$

where a_0 is the initial separation, and $t_{m,0}$ is the time to merger at the initial separation. We assume both the primary magnetized NS and secondary conducting NS have radii $R_{NS} = 12$km (Abbott et al., 2018; Lattimer, 2019) and masses $M = 1.4 M_\odot$. Substituting equations for $B(r, \theta, \phi)$ and β into Eq. (4.2), and using Eq. (4.5) we can write $E_\parallel(r, \theta, \phi, t)$ as:

$$
\begin{aligned}
E_\parallel &= f_1(r, \theta, \phi) B(r, \theta, \phi) \beta \\
&= f_2(r, \theta, \phi) \frac{B_s R_{NS}^3 \sqrt{GM}}{c a_0^{7/2}} \left(1 - \frac{t}{t_{m,0}}\right)^{-7/8}
\end{aligned}
\tag{4.6}
$$

Eq. (4.6) dictates the induced electric field around the surface of the conductor, where $f(r, \theta, \phi)$ varies at different spatial points around the conductor. It encapsulates the prefactor in Eq. (4.2), but also the depends on the magnetic field strength at each point. We also take into account the orbital motion of the magnetized object in the frame of the conductor, leading to asymmetric $E_\parallel$ field as $a \to a_{\min}$ as seen in Fig. 4.2. As expected, we find that $E_\parallel$ increases as $t \to t_{m,0}$, and thus particle acceleration and attainable radiation luminosity around the conductor increases as the inspiral progresses.

4.2.2   Numerical method: emission directed along field lines

To investigate the time-dependent and viewing angle dependent emission expected from these systems, we calculate the electromagnetic fields during the inspiral in 3 dimensions and map the parallel electric field component given by Eq. (4.1). To compensate for our assumption of uniform magnetic field strength around the conductor while building the electromagnetic model, we compute the local magnetic field value B at (t, r, θ, ϕ) surrounding the conductor by finding the distance to the centre of the primary magnetized neutron star, $a(r, \theta, \phi)$, and assuming the field decreases as $B \approx B_s \left(\dfrac{R_{NS}}{a(r, \theta, \phi)}\right)^3$. Assuming $\mathbf{B} = B\hat{\mathbf{z}}$ frees the uniform field condition even though the background field is still assumed to be parallel. Furthermore, the magnetic field lines expunged by the conductor are defined in Lyutikov (2019) as:

$$
\mathbf{B} = -B \cos(\theta) \left(1 - \frac{R^3}{r^3}\right) \hat{\mathbf{r}} + B \sin(\theta) \left(1 + \frac{R^3}{2r^3}\right) \hat{\boldsymbol{\theta}}
\tag{4.7}
$$

This equation is defined for uniform and parallel B, however, we perform computations with the assumption of separation-dependent magnetic field strength.

As we will show in Section 4.3, we expect particle acceleration and therefore any coherent radiation to be directed along the local magnetic field lines regardless of the specific radiation mechanism. The angle subtended by total field line $\mathbf{B}$ and the radial direction $\hat{\mathbf{r}}$ is given by: $\theta_{\hat{\mathbf{r}}, \mathbf{B}} = \arctan \dfrac{B_\theta}{B_r}$. Therefore in the frame of the conductor the direction of a local field line with respect to the $\hat{\mathbf{z}}$ direction at (r, θ, ϕ) is given by:

$$
\theta_B = \theta + \arctan \frac{B_\theta}{B_r}
\tag{4.8}
$$
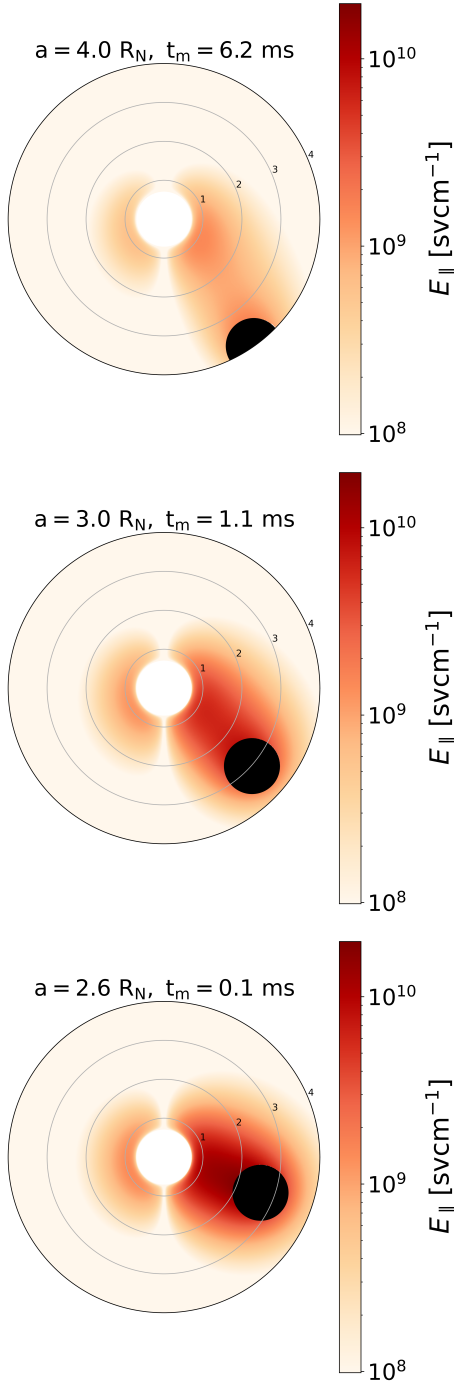
Figure 4.2: The parallel electric field surrounding the conducting NS (centre, white) and the magnetized primary NS (black) for three different binary separations a during the inspiral. Each panel is centered on the conductor as viewed from above the orbital plane. As the inspiral progresses and orbital separation decreases, regions of high parallel electric field surround the conductor, particularly in the region between the conducting NS and the primary NS due to the large local magnetic field. The view shows the $\theta = \frac{\pi}{4}$ plane as Eq. (4.2) tells us that $E_\parallel = 0$ if $\theta = \frac{\pi}{2}$, i.e., in the orbital plane. The electric field units are stated in statvolts per centimetre.

In the calculation, each cell in (r, θ, ϕ) is assigned a value of $E_\parallel$ via Eq. (4.2), a magnetic field vector **B** according to Eq. (4.8) and a volume element δV. To estimate the radio flux measured by an observer at (D, θ, ϕ) in the frame of the conductor, we find set of cells with magnetic field vectors whose solid angle subtended by a beaming angle $\theta_{\mathrm{beam,coh}} \approx 0.1$ radian [1] encompasses the observer. We then sum the luminosity of all cells aligned with the observer according to Eqs. (4.7) & (4.8), to produce lightcurves in Fig. 4.7. We find that emission is primarily observed at angles of $5 - 45 \deg$ from the background magnetic field, and this viewing angle dependent emission is discussed in Sect. 4.3.5. We omit general relativistic (GR) effects on the radiation such as gravitational redshift, gravitational lensing, Lense-Thirring precession, frame dragging and relativistic abberation ($\theta_{\mathrm{abb}} \approx 0.1\,\mathrm{rad}$) due to the orbital motion, which effect the magnetic field topology and therefore where emission is directed (e.g. Wasserman & Shapiro 1983; Gonthier & Harding 1994). These effects are generally small i.e. on the order of $\beta/2 \approx 20\%$ in the centre-of-mass frame, and are therefore neglected in our calculation and in the predictions of Section 4.3.6. For edge-on observers, conditions may be met for strong lensing of emission regions of the second by the primary, dependent on the magnetic field geometry. Considering how GR may modify the overall luminosity and the temporal morphology of the signal could be explored in a future work.

4.3 Particle acceleration and radiation

As orbital motion progresses and the motion of the conductor through the magnetic field of the primary induces a large parallel electric field $E_\parallel$, charged particles will be pulled from the secondary NS's surface and accelerated along field lines to high energies (e.g. Dai et al. 2016). In any case, Timokhin (2010); Timokhin & Arons (2013) have shown that a vacuum-like gap will be formed regardless of whether the surface is free to emit charges, as pair creation discharges are non-stationary and pairs are advected out of the acceleration zone. In Lyutikov (2019) it was noted that coherent radiation emitted in the radio band is the most feasible method by which to observe such precursor emission, given the relatively low total power as compared to e.g. gravitational waves or GRBs. This particle acceleration bears resemblances to two theories of coherent radiation: pulsar-like emission that invokes on pair production fronts across gaps developed to explain radio pulsars (Sturrock, 1971; Ruderman & Sutherland, 1975; Timokhin, 2010; Timokhin & Arons, 2013) and coherent curvature radiation which has been recently used to explain the origin of FRBs from magnetars (Katz, 2014; Kumar et al., 2017; Lu & Kumar, 2019; Cooper & Wijers, 2021). In the following section we discuss the former, and in Appendix 4.C we discuss the latter, in the context of the model.

---

[1] This choice, although motivated by observations of the pulsar duty cycle (neglecting period dependence e.g. Rankin 1993), is somewhat arbitrary in that it depends on the details of plasma EM mode propagation and decoupling within the magnetosphere.

4.3.1   Pulsar-like emission

As mentioned in previous works (Lipunov & Panchenko, 1996; Totani, 2013; Lyutikov, 2019), a NS-NS merger may revive pulsar-like emission. Although pulsar emission is poorly understood (see e.g. Melrose 2017), the merger of a 10^{12} G neutron star invokes similar electromagnetic conditions to those expected to power coherent radio emission from radio pulsars (see discussion above in Section 4.2). The radio luminosity during the inspiral may be much larger than typically observed from pulsars of similar magnetic field strength for two main reasons. Firstly, the spatial extent of the $E_{\parallel}$ acceleration region due to the motion of the secondary is large ($l_{E_{\parallel}} \approx R_{\mathrm{NS}} \approx 10^6$ cm), in contrast to pulsar cap models where $l_{\mathrm{pc}} \approx 10^4 \, P_0^{-1/2}$ cm. Secondly, the required charge density of the magnetosphere may be much higher than in the isolated pulsar. This is because the $B \times v$ motion of the magnetosphere is dominated by the binary orbital period $P_{\mathrm{orb}} \approx \dfrac{2\pi a}{v_{\mathrm{orb}}} \approx 10^{-3} \, a_{30km}^{3/2}$ seconds and not by the spin period of the aging magnetized 10^{12}G NS which is usually $P_{\mathrm{spin}} > 1$s. In the following, we explore the basics of pulsar-like emission in gap models, and calculate analytically the expected radio luminosity from NS merger systems.

4.3.2   Acceleration gap

In the polar cap models of pulsar emission (Ruderman & Sutherland, 1975; Daugherty & Harding, 1982), rotation-induced electric fields close to the surface of the NS accelerate particles along open magnetic field lines. The acceleration of these particles along curved magnetic field lines perpendicular to their velocity produces gamma-ray curvature radiation. These high-energy photons interact with magnetic fields through magnetic pair production to produce cascades of secondary pairs, where the ratio of primary to secondary pairs is known as the pair multiplicity: $\kappa = N_{\mathrm{sec}}/N_{\mathrm{pri}}$ and is $1 < \kappa \lesssim 10^3$ (Timokhin & Harding 2019; although see also Harding & Muslimov 2011 who find the multiplicity could be as high as 10^6 for multipolar field topologies). The secondary pairs inherit momenta and energy from the primaries, leading to nonstationary discharges that launch superluminal waves with an efficiency $\eta < 1$ (Philippov et al., 2020). We assume that the secondaries (and all subsequent orders) are energetically subdominant as compared to the primary particles that initiate the burst-like cascades. To understand the expected coherent luminosity in a viewing angle dependent manner, we estimate the radio luminosity through a pulsar-like mechanism in Section 4.3.3 using our numerical set-up described in Section 4.2.2. In the following, we calculate the gap height assuming it is one-dimensional and stationary, neglecting for simplicity that the gap will be non-stationary in reality.

The height of the acceleration gap h_{gap} is the distance from the initial acceleration point h_0 to a pair production front, where cascades occur efficiently enough to completely screen the electric field. This gap height is the sum of two length scales: $l_{\mathrm{acc,gap}}$ is the distance traversed by accelerated primaries before they attain enough energy such that emitted curvature photons are capable of pair production; and $l_{\gamma,\mathrm{gap}}$ is the distance traversed by curvature photons before pair production occurs. For larger values of $l_{\mathrm{acc,gap}}$, higher energy curvature photons

are produced and therefore smaller values of $l_{\gamma,\mathrm{gap}}$ are attained. Therefore to find the h_{gap} $= l_{\mathrm{acc,gap}} + l_{\gamma,\mathrm{gap}}$, we minimize h_{gap} to find the distance at which the pair creation cascade begins.

The maximum energy of primary pairs accelerated by $E_{\parallel}$ along the B-field is limited by either curvature radiation or resonant inverse-Compton scattering from soft X-rays (Baring et al., 2011; Wadiasingh et al., 2018). In the absence of other particle acceleration mechanisms, we do not expect a significant X-ray radiation field due to the relatively low magnetic field (compared to magnetars) and slow spin of the primary magnetized neutron stars. However, if there is tidal friction transmitted to the crust (rather than heating the interior and core) or crust shattering before merger this may not be the case. In this case, the equation of motion of the primary accelerated pairs is:

$$\frac{d\epsilon_{\mathrm{e}}}{dt} = qE_{\parallel}c - \dot{\epsilon}_{\mathrm{curv}} \tag{4.9}$$

Note that we used ϵ when referring to particle energies to make a clear distinction between energy and the electric field. It has been shown for both magnetars (Wadiasingh et al., 2020) and pulsars (Timokhin & Harding, 2015) that the gap terminates before the radiation reaction regime occurs, where the maximum energy of accelerated primary pairs is limited by the curvature radiation. In this case we can neglect curvature losses during the gap height calculation. However, as the NS merger system has very strong $E_{\parallel}$ and short acceleration timescales, in the following we show that even in the radiation reaction regime, the gap will still form. In the radiation reaction regime, the Lorentz factor of the accelerated pairs can be found by equating the acceleration power and loss power $P_{\mathrm{acc}} = P_{\mathrm{curv}}$:

$$qE_{\parallel}c = \frac{2qc\gamma^4}{3\rho_{\mathrm{c}}^2}$$
$$\gamma_{\mathrm{max}} = \left(\frac{3E_{\parallel}\rho_{\mathrm{c}}^2}{2}\right)^{1/4} = 3 \times 10^5 \, E_{\parallel,10}^{1/4} \, \rho_{\mathrm{cm},6}^{1/2} \tag{4.10}$$

Where ρ_{c} is the curvature radius. The energy of emitted curvature photons is therefore:

$$\epsilon_{\mathrm{ph}} = \hbar\omega = \frac{3\hbar c\gamma^3}{\rho_{\mathrm{c}}} = 8 \times 10^{-5} \, \mathrm{erg} = 500 \, \mathrm{GeV} \, \gamma_5^3 \, \rho_{\mathrm{c},6}^{-1} \tag{4.11}$$

At γ_{max} curvature photons are produced many orders of magnitude above the energetic threshold required for magnetic pair production, $\epsilon_{\mathrm{threshold}} \approx 2m_e c^2$, therefore even in this regime the gap will form. However, under the assumption that radiation reaction does not occur we neglect curvature losses during free acceleration such that the primaries' Lorentz factor as a function of path length l is:

$$\gamma(l) \approx \frac{qE_{\mathrm{gap}}l}{m_e c^2} \tag{4.12}$$

Where $E_{\mathrm{gap}} = 4\pi qnl_{\mathrm{acc}}$, and understanding the number density n is crucial to estimating E_{gap}. In the maximal case we take this to be equal to $E_{\parallel}$, referring to the case in which no significant current is present to screen the field. In the NS merger case, in contrast to the pulsar

emission case, current requirements vary significantly on timescale associated with the orbital period and therefore it is likely that the field will be unscreened. We can also consider a lower limit to the number density of accelerated particles to be the Goldreich-Julian density required by the rotation of the magnetosphere due to the orbit: $n = n_{GJ} = (2B)/(qcP_{\mathrm{orb}})$, where B is the local magnetic field. We find that for regions of the strongest emission, the difference between the lower limit to the number density ($n_{GJ} \approx 10^{13}\ \mathrm{cm}^{-3}\ B_{11}\ P_{\mathrm{orb},-3}^{-1}$) and the $E_{\mathrm{gap}} = E_{\parallel}$ upper limit ($n \approx 10^{16}\ \mathrm{cm}^{-3} E_{\parallel,10}\ l_{\mathrm{acc},2}^{-1}$) is approximately a factor of 10^{3}, and corresponds to a factor of 10^{6} in the overall luminosity (see Eq. (4.21) and Fig. 4.5). For the remainder of the paper, we consider the upper limit case and assume that $E_{\mathrm{gap}} = E_{\parallel}$, while considering a wide range of particle power to coherent luminosity efficiency values, η, to account for lower values of the number density n. We also include the analytic gap height calculation for the lower limit $n = n_{\mathrm{GJ}}$ case in Appendix 4.B.

In the $E_{\parallel} = E_{\mathrm{gap}}$ limit, the Lorentz factor of the primaries is:

$$\gamma(l) = \frac{qE_{\parallel}l_{\mathrm{acc}}}{m_e c^2} \tag{4.13}$$

Substituting into Eq. (4.11) we find:

$$\epsilon_{\mathrm{ph}} = \frac{3\hbar c}{\rho_{\mathrm{c}}}\left(\frac{qE_{\parallel}l_{\mathrm{acc}}}{m_e c^2}\right)^3 \tag{4.14}$$

For above-threshold pair production in fields $B \ll B_{\mathrm{c}}$ we require that:

$$\chi \equiv \frac{\epsilon_{\mathrm{ph}}}{2m_e c^2}\frac{B}{B_{\mathrm{c}}}\sin(\theta_{k,B}) \gtrsim \max[0.2, B/B_{\mathrm{c}}] \tag{4.15}$$

Where $\theta_{k,B}$ is the angle between the magnetic field B and the photon momentum, and can be approximated as $\sin(\theta_{k,B}) \approx \dfrac{l}{\rho_{\mathrm{c}}}$ due to small angles and curved magnetic field lines diverging linearly from the photons' paths. Therefore the distance photons must travel before pair production is:

$$l_{\gamma,\mathrm{gap}} \approx 0.2\rho_{\mathrm{c}}\frac{2m_e c^2}{\epsilon_{\mathrm{ph}}}\frac{B_{\mathrm{c}}}{B} \tag{4.16}$$

By substitution of Eq. (4.14), we find:

$$l_{\gamma,\mathrm{gap}} = \frac{2\rho_{\mathrm{c}}^2 m_e^4 c^7 B_c}{15\hbar B q^3 E_{\parallel}^3 l_{\mathrm{acc}}^3} \tag{4.17}$$

Let $k = \dfrac{2\rho_{\mathrm{c}}^2 m_e^4 c^7 B_c}{15\hbar B q^3 E_{\parallel}^3}$. By expressing $l_{\gamma,\mathrm{gap}}$ in terms of l_{acc}, we can minimize $h_{\mathrm{gap}} = l_{\gamma,\mathrm{gap}} + l_{\mathrm{acc}}$ with respect to variations in l_{acc} to find values for both length scales that satisfy $\dfrac{\delta h_{\mathrm{gap}}}{\delta l_{\mathrm{acc}}} = 0$:

$$l_{\mathrm{acc}} = (3k)^{1/4}$$
$$l_{\gamma,\mathrm{gap}} = \frac{k}{l_{\mathrm{acc}}^3} = \frac{k^{1/4}}{3^{3/4}} \tag{4.18}$$
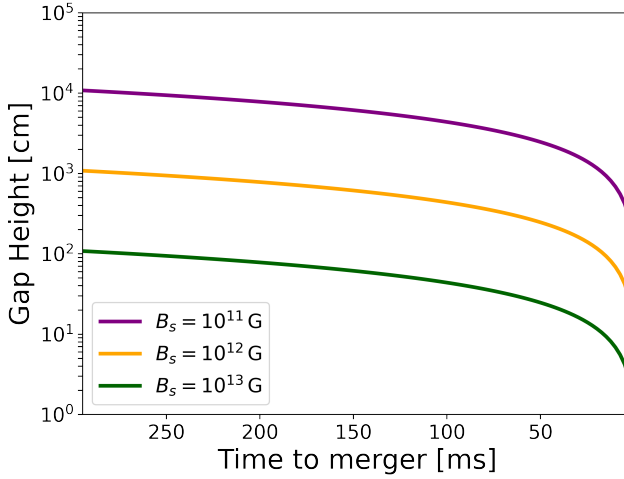
Figure 4.3: Gap height for a single point close to the secondary neutron star's surface as a function of time.

Therefore the h_{gap} is:

$$h_{\mathrm{gap}} = \frac{8k^{1/4}}{3^{3/4}} = \frac{8}{3^{3/4}} \left(\frac{2\rho_{\mathrm{c}}^2 m_e^4 c^7 B_c}{15\hbar B q^3 E_\parallel^3} \right)^{1/4}$$

$$= 40 \text{ cm } \rho_{\mathrm{c},6}^{1/2} \, B_{11}^{-1/4} \, E_{\parallel,10}^{-3/4} \tag{4.19}$$

Where we have included a factor of 2 to account for relative motion of pairs as in Wadiasingh et al. (2020). The approximate gap height as a function of time until merger is shown in Fig. 4.3 for short timescales, and Fig 4.4 on a longer timescale. The analytic gap height derivation assuming $E_{\mathrm{gap}} = 4\pi q n l_{\mathrm{acc}}$ where $n = n_{GJ} = (2B)/(qcP_{\mathrm{orb}})$ referred to here as the lower limit, is described in Appendix 4.B.

We show in Figs. 4.3 & 4.4 that for our timescales of interest this length scale is smaller than characteristic length scales for variations in both B and $E_\parallel$ as required for efficiency pair cascades (Timokhin & Harding, 2015), which are both on the order of the neutron star radius $R_{\mathrm{NS}} \approx 10^6$ cm. Furthermore, the fact that the gap length scale is smaller than the B variation length scale means that radio emission generated from pair cascades will be directed along local B-field lines. The superluminal O-modes will couple to plasma downstream of the cascades, be advected along B by adiabaticity and decouple at higher altitudes, transforming into vacuum EM modes.

Given this gap height, we can compute the potential difference across the gap:

$$\Phi = E_\parallel h_{\mathrm{gap}} \approx 10^{12} \text{ statvolt } E_{\parallel,10} \, h_{\mathrm{gap},2} \tag{4.20}$$

4
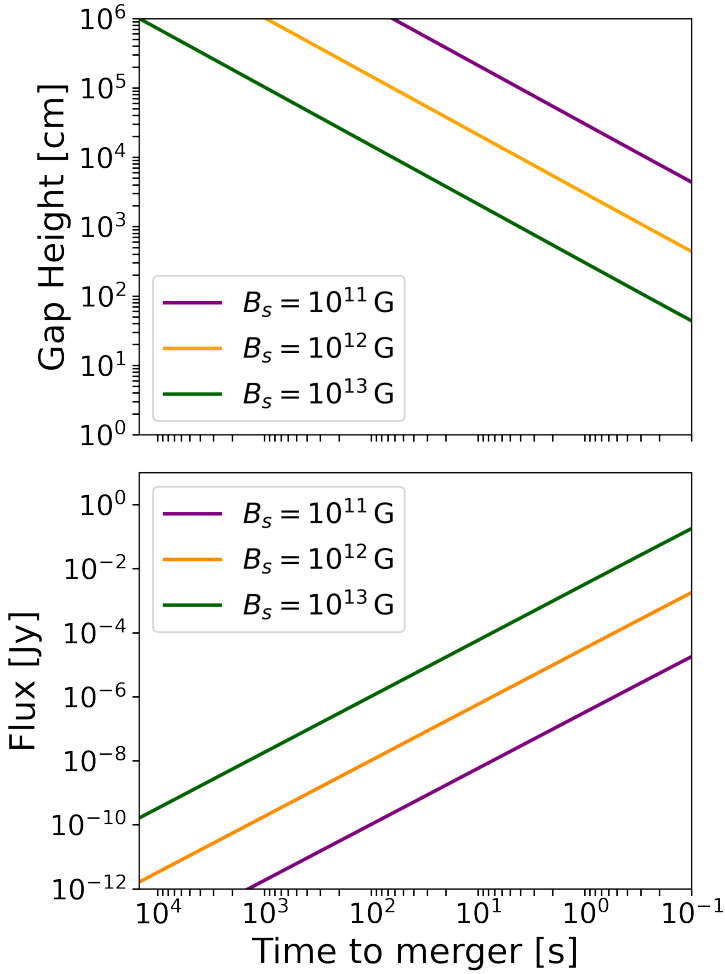
Figure 4.4: The approximate gap height and flux at $D = 100\,\mathrm{Mpc}$ for fiducial model parameters. A gap height $h_{\mathrm{gap}} < R_{\mathrm{NS}}, \rho_{\mathrm{c}} \approx 10^{6}\,$cm (corresponding to a typical separation of $10^{8}\,$cm) is where radio emission could be begin, albeit at a very low luminosities.

We note that this is higher than the minimum voltage of $\Phi = 10^{10}$ statvolt that is thought to be required for pulsar emission, which has been used to explain the pulsar 'death line' (Timokhin & Arons, 2013).

4.3.3   Radio luminosity proxy

As mentioned above, the radio emission is presumed to result from single-photon pair cascades from a significant $E_\parallel$ field component during the inspiral. In the Timokhin-Arons mechanism (Timokhin & Arons, 2013), the pair creation is a necessary and sufficient condition for generation of superluminal electromagnetic modes, while other mechanisms of the Ruderman-Sutherland type (Ruderman & Sutherland, 1975) require additional possibly unrealistic constraints and caveats. An upper limit for the radio luminosity in any scenario is the power furnished to free-accelerating primaries in the gap. The pulsar mechanism is broadband; in the Timokhin-Arons mechanism, this is due to the sum of a self-similar spectrum of non-stationary discharges in a scale invariant range of wavenumbers. For this simple estimate, we assume the entire radio luminosity is emitted across a bandwidth of $\delta\nu = 10\,\mathrm{GHz}$, although in a future work considering typical pulsar spectral index would provide better estimates for frequency dependent luminosities. In Appendix 4.C we discuss a Ruderman-Sutherland type coherent curvature radiation as an alternative radiation mechanism.

Below we show two methods of obtaining the luminosity of primaries, which in turn may be used as a proxy for the radio luminosity with the inclusion of an efficiency factor, η. This proxy is expected to capture the gross parameter scaling of coherent radio emission's luminosity involved in neutron stars, i.e. $L_{\mathrm{R}} \approx \eta L_{e^+e^-}$. The efficiency $\eta < 1$ moderates this estimate and depends on local conditions such as shape and extent of current regions with space-like or time-like regions (e.g. $J/(\rho_{\mathrm{q}}c)$ value and sign), the angle or shape of the pair formation front, and varying field curvature radii. In both derivations below, within factors of unity associated with geometric factors, the primary luminosity is $L_{e^+e^-} \sim 4\pi\rho_{\mathrm{q}}^2 h_{\mathrm{gap}}^2 Ac$ where A is a characteristic cross sectional area of flux tubes associated with the accelerating region, ρ_{q} is the required charge density to satisfy the transient conditions, and h_{gap} is the characteristic gap height appropriate to physical conditions for the cascades. For canonical rotation-powered radio pulsars, this calculation implies $\eta \sim 10^{-2}$ and is compatible with the voltage-like scaling of pulsar luminosity inferred by population studies with beaming models (e.g. Arzoumanian et al., 2002). Likewise, for seismically oscillating magnetars (Wadiasingh & Timokhin, 2019; Suvorov & Kokkotas, 2019; Wadiasingh et al., 2020; Wadiasingh & Chirenti, 2020) the pair luminosity estimate yields the correct energy scale $L_{e^+e^-} \sim 10^{39} - 10^{43}$ erg s^{-1} observed in cosmological FRBs (as well as the low-luminosity Galactic FRB observed from SGR 1935+2135 in April 2020). Correspondingly, as shown below, NS-NS inspirals where on NS has a large magnetic field $B_{\mathrm{s}} > 10^{13}$G also yield energy scales commensurate with observed FRBs albeit with possibly wider range in allowed luminosities for varying parameters. These varied luminosities, in addition to multi-messenger signals and chirps in FRB quasi-periodicity, may be a distinguishing characteristic of NS-NS mergers from magnetar progenitors in a sub-population of one-off FRBs.

4.3.3.1   Estimate due to energy in primaries

First, we compute the power of the primary particles accelerated across the gap: $P_{\text{particles}} = q\Phi_{\text{gap}}\dot{N}$ where $\dot{N}$ is the rate of primaries and $\Phi_{\text{gap}} = E_{\parallel}h_{\text{gap}}$ is the voltage drop across the gap. $\dot{N}$ scales linearly with the local plasma density n, which can be estimated using: $\dot{N} = nAc$ where A is the cross-sectional area of the acceleration region. For the analytical estimate, we use the characteristic size of the particle acceleration region of $A \approx 4\pi R_{\text{NS}}^2$, and use the fact that $n = \dfrac{E_{\text{gap}}}{4\pi q l_{\text{acc}}} \approx \dfrac{E_{\parallel}}{4\pi q h_{\text{gap}}}$. Therefore the total luminosity, inclusive of the efficiency factor η is:

$$
\begin{aligned}
L_r &= \eta q \Phi_{\text{gap}} \dot{N} = \eta q E_{\text{gap}} h_{\text{gap}} n A c \\
&= \eta E_{\parallel}^2 A c \approx 10^{40} \text{ erg s}^{-1} \, \eta_{-2} \, E_{\parallel,10}^2 \, R_{\text{NS},6}^2
\end{aligned}
\tag{4.21}
$$

We note that the radio luminosity estimate in the $E_{\text{gap}} = E_{\parallel}$ limit has no explicit dependence on the gap height. However at the timescales of interest the gap height is smaller than the characteristic size of the spatial extend of $E_{\parallel}$ and field line curvature radius ρ_{c} (Fig. 4.3).

4.3.3.2   Estimate due to energy in field

An alternate method of estimating the luminosity is by consideration that a fraction η of the total energy in the parallel electric field is converted to coherent radio luminosity each time the gap discharges. The total energy density in the gap electric field is $\dfrac{\epsilon_E}{V_{\text{gap}}} = \dfrac{E_{\text{gap}}^2}{8\pi} \approx \dfrac{E_{\parallel}^2}{8\pi}$. The gap volume is the cross-sectional area times the gap height: $V_{\text{gap}} = h_{\text{gap}}A$.

In the pulsar gap model, curvature photons emitted by the primary accelerated particle population will produce secondary pairs, with the efficiency of the cascade and therefore multiplicity κ dependent on the specific gap physics (Timokhin & Harding, 2015; Wadiasingh et al., 2020). The gap discharge is likely non-stationary, occurring on timescales longer than $h_{\text{gap}}/c \sim 10^{-7}$ s (Timokhin, 2010), but still shorter than the orbital timescale, thus we expect quasi-continuous emission whenever a large $E_{\parallel}$ field is present. Given this, we take h_{gap}/c as an estimate for the gap discharge timescale in the lower number density limit. Therefore the radio luminosity is estimated as:

$$
\begin{aligned}
L_r &= \eta \frac{\epsilon_E}{V} h_{\text{gap}} A \frac{c}{h_{\text{gap}}} \\
&= \frac{\eta}{8\pi} E_{\parallel}^2 A c = \frac{\eta}{2} E_{\parallel}^2 R_{\text{NS}} c
\end{aligned}
\tag{4.22}
$$

We see the two methods of approximating the coherent radio luminosity agree to within a factor of 2. The above calculation assumes implicitly that a single gap is sufficient to supply enough charge to satisfy current requirements along field lines with $E_{\parallel}$. If this is not the case, multiple gaps could develop in the longitudinal direction along field lines, meaning for a length scale $L \approx R_{\text{NS}}$ the number of gaps and thus radio luminosity would scale linearly with a filling factor $f = \dfrac{L}{h_{\text{gap}}}$. We assume that current provided by the gap discharge is sufficient
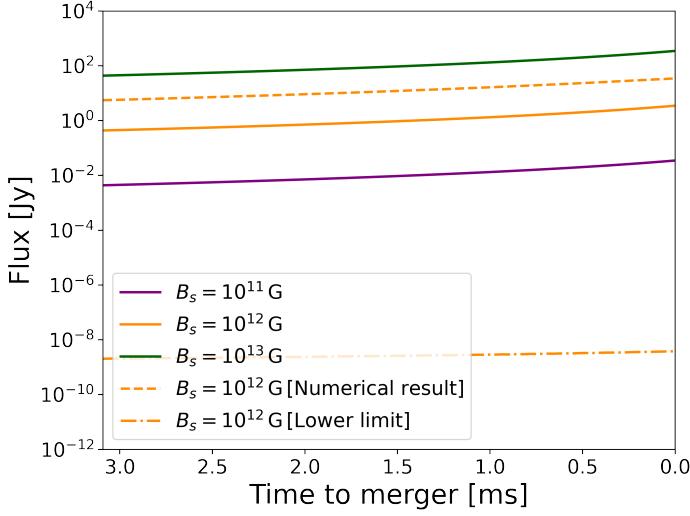
Figure 4.5: An analytic estimate of the total flux as a function of time to merger given by Eq. (4.21), assuming an emission bandwidth of $\delta\nu = 10^{10}$ Hz, $D = 100$ Mpc and $\eta = 10^{-2}$. For $B_{\rm s} = 10^{12}$G, we include both the analytic (solid), lower limit (dot-dashed) & numerical (dashed) fluxes as described in the text.

and thus take $f = 1$, but an upper limit for this dimensionless factor is: $f = 10^4 \, L_6 \, h_{\rm gap,2}$, and thus would represent a luminosity increase by a factor 10^4.

It is useful to compare the radio luminosity proxy to the Poynting luminosity of the binary. For an equal mass system where the magnetic moment of the primary $\mu_{\rm pri} \gg \mu_{\rm sec}$, the Poynting luminosity $L_{\rm P}$ is:

$$L_{\rm P} = \frac{2\mu_{\rm pri}^2}{3c^3} \left(\frac{\Omega}{\Omega_{\rm g}} \right)^{2/3} \Omega^4 \propto \Omega^{14/3} \propto a^{-7} \tag{4.23}$$

Where $\mu_{\rm pri} = B_{\rm s,pri} R_{\rm NS}^3$, Ω is the angular frequency of the binary defined in Eq. 4.26 and $\Omega_{\rm g}$ is the angular frequency defined at a point $R_{\rm g} \approx 3R_{\rm NS}$ (Medvedev & Loeb, 2013). In the $E_{\rm gap} = E_\parallel$ limit $L_{\rm R} \propto E_\parallel^2 \propto a^{-7}$ via Eq. 4.6, such that the radio luminosity scales similarly to the Poynting luminosity but it is always the case that $L_{\rm R} < L_{\rm P}$.

In the lower limit $E_{\rm gap} = 4\pi q n_{\rm GJ} h_{\rm gap}$ case, $L_{\rm R} \propto n_{\rm GJ}^2 h_{\rm gap}^2 \propto a^{-30/7}$ (Eqs. 4.43 & 4.44 in Appendix 4.B). In this case, we can define the time at which radiation mechanism ought to commence by finding the separation and time at which $L_{\rm R} = L_{\rm P}$, while $\eta = 1$:

$$a_{R=P} = 5 \times 10^8 \text{ cm } B_{\rm s,12}^{8/19} \, \eta_{-2}^{-7/19} \, \rho_{\rm c,6}^{-4/19} \, A_{12}^{-7/19}$$

$$t_{R=P} = 2 \times 10^5 \text{ seconds } B_{\rm s,12}^{32/19} \, \eta_0^{-28/19} \, \rho_{\rm c,6}^{-16/19} \, A_{12}^{-28/19} \tag{4.24}$$

The above equation suggests that in the $E_{\rm gap} = 4\pi q n_{\rm GJ} h_{\rm gap}$ limit, radio emission should turn on approximately one day before merger, albeit at a low luminosity. Despite this, the

---

[2] https://www.deepsynoptic.org/instrument
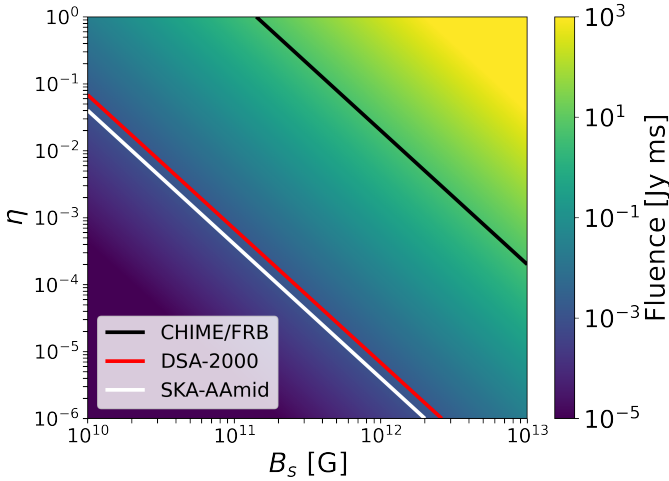
Figure 4.6: Total fluence of the last 3ms of the inspiral, corresponding to 2 orbital periods and thus 2 peaks of emission, for various values of efficiency η and surface magnetic field B_s. We assume an emission bandwidth of $\delta\nu = 10^{10}$ Hz, and distance to source of $D = 100$ Mpc. The assumed fluence limits are: CHIME/FRB 5 Jy ms (Josephy et al., 2021), DSA-2000 1.6 mJy ms^2 & SKA-mid 1 mJy ms (Torchinsky et al., 2016). The fluence predictions in this plot refer to the case where $E_\mathrm{gap} = E_\parallel$, and assume an optimal viewing angle.

necessary condition that $h_\mathrm{gap} < R_\mathrm{NS}$ (e.g. Fig. 4.4) is in general more constraining and therefore it is unlikely the radiation mechanism turns on before $10^3\, B_{\mathrm{s},12}$ seconds before the merger for NS-NS binaries.

4.3.4   Numerical Implementation

As mentioned in Section 4.2.2, we use a numerical set-up to estimate viewing angle dependence of the radio luminosity from the system. We calculate $E_\parallel$ surrounding the secondary conducting neutron star out to distance $R = 5R_\mathrm{NS}$, and compute the radio luminosity using Eq. (4.21). We calculate the gap height for each cell for each timestep, to ensure that pair production occurs within a fraction of the neutron star radius, as is required by our assumption of emission along field lines and to ensure the voltage is sufficient for pulsar-like emission using Eq. (4.20). We replace the cross-sectional area A with the cross sectional area of each cell, estimated as $(\delta V)^{2/3}$. As aforementioned we include an efficiency factor $\eta < 1$ to capture both the uncertainty related to the number of gaps that form and contribute to emission, but also the conversion of primary particle power to coherent radio radiation. We further assume an observing frequency of $\nu_\mathrm{obs} = 10^9$ Hz and a total spectral bandwidth of emission of $\delta\nu_\mathrm{obs} = 10^{10}$ Hz. In Fig. 4.5, we also show the total radio luminosity integrated over all viewing angles by way of comparison to the analytic calculation. The luminosity found using the numerical approach is slightly higher, attributed to the fact that we calcu-

late emission from a larger volume than assumed in the analytic calculation, and thus the total cross-sectional area A in the analytic calculation under-estimates the total area from which pulsar emission is expected.

We also estimate the maximum luminosity of the system assuming coherent curvature radiation, discussed in Appendix 4.C. We discuss only upper limits to the bunch luminosity based on electromagnetic considerations, and therefore instead of summing all emission in the direction of an observer as in the pulsar-like case, we simply find the maximum value associated with the set of field lines aligned with each observer.

4.3.5   Viewing angle dependence

The approach we take to the calculation of $E_\parallel$ in Section 4.2 assumes a uniform background magnetic field $\hat{\mathbf{B}} = -B\hat{\mathbf{z}}$ stemming from the primary NS's dipole magnetic field. This approximation limits a full understanding of the viewing angle dependence of emission, for two reasons. Firstly, the calculation of the expunged magnetic field will be different in a realistic dipole magnetic field, thus yielding a $E_\parallel$ field map having a different spatial morphology. Secondly, the perturbed magnetic field lines along which particle acceleration and radiation is directed may be offset to the directions described here. We expect the emission to be emitted in a slightly wider range of observing angles due to the dipole nature of the magnetic field, particularly at small values of orbital separation a where the dipole's deviation from a uniform field is greatest. However, the strongest $E_\parallel$ fields occur close to the NS surface (maximal value at $R = 1.23R_{\mathrm{NS}}$) and thus the direction of magnetic field lines is more strongly influenced by the perturbation of the field lines caused by the moving secondary NS, and not the background field orientation.

The perturbations of the magnetic field lines from their background orientation also result in variations of the radio luminosity at different observing angles. The maximum magnetic field line deflection occurs is quadrapole in nature (corresponding to maximal values of the absolute value of $\sin(\theta)$; see Fig. 4.1 & Eq. 4.2), which means emission is suppressed at larger angles to the background field. For field lines that are unperturbed (i.e. at $\theta = \pi/2$) there is no strong $E_\parallel$ field component, meaning radiation is suppressed for observers on-axis to the background field, as seen in Section 4.4. Corresponding to this, we see that the radio luminosity drops off substantially for observers at angles to the background field smaller than 10 degrees. As such, we find that almost all of the emission is emitted within 5-45 degrees of the magnetic axis of the field of the primary magnetized neutron star, with a peak of emission occurring at an angle offset from the background magnetic field ≈ 10 degrees.

It is crucial to remember that we do not necessarily expect the magnetic axis of the primary magnetized neutron star to be perpendicular to the orbital plane, as has been assumed throughout this work. However, our viewing angle dependent results need only be rotationally transformed to represent cases where the angle between the orbital plane and the magnetic axis of the primary NS is not 90 degrees, as shown in Fig. 4.8. This rotational symmetry for the uniform magnetic field at the secondary's position comes from the fact that

the motion of the conductor is orthogonal to the magnetic field lines. In the Figs 4.9-4.14 in Section 4.4, we assume the magnetic obliquity $\alpha_{\text{B,orb}} = 90 \deg$. Observing the coherent pre-merger emission could aid in constraining the magnetic obliquity of NS merger sources, and thus provide insights into the binary evolution of merging neutron stars.

As we consider that the primary NS has a dipole magnetic field, the value of the magnetic field strength B at a point (r, θ, ϕ) will change depending on the orientation of the axis to the point in question. For values of $\alpha_{\text{B,orb}} < 90 \deg$, the strength of this magnetic field at the secondary's position, for a separation a, will range between:

$$B_{\text{s}} \frac{R_{\text{NS}}^3}{a^3} \leq B \leq B_{\text{s}} \frac{R_{\text{NS}}^3}{a^3} \sqrt{1 + 3 \cos^2(\alpha_{\text{B,orb}})} \qquad (4.25)$$

where the maximal case occurs when the magnetic axis is tilted exactly towards the secondary $\alpha_{\text{B,orb}} = 0 \deg$. In this case, the magnetic field can increase by up to a factor of 2, resulting in a coherent luminosity increase by a factor of 4. These considerations have not been numerically implemented in any section, given their relatively small increase to the overall luminosity.

4.3.6   Temporal Morphology

In Section 4.4 we discuss how one may confirm a NS-merger origin of coherent precursor bursts discussed in this paper. One way in which these precursor bursts can be distinguished from FRBs from other sources is through analysis of the temporal morphology of the burst, which we discuss here (see also Gourdji et al. 2020).

In the model presented here, radio precursors of NS-NS mergers are modulated by the orbital period of the binary. In the Newtonian approximation, the angular frequency of the binary is:

$$\Omega = \frac{(G(M_1 + M_2))^{1/2}}{a^{3/2}} \approx 10^4 \, M_{\text{NS}}^{1/2} \, a_6^{-3/2} \text{ Hz} \qquad (4.26)$$

where M_1 & M_2 are the masses of the neutron stars and a is the separation. This is seen in Fig. 4.7, where observers at different azimuthal and polar angles to the orbital plane observe emission from different phases and magnetic field lines respectively. If coherent radio emission is bright enough to be observed at more than one orbital period, progressively brighter sub-millisecond bursts are observed with a decreasing separation between bursts as dictated the decreasing orbital period $P \approx \frac{2\pi a}{\beta c} \propto \sqrt{a} \propto \left(1 - \frac{t}{t_{\text{m,0}}}\right)^{1/8}$ using Eq. (4.5). Sub-millisecond periodicity has been claimed in a four FRB sources (The CHIME/FRB Collaboration et al., 2021b; Pastor-Marazuela et al., 2022), however explaining the periodicity as modulated by a compact object binary inspiral is generally disfavoured, as the period between sub-bursts does not appear to decrease as expected. We note that one could plausibly invoke eccentric orbits or unequal mass ratios in order to change the expected sub-burst morphology.

The characteristic increase of flux can also be used to distinguish such bursts, and the increase depends on the exact nature of the emission mechanism. In the upper limit assump-

tion that $n \propto \dfrac{E_\parallel}{4\pi q h_{\mathrm{gap}}}$, the radio luminosity scales as $L_r \propto E_\parallel^2$. This is also the case for the coherent curvature radiation mechanism (unless the coherent emission is limited by the magnetic field constraint of Kumar et al. (2017), see Appendix 4.C). By inspection of Eq. (4.2) & (4.6), we find that $E_\parallel^2 \propto B^2 \beta^2 \propto a^{-7} \propto \left(1 - \dfrac{t}{t_{\mathrm{m},0}}\right)^{-7/4}$. In the lower limit estimate where $n = n_{GJ}$ (Appendix 4.B), the characteristic flux increase is instead $L_r \propto h_{\mathrm{gap}}^2 B^2 P_{\mathrm{orb}}^{-2} \propto a^{-22/7} \propto \left(1 - \dfrac{t}{t_{\mathrm{m},0}}\right)^{-11/14}$. However, there may be spectro-temporal variations (with prejudice towards increasingly higher frequencies as the plasma density increases during inspiral) which may require broadband observations to ascertain this anticipated temporal dependence. Where sub-millisecond temporal resolution is available, we suggest that matched template technique could be used to identify NS-merger origin FRBs, and possibly to distinguish between the different emission mechanism limits discussed in this Section. Furthermore, identification of coherent radio emission modulated by the orbital period and phase will provide a measurement of the (combined) neutron star masses similarly to gravitational wave emission (Cutler & Flanagan, 1994) which may inform the neutron star equation of state. Close-by NS-mergers where one source has a high magnetic field are rare, but may be detectable over many orbital periods and may allow for detailed estimates of the neutron star masses.

4.3.7 Absorption

As discussed in Lyutikov (2019), it is possible that the radio signal predicted in this section may not escape the source. In particular, predictions of high-energy precursors to NS mergers invoke a dense shroud of particles surrounding the merging neutron stars (Metzger & Zivancev, 2016). The dense pair production front may prevent the propagation of radio emission, unless generated EM waves are superluminal relative to the plasma (e.g. Timokhin & Arons 2013). The absorption frequency of electromagnetic waves in a plasma is modified due to the magnetic environment (Arons & Barnard, 1986), and emission may propagate if $\omega > \dfrac{\omega_p^2}{\omega_B}$.

$$\omega > \frac{4\pi q n_{\mathrm{sec}} c}{B} = \frac{E_\parallel \kappa c}{B h_{\mathrm{gap}}}$$
$$= 300\, E_{\parallel,10}\, \kappa_1 B_{11}^{-1}\, h_{\mathrm{gap},2}\ \mathrm{Mhz} \tag{4.27}$$

Where we have used the fact that the density of the secondaries from which coherent emission is radiated is $n_{\mathrm{sec}} = \kappa n_{\mathrm{primaries}} \approx \dfrac{E_\parallel \kappa}{4\pi q h_{\mathrm{gap}}}$. Thus it is plausible that GHz emission escapes in regions of highest electric and magnetic field for typical multiplicity and gap height values, with a caveat that Arons & Barnard (1986) assume a homogeneous and stationary plasma which is not the case. These regions are also where we expect the strongest particle acceleration and therefore emission. Kumar et al. (2017) also argue that free-free absorption of GHz radiation will be negligible as long as the number density does not exceed $\sim 10^{18} \mathrm{cm}^{-3}$, implying that pair multiplicity in the secondary cascade region should not be
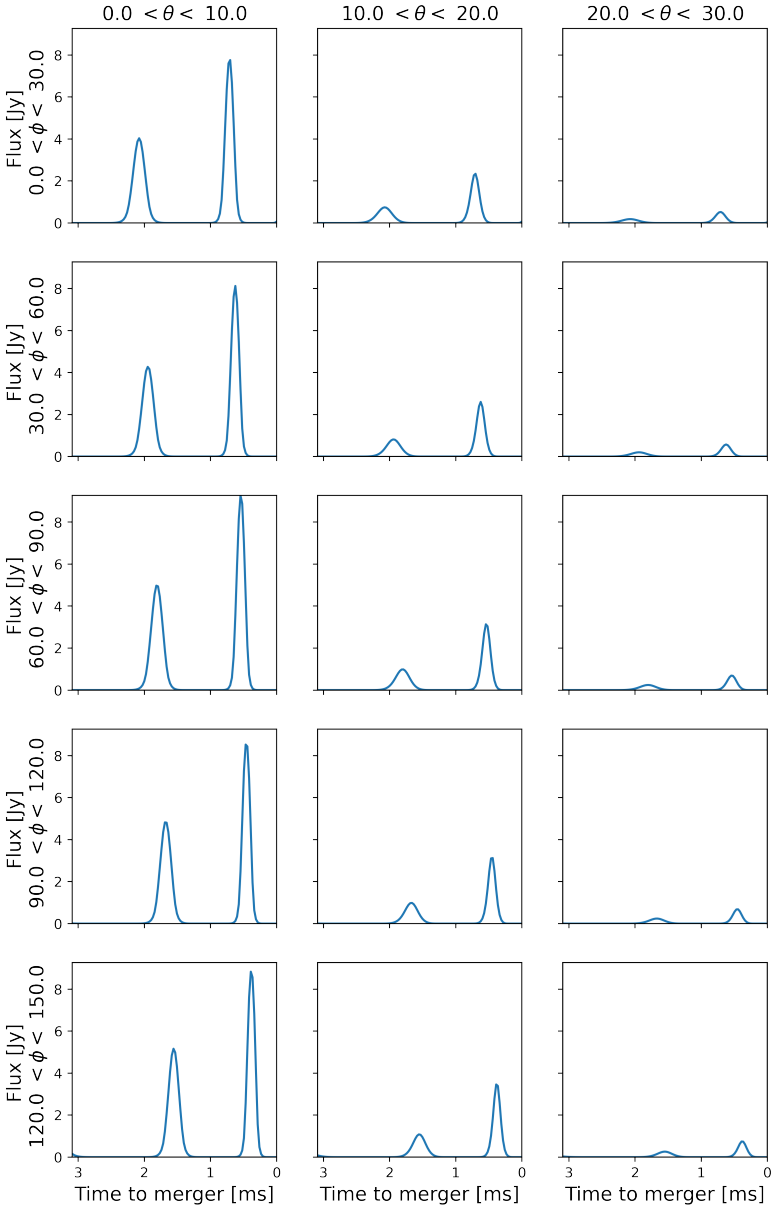
Figure 4.7: Example light curves for the final 3ms of the inspiral, covering the final 2 orbital periods. We show pulsar-like emission from NS-merger $\eta = 10^{-2}$ & $B_s = 10^{12}$G at $D = 100$ Mpc, for various observers positioned at different azimuthal and polar angles.

$\kappa \lesssim 100$ in this case. Furthermore, as the photons propagate through the magnetosphere of the primary, the magnetic field strength B and density n will both decrease linearly assuming a Goldreich-Julian charge density, meaning emission that escapes the immediate vicinity is expected to propagate to the observer. In Wang et al. (2016), the authors find that coherent radio emission of approximately $\nu \approx 1$ GHz may freely escape the magnetosphere during a NS-NS inspiral.

4.3.8 High-energy emission

Regardless of the specific mechanism of coherent emission, high-energy radiation will also be emitted. In the polar cap model of pulsar emission, this is explained by curvature & synchrotron photons emitted by accelerated pairs that do not meet energy requirements to interact with the magnetic field to produce pairs, and thus contribute to the gamma-ray flux (Daugherty & Harding, 1982, 1996). Gamma-ray emission modulated by the spin period has been observed for hundreds of isolated neutron stars (Abdo et al., 2013; Caraveo, 2014). In the NS-NS merger case, the most likely production mechanism would resemble those in observed gamma-ray pulsars, where radiation emerges from charged current sheets outside the light cylinder in the equatorial plane (relative to rotation) where large electric fields are likely realized for curvature radiation. The pulsar gamma-ray luminosity functions of Kalapotharakos et al. (2019, 2022) provide a gross baseline estimate, with the identification of spin period to orbital period, corresponding to $L_\gamma \approx 10^{37} \, \mathrm{ergs}^{-1}$, assuming $\epsilon_{\mathrm{cut-off}} = 1$ GeV, $\dot{P} = 10^{-12}$ and $P = P_{\mathrm{orb}} \approx 1$ ms. In the coherent curvature radiation model, high-energy emission may be emitted by the coherently radiating particles themselves due to the twisting of magnetic field lines by coherent bunches (Cooper & Wijers, 2021), or by a trapped fireball associated with a crustal trigger event (Yang & Zhang, 2021). In both cases, high-energy radiation is far too weak to be probed to extra-Galactic distances with current facilities.

Finally, Metzger & Zivancev (2016) consider an unspecified mechanism which converts a large fraction of available electromagnetic energy during the inspiral to gamma-ray radiation. In all cases, the lower sensitivity of gamma-ray detectors means that precursor emission is difficult to observe. Metzger & Zivancev (2016) found that even for very efficient conversion of electromagnetic energy to high-energy radiation, precursors are only observable to a distance $D \approx 10 \, \mathrm{Mpc} \, (B_{\mathrm{s}}/10^{14}\mathrm{G})^{3/4}$ with current instruments.

4.4 Multi-wavelength & multi-messenger detection prospects

In this Section we discuss the feasibility of (co-)detection of the coherent pre-merger emission discussed in this work in blind searches, triggered observations of multi-wavelength and multi-messenger signatures of neutron star mergers, and follow-up observations. We do not discuss all-sky radio telescopes such as the Survey for Transient Astronomical Radio Emission 2 (STARE-2; Bochenek et al. 2020b), the planned Galactic Radio Explorer (GReX; Connor et al. 2021), and the Amsterdam-ASTRON Radio Transients Facility And Analysis

	B_{s} [G]	GRB trigger	GW trigger	Radio afterglow	Kilonova
Current generation	10^{12}	✗	✗	✗	✗
	10^{14}	?	✓	?	?
Next generation	10^{12}	✓	✓	✓	?
	10^{14}	✓	✓	✓	✓

Table 4.1: Simplified summary of this section. For current/next-gen detectors and two surface magnetic field strengths, we show whether the coherent emission model is likely to be probed from NS-NS mergers (GRB & GW triggers) or given an observed radio burst, can a NS-NS merger origin be verified (afterglow & kilonova). The afterglow & kilonova possibilities rely on the current & future generation FRB facilities as detailed in Section. 4.4.1. We have assumed an optimal viewing angle and magnetic obliquity $\alpha_{\mathrm{B,orb}}$ for each observing method, and question marks represent uncertainties in the merger rate and/or model parameters. Much more detail is given in the text of each section, including current observational status, methodology & expected next generation capabilities.

Center (AARTFAAC; Prasad et al. 2016) in detail as they are not in general sensitive enough to detect extra-Galactic coherent radio emission from the model presented here.

In Section 4.4.1, we discuss the prospects for detecting coherent pre-merger emission from NS mergers through blind FRB surveys. In Section 4.4.2 we discuss rapid and triggered observations of sGRBs, putting past rapid observations of sGRBs with MWA and LOFAR in the context of this work, and make predictions for future observations with SKA. In Section 4.4.3 we discuss prospects for rapid observations of gravitational-wave detected mergers and detection of pre-merger emission. Finally in Sections 4.4.4 & 4.4.5 we discuss how follow-up observation of one-off FRBs without a GRB or GW counterpart could be confirmed to be of merger-origin using radio and optical facilities. A full description of the instruments discussed in the text is available in Table 4.2. In all cases, we show the co-detection space as a function of binary inclination angle (assuming the magnetic axis and orbital plane are perpendicular: $\alpha_{\mathrm{B,orb}} = 90 \deg$) and distance, assuming fluence sensitivity for coherent bursts with next-generation radio telescopes. In Fig. 4.8, we show how the magnetic obliquity $\alpha_{\mathrm{B,orb}}$ changes the inclination angle dependent detectability horizon. In Table 4.1 we provide a highly simplified summary of this Section, and in Table 4.2 we provide a description of the properties of the current and future instrumentation considered in this study.

4.4.1   Fast radio burst surveys

The simplest method of detecting coherent radio bursts from NS merger events is through blind FRB surveys. FRBs are extra-Galactic, (sub)-millisecond duration radio bursts, and many hundreds of bursts have now been seen since their discovery (Lorimer et al., 2007; CHIME/FRB Collaboration et al., 2021). FRBs are classified as either repeating or non-repeating sources, and the burst properties of these two classes appear quite different, particularly the spectral bandwidth and burst duration (Pleunis et al., 2021a), which may be

---

[3]see also: https://www.skatelescope.org/wp-content/uploads/2012/07/SKA-TEL-SKO-DD-001-1_BaselineDesign1.pdf
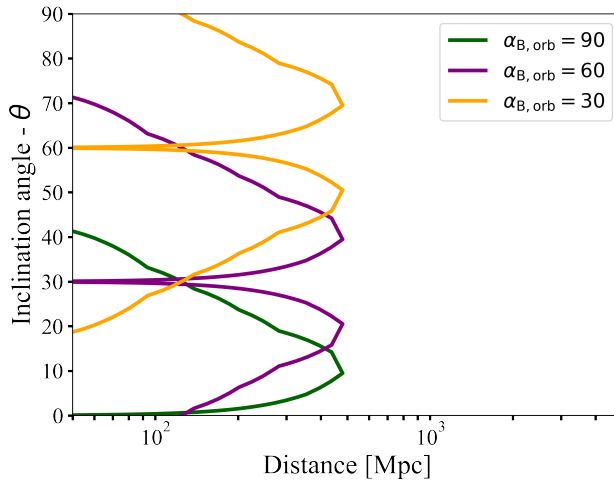
Figure 4.8: Inclination angle dependent observing horizon for SKA-mid for NS merger radio bursts from mergers with different magnetic obliquities $\alpha_{\mathrm{B,orb}}$; the angle between the magnetic axis of the primary magnetized neutron star and the orbital plane. The symmetry is due to the $E_{\parallel}$ azimuthal symmetry, i.e. the two peaks refer to particle acceleration in the red and blue regions of Fig. 4.1. We assume pulsar-like emission with parameters, $\eta = 10^{-4}$, $B_{\mathrm{s}} = 10^{12}$ G as explained in Section. 4.3. For the rest of the plots in this section, we show only the $\alpha_{\mathrm{B,orb}} = 90$ horizon for readability.

suggestive of different progenitors. The all-sky FRB rate is large, with the latest estimate from FAST (Nan, 2006) putting the rate at $1.24^{+1.94}_{-0.99} \times 10^5 \, \mathrm{sky}^{-1} \, \mathrm{day}^{-1}$ above 0.0146 Jy ms (95% confidence interval; Niu et al. 2021b). Instruments with large fields of view and sufficient sensitivity are best suited to finding them, including CHIME/FRB (CHIME/FRB Collaboration et al., 2021), ASKAP (Macquart et al., 2010) & DSA (Hallinan et al., 2019) to name three of the most prolific. Of current FRB instruments, FRBs are found most frequently by the Canadian Hydrogen Intensity Mapping Experiment (CHIME)/FRB team (CHIME/FRB Collaboration et al., 2018), reporting over 500 FRBs in the first catalog (CHIME/FRB Collaboration et al., 2021), and the Australian Square Kilometre Array Pathfinder (ASKAP) (Macquart et al., 2010) has had success in localizing one-off bursts to their host galaxies (Bhandari et al., 2020b; Heintz et al., 2020; Day et al., 2021; Bhandari et al., 2022). Despite this, poor localizations of CHIME FRBs and high redshift sources present difficulties in finding persistent or variable counterparts to non-repeating FRBs (Gourdji et al., 2020). Many authors have suggested that coherent bursts originating from NS mergers may be detected as one-off FRBs (e.g. Totani 2013) without an observed multi-messenger or multi-wavelength counterpart, but the volumetric rate of NS-NS mergers appears to be a factor of 10-100 too low to explain all FRBs (Ravi, 2019; Lu & Piro, 2019; Luo et al., 2020; Mandel & Broekgaarden, 2021). In this subsection, we consider whether pre-merger coherent emission could be probed by the CHIME/FRB radio telescope, but also future FRB survey instruments, namely the upcoming Deep Synoptic Array (DSA-2000; Hallinan et al. 2019), the CHIME/FRB successor the Canadian Hydrogen Observatory and Radio-transient Detector (CHORD; Vanderlinde et al. 2019 and the Square Kilometre Array (SKA; Dewdney et al. 2009; Torchinsky et al. 2016) observatories.

4.4.1.1   Current generation

In the model presented here, the number of pre-merger coherent radio bursts that would be detectable as one-off FRBs depends sensitively on the surface magnetic field of the primary neutron star B_{s} and the radio efficiency η. We show the fluence of radio bursts for a range of parameters B_{s} and η in Fig. 4.6, assuming a distance to the source of $D = 100 \, \mathrm{Mpc}$. In order to estimate the rate of FRBs, we assume that all NS mergers contain a 10^{12} G neutron star, and pulsar-like emission occurs with an efficiency of $\eta = 10^{-2}$ (henceforth the fiducial parameters), but include parameter scalings for the horizon and rate. In this case, the CHIME/FRB fluence horizon of the pulsar-like emission at optimal viewing angles is: $D_{\mathrm{horizon,CHIME}} \approx 70 \, \eta_{-2}^{1/2} \, B_{s,12}$ Mpc. Assuming a universal volumetric NS-NS merger rate of $\mathcal{R} = 10^3 \, \mathrm{Gpc}^{-3} \mathrm{yr}^{-1}$ (see e.g. Mandel & Broekgaarden 2021) and CHIME/FRB FoV of 250 deg, this corresponds to just $N_{\mathrm{CHIME}} = 0.002 \, \eta_{-2}^{3/2} \, B_{s,12}^3 \, \mathcal{R}_3$ events per year and thus cannot explain observed CHIME events, without invoking magnetar strength magnetic fields. We note that if just 20% of all mergers involved a magnetar with $B_{\mathrm{s}} = 10^{14}$G, the observed CHIME rate could be explained, however this contradicts two observed facts. Firstly, the volumetric NS-NS rate is too low (Ravi, 2019) and as most of the mergers capable of producing FRBs would have dispersion measures too high to be compatible with the observed population. Secondly, one would be required to explain why the characteristic temporal

morphology is not observed in the brightest FRBs where multiple orbital periods would be bright enough to be observed if allowed by temporal resolution[4]. We therefore suggest it is unlikely that a significant population of the current observed CHIME/FRBs are powered by this mechanism, but searches for the temporal morphology suggested in Sect. 4.3.6 could yield a sub-population of mergers containing NS with $B_{\rm s} \approx 10^{14}$G.

4.4.1.2   Next generation

In Table 4.4, we show the detection horizons and expected event rate of the fiducial coherent pre-merger emission of current and next generation FRB facilities. For DSA-2000, the smaller FoV is greatly offset by the expected increase in sensitivity, and thus the observed event rate is much larger than for either CHIME/FRB or CHORD. For SKA-AAmid, an unconfirmed extension to SKA-mid, the large FoV coupled with sensitivity produces many hundreds of detectable events per year. We note that these values are larger than expected by a factor of a few due to viewing angle dependencies discussed in Sect. 4.3.5. However, the sensitive dependence on the magnetic field strength means that if just a few merging neutron stars have magnetic fields $B_{\rm s} > 10^{12}$G, the event rate will increase dramatically.

4

4.4.1.3   Other considerations

The temporal resolution of CHIME/FRB intensity data (i.e. without triggering raw baseband data recording; see Chime/Frb Collaboration et al. 2020; Michilli et al. 2021) is approximately 1ms (CHIME/FRB Collaboration et al., 2018), although simulations have shown that sub-burst timescales down to 0.1ms can be probed in a few cases (CHIME/FRB Collaboration et al., 2021). The temporal morphology of coherent pre-merger bursts predicted in this paper is sub-millisecond peaks separated by the orbital period and increasing in intensity (as $\propto (1 - t/t_{\rm m})^{-7/4}$; see Sect. 4.3.6). Such morphology may be detectable by CHIME/FRB depending on the signal-to-noise, scattering due to multi-path propagation (Chawla et al., 2022) and bandwidth of bursts. SKA-mid not only has a higher sensitivity such that many peaks could be observed from orbital phases before merger, but is also expected to have temporal resolution on the order of 1-100 nanoseconds. If these coherent burst from NS-NS mergers are observed with SKA, they will likely be identifiable by their temporal morphology.

4.4.2   Short gamma-ray bursts

There have been many successful rapid radio observations of GRBs dating back decades (e.g. Green et al. 1995), but to detect pre-merger emission instruments must be on source of sGRBs extremely quickly. Some radio telescopes employ rapid-response modes, such that repointing can occur automatically in response to transient alerts issued by other facilities on

---

[4]It is plausible this is explained by a radiation mechanism only producing the cosmological radio bursts at threshold electromagnetic conditions, which we aim to explore in a future extension to this work.

platforms such as the VOEvent network (Williams & Seaman, 2006), which allow machine-readable astronomical event distribution. In particular software telescopes that do not require physical repointing can respond to alerts and be on source within minutes, and sometimes seconds (Hancock et al., 2019). Rapid radio observations of sGRBs observed by *Fermi-GBM* and *Swift-BAT* are possible for a few reasons: a high GRB event rate owing to a large field of view (1.4 steradians and 2π steradians respectively; Meegan et al. 2009; Gehrels et al. 2004); a large horizon of detection resulting in large dispersion delays (although sGRB tend to have redshift z < 2 Fong & Berger 2013); rapid notification of detections through the GCN (Barthelmy et al., 1998) and VOEvent systems; and the precise localization of sources to within 1-4 arcmin for *Swift-BAT* and 1-10 deg for *Fermi-GBM*. Furthermore, upgrades to the *Swift-BAT* pipeline are expected to increase the number of localized nearby sGRBs by a factor 3-4 in the near future (DeLaunay & Tohuvavohu 2021, see also Tohuvavohu et al. 2020). Thus far, rapid response observations of NS-NS mergers have been triggered in response to sGRBs as reported by *Swift-BAT* by the Low Frequency Array (LOFAR; Rowlinson et al. 2021), the Murchison Widefield Array (MWA; Anderson et al. 2021b; Tian et al. 2022), Arcminute Microkelvin Imager (AMI; Anderson et al. 2018, the Australian Compact Telescope Array (ATCA; Anderson et al. 2021a), and a 12m dish at the Parkes radio observatory (Bannister et al., 2012).

The small opening angles of collimated GRB jets mean that triggered radio observations will probe NS merger systems with small viewing angles with respect to relativistic jets, which we assume to be perpendicular to the orbital plane. The opening angles of long GRBs are often determined through jet breaks in the afterglow emission (Sari et al., 1999) and range between approximately $\theta_{\mathrm{core}} \approx 3 - 10 \deg$ (Berger, 2014). Afterglow observations of sGRBs are sparse, but jet breaks are thought to have been observed in a few sources, corresponding to estimated opening angles of $\theta_{\mathrm{core}} \approx 4 - 8 \deg$ (Soderberg et al., 2006; Fong et al., 2012). Aksulu et al. (2022) perform multi-wavelength afterglow modelling of 4 sGRBs and 3 out of the 4 sources have opening angles $\theta_{\mathrm{core}} \lesssim 6 \deg$, and one source is found to have a much larger opening angle of $\theta_{\mathrm{core}} \approx 34 \deg$. If the orbital plane and primary magnetic axis are perpendicular ($\alpha_{\mathrm{B,orb}} = 90 \deg$) as discussed in Sect. 4.3.5, it is likely that the set of mergers from which prompt emission is observable does not substantially overlap with the set of mergers from which coherent radio bursts are luminous enough to be observed. Rapid radio observations of sGRBs will probe NS mergers with specific magnetic obliquities which direct coherent radiation along the jet axis; i.e. when $\alpha_{\mathrm{B,orb}}$ is 10-30 degrees misaligned with the jet axis (see. Fig. 4.8). In any case, the radio emission predicted in this paper is radiated into a much larger solid angle than the prompt GRB emission.

4.4.2.1 Current generation

LOFAR has performed successful triggered observations of GRB 180706A (Rowlinson et al., 2019) & GRB 181123B (Rowlinson et al., 2021). The former was a long GRB but the latter was a short GRB, and its afterglow has been associated with a galaxy at z=1.8 (Paterson et al., 2020) with a chance alignment of 0.44%. Assuming a DM-redshift relation (DM = 1200 z pc cm^{-3}; Ioka 2003, and the NE2001 Galaxy model; Cordes & Lazio 2002), it is

very likely that the dispersion delay from the source to the telescope was large enough ($\tau_{\mathrm{delay}} = \dfrac{DM}{241\nu_{\mathrm{GHz}}^2} > 400$ seconds) such that LOFAR probed pre-merger radio emission. The attainable FRB fluence limits depend sensitively on the dispersion measure (i.e. Fig. 3 of Rowlinson et al. 2021), primarily due to the extent to which the dispersed burst fills each snapshot image. Assuming the galaxy association suggested by Paterson et al. (2020), fluence limits of 2×10^4 Jy ms can be placed for millisecond FRB emission and can be used to constrain our model. Assuming standard cosmological parameters ($H_0 = 70$, $\Lambda_{\mathrm{M}} = 0.286$, flat universe; Wright 2006), a redshift of $z = 1.8$ corresponds to a luminosity distance of ~ 14 Gpc. This means that the LOFAR observations of GRB 181123B can constrain the pre-merger radio emission in the present model to a primary NS magnetic field strength of $B_s < 10^{16}$ G, assuming $\eta = 10^{-2}$ and optimal magnetic obliquity.

The Murchison Widefield Array (MWA) successfully triggered on sGRB 180805A (Anderson et al., 2021b), and was on source 84 seconds after the burst. For most typical sGRB redshifts & DMs, coherent emission during the inspiral would have been probed. The resulting fluence limits ranged from 570 Jy ms to 1750 Jy ms depending on the assumed dispersion measure, but a reliable constraint for our model cannot be placed without a distance measurement. In Tian et al. (2022), the authors present a catalog of rapid radio limits with MWA for a total of 9 sGRBs. Tian et al. (2022) make use of image-plane de-dispersion techniques to report triggered observations with deep fluence limits of $80 - 12000$ Jy ms, with most limits clustered around 1000 Jy ms. GRB 190627A was the only event in this sample with an associated redshift ($z = 1.942$; Japelj et al. 2019), corresponding to an approximate luminosity distance of 15 Gpc assuming the same cosmological parameters as before. The authors were able use their derived fluence limit of ≈ 80 Jy ms to constrain efficiency parameters for various models of prompt radio emission during GRB 190627A to reasonable values for the first time. For optimally aligned pulsar-like emission in the model presented here, the fluence limit presented by Tian et al. (2022) constrains the primary NS magnetic field to $B_{\mathrm{s}} \lesssim 10^{15}$ G, assuming an efficiency $\eta \approx 10^{-2}$.

Making use of direction-dependent calibration and source subtraction techniques, Rowlinson et al. (2019) were able to place deep fluence limits, corresponding to 3×10^3 Jy ms for a typical sGRB of redshift $z = 1$.[5] Given this, and the results of Tian et al. (2022), we find that triggered observations by LOFAR and MWA will detect pre-merger coherent emission to a distance of approximately $3 - 5 \, \eta_{-2}^{1/2} \, B_{s,12}$ Mpc, using detection limits in Table 4.2. Although this distance may be an under-estimate, as the low DM expected for mergers at this short distance will aid snapshot sensitivity, such a low DM would also mean that LOFAR will not be on source fast enough to observe pre-merger emission. However, MWA's rapid triggering could probe dispersed bursts at ≈ 300 Mpc, and would be sensitive to pulsar-like emission from NS mergers at this distance if $B_{\mathrm{s}} \gtrsim 6 \times 10^{13}$ G. Such a close sGRB would be rare, but *Swift-BAT* pipeline upgrades discussed above may provide triggering opportunities in the near future for off-axis sGRBs.

---

[5]In the near future, image-plane de-dispersion will be implemented in the LOFAR rapid response pipeline, significantly improving sensitivity.

Other instruments that have performed rapid observations of GRBs, namely Parkes, AMI, & ATCA, (Bannister et al., 2012; Anderson et al., 2018, 2021a) nominally begin observations with delay times incompatible with pre-merger observation, instead probing early radio afterglow emission.

4.4.2.2 Next generation

The upgraded LOFAR 2.0 will allow simultaneous imaging and beam-formed triggered observations, which will allow more sensitive high-time resolution burst searches for well-localized GRBs (Gourdji et al., 2022). A tied-array beam (TAB) set-up using the LOFAR core stations could be utilized to perform time-domain search for dispersed radio bursts across the most likely localization region of *Swift* GRBs. Pleunis et al. (2021b) used such a set-up to search for FRBs, achieving a fluence limit of 26 Jy ms for bursts with an assumed 50ms duration. Importantly, the ~ 3 arcmin full-width half maximum (FWHM) of the TAB is approximately the same as the *Swift-BAT* localization region and therefore could be used for prompt GRB searches. The large scattering timescale of FRBs at LOFAR frequencies will reduce the signal-to-noise of bursts, but 100 Jy ms is a reasonable fluence target for the coherent pre-merger bursts which may be observable for many milliseconds, as the fluence limit scales as $\sqrt{\frac{t_{\rm scatt}}{t_{\rm burst}}}$. This would allow LOFAR 2.0 to probe NS-NS merger emission to 15 $\eta_{-2}^{1/2} B_{s,12}$ Mpc, notably probing mergers with $B_s = 10^{14}$G to Gpc distances.

Comparatively, the fiducial horizon distance for SKA-mid at full sensitivity of 1 mJy ms is 5000 $\eta_{-2}^{1/2} B_{s,12}$ Mpc, corresponding to a redshift $z \approx 0.8$. The large dispersion measure expected from these sources, coupled with the precise localization particularly by *Swift-BAT* mean that triggered observations may allow deep radio observations of sGRBs. The dispersion delay to $z \approx 0.8$ to 770 MHz and 110 MHz (i.e. lowest nominal observing frequencies of SKA-mid and SKA-low) is 7 seconds and 330 seconds respectively, assuming a DM-redshift relation (Ioka, 2003). SKA-mid is expected to respond to alerts within seconds, but assuming a similar slew speed to its precursor MeerKAT ($\approx 2 \deg {\rm s}^{-1}$) repointing could take 0.1-10 minutes and thus is unlikely to be able to detect pre-merger emission via triggered observations. SKA-low, assuming a similar triggering performance to MWA, should be on source within 20 seconds and thus should be sensitive to radio emission from sGRBs. To estimate the rate for SKA, we assume that SKA-low telescope triggers rapid observation on half of all *Swift-BAT* and *Fermi-GBM* detections of likely sGRBs: 10 and 45 per year respectively (Burns et al., 2016). Gompertz et al. (2020) find that in a sample of 39 *Swift-BAT* observed (likely) sGRBs with known redshifts, three quarters have redshifts of $z < 0.8$. SKA-low's large FoV means the entire *Swift-BAT* localization region and most (if not all) of *Fermi-GBM* can be probed. Given this, and extrapolating to *Fermi-GBM* sGRBs, we could expect SKA to be sensitive to fiducial pulsar-like emission from $\approx 20 - 30$ sGRB events per year.

4.4.2.3 Other considerations

We note that Gourdji et al. (2020) search for sGRB counterparts to two well-localized, non-repeating FRBs: FRB 180924 and FRB 190523. Non-detections of sub-threshold *Fermi* counterparts in both cases constrain FRB models in which coherent radiation is emitted along the same axis as a GRB. We note that in model we present here, sGRBs may not be aligned along the same axis as the emitted coherent radio emission, thus non-detection of gamma rays may not preclude a NS-merger origin. Moreover, the authors disfavour FRB models where coherent radio emission is powered by the inspiral, as the predicted flux as a function of time is not compatible with the observed temporal morphology of the FRBs. This severely constrains the present models ability to reproduce FRB lightcurves (see discussion at the end of Sect. 4.4.1).

4.4.3 Gravitational wave events

NS merger events are also observable using gravitational wave (GW) detections of compact object mergers, where many of the rapid, multi-wavelength observing techniques discussed in Sect. 4.4.2 can be utilized. The fourth observing run (O4) of the GW detector network is expected to start in March 2023[6].

4.4.3.1 Current generation

The three detectors of the third observing run (O3) will be operational during O4 at improved sensitivities: the two Advanced Laser Interferometer Gravitational-Wave Observatory (aLIGO; Abramovici et al. 1992; Abbott et al. 2009) detectors near their design sensitivities with a BNS range $D_{\mathrm{BNS}} \approx 160$ - 190 Mpc, and the advanced Virgo (AdV; Caron et al. 1997) detector with $D_{\mathrm{BNS}} \approx 80$ - 115 Mpc (Abbott et al., 2020). A fourth detector the Kamioka Gravitational Wave Detector (KAGRA; Kagra Collaboration et al. 2019; KAGRA Collaboration et al. 2022) will be starting operations as well but the anticipated sensitivity is limited with $D_{\mathrm{BNS}} \approx 1$ - 10 Mpc. In Abbott et al. (2020), it is estimated that 10^{+52}_{-10} BNS detections will occur in O4 with a median 90% localisation area of 33 $\deg^2$. These predictions assume $D_{\mathrm{BNS}} = 80$ Mpc for KAGRA, however this is likely well above the horizon that will be obtained in O4 for that detector. We therefore use a more likely 100 $\deg^2$ for O4.

In this Section, we estimate the distance to which BNS GW signals can be detected, averaged over sky position but, not over the inclination angle, due to the strong inclination angle dependence of the pre-merger emission. We compute the inclination angle dependent GW signal-to-noise ratio (SNR), averaged over thirty random sky positions, using various GW detector network setups (see Figs. 4.9 and 4.10). We calculate the SNR with the pycbc Python package using the prescription of Cutler & Flanagan (1994), using the standards PSDs in pycbc for the current generation detectors (aLIGO, AdV, KAGRA) at design sensitivity. For the PSDs of future detectors (LIGO A+, LIGO Voyager, AdV+, KAGRA+, ET, CE),

---

[6] https://observing.docs.ligo.org/plan/
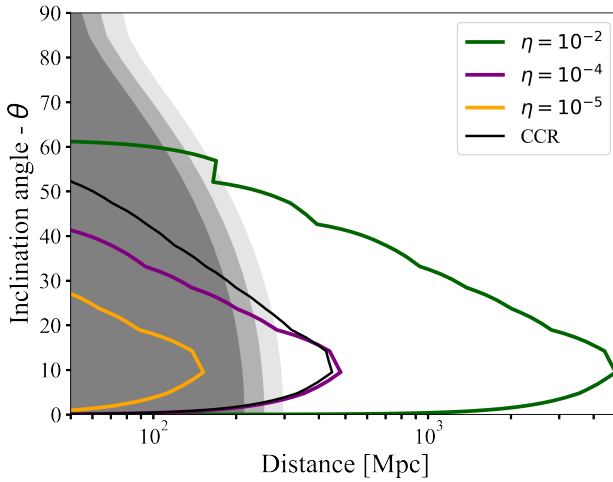
Figure 4.9: We show the inclination angle dependent observing horizon for SKA-mid for NS merger radio bursts powered by pulsar-like emission (for three efficiency values η, Sect. 4.3) and coherent curvature radiation (Sect. 4.C). The apparently increase in horizon for $\eta = 10^{-2}$ at 50 deg is a artifact related to the way in which inclination angle dependent horizons are calculated. In the background grey are detection limits (assuming detections for SNR =8) for the fourth observing run of 2nd generation gravitational wave instruments: LIGO (Hanford + Livingston) (darkest shade), LIGO-VIRGO (medium shade) and LIGO-VIRGO-KAGRA (lightest).

we follow Borhanian & Sathyaprakash (2022) and take them from ce_curves.zip[7]. For our template waveform h, we use the de facto standard waveform model for BNS mergers "IM-RPhenomD_NRTidalv2" (Dietrich et al., 2019). We vary the component masses of the BNS merger but set the NS spins to zero.

4.4.3.2 Current generation

To make predictions for the fourth gravitational-wave observing run, we assume 10^{+52}_{-10} BNS gravitational wave detections all with localization area of 100 $\deg^2$ as mentioned. The dispersion delay to the maximum BNS range of 190 Mpc ($z \approx 0.043$) is approximately 10 seconds at 144 MHz and 30 seconds at 80 MHz. This means that although LOFAR would not be on source quick enough for pre-merger detection, we note that if LOFAR 2.0 can be on source within 10-15 seconds, precursor emission from NS mergers in O5 could be probed. However, MWA's quicker triggering time will probe the most distant events in O4, at least at the lowest frequencies. Assuming MWA is well-positioned to respond to half of all alerts (neglecting sensitivity drop off towards a non-optimal declination), this corresponds to 5 BNS events, where the large FoV means the entire localization region can be covered. Assuming a distance of 190 Mpc and $\eta = 10^{-2}$, MWA will be sensitive to emission for a surface

---

[7] https://dcc.cosmicexplorer.org/public/0163/T2000007/005/ce_curves.zip

magnetic field of $B_s \approx 4 \times 10^{13}$G (assuming optimal viewing angle), therefore some limits attainable during the O4 run will be constraining for this model.

4.4.3.3   Next generation

After O4, all current detectors are planned to undergo significant upgrades towards the fifth observing run (O5). For the aLIGO detectors, this entails the A+ upgrade targeting a maximum $D_{\mathrm{BNS}} \approx 325$ Mpc, similarly AdV will be upgraded to the AdV+ configuration with a maximum $D_{\mathrm{BNS}} \approx 260$ Mpc (Abbott et al., 2020). KAGRA (Kuroda & LCGT Collaboration, 2010; Kagra Collaboration et al., 2019) is expected to reach $D_{\mathrm{BNS}} \approx 130$ Mpc and could potentially gain more sensitivity with the KAGRA+ upgrade. Furthermore, a fifth detector, LIGO-India, is planned to join the global GW network starting operations around $\sim$2025(Abbott et al., 2020). LIGO-India is expected to have identical specifications to the other two LIGO detectors and thus very similar sensitivity. Borhanian & Sathyaprakash (2022) make predictions for the scientific capabilities of such a five detector network at optimal sensitivity. They find that this network will detect around 200 BNS mergers per year with approximately six of those detections having a 90% localisation area of $\leq 1\deg^2$, and the median 90% localization region is 9–12 $\deg^2$ (Corsi et al., 2019).

As discussed in Section 4.4.2, LOFAR 2.0 will allow for faster triggering, and simultaneous imaging and beam-formed triggers, allowing it to probe a wider variety of the predicted radio emission associated with NS mergers. In terms of detecting millisecond radio bursts, beam-formed observations would allow improve sensitivity, as well as grant greater flexibility de-dispersion techniques. For gravitational wave events where the localization is general much poorer than GRBs, the one possible observing set-up would be to use the LOFAR Tied-Array All-Sky Survey (LOTAAS) survey (Sanidas et al., 2019) beam structure in addition to interferometric imaging beams. In this case, coherent tied-array beams cover 12 $\deg^2$ allowing sensitive high time resolution searches, with additional incoherent beams providing lower sensitivity coverage up to 68 $\deg^2$. The latter of which were used for an FRB search in ter Veen et al. (2019) to achieve a fluence limit of approximately 1600 Jy ms. The larger field-of-view of the incoherent beams would allow better coverage of the localization region, where roughly half of the 90% localization region may be covered by incoherent beams, and a smaller portion by the tied-array beams. If LOFAR 2.0 can trigger within 15 seconds, the dispersion measure expected from the O5 observing horizon distance of ~ 300 Mpc, would be compatible with pre-merger detection. In this case, incoherent beams would be able to cover the entire localization region and probe emission from a $B_s = 10^{14}$G merger, and the tied-array beam could cover a portion of the $1\deg$ 90% region, and be sensitive to lower magnetic field.

First light for SKA is predicted to be in 2027, when we expect a 5-detector network to be running with 200 mergers per year with a horizon of $D_{\mathrm{BNS}} \approx 325$ Mpc, and a typical $10\deg^2$ localization. The dispersion delay to 150 MHz at 325 Mpc is approximately 15 seconds, and the delay across the entire 50-350MHz band is ≈ 130 seconds. These values may be higher depending on the local source and Milky Way contributions. SKA1-low will be able to save

$\sim$ 30 seconds of raw voltage data per station. Assuming repointing can occur within 10 seconds upon receipt of a gravitational wave alert, pre-merger emission at low frequencies should be observed. Assuming $\eta = 10^{-2}$, SKA-low will be able to test the model presented here for NS mergers with $B_{\mathrm{s}} = 10^{11}$ G for $D = 300$ Mpc, and therefore will be able to verify the model.

The capabilities of future post O5 GW detectors are promising, though speculative. LIGO Voyager, expected around 2030, will first upgrade the three LIGO detectors to a range of $D_{\mathrm{BNS}} \approx 1$ Gpc (Adhikari et al., 2020). The Einstein Telescope (ET; Punturo et al. 2010) and Cosmic Explorer (CE; Abbott et al. 2017a) will instead be completely new, next generation GW detectors and bring tremendous, ten-fold increases in sensitivity. The definitive range of LIGO Voyager, ET and CE will strongly depend on the final design configurations, which are subject to uncertainty in the technological improvements reached in the next decade. Still, preliminary sensitivity curves exist for these future detectors and can give insight into their potential (Borhanian & Sathyaprakash, 2022). A network of three LIGO Voyager detectors, AdV+ and KAGRA+ will detect on the order of 2000 BNS mergers per year with one percent of the detections having a 90% localisation area of $\leq 1 \mathrm{deg}^2$. Astonishingly, if three next generation detectors become operational, i.e. ET and two CEs, on the order of 300,000 BNS mergers will be detected per year with again, around one percent of the detections having a 90% localisation area of $\leq 1 \mathrm{deg}^2$ corresponding to roughly 2000 precisely localised BNS mergers per year. The inclination angle dependent horizons for these next-generation GW detectors are shown in Fig. 4.10.

4.4.3.4   Other considerations

Pre-merger alerts will be issued by gravitational wave observatories in the coming observing runs (Chu et al., 2016; Magee & Borhanian, 2022), and radio emission could be observable seconds before the merger event (Fig. 4.11). Assuming 100% duty cycle and design sensitivities, Magee & Borhanian (2022) find that during a four detector network O4/O5 run there will be 3.5 and 1.5 events per year that can be reported 1 second and 10 seconds before the merger respectively. For a five detector network during O5, these values rise to 30 and 15 events per year respectively. Such pre-merger alerts will be invaluable for radio observatories to begin slew and repointing, even if only approximate localizations can be provided in early reporting (Chu et al., 2016). Finally, we note that mergers that occur at a smaller distances (and therefore with shorter dispersion delays) will be detected with more GW detectors and therefore will have better localizations.

4.4.4   Gamma-ray burst radio afterglows

The relativistic jetted outflows powering sGRBs plough into the circumburst medium, resulting in shocks and particle acceleration. This particle acceleration leads to broadband synchrotron emission visible first at higher energies with X-ray telescopes and then at lower frequencies at later times (Rees & Meszaros, 1992). Such afterglow emission usually detected during follow-up observations triggered by gamma-ray burst detectors, or occasion-
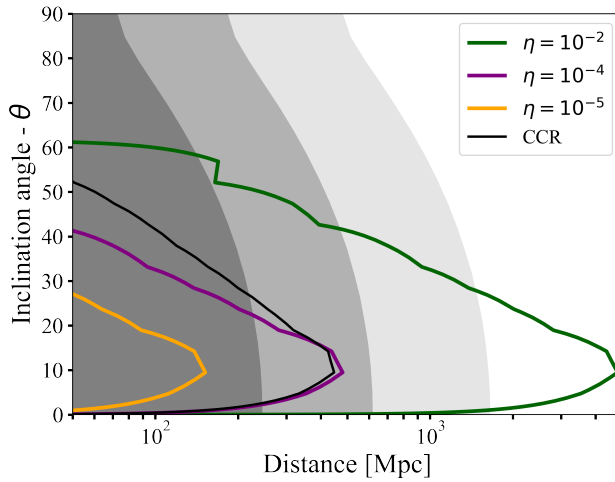
Figure 4.10: We show the inclination angle dependent observing horizon for SKA for NS merger radio bursts powered by pulsar-like emission (for three efficiency values η, Sect. 4.3) and coherent curvature radiation (black line, Sect. 4.C). In the background grey are detection limits (assuming detections for SNR =8) for 2nd and 3rd generation gravitational wave instruments for single detector setups of LIGO+ (darkest shade), LIGO Voyager (medium shade) and the Einstein Telescope (lightest shade).
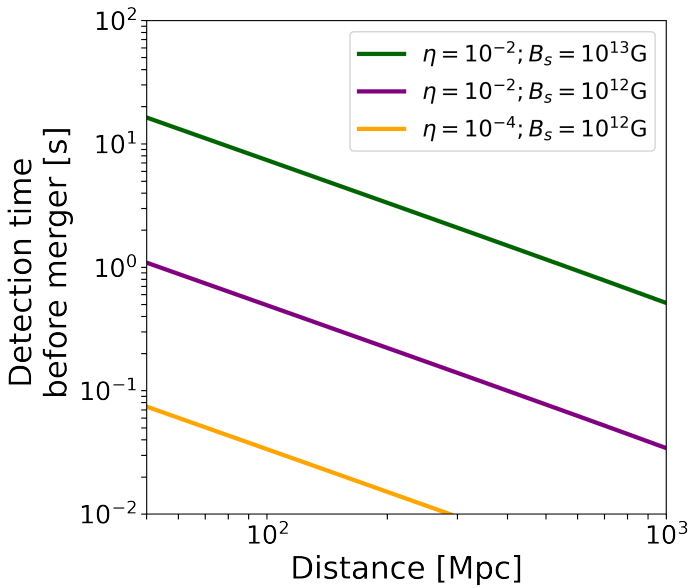
Figure 4.11: Expected detection time before the merger time in seconds, assuming an SKA fluence sensitivity of 1 mJy ms and averaging over phase dependence.

ally as so-called 'orphan' afterglows without prompt gamma ray emission (Levinson et al., 2002; Ghirlanda et al., 2015; Law et al., 2018) or by follow-up observations of kilonovae (Ho et al., 2020; Andreoni et al., 2021a). It is expected that future radio facilities such as SKA-mid will detect afterglows both serendipitously during transient surveys, and in gravitational wave event follow-up (Dobie et al., 2021) to Gpc distances (Fig. 4.12). Prospects for detection of radio afterglows from compact object merger events is covered in much more detail, including specific follow-up observing strategies, in the excellent work by Dobie et al. (2021), to which we refer the interested reader.

Late-time radio follow-up of non-repeating FRBs to look for persistent and long-term variable counterparts has been performed for a few well-localized sources. Bhandari et al. (2018) report on multi-wavelength and multi-messenger follow-up observations of four apparently non-repeating FRBs as discovered by the Parkes telescope. No radio afterglow emission was observed, although the large inferred luminosity distances (ranging from 4.8 Gpc to 17.2 Gpc) mean that afterglow emission would be difficult to detect. Similarly, Bhandari et al. (2020b) report on four FRBs localized by ASKAP and find no significant radio transient sources, and observed emission is attributed to the host galaxy. Lastly, Bhandari et al. (2020a) report on precursor and follow-up of a well-localized FRBs, again with a non-detection that cannot meaningfully constrain radio afterglow models.

To investigate whether the NS-NS merger origin of coherent radio bursts could be confirmed by detection of late-time afterglow emission, we used the python package AFTERGLOW.PY (Ryan et al., 2020). In Table 4.4.4, we list the assumed fiducial parameters for the radio afterglows as in Ryan et al. (2020), where reasonable values are chosen given multi-wavelength fits to GRB afterglows (e.g. Aksulu et al. 2022). In particular, the circumburst density n_0 is quite uncertain and has a large effect on the detectability horizon of radio afterglows and therefore we take a broad range of values of between 10^{-5} and 10^{-1} to give an approximate idea of the uncertainties involved. We consider both structured (gaussian) jets and tophat jets.

Parameter	Fiducial value	Meaning [units]
E_0	10^{53}	Isotropic-equivalent energy [erg]
θ_{core}	0.05	Half-opening angle [rad]
θ_{wing}	0.2	Wing angle for gaussian jet [rad]
n_0	10^{-5}-10^{-1}	Circumburst density [cm^{-3}]
p	2.2	Electron energy powerlaw index
ϵ_e	0.1	Fraction of energy in electrons
ϵ_B	0.01	Fraction of energy in magnetic field
ξ_N	1.0	Fraction of electrons accelerated

4.4.4.1 Current generation

We find that for circumburst densities of 10^{-5} and 10^{-1} respectively, MeerKAT should be sensitive to many afterglows from NS-mergers from distances of 200 Mpc to 2 Gpc for gaus-
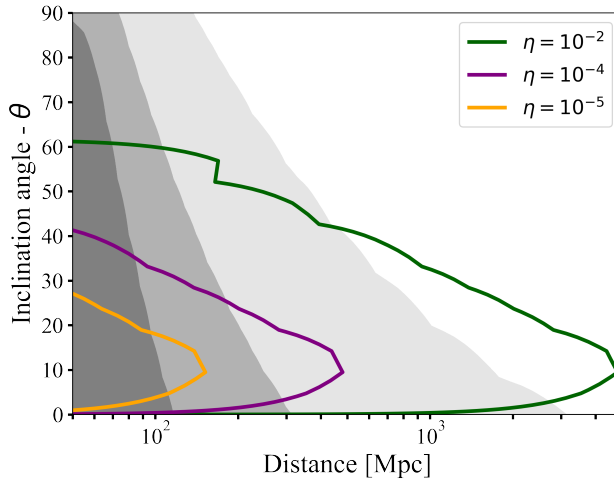
Figure 4.12: Background colours show MeerKAT detection horizons for peak flux of gaussian jets at $\nu = 1.43$ Hz assuming detection threshold of 700 μJy. Shades of gray correspond to varying circumburst densities (Darkest $n = 10^{-5}$; medium $n = 10^{-3}$; lightest $n = 10^{-1}$).

sian jets (Fig. 4.12) and tophat jets (Fig. 4.15), assuming optimal magnetic obliquity for pre-merger radio bursts. For off-axis jets, the horizon is reduced drastically to 10-200 Mpc, dependent on the assumed afterglow parameters, in particular the circumburst medium density. One of the primary limitations with the current generation of instrumentation is the low number of localized one-off FRBs at distances close enough such that an afterglow can be definitively constrained.

4.4.4.2 Next generation

If $n_0 > 10^{-3}$, SKA-mid should be sensitive to almost all afterglows from NS-mergers that can power coherent bursts with fiducial efficiency and surface magnetic field values ($\eta = 10^{-2}$; $B_s = 10^{12}$G), as shown in Figs. 4.13 & 4.16 for gaussian structured and tophat jets respectively. As we have shown in Sect. 4.4.1, it is unlikely that all non-repeating FRBs are powered by NS mergers. Nevertheless, follow-up radio campaigns to trigger sensitive observations on localized FRBs (hundreds per year with the CHIME/FRB outrigger and CHORD projects; Leung et al. 2021; Vanderlinde et al. 2019) could certainly confirm the NS-merger origin of Gpc coherent radio bursts by detecting late-time afterglow emission. We note that in our calculation, detection critera depends only on the peak flux of the afterglow, and therefore well-timed observations with multiple epochs or frequencies would be required in practice to confirm an afterglow.
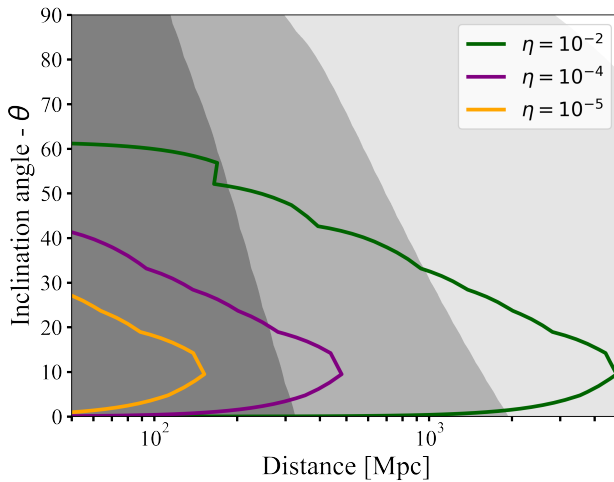
Figure 4.13: Background colours show SKA detection horizons for peak flux of gaussian jets at $\nu = 1.43$ Hz assuming detection threshold of 2 μJy. Shades of gray correspond to varying circumburst densities (Darkest $n = 10^{-5}$; medium $n = 10^{-3}$; lightest $n = 10^{-1}$). Coloured contours show viewing angle-dependent SKA detection horizon of pulsar-like coherent pre-merger emission assuming $\eta = 10^{-2}$, $B_s = 10^{12}$G.

4.4.5 Kilonovae

An alternative method of identifying coherent radio bursts of NS merger origin (if the burst is sufficiently localized), is to perform optical follow-up in search of a kilonova counterpart. Thus far, optical follow-up of fast radio bursts has largely focused on well-localized repeating sources (Andreoni et al., 2019, 2020; Kilpatrick et al., 2021; Andreoni et al., 2021b), and not the one-off bursts discussed in this work. For non-repeating sources, Petroff et al. (2015) performed multi-wavelength follow-up, including optical facility DECAM, of FRB 140514 and were able to rule out supernovae and long GRB progenitor, but were not sensitive enough to rule out kilnova models. Marnoch et al. (2020) & Núñez et al. (2021) performed follow-up observations with the Very Large Telescope (VLT) and Las Cumbres Observatory Global Telescope (LCOGT) respectively on well-localized, one-off FRBs as discovered by ASKAP (Bhandari et al., 2018). Marnoch et al. (2020) find that it is unlikely that the bursts that were observed are coincident with Type Ia or Type IIn supernova explosions, and similarly Núñez et al. (2021) rule out bright supernovae. Neither work is able to rule out coincident kilonovae, due to a lack of sensitivity. Tominaga et al. (2018) report on optical follow-up with the Subaru/Hyper Suprime-Cam on week-long timescales of FRB 151230 and again find no evidence of Type Ia supernovae, but lack the sensitivity to probe kilonovae emission.

In order to examine this method of confirming a merger origin of one-off FRBs, particularly in expectation of many more localizations through the CHIME/FRB outrigger project (Leung et al., 2021; Vanderlinde et al., 2019) we make use of the kilonova model grid pre-
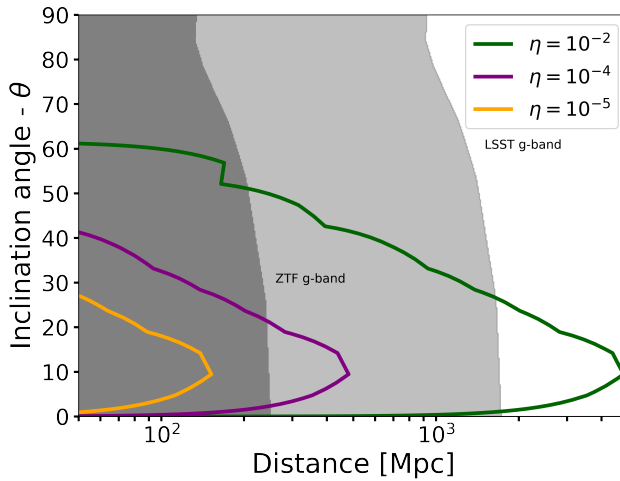
Figure 4.14: Background colours show ZTF and LSST g-band (darker and lighter shades respectively) detection horizons for peak flux of GW170817-like kilonovae models using models from Bulla (2019). Coloured contours show viewing angle-dependent SKA detection horizon of pulsar-like coherent pre-merger emission assuming $\eta = 10^{-2}$, $B_\mathrm{s} = 10^{12}$G.

sented in Bulla (2019). The grid was generated via radiative transfer simulations sensitive to the viewing angle parameter, allowing viewing angle dependent lightcurve predictions. We select the kilonova model that best fits the GW170817 observations, with dynamic ejecta mass $M_\mathrm{dyn} = 0.005$ M$_\odot$, disk wind ejecta mass $M_\mathrm{wind} = 0.05$ M$_\odot$, and half opening angle of the lanthanide-rich dynamical ejecta component $\theta_\mathrm{core,kn} = 30$ deg. In Figs. 4.14, 4.17 & 4.18 show viewing-angle dependent detector horizons for the GW170817-like kilonova model as observed by Zwicky Transient Facility (ZTF; Bellm et al. 2019) & Vera C. Rubin Observatory's Legacy Survey of Space and Time (LSST; Ivezić et al. 2019) in g, r and i bands respectively. ZTF can detect kilnovae from NS-NS mergers to $100 - 200$ Mpc, and LSST to ≈ 1 Gpc, with a modest drop off for highly inclined viewing angles. As in the previous section, we suggest that sensitive optical follow-up of close-by (low DM) one-off FRBs, or those with quasi-periodic structure (timescale of the orbital period of short separation binaries $\sim$ 1ms) may yield a kilonova detection that could confirm NS-merger origin. For well-localized one-off FRBs, as expected in 2023 with the CHIME outrigger project, pointed target-of-opportunity optical observations may probe kilonova at cosmological distances. In lieu of triggered observations, large FoV optical survey data (e.g. ZTF) could also be searched for kilonova-like emission on the position of reported one-off FRBs.

4.5 Discussion

4.5.1 Binary evolution of highly magnetized NS mergers

The evolution of a neutron star's magnetic field is complicated, making it difficult to estimate the surface magnetic field strength at the time of merger (see Igoshev et al. (2021) for a recent review). Observable emission through the mechanism described in this work requires one of the two merging neutron stars to have a surface magnetic field $B_{\rm s} \gtrsim 10^{12}$G for detection of precursor emission. Traditional binary evolution channels for NS-NS mergers (e.g. Bhattacharya & van den Heuvel 1991) suggest that these systems take 100 Myr-Gyr to merge due to gravitational radiation (Tauris et al., 2017). It is expected from evolutionary arguments that one old, recycled $\approx 10^{9}$G millisecond pulsar will merge with a younger, more slowly spinning 10^{12}G neutron star (Bhattacharya & van den Heuvel, 1991), as is observed in Galactic double pulsar systems (Burgay et al., 2003; Lyne et al., 2004).

The characteristic lifetime of a pulsar is:

$$\tau = \frac{P}{\dot{P}} \propto \frac{P^2}{B_{\rm s}^2} \qquad (4.28)$$

where P is the spin period, $\dot{P}$ is the spin period time derivative, $B_{\rm s}$ is the surface magnetic field. In Eq. (4.28) we have used the fact that the characteristic magnetic field of a neutron star is $B_{\rm s} \propto P^{1/2}\dot{P}^{1/2}$, and the spin down luminosity $L \propto P^{-3}\dot{P} \propto B^2 P^{-4}$. We know of around 25 magnetar strength neutron stars in the Galaxy, with typical periods and magnetic fields $P = 10$s and $B_{\rm s} = 10^{14}$G, in contrast to approximately 2500 non-recycled radio pulsars with $P \approx 1$s and $B_{\rm s} = 10^{12}$G. Assuming spin-down occurs on the characteristic timescale of Eq. (4.28), this implies the birthrate of 10^{12}G and 10^{14}G neutron stars may be of the same order of magnitude (see also Beniamini et al. 2019). A highly magnetized neutron star's magnetic field are thought to decay primarily through Ohmic decay and Hall drift (Goldreich & Reisenegger, 1992), where typical timescales are on the order of 100s Myr. This within a factor of 3 of the merger timescale of the Hulse-Taylor neutron star binary system (Weisberg et al., 1981). We therefore may not necessarily expect the field to substantially decay before the merger, and a portion of NS mergers likely contain a highly magnetized neutron star as required for bright FRB-like emission during the inspiral 4.4.1. The possibility that high magnetic field neutron stars may retain strong fields for at least 10-100s Myrs is bolstered by recent discoveries of ultra-long period magnetars (Hurley-Walker et al., 2022; Caleb et al., 2022), as well as theoretical work on spin period evolution of highly magnetized neutron stars (Beniamini et al., 2020).

Moreover, alternative evolutionary channels have been proposed in which one NS may be much younger during merger, and share properties with observed Galactic magnetars. To explain the observed short-period low-mass X-ray binaries, Kalogera (1998) suggested that some initially wide binaries could be brought together by the supernova kick itself, in a formation channel known as direct supernova. Very wide binaries would bypass the common envelope phase during the first supernova, and a small proportion of these systems would undergo a fortuitous kick resulting in a tight orbital separation. Voss & Tauris (2003) noted

that if the first supernova kick results in a close X-ray binary, and the second star's demise also results in a NS, the resulting compact object binary could have a relatively small separation and thus could merge relatively quickly. They estimate that up to 5% of all NS-NS mergers could be produced in this way. Specifically, they predict a small number of NS-NS mergers requiring just 10^{2-4} yrs to merge, which may imply a subset of mergers containing young, highly magnetized neutron stars. Furthermore, in Vigna-Gómez et al. (2018), the authors' fiducial model contains a few NS-NS binaries created with periods of around 10^{-2} days, representing systems that would merge in 10^{2-4} years. These outliers represent just a few systems in a simulation containing $\sim 10^3$ binaries, and the authors note they are the product of fortuitous kicks as discussed in Kalogera (1998). Another possible evolutionary channel leading to a fast merger time was proposed by Dewi & Pols (2003). In this scenario, a binary containing a $2.8 - 6.4 M_\odot$ helium star and a NS could produce a NS-NS binary with very short periods ($P \sim 0.01$ days), if the NS has sufficient time to spiral in the helium stars' envelope before core collapse. Various models in Dewi & Pols (2003) suggest merger timescales of between 10^4 and 10^6 yrs, such that a significant magnetic field may still be present. We note that dynamical channels such as N-body interactions in globular clusters that may significantly contribute to BH-BH merger events, are disfavoured to contribute to the rate of lower mass compact object mergers such as NS-NS and NS-BH events (Ye et al., 2020).

4.5.2   Neutron star - black hole mergers

The model outlined in this paper required the presence of a magnetized NS merging with an object that acts as a conductor, which we have assumed throughout to be a secondary, less magnetized NS. However, a stellar-mass BH will also act as conductor and result in similar emission. The rates of of NS-BH mergers are generally thought to be lower than NS-NS mergers (Mandel & Broekgaarden, 2021), however typical binary evolution suggests that the NS in a NS-BH merger would be highly magnetized. This is because the more massive star in a binary has a shorter lifetime, will undergo supernovae first and is more likely to result in a BH, such that the younger compact object is the (unrecycled) NS. Therefore such systems may still contribute significantly to the volumetric rate of coherent bursts from compact object mergers, and will also emit multi-wavelength and multi-messenger signals discussed in Section 4.4 that can provide paths for detection (McWilliams & Levin, 2011; Boersma & van Leeuwen, 2022). Lastly, the gravitational wave detection horizon for NS-BH mergers is larger than for NS-NS mergers by a factor of 2 (for a recent detection see Abbott et al. 2021), which may allow automatic triggering of buffer boards or observations on a much larger number of gravitational wave events than discussed in Section 4.4.3 [8].

4.6   Conclusions

We have presented an model for coherent pre-merger bursts from NS mergers, based on an adapted version of the model presented by Lyutikov (2019) (Section 4.2). We primar-

---

[8] https://dcc.ligo.org/public/0161/P1900218/002/SummaryForObservers.pdf

ily consider pulsar-like emission expected as the inspiral revives electromagnetic conditions required for gap particle acceleration. We find that bursts are observable to Mpc - Gpc distances depending on the efficiency, if the mechanism operates maximally ($E_{\mathrm{gap}} = E_{\parallel}$) and one NS has a significant magnetic field $B_{\mathrm{s}} \approx 10^{12}$G as expected from evolutionary arguments (Section 4.3). Radio emission is emitted along magnetic field lines, and the inclination angle between the background dipole magnetic field of the primary NS determines the set of observers for whom the radio burst is visible. (Section 4.3.5). Coherent precursor bursts can be distinguished from FRBs from other sources by way confirmation of modulation on the orbital period and characteristic flux increase, which may aid in inferring properties of merging neutron stars (Section 4.3.6). We have made predictions for detecting these bursts through fast radio burst surveys and triggered observations of short gamma-ray bursts and gravitational wave events (Section 4.4). We further suggest follow-up of some fast radio bursts in the optical and radio wavelengths to confirm merger origin. Our main observational conclusions are listed below:

1. Coherent pre-merger emission is directed along the perturbed magnetic field lines of the primary magnetized neutron star and multi-wavelength & multi-messenger campaigns with next generation of instruments will probe fiducial emission parameters, particularly for systems with magnetic obliquity of $\alpha_{\mathrm{B,orb}} \gtrsim 45$

2. Coherent emission is expected to turn on at a time $t \approx 10^{3} B_{\mathrm{s},12}$ seconds before merger

3. CHIME/FRB does not in general observed coherent emission from mergers with $B_{\mathrm{s}} = 10^{12}$G, but a sub-population of FRBs may involve mergers with 10^{14} G fields (Section 4.4.1)

4. DSA-2000 and SKA FRB surveys will detect tens of bursts per year assuming fiducial parameters $\eta_{-2} B_{s,12}^{2}$ (Section 4.4.1)

5. Triggered observations of sGRBs and GW events by MWA & LOFAR have probed the most optimistic models, and LOFAR 2.0 & especially SKA will constrain fiducial parameters (Sections 4.4.2 & 4.4.3)

6. Late-time observations in optical and radio of low redshift, one-off FRBs with quasi-periodic or increasing temporal structure is recommended (Section 4.4.4 & 4.4.5)

Acknowledgements

---

[9] https://aspire.science.uva.nl/

Data Availability

A reproduction package providing the scripts required to reproduce the figures of this paper will be available upon publication.

4

Table 4.2: Here we list the properties of the telescopes discussed in the text and figures of this work including CHIME/FRB (CHIME/FRB Collaboration et al., 2018, 2021), CHORD (Vanderlinde et al., 2019), DSA-2000 (Hallinan et al., 2019), LOFAR (van Haarlem et al., 2013), MWA (Tingay et al., 2013), ZTF (Bellm et al., 2019), LSST (Tyson, 2002), MeerKAT (Jonas & MeerKAT Team, 2016), SKA1[3] (Dewdney et al., 2009; Braun et al., 2019) and SKA-AAmid (Torchinsky et al., 2016). In each case we list specifications and assumed values given the use of the instrument within the context of this work, as a blind-FRB survey instrument, a GW/GRB rapid response instrument, and optical and radio afterglow follow-up. The assumed sensitivity, field-of-view and localization refer to those values at typical observing frequencies in the centre of bandwidths. For SKA-AAmid, we assume coherent bursts are are searched in real time over the entire 200 deg² FoV as discussed in (Torchinsky et al., 2016; Hashimoto et al., 2020b). Typical LOFAR and MWA fluence sensitivities are used based on past successful triggers of GRBs, and the FoVs are taken from Chu et al. (2016) but vary depending on observing setup. Transient buffer board capabilities of MWA's voltage capture system are detailed in Tremblay et al. (2015). Fluence detection thresholds for future instruments are estimated by scaling continuum sensitivities to millisecond integration. Finally we note that in 2023, the CHIME/FRB localization is expected to reach 50 milliarcseconds for a majority of sources thanks to the Outrigger project (Leung et al., 2021) and the beginning of CHORD. For CHORD sensitivity, we assume a 1ms burst that emits over the entire observing bandwidth.

Type	Telescope	Frequency [MHz]	Sensitivity	FOV [deg²]
FRB Survey	CHIME	400-800	5 Jy ms	250
	DSA-2000	700–2000	1.8 mJy ms	10.6
	CHORD	300-1500	60 mJy ms	65
	SKA-AAmid	450-1450	1 mJy ms	200
GW/GRB Trigger	LOFAR (imaging)	120-240	3000 Jy ms	48
	LOFAR (beamformed)	120-240	25-1000 Jy ms	0.05-16
	MWA	80-300	1000 Jy ms	610
	SKA1-low	50-350	4 mJy [1ms int]	27
Follow-up	ZTF	464-806 [nm]	m19.9 [i] - m20.8 [g]	47.7
	LSST	0.3-1 [μm]	m24.0 [i] - m25.0 [g]	9.6
	MeerKAT	580–2500	700 μJy [2hr int]	0.85
	SKA1-mid	350-1500	2 μJy [1hr int]	0.48

4

Table 4.3: Continuation of Table 4.2

Type	Telescope	Localization/Resolution [arcsec]	Trigger time	TBB
FRB Survey	CHIME	1 deg	n/a	n/a
	DSA-2000	3.5	n/a	n/a
	CHORD	0.05	n/a	n/a
	SKA-AAmid	0.22	n/a	n/a
GW/GRB Trigger	LOFAR (imaging)	6	3-4 min	5 s
	LOFAR (beamformed)	n/a	3-4 min	5 s
	MWA	100	20-30 s	$\leq$ 100 s
	SKA1-low	11	<20 s	30 s
Follow-up	ZTF	2	n/a	n/a
	LSST	0.7	n/a	n/a
	MeerKAT	10	n/a	n/a
	SKA1-mid	0.22	1-10 min	>9 min

4

Telescope	Horizon [Mpc] $\left(\eta_{-2}^{3/2}\,B_{s,12}^3\right)$	Event rate [yr^{-1}] $\left(\eta_{-2}^{3/2}\,B_{s,12}^3\,\mathcal{R}_3\right)$
CHIME	70	0.002
CHORD	650	0.4
DSA-2000	3700	15
SKA-AAmid	5000	600

Table 4.4: Observing horizon and the 100% duty cycle detection rate for current leading and future FRB facilities. We assume fiducial model parameters for the efficiency η and surface magnetic field B_{s}, as well as a volumetric NS-NS merger rate $\mathcal{R} = 10^3\;\mathrm{Gpc}^{-3}\,\mathrm{yr}^{-1}$

Appendices

4.A   Correction to the parallel electric field calculation

The assumption that the magnetic field of the primary at the position of the secondary is uniform leads to the form of the magnetic flux density given by $\mathbf{B} = -B\hat{\mathbf{z}}$. This further assumes that the magnetic dipole moment of the primary is perpendicular to the orbital plane. In the inertial reference frame co-moving with the non-rotating primary, designated as frame S, the electric field $\mathbf{E} = 0$. We initially consider that only the primary is present in frame S.

We transform to a frame of reference S' which is moving with velocity $\boldsymbol{\beta}' = \beta\hat{\mathbf{y}}$ with respect to frame S. The magnetic field in this frame $\mathbf{B}' = \mathbf{B} + O(\beta^2)$, where we will ignore second-order terms in β. Lorentz transformation of the electric field for non-relativistic velocities follows

$$\mathbf{E}'_{\mathrm{LT}} = \mathbf{E} + \boldsymbol{\beta}' \times \mathbf{B} = (\beta\hat{\mathbf{y}}) \times (-B\hat{\mathbf{z}}) = -\beta B\hat{\mathbf{x}} \tag{4.29}$$

The secondary is considered to be a perfect electrical conductor with negligible magnetization and a vanishing internal magnetic field intensity. When the secondary is placed in the approximately uniform field $\mathbf{B}'$, it will expel the magnetic field from the inside by generating surface currents. The magnetic field outside the secondary in frame S' is then given by,

$$\mathbf{B}' = -B\cos\theta\Big(1 - \frac{R^3}{r^3}\Big)\hat{\mathbf{r}} + B\sin\theta\Big(1 + \frac{R^3}{2r^3}\Big)\hat{\boldsymbol{\theta}} \tag{4.30}$$

Given that a uniform static electric field exists anti-parallel to the x-axis in S', the conductor will generate a dipole field oriented along the x-direction in response to keep the sphere at uniform potential. Taking the dipole moment to be $\mathbf{p}$, we can write,

$$V'_{\mathrm{dipole}} = \frac{\mathbf{p}.\hat{\mathbf{r}}}{r^2} = \frac{p\sin\theta\cos\theta}{r^2}$$

$$V'_{\mathrm{uniform}} = \beta Bx = \beta Br\sin\theta\cos\phi$$

$$V'_{\mathrm{tot}} = V'_{\mathrm{uniform}} + V'_{\mathrm{dipole}} = \Big(\frac{p}{r^2} + \beta Br\Big)\sin\theta\cos\phi$$

As the secondary has an equipotential surface we can choose $V'_{\mathrm{tot}} = 0$ at $r = R$. This implies that $p = -\beta BR^3$. As such,

$$V'_{\mathrm{tot}} = \Big(r - \frac{R^3}{r^2}\Big)\beta B\sin\theta\cos\phi \tag{4.31}$$

Therefore, electric field outside the secondary in frame S',

$$\mathbf{E}' = -\nabla V'_{\text{tot}}$$

$$= -\left\{ \left(\frac{2R^3}{r^3} + 1 \right) \sin\theta\cos\phi, \left(1 - \frac{R^3}{r^3} \right) \cos\theta\cos\phi, \left(\frac{R^3}{r^3} - 1 \right) \sin\phi \right\} \beta B \qquad (4.32)$$

With the secondary being stationary in S', we can apply the electromagnetic interface conditions in this frame. Using the normal field boundary condition,

$$\mathbf{E}'.\hat{r}|_{r=R} = -3\beta B \sin\theta\cos\phi = 4\pi\sigma' \qquad (4.33)$$

Surface currents responsible for inducing the magnetic dipole field component of Eq. (4.30) are given by $\mathbf{K}' = \frac{c}{4\pi} \mathbf{n} \times \mathbf{B}'|_{r=R} = \frac{3c}{8\pi} B \sin\theta\hat{\phi}$. For Lorentz transformations, we also need to convert the surface current density and the surface charge distribution to the form of the current 4-vector.

$$\mathbf{J}' = \frac{3c}{8\pi} B \sin\theta\delta(r-R)\hat{\phi} \qquad (4.34)$$

$$\rho'_q = -\frac{3}{4\pi} \beta B \sin\theta\cos\phi\delta(r-R) \qquad (4.35)$$

This conversion from surface density to volume density requires the usage of the Dirac-delta function centered at R in the radial direction.

Now, we transform to a frame of reference S'' where the secondary neutron star moves with velocity $\beta\hat{\mathbf{y}}$. This means that, S'' must be moving with $\beta'' = -\beta\hat{\mathbf{y}}$ with respect to the frame S'. Note that S'' is essentially the frame S, but whereas S did not have the secondary neutron star and its associated fields, S'' will have all the transformed fields from S'. The designation of S'' as such is only done for convenience. The magnetic field exhibits no change for $\beta << 1$, $\mathbf{B}'' = \mathbf{B}' - \frac{1}{c}(-\beta\hat{\mathbf{y}}) \times \mathbf{E}' = \mathbf{B}' + O(\beta^2/c)$. The electric field $\mathbf{E}'' = \mathbf{E}' + (-\beta\hat{\mathbf{y}}) \times \mathbf{B}'$.

$$\hat{\mathbf{y}} \times \mathbf{B}' = \{\sin\theta\sin\phi, \cos\theta\sin\phi, \cos\phi\} \times \mathbf{B}'$$

$$= -\left(1 + \frac{R^3}{2r^3} \right) B \sin\theta\cos\phi\hat{\mathbf{r}} + \left(\frac{R^3}{r^3} - 1 \right) B \cos\theta\cos\phi\hat{\boldsymbol{\theta}}$$

$$+ \left(1 + \frac{R^3}{2r^3} (\sin^2\theta - 2\cos^2\theta) \right) B \sin\phi\hat{\phi}$$

$$\Rightarrow \mathbf{E}'' = -\left\{ \frac{3}{2} \sin\theta\cos\phi, 0, \frac{3}{2} \sin^2\theta\sin\phi \right\} \frac{\beta B R^3}{r^3} \qquad (4.36)$$

The volume current density and the volume charge in S'' frame, then, are

$$\mathbf{J}'' = \mathbf{J}' - \rho'_q(-\beta\hat{\mathbf{y}}) = \frac{3c}{8\pi} B \sin\theta\delta(r-R)\hat{\phi} + O(\beta^2) \qquad (4.37)$$

$$\rho''_q = \rho'_q - \frac{1}{c}\mathbf{J}'.(-\beta\hat{\mathbf{y}})$$

$$= -\frac{3}{4\pi} \beta B \sin\theta\cos\phi\delta(r-R) - \frac{1}{c}\left(\frac{3c}{8\pi} B \sin\theta\delta(r-R) \right)(-\beta\cos\phi)$$

$$= -\frac{3}{8\pi} \beta B \sin\theta\cos\phi\delta(r-R) \qquad (4.38)$$

As a result, the surface current density and the surface charge density in S'' frame are obtained to be $\mathbf{K}'' = \dfrac{3c}{8\pi} B \sin\theta \hat{\phi}$ and $\sigma'' = -\dfrac{3}{8\pi}\beta B \sin\theta \cos\phi$ respectively.

$\mathbf{E}''$ is the total electric field vector outside the secondary neutron star in S''. Using this, we can calculate the component of the electric field in the direction of the magnetic field $\mathbf{B}''$.

$$
\begin{aligned}
E_\parallel'' &= \frac{\mathbf{E}''.\mathbf{B}''}{|\mathbf{B}''|} = \frac{1}{|\mathbf{B}''|}\frac{3\beta B^2 R^3}{2r^3}\left(1 - \frac{R^3}{r^3}\right)\sin\theta\cos\theta\cos\phi \\
&= \frac{3\sin\theta\cos\theta\cos\phi\left(1 - \frac{R^3}{r^3}\right)}{\sqrt{4\cos^2\theta\left(1 - \frac{R^3}{r^3}\right)^2 + \sin^2\theta\left(2 + \frac{R^3}{r^3}\right)^2}}\beta B\frac{R^3}{r^3}
\end{aligned}
\tag{4.39}
$$

This corresponds to Eq. (4.2) herein.

4.B   Gap height derivation for lower number density case

We present the lower limit to the analytic gap height, assuming that $E_{\text{gap}} = 4\pi q n h_{\text{gap}}$ and n is given by the Goldreich-Julian density due to the motion of the magnetosphere in orbit: $n = n_{GJ} = (2B)/(qcP_{\text{orb}})$, where B is the local magnetic field.

Starting from Eq. (4.12), the Lorentz factor of the primaries is:

$$
\gamma(l) = \frac{qE_{\text{gap}}l_{\text{acc}}}{m_e c^2}
\tag{4.40}
$$

By way of Eqs. (4.14) & (4.15) and by substitution we find:

$$
\begin{aligned}
l_{\gamma,\text{gap}} &= 0.4\rho_c m_e c^2 \frac{B_c}{B}\frac{\rho_c}{3\hbar c}\left(\frac{m_e c^2}{4\pi q^2 n_{GJ} l_{\text{acc}}^2}\right)^3 \\
&= \frac{0.4\rho_c^2 m_e^4 c^7}{192\pi^3 \hbar q^6 n_{GJ}^3 l_{\text{acc}}^6}\frac{B_c}{B}
\end{aligned}
\tag{4.41}
$$

Let $k_2 = \dfrac{0.4\rho_c^2 m_e^4 c^7 B_c}{192\pi^3 \hbar q^6 n_{GJ}^3 B}$. Minimizing $h_{\text{gap}} = l_{\gamma,\text{gap}} + l_{\text{acc}}$ we find:

$$
\begin{aligned}
l_{\text{acc}} &= (6k_2)^{1/7} \\
l_{\gamma,\text{gap}} &= k_2(6k_2)^{-6/7} = \frac{k_2^{1/7}}{6^{6/7}}
\end{aligned}
\tag{4.42}
$$

Therefore the h_{gap}, in the lower number density limit, is:

$$
\begin{aligned}
h_{\text{gap}} &= \frac{k_2^{1/7}}{6^{6/7}} + (6k_2)^{1/7} = \frac{7k_2^{1/7}}{6^{6/7}} \\
&= \frac{14}{6^{6/7}}\left(\frac{\rho_c^2 m_e^4 c^{10} B_c P_{\text{orb}}^3}{3840\pi^3 \hbar q^3 B^4}\right)^{1/7}
\end{aligned}
\tag{4.43}
$$

Where we have included a factor of 2 to account for relative motion of pairs as before. Making use of the fact that $E_{\text{gap}} \approx 4\pi q n_{\text{GJ}} h_{\text{gap}}$, we can estimate the radio luminosity as:

$$
\begin{aligned}
L_r &= \eta q \Phi_{\text{gap}} \dot{N} \\
&= \eta q E_{\text{gap}} h_{\text{gap}} n_{\text{GJ}} A c \\
&= 4\pi \eta q^2 h_{\text{gap}}^2 n_{\text{GJ}}^2 A c \\
&= 8 \times 10^{35} \, \eta_{-2} \, h_{\text{gap},2}^2 \, B_{12}^2 \, P_{-3}^{-2} \, \text{erg} \, \text{s}^{-1}
\end{aligned}
\tag{4.44}
$$

We note here that in this derivation of the coherent radio luminosity, there is no explicit dependence on the value of $E_{\parallel}$.

4.C Coherent curvature radiation as an alternative radiation mechanism

In light of the discovery of FRBs (Lorimer et al., 2007; Thornton et al., 2013; Petroff et al., 2022), a variety of radiation models have been proposed to explain their origin. A large fraction of the proposed theories rely on highly magnetized neutron stars as progenitors (e.g. Keane et al. 2012; Popov & Postnov 2013; Katz 2016; Beloborodov 2017). Coherent curvature radiation is one such model that has the flexibility to explain many of the observed properties of these enigmatic bursts (Kumar et al., 2017; Katz, 2018; Ghisellini & Locatelli, 2018; Lu & Kumar, 2018; Lu et al., 2020; Cooper & Wijers, 2021). The model relies on the formation of overdensities (bunches) of pairs, for example due to the two-stream instability Lu & Kumar (2018); Kumar & Bošnjak (2020), such that curvature radiation is emitted coherently. Critics argue that the formation and maintance of particle bunches in spite of repellent electromagnetic forces (Lyubarsky, 2021). However, if bunches are formed, one could expect the conditions of the NS-NS merger ($E_{\parallel} \sim 10^{10}$ esu, $B \approx 10^{12}$ G) to be conducive to coherent curvature emission in a similar manner to models of FRBs from magnetospheres. It is however less clear that the coherent curvature mechanism would continuously operate effectively at all times that necessary electromagnetic conditions demanded of B and $E_{\parallel}$ are met. In the following we estimate the coherent radio luminosity of this mechanism during a NS-NS merger inspiral.

The critical frequency of curvature radiation $\nu_c = \frac{c\gamma^3}{2\pi \rho_c}$ where γ is the Lorentz factor of radiating electrons and ρ_c is the magnetic field line curvature radius; implying emission observed at ν_{obs} is emitted by electrons with $\gamma \approx 60 \, \rho_{c,6}^{1/3} \, \nu_9^{1/3}$. The radiation formation length scale is $\sim \rho_c/\gamma \approx 10^4$ cm (Lu & Kumar, 2018), much smaller than the spatial extent of $E_{\parallel}$ which is $\sim 10^6$ cm. As in Kumar et al. (2017), the isotropic equivalent luminosity can be estimated as:

$$
\begin{aligned}
L_{\text{iso}} &\approx \frac{c^7 q^2 \gamma^{10} n_e^{'2}}{3 \nu_{\text{obs}}^6 \rho_c^2} \\
&= 2 \times 10^{37} \, \text{erg} \, \text{s}^{-1} \, \nu_9^{-8/3} \, n_{e,12}^{'2} \, \rho_{c,6}^{4/3}
\end{aligned}
\tag{4.45}
$$

Where we have replaced γ in terms of ν_{obs} & ρ_{c}. In the following, we briefly discuss 2 curvature radiation luminosity limits to gauge plausible luminosities in the NS-NS merger scenario.

In Lu & Kumar (2019), the authors discuss the maximum luminosity of FRBs in the curvature radiation model due to the rapid production of Schwinger pairs which screen the $E_{\parallel}$ field on very short timescales if $E > E_s \approx \dfrac{m_e^2 c^3}{q\hbar}$. In the proof, the authors derive generic constraints (i.e. unrelated to extreme Schwinger electric field) on the isotropic equivalent luminosity of coherent emission:

$$L_{\mathrm{iso}} < E_{\parallel}^2 \rho_{\mathrm{c}}^2 c = 3 \times 10^{42} \,\mathrm{erg\,s^{-1}} \, E_{\parallel,10}^2 \, \rho_{\mathrm{c},6}^2 \tag{4.46}$$

Where $E_{\parallel}$ is the magnitude of the parallel electric field component and ρ_{c} is the local curvature radius.

In Kumar et al. (2017), the authors note that particles emitting coherent curvature radiation induce a perpendicular component to the magnetic field $B_{\perp} = 8\pi l_{\perp} q n_{\mathrm{e}}$, where $l_{\perp}$ is the spatial extend of the coherently radiating particles perpendicular to their motion, and n_e is the number density. For the particles to remain coherent, their momenta should remain aligned to a factor $\dfrac{\delta \boldsymbol{p}}{|p|} < \dfrac{1}{\gamma}$, where γ is the Lorentz factor of the accelerated particles. Particles are in the lowest landau state and move only along magnetic field lines, therefore we should also require that $\dfrac{B_{\perp}}{B} < \dfrac{1}{\gamma}$. The results in a maximum luminosity of coherent curvature radiation within a local magnetic field strength B of:

$$L_{\mathrm{iso}} < 6 \times 10^{40} \,\mathrm{erg\,s^{-1}} \, B_{12}^2 \, \nu_9^{-4/3} \, \rho_{\mathrm{c},6}^{2/3} \tag{4.47}$$

We neglect to include maximum luminosity constraints discussed in Cooper & Wijers (2021) to remain agnostic about the unknown particle number density in the NS-NS merger case. Combining these constraints, we can estimate the maximum isotropic luminosity as:

$$
\begin{aligned}
L_{\mathrm{iso,max}} = \min \big(& 3 \times 10^{42} \, E_{\parallel,10}^2 \, \rho_{\mathrm{c},6}^2, \\
& 6 \times 10^{40} \, B_{12}^2 \, \nu_9^{-4/3} \, \rho_{\mathrm{c},6}^{2/3} \big) \,\mathrm{erg\,s^{-1}}
\end{aligned}
\tag{4.48}
$$

The number of coherent bunches that may radiate towards the same observer is uncertain, as is the beaming factor of each curvature powered radio burst. In our numerical implementation for the luminosity estimate of the coherent curvature radiation mechanism, we simply show the maximum allowed luminosity directed within a 0.1 radian solid angle of the observer. The primary result of this subsection is shown in Fig. 4.9, where the black line denotes viewing angle dependent maximum CCR luminosity of a merger involving a 10^{12}G neutron star. We note that the luminosity profile approximately matches the pulsar-like case with an efficiency of approximately $\eta = 10^{-4}$ and therefore we do not show the CCR luminosity profile in the remainder of our results and discussion. The viewing-angle dependent luminosity profile of CCR is different to the pulsar-like case. This is because it is
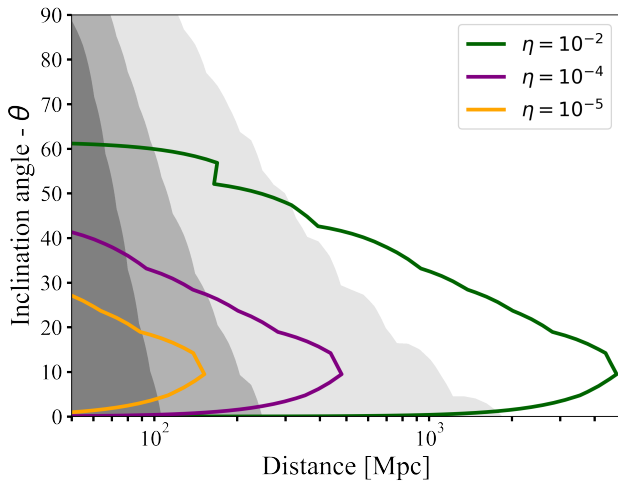
Figure 4.15: Background colours show MeerKAT detection horizons for peak flux of tophat jets at $\nu = 1.43$ Hz assuming detection threshold of 700 μJy. Shades of gray correspond to varying circumburst densities (Darkest $n = 10^{-5}$; medium $n = 10^{-3}$; lightest $n = 10^{-1}$).

calculated by finding the maximum possible CCR luminosity (using Eq. 4.48) for the set of field lines directed towards each observer, rather than the sum of the luminosity along the all observer-aligned field lines.

4.D   Additional co-detectability plots

In this Section we include additional plots as referenced in the main text. In all cases, over-plotted are flux sensitivity curves for various efficiency parameters and $B_s = 10^{12}$G, assuming a fluence limit of the Square Kilometre Array of 1 mJy ms.
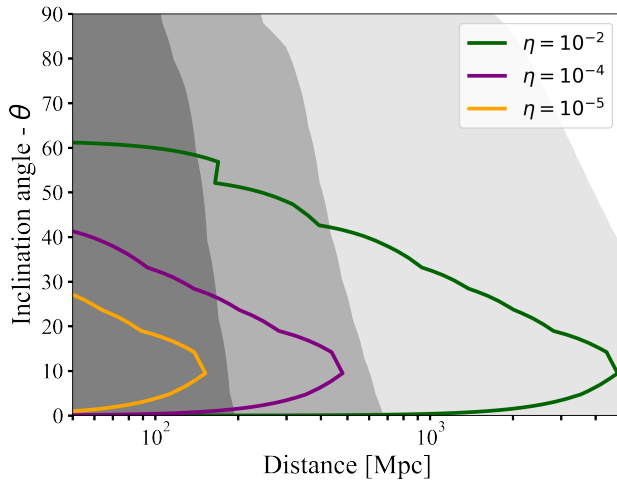
Figure 4.16: Background colours show SKA detection horizons for peak flux of tophat jets at $\nu = 1.43$ Hz assuming detection threshold of 2 μJy. Shades of gray correspond to varying circumburst densities (Darkest $n = 10^{-5}$; medium $n = 10^{-3}$; lightest $n = 10^{-1}$).

4
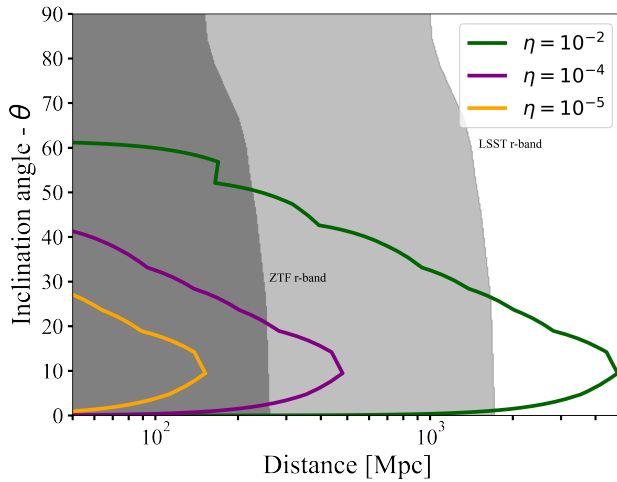
Figure 4.17: Background colours show ZTF and LSST r-band (darker and lighter shades respectively) detection horizons for peak flux of GW170817-like kilonovae models using models from Bulla (2019). Coloured contours show viewing angle-dependent SKA detection horizon of pulsar-like coherent pre-merger emission assuming $\eta = 10^{-2}$, $B_{\rm s} = 10^{12}$G.

4
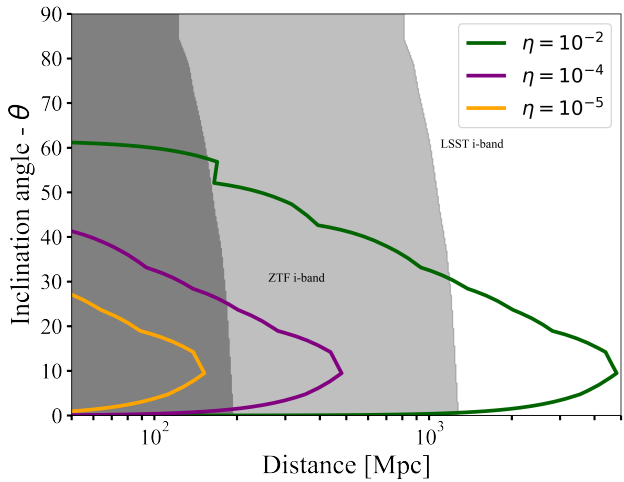
Figure 4.18: Background colours show ZTF and LSST i-band (darker and lighter shades respectively) detection horizons for peak flux of GW170817-like kilonovae models using models from Bulla (2019). Coloured contours show viewing angle-dependent SKA detection horizon of pulsar-like coherent pre-merger emission assuming $\eta = 10^{-2}$, $B_{\rm s} = 10^{12}$G.

Chapter **5**

Testing afterglow models of FRB 200428 with early post-burst observations of SGR 1935+2154

A. J. Cooper, A. Rowlinson, R. A. M. J. Wijers, C. Bassa, K. Gourdji, J. Hessels, A. J. van der Horst, V. Kondratiev, D. Michilli, Z. Pleunis, T. Shimwell, S. ter Veen

Abstract

We present LOFAR imaging observations from the April/May 2020 active episode of magnetar SGR 1935+2154. We place the earliest radio limits on persistent emission following the low-luminosity fast radio burst FRB 200428 from the magnetar. We also perform an image-plane search for transient emission and find no radio flares during our observations. We examine post-FRB radio upper limits in the literature and find that all are consistent with the multi-wavelength afterglow predicted by the synchrotron maser shock model interpretation of FRB 200428. However, early optical observations appear to rule out the simple versions of the afterglow model with constant-density circumburst media. We show that these constraints may be mitigated by adapting the model for a wind-like environment, but only for a limited parameter range. In addition, we suggest that late-time non-thermal particle acceleration occurs within the afterglow model when the shock is no longer relativistic, which may prove vital for detecting afterglows from other Galactic FRBs. We also discuss future observing strategies for verifying either magnetospheric or maser shock FRB models via rapid radio observations of Galactic magnetars and nearby FRBs.

5.1   Introduction

Fast radio bursts (FRBs) are bright, millisecond duration flashes of coherent radio emission (Lorimer et al., 2007; Thornton et al., 2013; Petroff et al., 2016; The CHIME/FRB Collaboration et al., 2021a). Over 20 FRBs have now been localized[1] to their host Galaxies (Chatterjee et al., 2017; Ravi, 2019; Bannister et al., 2019; Marcote et al., 2020; Nimmo et al., 2021; Heintz et al., 2020; Bhandari et al., 2020b), confirming that these bursts are (usually) of extragalactic origin, as was already implied by large dispersion measures. Two varieties of FRB source have been identified, categorized by whether the source is observed to repeat or not. Bursts observed from these different categories of sources appear to have different properties (Pleunis et al., 2021a), which may be suggestive of different progenitors or emission mechanisms.

Since the discovery of FRBs, many theoretical models have been presented to explain the bursts involving various astrophysical sources and radiation mechanisms (Platts et al., 2019). Many of these models focus on highly magnetized neutron stars as prime progenitor candidates for a few reasons. Firstly, the millisecond emission timescale implies compact emission regions $R \approx ct_{\mathrm{FRB}}\Gamma^2 \approx 10^6\, t_{\mathrm{FRB},-3}\,\Gamma_0^2$ cm, where Γ is the bulk Lorentz factor of the emission region towards the observer and we have used the convenient notation $X_{\mathrm{n}} \equiv X/10^n$. In addition, the luminosity of FRBs (≈ 8 orders of magnitude larger than giant millisecond radio pulses in the Milky Way) might imply they are powered by the large magnetic energy reservoir in the magnetospheres of highly magnetized neutron stars known as magnetars. For decades, magnetars within our Galaxy have been observed to emit spontaneous X-ray bursts, which appear to follow a similar wait time distribution and luminosity function to FRBs (SGR 1900+14 Göğüş et al. 1999; SGR 1806-20 Göğüş et al. 2000; FRB 121102 Gourdji et al. 2019), as well as periods of activity and quiescence. Finally, other observed properties of FRBs can be explained within a magnetized neutron star progenitor model: large rotation measures (Michilli et al., 2018), downward drifting sub-bursts (e.g. Hessels et al. 2019), and polarisation angle swings across bursts (Luo et al., 2020).

The exact radiation mechanism within a magnetar progenitor framework is also not understood, with the two primary classes of models distinguished by where the FRB is emitted: close to the surface of the neutron star in magnetospheric models (Katz, 2016; Kumar et al., 2017; Lu & Kumar, 2018; Kumar & Bošnjak, 2020; Wadiasingh & Timokhin, 2019; Lyutikov & Popov, 2020), and far away from the surface in models which rely on maser emission in magnetized shocks (Beloborodov, 2017; Metzger et al., 2019; Beloborodov, 2020). Both classes of radiation model appear to explain the basic properties of FRBs.

Magnetospheric models of FRBs require the coherent radiation of accelerated particles from close to the neutron star surface, through e.g. curvature emission (Kumar et al., 2017). It has been shown that many of the observed properties of FRBs discussed above can be reproduced within this model (e.g. Lu & Kumar 2018; Wang et al. 2019; Cooper & Wijers 2021; Yang & Zhang 2021; Wang et al. 2022). Coherent curvature radiation requires spatial inhomogeneities in the particle distribution ('clumps' or 'bunches'), which may be created

---

[1] http://frbhosts.org

during the particle acceleration phase through the two-stream instability (Cheng & Ruderman, 1977; Usov, 1987; Lu & Kumar, 2018). However, whether clumps form on the required timescales is less clear (see Melrose et al. 2021 and references therein for critical discussion of curvature radiation as a pulsar mechanism), and it has further been suggested that the FRBs produced within the magnetosphere may fail to propagate to an observer (Beloborodov, 2021).

The maser shock model appears to be a theoretically robust way in which coherent emission can be produced, as the maser has been shown to emit narrow-band radio emission in 1D & 3D particle-in-cell (PIC) simulations of magnetized, relativistic shocks (Plotnikov & Sironi, 2019; Sironi et al., 2021). Furthermore, such emission could be ubiquitous in nature wherever such shocks occur, and non-magnetar progenitors have been invoked to explain observed periodicity in repeating sources (Sridhar et al., 2021). Such ubiquity could account for the high observed volumetric rate of FRBs (Ravi, 2019; Lu & Piro, 2019; Luo et al., 2020). However, the specific properties of recently reported FRBs are difficult to explain in a maser shock scenario. In particular, the microsecond variability of FRB 20180916B (Nimmo et al., 2021) and the 30ms separation between distinct sub-bursts in Galactic FRB 200428 (CHIME/FRB Collaboration et al., 2020) appear to be contradictory to the large length scales associated with the synchrotron maser emission region.

In magnetar models of FRBs, multi-wavelength or multi-messenger counterparts to emission provide invaluable observing opportunities with which to distinguish between theoretical models. Both magnetospheric and maser shock models predict a high-energy counterpart to FRB emission (Metzger et al., 2019; Cooper & Wijers, 2021; Yang & Zhang, 2021), however the large distances to extragalactic FRBs mean predicted X-ray/gamma-ray fluxes are below the detection threshold of current instrumentation. The first version of the synchrotron maser shock model (Lyubarsky, 2014), in which relativistic magnetar hyperflares ($U_B \approx 10^{48}$ erg) interact with pulsar wind nebula, predicted a very high-energy TeV component to FRBs. In Metzger et al. (2019) this model was adapted to consider interaction with a wind-like environment, or a mildly relativistic baryonic shell emitted from a previous flare. Using these models, Metzger et al. (2019) predict a multi-wavelength afterglow due to thermal synchrotron emission, based on gamma-ray burst (GRB) afterglow models (Sari et al., 1998). Notably, as the shocks required for the maser are highly magnetized & relativistic, magnetic field lines are compressed such that shocks are quasi-perpendicular. For this reason, shock accelerated non-thermal electrons are not necessarily expected (Sironi & Spitkovsky, 2009), in contrast to what is observed in other astrophysical shocks. Observationally, identifying a multi-wavelength afterglow could confirm the synchrotron maser model of FRBs, since magnetospheric models are not predicted to produce them. Persistent radio counterparts have been identified in two localized repeating FRB sources: FRB 121102 (Chatterjee et al., 2017) and FRB 20190520B (Niu et al., 2021a). The origin of the persistent radio emission is not definitively known, the spectra and lack of variability may imply the compact source is an AGN that resides relatively close to the FRB source. Follow-up of all other localized FRBs have yielded only upper limits to afterglow counterparts (Bhandari et al., 2018), although these are generally not constraining for the maser shock model.

5

In this work, we present Low Frequency Array (LOFAR; van Haarlem et al. 2013) imaging results of SGR 1935+2154, and discuss more broadly the multi-wavelength afterglow predicted after FRB 200428 in the maser shock model. In Section 5.2 we discuss the behaviour of magnetar SGR 1935+2154 before and during the 2020 active phase. In Section 5.3, we present the LOFAR imaging results, where we perform a search for bright radio bursts observable in the image-plane (see Bailes et al. 2021 for the time-domain search, as well as other radio observations) and provide limits for persistent low-frequency emission. In Section 5.4 we interpret the LOFAR results and suggest observing strategies for verification of FRB emission mechanisms. In Section 5.5, we discuss the synchrotron maser shock model and its application to FRB 200428. In particular, we find that early time upper limits appear to rule out simple versions of the maser shock model as applied to the Galactic FRB. We further discuss extensions to the model including non-thermal radiation at late times, and make afterglow predictions for Galactic and nearby, extragalactic FRBs. We conclude our findings in Section 5.6.

5.2   SGR 1935+2154

Galactic magnetar SGR 1935+2154 was discovered in July 2014 through a series of short X-ray bursts (Cummings et al., 2014; Lien et al., 2014; Israel et al., 2016), and past X-ray activity from 2011 was found in an archival search (Campana et al., 2014). Further observations in 2015 with *CHANDRA* & *XMM-Newton* found many more X-ray bursts (Israel et al., 2016), as well as the first intermediate flares (Kozlova et al., 2016). This led to the first measurements of a spin period and spin-down rate of $P = 3.245$ seconds (Israel et al., 2016) and $\dot{P} = 1.43 \times 10^{-11}$, relatively typical values for a Galactic magnetar. Using these measured values, Israel et al. (2016) derive the characteristic age and surface magnetic field of the magnetar as: $\tau_c = \dfrac{P}{2\dot{P}} \approx 3.6$ kyr and $B_s = \sqrt{\dfrac{3c^3 I P \dot{P}}{8\pi^2 R_{\mathrm{NS}}^6}} \approx 2.2 \times 10^{14}$ G. Interestingly, $\dot{P}$ shows a decreasing trend, with a measured negative $\ddot{P} = 3.5(7) \times 10^{-19}\,\mathrm{s}^{-1}$ observed. The source position was determined to be at $\mathrm{R.A.} = 19:34:55.5978$, $\mathrm{Dec.} = 21:53:47.7864$, with an accuracy of 0.6" (90% confidence, Israel et al. 2016; see also the discovery of an infrared counterpart by Levan et al. 2018 at Galactic coordinates $\mathrm{b} = 293.73128$, $\mathrm{l} = 21.896608$). The magnetar was associated with a supernova remnant SNR G57.2+0.8 by Gaensler (2014), with a full multi-wavelength radio study of continuum and persistent emission presented in Kothes et al. (2018). The authors find that the age of the SNR is approximately 41 kyr, i.e. much older than the characteristic age of the magnetar derived from its spin properties (Israel et al., 2016). The distance to SNR G57.2+0.8 was revised by Zhou et al. (2020), finding that the SNR and thus the magnetar is likely closer than the 10 kpc previously assumed, at just $D = 6.6 \pm 0.7$ kpc.

In late 2019 (Wood et al., 2019; Ambrosi et al., 2019) and especially in early 2020 (Palmer, 2020; Younes et al., 2020), the magnetar entered a new phase of extreme activity. On the 27th April 2020 at 14:34:24, an extremely bright radio burst was emitted from SGR 1935+2154. The burst was observed by the Survey for Transient Astronomical Radio Emis-

sion 2 (*STARE-2*; Bochenek et al. 2020b) an all-sky radio telescope (Bochenek et al., 2020a). It was also detected in the side lobes of *CHIME*, the Canadian Hydrogen Intensity Mapping Experiment telescope (CHIME/FRB Collaboration et al., 2020). *STARE-2* detected the burst with a $1.281 - 1.468$ GHz lower limit fluence of $1.5 \pm 0.3 \times 10^6$ Jy ms and a full-width half-maximum duration of 0.61 ms. *CHIME/FRB* observed two bursts separated by 28.9 ms, with $400 - 800$ MHz durations of 0.585 ± 0.014 ms and 0.335 ± 0.007 ms respectively, and average fluences of $0.48 \pm_{0.24}^{0.48} \times 10^6$ Jy ms and $0.22 \pm_{0.11}^{0.22} \times 10^6$ Jy ms. The lower observed fluence could be attributed to a steep spectral rise with frequency such that the burst is brighter at the *STARE-2* observing frequency. The implied luminosity was lower than extragalactic FRBs by ≈ 4 orders of magnitude, but was brighter than any other coherent radio emission observed from within our Galaxy with the possible exception of the brightest 2 MJy nanoshot observed from the Crab pulsar (Hankins & Eilek, 2007). On 30th April, a weak radio burst (0.06 Jy ms) was reported by Zhang (2020), and two further radio bursts were reported later by Kirsten et al. (2021) with fluences of 112 Jy ms and 24 Jy ms.

FRB 200428 occurred during a very active period of high-energy bursts from SGR 1935+2154, and many hundreds of short X-ray bursts were observed by NICER, Fermi, Swift, AGILE, IN-TEGRAL, Insight-HXMT, Konus-Wind and other X-ray satellite observatories (Fig. 5.4; for catalogues of X-ray bursts see Younes et al. 2020; Cai et al. 2022b; Li et al. 2022). Remarkably, an X-ray burst temporally coincident with the FRB was observed by four X-ray instruments: Integral (Mereghetti et al., 2020), Insight-HXMT (Li et al., 2021), AGILE (Tavani et al., 2021) and Konus-Wind (Ridnaia et al., 2021). The X-ray/radio energy ratio of the radio burst was $\frac{E_X}{E_r} \approx 10^5$. The radio-coincident X-ray burst had a harder spectrum than other bursts seen from SGR 1935+2154 in the same window of activity, extending to 250 keV (Mereghetti et al., 2020; Li et al., 2021) despite a relatively typical total fluence. The stark contrast is clear when the X-ray burst is compared to the many Fermi-GBM and NICER observed bursts in Younes et al. (2021). Within magnetospheric models of FRBs, this can plausibly be explained by a non-thermal counterpart observable only when an FRB is observed (Cooper & Wijers, 2021), in addition to a regular short magnetar burst; or due to rapid relaxation of perturbed magnetic field lines (Yang et al., 2020). In the synchrotron maser shock picture of FRBs, the hard X-ray burst represents the initial peak of the afterglow emission that is observable at lower frequencies at later times (Margalit et al., 2020a).

5.3 LOFAR observations

SGR 1935+2154 entered an active phase in April 2020. We obtained Directors Discretionary Time observations using LOFAR, comprising of 14 hours spread over 3 dates in 2020. The observation details are provided in Table 5.1. Each observation was obtained using the LOFAR High Band Antennas (HBA) and the full Dutch array (24 core stations and 14 remote stations), covering a frequency range of 120–168 MHz and a central frequency of 144 MHz. The frequency range is divided into 244 sub-bands with bandwidths of 195.3 kHz. The recorded data have a time resolution of 1s, and a frequency resolution of 64 channels per sub-band. These data were pre-processed using the standard methods for LOFAR.
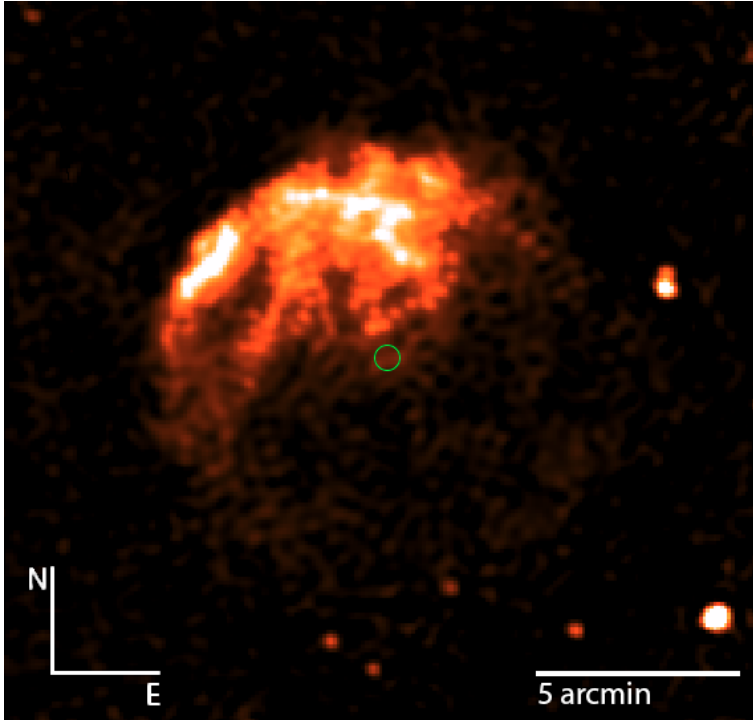
Figure 5.1: LOFAR image of SGR 1935+2154 (denoted by the green circle) and the surrounding remnant SNR G57.2+0.8. This image makes use of the full datasets from all epochs.

Observation ID	Start Date (UTC)	Start Time (UTC)	Calibrator ID
L780243	April 29 2020	03:08	L780239
L780251	April 29 2020	05:20	L780247
L780651	May 11 2020	01:49	L780655
L780659	May 11 2020	04:01	L780655
L780667	May 11 2020	06:13	L780671
L797090	October 21 2020	14:30	L797092
L797094	October 21 2020	16:42	L797096

Table 5.1: The observations attained of SGR 1935+2154. The ID numbers correspond to the IDs for the preprocessed data in the LOFAR Long Term Archive[2]. The duration of each target observation was 2 hours, separated by 10 minute calibrator observations of 3C295.

To calibrate these LOFAR data, we used the PREFACTOR pipeline (version 3.2)[3] developed by the LOFAR Radio Observatory with the default parameters and version 3.1 of the LO-FAR software. The calibrator source chosen for these observations was 3C48. As the field of SGR 1935+2154 is close to the A-Team source Cygnus A, we used the PREFACTOR demixing options to subtract the contribution of Cygnus A from the target data. The data were averaged to a time step of 8 seconds and a frequency resolution of 48.82 kHz (4 channels per subband).

5.3.1 Epoch imaging

All imaging of these data was conducted using WSCLEAN version 2.7.0[4] (Offringa et al., 2014). The imaging settings used for these observations are outlined in Table 5.2. Deep images of the field were created for the 3 observation days separately, as well as a fully combined image. Two versions of the deep images were created; one with the full dataset and the second with a minimum baseline length of 1000λ to remove the extended emission from the supernova remnant. These images were used to search for faint persistent emission from the location of SGR 1935+2154. No persistent emission was detected at the location of SGR 1935+2154 and the limits obtained for persistent emission from SGR 1935+2154 are provided in Table 5.3. We provide a constrained flux density measurement at the position of SGR 1935+2154 obtained using PySE (Carbone et al., 2018) and assuming the restoring beam parameters. Additionally, we measure the rms noise in a 30×30 pixel box centred on the position of SGR 1935+2154 and use the rms noise to calculate a 3σ upper limit.

5.3.2 Snapshot imaging

To search for bright pulses from SGR 1935+2154, we also imaged the observations on shorter snapshot timescales. We integrated across the observed frequencies to create a single image. As SGR 1935+2154 has a high dispersion measure ($332.7\mathrm{pc\ cm^{-3}}$; CHIME/FRB Collaboration et al. 2020), it takes time for a dispersed pulse to traverse the bandwidth of the HBA observation. This time is calculated using:

$$\tau_{\mathrm{DM}} = 8.3\Delta\nu DM\nu^{-3}\mu s,\qquad(5.1)$$

where τ_{DM} is the dispersion delay in seconds, $\Delta\nu$ is the bandwidth in MHz, ν is the observing frequency in GHz, and DM is the dispersion measure in pc cm^{-3} (Taylor & Cordes, 1993). For these LOFAR observations, we find that the dispersion delay corresponds to 44 seconds. Therefore, we create snapshot images of 40 seconds in duration (as the data are integrated to 8 second intervals) and obtained 1081 images in total. We note that we could conduct de-dispersion imaging (e.g. Anderson et al. 2021b; Tian et al. 2022) to obtain deeper constraints on very short duration dispersed pulses such as FRBs. However, beam-formed observations

---

Paramter	Deep Images	Snapshot Images
Size (pixels)	4096×4096	2048×2048
Pixel Scale (arcsec)	5	5
-mgain	10	10
-j	10	10
Automatic masking of sources (σ)	10	10
Maximum baseline length (λ)	8000	8000
Minimum baseline length (λ)	0/1000	700
Number of frequency channels	6	1
Automatic threshold (σ)	3	3
Briggs weighting robustness	-0.5	-0.5
Number of iterations	10000	10000
Primary beam applied	True	False
Weighting rank filter	3	3
Clean border	0	0
Reorder visibilities	True	False
Fit restoring beam	True	True
Number of time intervals	1	180

Table 5.2: The parameters used for imaging each observation set in WSClean. Deep images are created using two different minimum baselines.

Observation Date	Flux density (mJy)	3σ upper limit (mJy/beam)
April 29 2020	2.2 ± 5.8	9.5
May 11 2020	1.8 ± 4.3	6.8
October 21 2020	0.7 ± 4.6	7.9
All	1.5 ± 3.8	6.0

Table 5.3: The flux density measurements at the location of SGR 1935+2154 for each observing epoch and a combined image. The flux density measurements were obtained via a constrained flux density measurement using PySE. The 3σ upper limits are obtained by measuring the rms noise in a region surrounding SGR 1935+2154.

were also attained for these observations and very short duration dispersed pulses would be optimally detected in those observations (Bailes et al., 2021). Our snapshot images targeted longer duration flares that may not have been detectable in the beam-formed searches. The snapshot images were created using the settings given in Table 5.2. A minimum baseline length of 700λ was used so that the extended emission from the supernova remnant was not visible in the snapshot images as this leads to a better constraint on emission from a point source at the location of SGR 1935+2154.

Following the method outlined in Rowlinson et al. (2022), we correct for any systematic flux density variations between the snapshot images produced by assuming that the majority of sources are not variable. As SGR 1935+2154 is in the centre of the field, we consider sources out to a radius of 1 degree (covering the inner 50% of the full width half maximum of the LOFAR HBA beam at 150 MHz[5]). We extract all sources in the first 40 second snapshot image within that radius using PySE with a detection threshold of 8σ and confirm they are point sources by visual inspection (one source was rejected as it consisted of 2 blended point sources). These selection criteria resulted in 10 sources that were input into the LOFAR Transients Pipeline (TraP; Swinbank et al., 2015) using the monitoring list capability. A flux density correction factor is then calculated and applied to each individual image[6]. The average flux density correction is $\sim$6%.

Following the correction for systematic flux density variations, we conduct image quality control by measuring the rms noise in the inner eighth of each image and plot a histogram of these data in Figure 5.2. We fit the typical rms noise distribution for the images with a Gaussian distribution to give an average rms value of $17.4^{+2.6}_{-2.3}$ mJy/beam. Any image with an rms noise that is more than 3σ deviant from the average rms value is rejected. This analysis rejected 110 images, corresponding to 10% of the sample.

To search for emission at the location of SGR 1935+2154, we processed the images using TraP and monitor the position of SGR 1935+2154 to provide a flux measurement in each epoch. We used the standard TraP settings apart from using a 4σ detection threshold and setting the force beam parameter to True. As we are focusing on the location of SGR 1935+2154, which lies at the centre of the field, we use a small extraction radius of 120 pixels (corresponding to 10 arcmin). We detect no emission at the location of SGR 1935+2154. In Figure 5.3, we plot a histogram of the flux density values measured at the location of SGR 1935+2154 and fit the distribution with a Gaussian distribution. The fitted Gaussian distribution gives an average flux density measurement per epoch of 13 ± 0.7 mJy with a standard deviation of 23 mJy, corresponding to a 3σ upper limit for persistent point source emission of 82 mJy. This suggests the flux at the location of SGR 1935+2154 is significantly non-zero, which by inspection of Fig. 5.1, can be attributed to extended emission from the surrounding SNR.

---

[5] http://old.astron.nl/radio-observatory/astronomers/lofar-imaging-capabilities-sensitivity/lofar-imaging-capabilities/lofa

[6] using the script https://github.com/transientskp/TraP_tools/blob/master/exampleScripts/correctSystematicFluxOffset.py
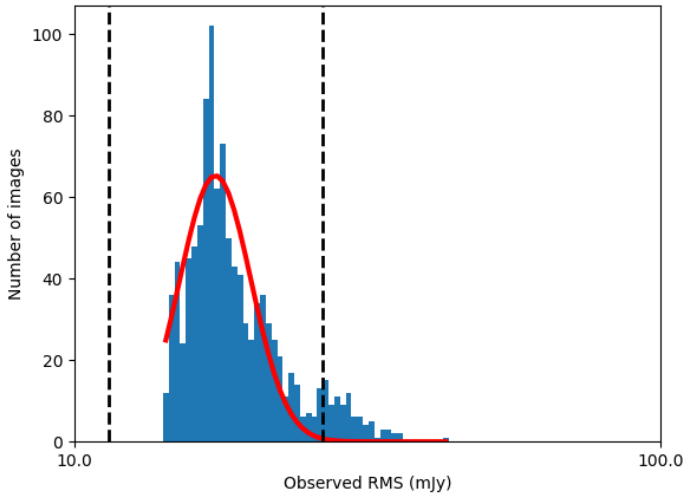
Figure 5.2: Histogram of the rms values of the inner eighth of all the 40 second snapshot images used. The values are fit with a Gaussian distribution shown by the solid red curve. All images that are $> 3\sigma$ deviant from the average rms are rejected and the thresholds are shown with the black dashed lines.
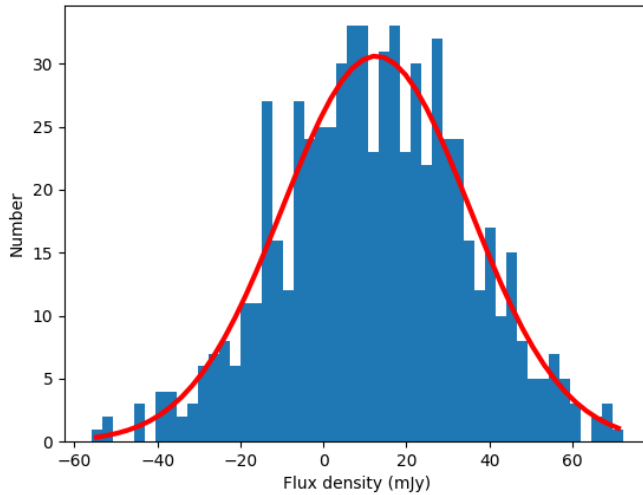
Figure 5.3: A histogram of the flux density values for SGR 1935+2154 obtained by conducting a constrained fit at the location in each snapshot image.
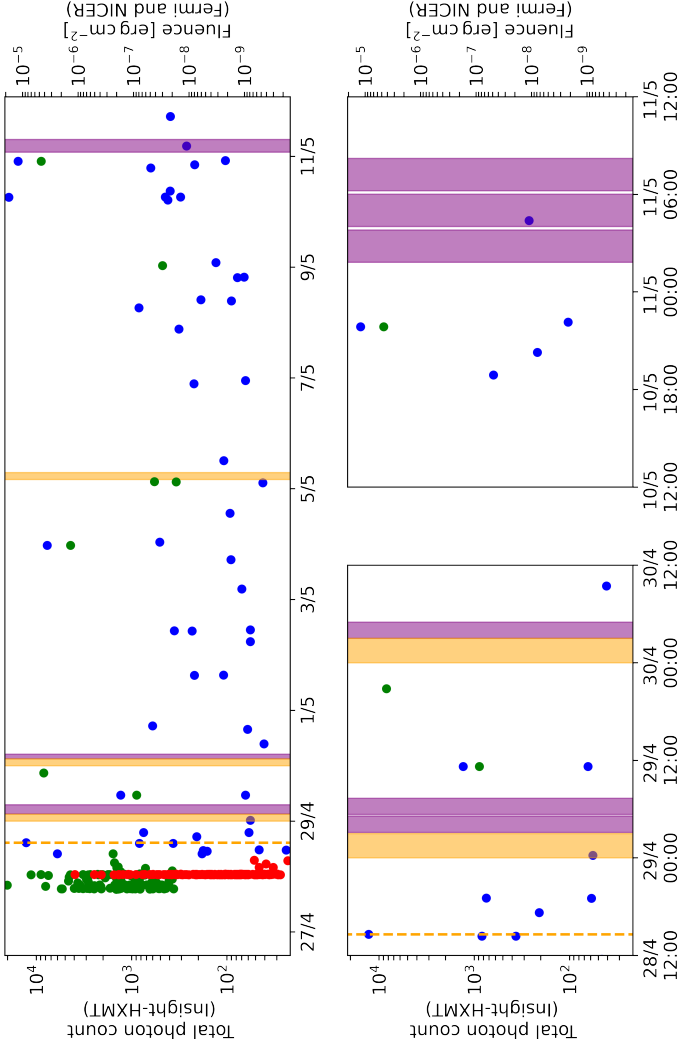
Figure 5.4: We show the times of LOFAR observations (denoted by orange background hue) and AARTFAAC (Prasad et al., 2016) observations (denoted by purple background hue) of SGR 1935+2154 during the April/May 2020 active episode. We note that observations on the 30th April were beamformed only, and therefore do not appear in our imaging analysis Section 5.3. The time of the FRB as observed by CHIME & STARE-2 is denoted by the vertical dashed orange line. We also show counts/fluence and times of X-ray bursts as observed by Insight-HXMT (blue dots; Cai et al. 2022b), NICER (red dots; Younes et al. 2020) and Fermi-GBM (green dots; Lin et al. 2020). Insight-HXMT data points refer to the total number of photon counts in the burst across all detectors (left y-axis), whereas NICER and Fermi-GBM data points refer to the total fluence of the burst in the 0.5-10 keV and 8-200 keV bands respectively. The second row of plots show timeline zoomed in on LOFAR observations, where 10 minute calibrator scans are visible, as are the two X-ray bursts for which we were on source. Interpretation of these observations is discussed in Section 5.4.

5.4   Interpretation of LOFAR observations & discussion

5.4.1   Simultaneous radio & X-ray limits on transient flares

Low-frequency image-plane searches for radio transients have recently yielded detections of new types of coherent radio transient with long periods (Hurley-Walker et al., 2022; Caleb et al., 2022). These new sources have inferred surface magnetic fields consistent with magnetars. We have performed a search for transient low-frequency emission in snapshot images on timescales of 40 seconds (i.e. the dispersion delay across the LOFAR band of a burst from SGR 1935+2154) and find no transient emission at the location of the magnetar. Given the non-detections in the LOFAR time-domain search presented in Bailes et al. (2021), coupled with the fact that second-hour timescale transient radio emission has not been yet observed from Galactic magnetars, we did not necessarily expect a detection from this search.

One of the primary motivators of radio observations of magnetars in active phases, other than detecting period-modulated radio pulses from magnetars (see Sect. 5.4.2), is to obtain constraints on the X-ray/radio luminosity ratio during X-ray magnetar bursts. In Fig. 5.4 we show the times of LOFAR and AARTFAAC observations, overplotted with high-energy bursts observed by various X-ray observatories. One high-energy burst observed by Insight-HXMT (burst number 56 in Cai et al. 2022b) occurred during our LOFAR observations on 11/5/2022. The burst had a reported 1-250 keV flux of $2.29^{+0.18}_{-0.17} \times 10^{-7} \mathrm{\ erg\ s^{-1}\ cm^{-2}}$ (Cai et al., 2022a). The duration of this burst was 0.093, 0.06 and 0.076 seconds in the high-energy (HE), medium-energy (ME) and low-energy (LE) detectors respectively, resulting in a X-ray fluence of approximately $2 \times 10^{-8} \mathrm{\ erg\ cm^{-2}}$. The time-domain search for LOFAR bursts in this observation provided upper limits to the spectral fluence of a 1ms width radio burst of 0.075 Jy ms (Bailes et al., 2021). Assuming the bandwidth of a typical radio burst is $\delta\nu = 10^9 \mathrm{\ Hz}$ (i.e. similar to FRB 200428 observed from SGR 1935+2154), we find a fluence limit of $7.5 \times 10^{-18} \mathrm{\ erg\ cm^{-2}}$, resulting in a minimum X-ray/radio fluence ratio of

$$\frac{\mathcal{F}_{\mathrm{X}}}{\mathcal{F}_{\mathrm{r,144MHz}}} > 3 \times 10^9.$$ This ratio is very constraining, as shock models of FRBs typically predict luminosity ratios of approximately 10^5 (Margalit et al., 2020a).

The Amsterdam-ASTRON Radio Transient Facility And Analysis Centre (AARTFAAC), is an all-sky radio transient monitor operating in parallel with LOFAR (Prasad et al., 2016), sensitive to bright transient and variable emission at low-frequencies. AARTFAAC was operating with 16 subbands spanning $60.15 - 64.84$ MHz during an X-ray burst observed from SGR 1935+2154 by Insight-HXMT (burst 19 in Cai et al. 2022b). The dispersion delay from SGR 1935+2154 from the Insight-HXMT X-ray band to the AARTFAAC band is $\tau_{\mathrm{X-ray}} = 324$ seconds, and the in-band dispersion delay across $60.15 - 64.84$ MHz is $\tau_{\mathrm{in-band}} = 54$ seconds. No radio transient was detected at the time of the X-ray burst. We can derive a meaningful fluence sensitivity by comparing the weakest bursts observed in Kuiack et al. (2020) from PSR B0950+08 (4×10^4 Jy ms), and rescaling by a factor proportional to the square root of the ratio of in-band dispersion delay from the different sources to account for a loss of sensitivity due to pulse smearing: $\left(\frac{\tau_{\mathrm{PSR\ B0950+08}}}{\tau_{\mathrm{SGR\ 1935+2154}}} \right)^{1/2} \approx 11$. We therefore find a conservative fluence

sensitivity of approximately 10^6 Jy ms for the dispersed burst from SGR 1935+2154, and we can constrain the fluence ratio of the X-ray burst observed by Insight-HXMT to $\frac{\mathcal{F}_{\mathrm{X}}}{\mathcal{F}_{\mathrm{r}}} \gtrsim 10^2$.

Some magnetospheric models of FRBs predict that FRBs are always produced with short magnetar X-ray bursts, but are only beamed towards the observer in a small number of cases $\approx \Gamma^{-1}$ (Lu et al., 2020). Here, Γ is the Lorentz factor of the emitting set of particles, and is on the order of $50 - 1000$ (Kumar et al., 2017). In the context of these models, coordinated radio and X-ray observations of active magnetars will either lead to the detection of another Galactic FRB, or build up a sample of radio-quiet magnetar bursts. If such a sample is significantly large (i.e. $N \gg \Gamma$) it can be used to statistically constrain Γ, and thus magnetospheric models of FRBs more broadly. Using single-dish 25m class telescopes, Kirsten et al. (2021) were able to place strong limits on radio counterparts to 59 high-energy bursts from SGR 1935+2154, effectively ruling out values of $\Gamma \ll 50$. Furthermore, Lin et al. (2020) found that 29 Fermi-GBM bursts were co-observed during one observing epoch with the FAST radio telescope, providing stringent upper limits on the radio/X-ray ratio of these bursts. The caveats with pursuing these kinds of simultaneous observation are two-fold. Firstly, we know that (repeating) FRBs generally have a narrow bandwidth (e.g. The CHIME/FRB Collaboration et al. 2021a) and therefore observing at a one frequency does not necessarily preclude the emission of a radio burst at another. Second, magnetar X-ray bursts are stochastic and difficult to predict. Building such a sample will require either a pipeline from X-ray detections to radio observatories that enable rapid target-of-opportunity observations[7]; or long-term observations of magnetars with underutilized radio telescopes. For the latter, we note that achieving a constraint of $\frac{L_{\mathrm{X}}}{L_{\mathrm{r}}} > 10^5$ for a typical Galactic magnetar bursts only requires fluence limits on the order of $100 - 1000$ Jy ms, and therefore does not require time on extremely sensitive radio instruments.

5.4.2   Radio-quiet magnetars as FRB sources

Pulsed, persistent emission is observed from a sub-population of magnetars which are radio-loud (Camilo et al., 2006, 2007; Kramer et al., 2007; Levin et al., 2010; Anderson et al., 2012; Lower et al., 2020; Esposito et al., 2020). In Rea et al. (2012), the authors describe the fundamental plane of radio magnetars, suggesting that in general radio-loud magnetars have quiescent $2 - 10$ keV X-ray luminosities below their rotational energy loss rate $L_{\mathrm{rot}} = 4\pi^2 I P \dot{P}^{-3}$, where I is the neutron star moment of inertia. The conjecture that enhanced X-ray emission precludes radio emission (or vice versa) is supported by observations of PSR J1119-6127, a radio pulsar with a high magnetic field where radio pulses shut off when X-ray bursts are observed (Archibald et al., 2017). Similar X-ray and radio mode switches have also been observed in older (but non-recycled) pulsars with modest inferred magnetic

---

[7]A possible observation strategy would be to use low-frequency radio telescopes and utilize the dispersion delay of radio emission to probe radio bursts associated with rapidly reported X-ray bursts. Alternatively, one may attempt to identify X-ray burst storms to trigger observations when more X-ray bursts are expected within the observation duration.

fields, including PSR B0943+10 (Hermsen et al., 2013) and PSR B0823+26 (Hermsen et al., 2018).

SGR 1935+2154 is thus far the only Galactic magnetar to have produced a bright radio burst, and the radio limits presented here and in Bailes et al. (2021) suggest SGR 1935+2154 is not a radio-loud magnetar. This is consistent with the fundamental plane of Rea et al. (2012) given the observed persistent X-ray luminosity of SGR 1935+2154. Three individual radio bursts/pulses were reported after the FRB (Zhang, 2020; Kirsten et al., 2021), albeit at lower luminosities. The one-off radio bursts and pulses strongly suggest that high X-ray bursting activity does not disrupt a magnetar's ability to produce *transient* radio bursts, and possibly that persistent pulsed radio emission precludes transient bursts. The association between radio-quiet magnetars and FRB-emitting magnetars is more intriguing when considered in the context of the recent discovery of highly magnetized neutron stars which exist beyond the canonical pulsar death lines (e.g. Ruderman & Sutherland 1975; Chen & Ruderman 1993) in $\dot{P} - P$ phase space (Caleb et al. 2022; see also Hurley-Walker et al. 2022). The implication that a neutron star's inability to produce typical pulsar-like emission could be a prerequisite for a FRB production may hint that pulsed radio emission observed from (ultra) long period magnetars is powered by a different emission mechanism than pulsars, possibly more similar to the radiation mechanism that powers FRBs. Understanding the particle acceleration and coherent radiation mechanism operating in these long period sources may advance our understanding of how FRBs are generated.

5.5   Maser shock model & afterglow constraints

In the synchrotron maser shock model of FRBs, coherent radiation is generated by the gyration of particles in relativistic, magnetized shocks (Lyubarsky, 2014; Beloborodov, 2017; Metzger et al., 2019; Beloborodov, 2020; Sironi et al., 2021), as has been previously discussed in the literature before the discovery of FRBs (Langdon et al., 1988; Hoshino et al., 1992; Gallant et al., 1992; Usov & Katz, 2000). The model suggests that flaring magnetars can produce relativistic ejecta, which provide conditions conducive to synchrotron maser emission upon interaction with external material in a surrounding nebula (Lyubarsky, 2014), or from a previous flare (Metzger et al., 2019). As the shock propagates relativistically, a multi-wavelength afterglow is expected (Metzger et al., 2019), with emission peaking at successively lower frequencies due to absorption and a decreasing bulk Lorentz factor Γ.

5.5.1   Afterglow model

We present relevant dynamical & radiation models, following the afterglow prescription detailed in Metzger et al. (2019) & Margalit et al. (2020a) in this subsection. We extend the model of Metzger et al. (2019) into the non-relativistic expansion phase relevant for late-time radio observations, remaining agnostic about the nature of the circumburst medium. Much of the early afterglow model is similar to models developed for GRB afterglows (e.g. Mészáros et al. 1998; Sari et al. 1998). The late-time dynamics of interest here after a deceleration time t_{dec} rely on the self-similar model of blast-waves described in Blandford &

McKee (1976) and non-relativistic Sedov-Taylor model of an expanding blast-wave (Sedov, 1959; Taylor, 1950). Using these models we can make detailed predictions of the evolution of the shock and multi-wavelength afterglow.

5.5.1.1 Deceleration phase

As shown in Metzger et al. (2019), the shock reaches the deceleration radius r_{dec} in a time t_{dec}, which is equal to the central engine activity time, i.e. $t_{\mathrm{dec}} \approx t_{\mathrm{FRB}} \approx 1$ ms, such that we use these subscripts interchangeably. All parameters denoted with these subscripts refer to the value at the deceleration time. All timescales of interest for emission below the X-ray band occur at $t \gg t_{\mathrm{dec}}$, therefore we are only interested in solutions to the dynamics and radiation in the deceleration and non-relativistic phases. The bulk Lorentz factor for an adiabatically evolving shock at times $t \gg t_{\mathrm{FRB}}$ is:

$$\Gamma(r > r_{\mathrm{FRB}}) = \left(\frac{E_{\mathrm{flare}}(17 - 4k)}{16\pi m_p n_{\mathrm{ext}} r^3 c^2} \right)^{1/2}$$

$$= \Gamma_{\mathrm{FRB}} \left(\frac{r}{r_{\mathrm{FRB}}} \right)^{\frac{k-3}{2}} \tag{5.2}$$

Where r and n_{ext} are the radius of the shock from the central engine and the external number density of the local environment that the shock ploughs into. n_{ext} depends on the type of environment considered and in general has the form $n_{\mathrm{ext}} \propto r^{-k}$ where $0 \leq k < 3$. Wind-like medium ($k = 2$) and constant medium ($k = 0$) are commonly used, and either may be applicable to the environment surrounding a magnetar (Metzger et al., 2019). Assuming an external density at $n_{\mathrm{ext}}(r_{\mathrm{FRB}})$ at $r = r_{\mathrm{FRB}}$:

$$n_{\mathrm{ext}}(r) = n_{\mathrm{ext}}(r_{\mathrm{FRB}}) \left(\frac{r}{r_{\mathrm{FRB}}} \right)^{-k} \tag{5.3}$$

In the observer frame, the distance of the adiabatic shock front from the central engine as a function of time is:

$$r(t > t_{\mathrm{FRB}}) = 2c\Gamma^2 t = 2ct\Gamma_{\mathrm{FRB}}^2 \left(\frac{r}{r_{\mathrm{FRB}}} \right)^{k-3}$$

$$\propto t^{\frac{1}{4-k}} \tag{5.4}$$

Therefore, by Eqs. 5.2 & 5.4 the shock Lorentz factor varies as a function of observer time as:

$$\Gamma(r > r_{\mathrm{FRB}}) = \Gamma_{\mathrm{FRB}} \left(\frac{1}{r_{\mathrm{FRB}}} \right)^{\frac{k-3}{2}} \left(\left(2ct\Gamma_{\mathrm{FRB}}^2 \right)^{\frac{1}{4-k}} r_{\mathrm{FRB}}^{\frac{3-k}{4-k}} \right)^{\frac{k-3}{2}}$$

$$\propto t^{\frac{k-3}{8-2k}} \tag{5.5}$$

Given this, Metzger et al. (2019) compute the afterglow emission during this deceleration phase. Electrons in the shock are assumed to be in energetic equipartition with the ions

5

such that their mean thermal Lorentz factor is: $\gamma_{\text{therm}} = \dfrac{m_p}{2m_e}\Gamma$. Particles are assumed not to undergo non-thermal acceleration by the shock (see Sect. 5.5.5). The magnetic field is parameterized in terms of the magnetization parameter σ as a fraction of the thermal energy density of the shock such that:

$$B(t > t_{\text{FRB}}) = \sqrt{64\pi\sigma\Gamma^2 m_p c^2 n_{\text{ext}}} \propto t^{\frac{-3}{8-2k}}, \tag{5.6}$$

where we assume throughout $0.1 \leq \sigma \leq 1$, as required for coherent maser emission. As in GRB afterglows, the critical synchrotron frequency ν_{sync} and the cooling frequency ν_{cool} (Sari et al., 1998) in the observer frame is:

$$\nu_{\text{sync}} = \frac{qB\gamma_{\text{therm}}^2\Gamma}{2\pi m_e c} \propto t^{\frac{3k-12}{8-2k}}$$
$$\nu_{\text{cool}} = \frac{qB}{m_e c}\gamma_{\text{c,cool}}^2\Gamma \propto t^{\frac{3k-10}{8-2k}} \tag{5.7}$$

Where $\gamma_{\text{c,cool}} = \dfrac{6\pi m_e c}{\sigma_{\text{T}}\Gamma B^2 t}$. Using the parameter values of Margalit et al. (2020a), we find that for the flare associated with FRB 200428 from SGR 1935+2154, $\nu_{\text{sync}} < \nu_{\text{cool}}$ after a time of just $t = 0.99\,\sigma_{-1}^2$ seconds. This means that for even the earliest optical data discussed in Section 5.5.3, the slow cooling regime holds. We note that for larger magnetization values (i.e. $\sigma = 1$) the earliest time predictions within a minute of the burst (e.g. Figs. 5.6 & 5.7) will be affected.

The spectral luminosity at the critical synchrotron frequency is:

$$L_{\nu,\text{sync}} \propto N_{\text{therm}}\Gamma B, \tag{5.8}$$

where $N_{\text{therm}} \propto n_{\text{ext}} R_{\text{sh}}^3$ is the number of radiating thermal electrons. In the slow-cooling regime (Sari et al., 1998; Margalit et al., 2020a), the spectral luminosity is:

$$L_\nu = \begin{cases} L_{\nu,\text{sync}}\left(\frac{\nu}{\nu_{\text{sync}}}\right)^{1/3} & \nu < \nu_{\text{sync}} \\ L_{\nu,\text{sync}}\exp\left(\left(-\frac{\nu}{\nu_{\text{sync}}}\right)^{1/3}\right) & \nu > \nu_{\text{sync}}, \end{cases} \tag{5.9}$$

where the 1/3 exponent in the second line reflects recent theoretical work by Margalit & Quataert (2021). In practice, for FRB 200428 we compute the predicted afterglow by fitting the initial X-ray data point and using the temporal scaling relations developed for GRB afterglow models described below (Mészáros et al., 1998; Sari et al., 1998; Metzger et al., 2019). To approximate the absorption of lower frequency emission, we follow the method of Margalit et al. (2020a) used in their Fig. 9, by ensuring the spectral luminosity is not larger than the expected synchrotron self-absorption value of:

$$L_{\nu,\text{SSA}} \approx \frac{8}{3}\pi^2 m_e R_{\text{sh}}^2 \nu^2 \gamma_{\text{therm}} \tag{5.10}$$

5.5.1.2 Non-relativistic phase

The low luminosity of FRB 200428 means it enters a non-relativistic expansion phase much earlier than a bright FRB (Margalit et al., 2020a). We can model this phase by comparison to the dynamics of supernova remnants, i.e. Sedov-Taylor expansion (Taylor, 1950; Sedov, 1959). We can find the time at which the shock enters this phase by considering when $\Gamma \approx 1$. Inspection of Eqs. 5.4 & 5.5 tell us $\Gamma(t > t_{\text{FRB}}) \propto t^{\frac{k-3}{8-2k}}$ such that the approximate time and radius at which the shock becomes non-relativistic as:

$$t_{\text{non-rel}} \approx t_{\text{FRB}} \left(\frac{1}{\Gamma_{\text{FRB}}} \right)^{\frac{8-2k}{k-3}}$$

$$r_{\text{non-rel}} \approx r_{\text{FRB}} \left(\frac{t_{\text{non-rel}}}{t_{\text{FRB}}} \right)^{\frac{1}{4-k}} \tag{5.11}$$

For FRB 200428, we find that $t_{\text{non-rel}} \approx 45$ seconds. We can find the synchrotron frequency and spectral luminosity of the thermal electrons at the time the shock is non-relativistic by Eq. 5.7:

$$\nu_{\text{sync,non-rel}} = \nu_{\text{sync,dec}} \left(\frac{t_{\text{non-rel}}}{t_{\text{FRB}}} \right)^{\frac{3k-12}{8-2k}} \tag{5.12}$$

In the slow-cooling regime, $L_{\nu,\text{sync}} \approx$ constant in the deceleration phase (Sari et al., 1998) such that:

$$L_{\nu,\text{sync,non-rel}} = L_{\nu,\text{sync,dec}} \tag{5.13}$$

After defining these quantities at the non-relativistic transition time, we can make predictions for this phase. Using the well-known Sedov-Taylor expansion solution in a constant medium, the shock radius in this regime is:

$$r(r > r_{\text{non-rel}}) = r_{\text{non-rel}} \left(\frac{t}{t_{\text{non-rel}}} \right)^{2/5} \tag{5.14}$$

In the slow-cooling non relativistic regime, the critical thermal synchrotron frequency and synchrotron luminosity are:

$$\nu_{\text{sync}}(t > t_{\text{non-rel}}) = \nu_{\text{sync,non-rel}} \left(\frac{t}{t_{\text{non-rel}}} \right)^{-3}$$

$$L_{\nu,\text{sync}}(t > t_{\text{non-rel}}) = L_{\nu,\text{sync,non-rel}} \left(\frac{t}{t_{\text{non-rel}}} \right)^{\frac{3}{5}} \tag{5.15}$$

The above description assumes the thermal particles are relativistic, and therefore is valid while $\gamma_{\text{therm}} \gg 1$. For FRB 200428, in the constant medium case the thermal electrons become non-relativistic approximately 1 day post-burst due to the low initial Lorentz factor. By this time the synchrotron cut-off frequency has dropped below the observing frequency for radio wavelengths of interest (see Fig. 5.5). However, extrapolating afterglow lightcurves

beyond this time will require additional consideration of the deep-Newtonian regime similarly to GRB afterglows (e.g. Barniol Duran & Giannios 2015). Finally, we note that similar to SNR evolution, the shock is expected to enter the radiative snow-plough phase at a threshold velocity $v_{\mathrm{sh}} \approx \sqrt{\dfrac{kT}{m_e}} \approx 10^7 \, \mathrm{cm \, s^{-1}}$. For the constant medium case, this occurs for the FRB 200428 at approximately 1000 days post-burst affecting the predicted shock dynamics and lightcurves at very late times, which are not relevant for the observed upper limits.

Using the above, we can make lightcurve predictions through the deceleration and non-relativistic phases for a variety of FRB bursts, as in Margalit et al. (2020b). Following the prescription of Margalit et al. (2020a), we use the observed properties of FRB 200428 & and the coincident X-ray burst to normalize the initial values r_{FRB}, Γ_{FRB}, t_{FRB} given the requirements of the maser and the high-energy burst. Crucially, the peak of the X-ray afterglow at t_{FRB} is normalized to the fluence and peak frequency observed by Insight-HXMT ($\mathcal{F} \approx 7 \times 10^{-7} \, \mathrm{erg \, cm^{-2}}$; $\nu_{\mathrm{peak}} \approx 50$ keV; Li et al. 2021). These parameters are outlined for FRB 200428 from SGR 1935+2154 in Margalit et al. (2020a) (Eqs. 10-13; used in Figs. 5.5 & 5.9).

5.5.2   Radio afterglow

In Fig. 5.5, we show predicted afterglow lightcurves for four frequencies for which radio limits were obtained within a short time after the initial burst (Bailes et al., 2021), assuming a constant medium ($k = 0$). We find that that model-constraining observations could have been attained with the Karl G. Jansky Very Large Array (VLA; Thompson et al. 1980) & European VLBI Network (EVN[8]) at 6 and 1.67 GHz respectively if these instruments were on source before the synchrotron frequency of thermal electrons falls below the observing frequency. However, this would necessitate observations beginning just hours after the initial burst, which is incompatible with typical target-of-opportunity delay for large-scale radio facilities. In this case the obtained LOFAR limits presented in Section 5.3 are not very constraining, primarily attributable to the brightness of the extended emission from SNR G57.2+0.8 at 144 MHz.

5.5.3   Optical afterglow

In Lin et al. (2020), the authors report on *FAST* observations of SGR 1935+2154, as well as a multi-wavelength campaign spanning X-ray, optical and radio observations taken after FRB 200428. Of particular note is a minute-long z-band BOOTES-3 (Castro-Tirado et al., 1999) observation that occurred simultaneously with the FRB 200428. The observation began on the 28th April 2020 at 14:34:24.00 (Extended Data Table 1; Lin et al. 2020), concluding a minute later and setting an upper limit of 17.9 mag. The authors revise this to just 11.7 mag when corrected for dust extinction of 6.2 mag, corresponding to a flux density of approximately 75 mJy. The peak of the X-ray burst coincident with the FRB 200428 occurred after the optical observations began (Mereghetti et al., 2020; Ridnaia et al., 2021), mean-

---

[8] https://www.evlbi.org/
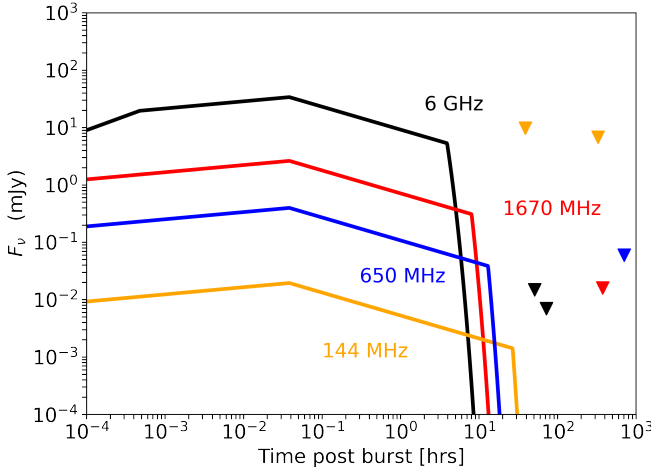
Figure 5.5: Radio afterglow lightcurves following the FRB from SGR 1935+2154, following the prescription of Margalit et al. (2020a) as discussed in the text. We show those frequencies with the most stringent and earliest radio observations (Bailes et al., 2021), including the LOFAR limits we present in this work. The lack of non-thermal particles leads to a steep decline in all lightcurves after just hours as the synchrotron frequency drops below the observing frequency.

ing the optical limit is constraining for the very early time afterglow of the FRB. Lin et al. (2020) discuss the limit with respect to fast optical bursts (FOBs) predicted by Yang et al. (2019) to be produced coincident with FRBs. In Fig. 5.6, we show z-band lightcurves using the above method (see also Fig. 9 in Margalit et al. 2020a), and note that the BOOTES-3 upper limit significantly constrains the FRB afterglow. We assume that the flux limit scales as $F_{\mathrm{lim}} \propto (T_{\mathrm{obs}})^{-1/2}$ and that limits could be placed 1 second after the FRB and the start of the observations. We note that there are uncertainties with extrapolating the upper limit to the start time of the observation in this manner. Even without such extrapolation, the reported data strongly suggests that the predicted afterglow of the maser shock model in a uniform medium presented in Margalit et al. (2020a) is not compatible with the observed upper limit.

5.5.3.1 Wind-like case

One way in which the maser shock model could circumvent the optical upper limit is to invoke a more complex, non-uniform environment. In this subsection, we consider the FRB 200428 afterglow shock propagating into a wind-like ($k = 2$) medium at early times. To correct the initial values of Γ_{FRB} & r_{FRB} we refer to the wind-like case in Section 2.2.3 of Metzger et al. (2019).

$$\Gamma_{\mathrm{FRB}} = 2.8 \, E_{\mathrm{flare}}^{1/4} \, \dot{M}_{19}^{-1/4} \, \beta_{\mathrm{W}}^{1/2} \, \delta t^{1/2} \tag{5.16}$$
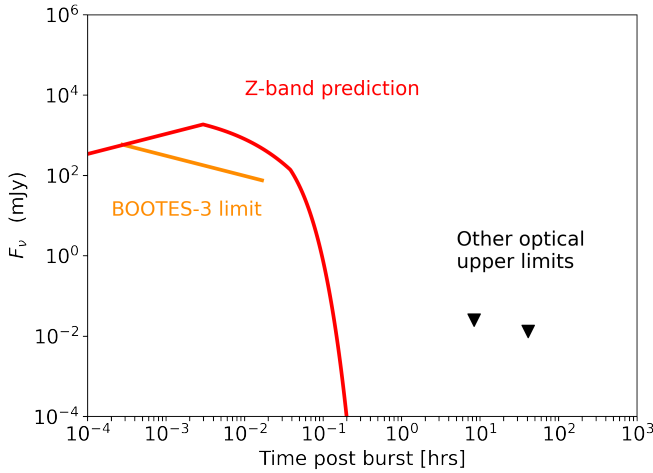
Figure 5.6: We show in red the z-band lightcurve following the FRB from SGR 1935+2154, following the prescription of Margalit et al. (2020a). In orange, the span of the observation taken by BOOTES-3 telescope (after 1 second on source), and in black we include additional optical upper limits by BOOTES-2 and LCOGT presented in Lin et al. (2020). The peak of the predicted flux is approximately one order of magnitude above the extinction-corrected limit set by the BOOTES-3 observation.

$$r_{\mathrm{FRB}} = 1.5 \times 10^9 \text{ cm } E_{\mathrm{flare}}^{1/2} \dot{M}_{19}^{-1/2} \beta_{\mathrm{W}}^{1/2} \delta t^{1/2} \tag{5.17}$$

Where E_{flare} is the total energy of the flare, $\dot{M}$ is the mass injection rate in units of grams per second, and $\beta_{\mathrm{W}} = v_{\mathrm{w}}/c$ is the time-averaged magnetar wind velocity divided by the speed of light. We note that the Lorentz factor required to explain the low-luminosity X-ray flare is relatively low, challenging the implicit assumption required for maser emission that the flare is initially ultra-relativistic. As a lower limit to the flare energy E_{flare}, we adopt the X-ray luminosity of the coincident flare so that $E_{\mathrm{flare}} = 7 \times 10^{39}$ erg. We also consider a range of values for the unknown mass injection rate for this source: $\dot{M} = 10^{17-21}$ g s^{-1}. Values of $\dot{M} = 10^{19-21}$ g s^{-1} have been shown to be consistent with the persistent radio nebula and rotation measure of FRBs from FRB 121102 (Margalit & Metzger, 2018). However, we also consider values $\dot{M} < 10^{19}$ g s^{-1} due to the lack of any persistent radio nebula at the location of SGR 1935+2154 in Section 5.3, and the fact that this source does not appear to be a prolific FRB emitter. In the non-relativistic regime, we use the Sedov-Taylor expansion solution corrected for wind-like media such that $R \propto t^{2/3}$.

In Fig. 5.7 we show the z-band predictions for the wind-like medium case, considering a range of values for $\dot{M}$. We also show the flux limits obtained by BOOTES-3, again assuming that the flux limit sensitivity scales as $T_{\mathrm{obs}}^{-1/2}$ from one second after the start of the observation. We find that the optical limits are consistent with scenarios in which $\dot{M} > 10^{19}$ g s^{-1}, but caution that a more detailed analysis of the earliest second of the optical dataset may
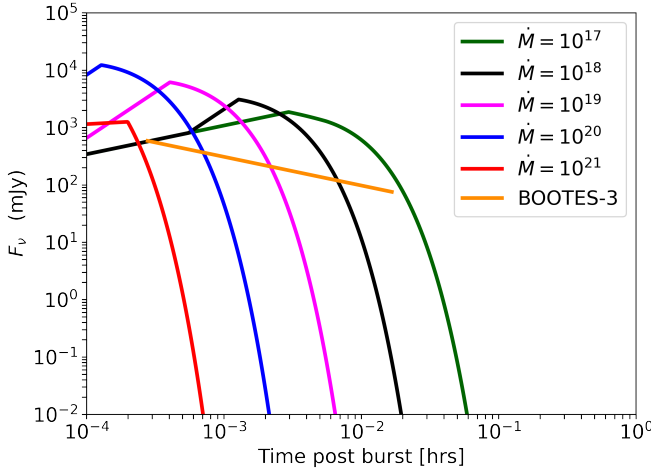
Figure 5.7: Afterglow z-band lightcurves the wind-like environment case for various values of the mass injection rate $\dot{M}$. The flux sensitivity of the BOOTES-3 limit is assumed to scale as $T_{\mathrm{obs}}^{-1/2}$ and we show only limits from one second after the start of the observation. This appears to rule out the most reasonable values of the mass injection rate, however extrapolation of the observations to the time of the FRB may completely rule out the maser shock model of FRB 200428.

rule out all values of $\dot{M} < 10^{21}$ g s^{-1}. Finally, we note that $n \propto R^{-k}$ where $k > 2$ might be expected during the early-time deceleration phase at the time of the BOOTES-3 observation. This is because the charge density of the magnetar's magnetosphere (which has a radial dependence of $k \approx 3$) likely contributes to the local density at $r \approx 10^9$ cm. Estimated in terms of the Goldreich-Julian density (Goldreich & Julian, 1969), the contribution is:

$$n_{\mathrm{GJ}}(r_{\mathrm{FRB}}) \approx \frac{2B_s}{cqP}\left(\frac{R_{\mathrm{NS}}}{R}\right)^{-3} \approx 10^4 \ \mathrm{cm}^{-3} \ B_{s,14} \ P_0^{-1} \tag{5.18}$$

This is comparable to the required value of $n_{\mathrm{ext}} = 4 \times 10^4 \ \mathrm{cm}^{-3}$ in the maser shock model of FRB 2000428 in Eq. 12 of Margalit et al. (2020a), therefore considering variable values of k as a function of r may be required for a more accurate description of the afterglow.

5.5.4 Prospects of radio afterglow detection for the next Galactic FRB

As aforementioned, the lower limit to the radio luminosity of the Galactic FRB 200428 from SGR 1935+2154 was approximately 4-5 orders of magnitude less than typical FRB luminosities. In this subsection, we discuss strategies with which to detect an afterglow for a future Galactic FRB.
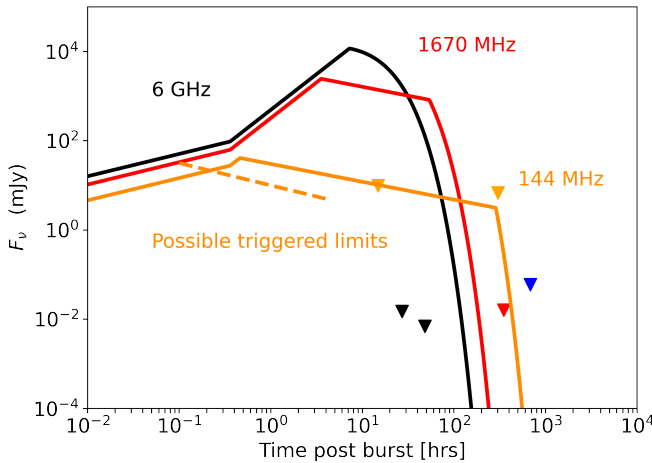
Figure 5.8: Radio afterglow predictions for a typical luminosity FRB from SGR 1935+2154, at frequencies for which early upper limits were obtained for FRB 200428. We include the expected sensitivity from triggered observations with low-frequency radio telescopes that have rapid response capabilities, such as LOFAR or the Murchison Wide Array (MWA; Tingay et al. 2013). We assume a conservative 5 mJy sensitivity for a 4 hr integration at 144 MHz, and that sensitivity increases as $\sqrt{T}$ where T is the observation time (dashed orange line). The observations are presumed to begin 6 minutes after the burst, longer than LOFAR's current rapid response capability. Inverted triangles correspond to radio upper limits at different frequencies from Bailes et al. (2021) as in Fig 5.5.

A bright FRB occurring within the Galaxy could be detected by all-sky radio telescopes such as STARE-2[9] or AARTFAAC (Prasad et al., 2016), or in the side-lobes of smaller field-of-view radio telescopes. Furthermore, the prompt X-ray component of the afterglow (or coincident magnetar X-ray burst) will be very bright and possibly detected by wide-field gamma-ray instruments such as *Fermi-GBM*, or other X-ray instruments as in the case of the burst from SGR 1935+2154.

In Fig. 5.8, we present 6 GHz, 1.67 GHz and 144 MHz afterglow lightcurves for a 'typical' luminosity ($E_{\rm flare} = 10^{43}$ erg) FRB from within our Galaxy, along with obtained radio limits for the SGR 1934+2154. The afterglow in this Figure is calculated using the reference values of $r_{\rm FRB}$, $\Gamma_{\rm FRB}$, $t_{\rm FRB}$ & $\nu_{\rm sync,dec}$ for a typical FRB described in Eqs. 30-32, 57 in Metzger et al. (2019). We scale the early X-ray afterglow fluence appropriately such that the $\mathcal{F}_{\nu,\rm sync,max} \approx E_{\rm flare}/(4\pi D^2)$. We find that of the radio limits attained after the 2020 burst, only the earliest LOFAR & VLA limits can constrain the model in its current form. We note that for this brighter burst, the condition that $\gamma_{\rm therm} > 1$ as required by the afterglow model holds until 1000 hrs post-burst, i.e. the entire time of interest for the radio afterglow.

We also show in Fig. 5.8 plausible flux limits that could have been attained if radio telescopes capable of rapid automated response such as LOFAR (van Haarlem et al., 2013; Rowlinson

---

[9]STARE-2 is now decommissioned, but a successor instrument to the project is planned: Connor et al. (2021)

et al., 2022) and MWA (Tremblay et al., 2015; Hancock et al., 2019; Anderson et al., 2021b) were triggered on the initial burst and were on source within 10 minutes. We have assumed a 5 mJy flux limit after 4 hr observation, where the flux limit scales as $F_{\lim} \propto (T_{\mathrm{obs}})^{-1/2}$ as generally expected, unless the flux threshold is limited by poor u-v coverage for very short integration times. If we are fortunate enough to observe a bonafide FRB from within our Galaxy, rapid optical & radio observations on minute to day timescales will be crucial to observe the afterglow and verify or falsify the maser shock model of FRBs. Such observations are only possible if the FRB event is reported in a timely manner on networks that distribute astronomical alerts rapidly (such as GCN Barthelmy et al. 1998 or VOEvent Williams & Seaman 2006 networks), and radio telescopes have programs in which observations can be interrupted for rapid or automatic repointing.

5.5.5 Non-thermal radio afterglows

Shock acceleration of particles resulting in non-thermal distributions and radiation occurs almost ubiquitously in high energy astrophysical transients such as supernovae remnants (Yuan et al., 2011; Ackermann et al., 2013), gamma-ray bursts (Waxman, 1997), active galactic nuclei (Blandford & Königl, 1979) and X-ray binary jets (Markoff et al., 2001). However, particle-in-cell (PIC) simulations of relativistic, magnetized shocks suggest that particle acceleration in shocks does not occur very efficiently (Sironi & Spitkovsky, 2009; Sironi et al., 2015a). As relativistic shocks sweep up organised magnetic field lines, they are compressed into the downstream shocked medium. As compression occurs, the angle between the magnetic field lines and the shock velocity θ increases, such that they are quasi-perpendicular $\theta \approx 90$ deg. PIC simulations show no significant self-generated turbulence or magnetic field from particles in relativistic magnetized shocks (Sironi & Spitkovsky, 2011), and as such the particles are forced to slide along the background magnetic field lines. As these field lines run perpendicular to the shock velocity, particles do not escape the shock and therefore do not undergo repeated shock crossings required for Fermi-like shock acceleration. This is quantified in Sironi & Spitkovsky (2009), where the authors define a critical angle θ_{crit}, such that if $\theta > \theta_{\mathrm{crit}}$, particles would have to propagate at greater than the speed of light in order to outrun the shock and undergo multiple shock crossings as required for non-thermal acceleration. For this reason, the FRB afterglow model presented in Metzger et al. (2019); Margalit et al. (2020a) assumes purely thermal radiation, nor are non-thermal particles included in Figs. 5.5, 5.6, 5.7 or 5.8.

As the FRB-initiating shock wave progresses it decelerates to smaller bulk Lorentz factors and propagates into regions of lower magnetic field strength (Eqs. 5.5 & 5.6). The typical magnetization and Lorentz factor values assumed in simulations of relativistic, magnetized shocks are $\sigma > 0.1$ and $\Gamma > 10$. For the SGR 1935+2154 burst, the afterglow model in Margalit et al. (2020a) suggests the shock enters a non-relativistic Sedov-Taylor phase at $t_{\mathrm{non-rel}} \approx 45$ seconds via Eq. 5.11. This is exceptionally early due to the low-luminosity of this FRB: $t_{\mathrm{non-rel}}$ will be larger by a factor of approximately 100 for a bright FRB, using the shock values from Margalit et al. (2020b), corresponding to a time $t_{\mathrm{non-rel}} \approx 1.5$ hours.

5

We suggest that in this non-relativistic phase, particles are able to undergo multiple shock crossing as has been observed in magnetized shocks of supernovae remnants.

To model the non-thermal radiation in the Sedov-Taylor phase, we assume 10% of the total (constant) energy of the shock $E_{\mathrm{sh}} = \frac{4}{3}\pi R_{\mathrm{sh}}^3 n_{\mathrm{ext}} m_{\mathrm{p}} v_{\mathrm{sh}}^2 \propto t^0$ is available for non-thermal particle acceleration, as is canonically expected for cosmic ray acceleration in SNRs (e.g. Strong et al. 2007). We further assume an equipartition in energy between hadronic and leptonic acceleration. For this calculation we assume a uniform density medium throughout such that $n_{\mathrm{ext}} = n_{\mathrm{FRB}}$, noting that if the constant density does not extend to such radii, the non-thermal radiation would be lower than predicted here. Non-thermal radiation strongly depends on the magnetic field at the shock. However, in the non-relativistic regime the shock's magnetic field strength is uncertain due to the unknown magnetization of the magnetosphere-ISM transition medium, and possible amplification of the compressed magnetic field due to non-resonant Bell instability (Vink & Laming, 2003; Bell, 2004). We parameterize the magnetic field in terms of a fraction of the thermal energy density (i.e. Eq. 5.6) and the shock-amplified ISM value, such that:

$$B = \max\left(\sqrt{64\pi\sigma\beta^2 m_p c^2 n_{\mathrm{ext}}} \ , \ \chi_{\mathrm{sh}} B_{\mathrm{ISM}} \right) \tag{5.19}$$

Where $\chi_{\mathrm{sh}} \approx 4$ is the shock compression ratio, the magnetization $\sigma = 0.1 - 1$ (Metzger et al., 2019), β is the velocity of the blast-wave in units of the speed of light, and we assume $B_{\mathrm{ISM}} \approx 3 \ \mu$G. The minimum electron energy can be expressed in terms of the thermal particle energy:

$$E_{\mathrm{min}} = \epsilon_{\mathrm{e}} \frac{(p-2)}{2(p-1)} \frac{m_{\mathrm{p}}\beta^2 c^2}{m_{\mathrm{e}}} + m_e c^2 \tag{5.20}$$

Where $\epsilon_{\mathrm{e}} = 0.05$ is the fraction of shock energy (i.e. half of 10% of the total energy due to equipartition) that goes into accelerating electrons and p is the slope of the power law distribution of shock-acceleration electrons which we assume to be $p = 2.2$ (Sironi & Giannios, 2013). The spectral luminosity in the slow cooling regime relevant for the radio afterglow is therefore:

$$L_\nu \propto \frac{K}{p+1}\nu^{-(p-1)/2}B^{(p+1)/2} \tag{5.21}$$

where $K = E_{\mathrm{sh}}\epsilon_{\mathrm{e}}(p-2)E_{\mathrm{min}}^{p-2}$ is the normalization factor of the non-thermal electron distribution. We note that exponential suppression of non-thermal particle radiation is assumed for times $t < t_{\mathrm{non-rel}}$, since we do not expect shock acceleration at these times (see above). We treat synchrotron self-absorption using Eq. 5.10, replacing γ_{therm} with the Lorentz factor for which the critical synchrotron frequency is the observing frequency ν.

In Fig. 5.9, we show the predicted thermal (dashed) and non-thermal (solid) afterglow lightcurves for two observing frequencies. For FRB 200428, the weak burst means the afterglow is relatively dim, and does not challenge the radio upper limits previously discussed. However, we note that particularly at low frequencies the non-thermal radiation could contribute to the overall flux shortly before the thermal synchrotron cut-off. In Fig. 5.10, we
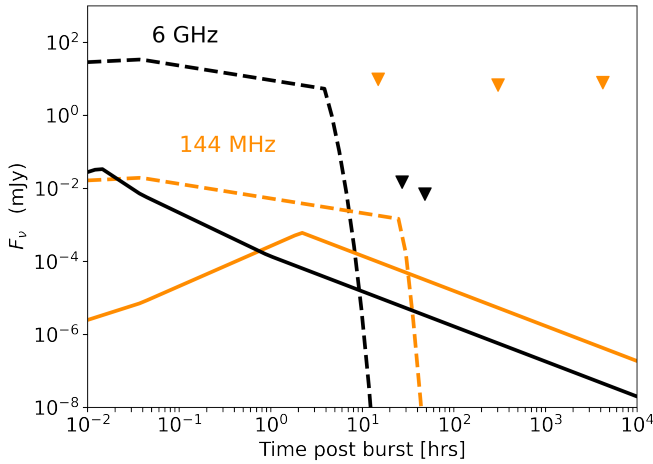
Figure 5.9: Dotted and solid lines denote the thermal and non-thermal components respectively to the afterglow associated with the FRB from SGR 1935+2154, as described in the text. The major break denotes the time at which the emission becomes optically thin. The non-thermal afterglow contributes most significantly for lower frequencies and at later times, near the thermal synchrotron cut-off. For all times of interest, the shock magnetic field strength is always greater than the amplified ISM value. Black and orange inverted triangles correspond radio upper limits taken after FRB 200428 by VLA and LOFAR at 6 GHz and 144 MHz respectively.

show a similar plot for a bright FRB for two distances, corresponding to Galactic or nearby extragalactic FRBs. For a bright Galactic FRB, non-thermal radio emission could be detectable up to years after the initial burst. Long-term monitoring of such a source would provide opportunities for detailed modelling of the afterglow, contributing to our understanding of shocks more generally. However, non-thermal radio emission from even a nearby extragalactic FRB is not likely to be bright enough to probe.

The closest repeating FRB resides at a distance of $D \approx 3.6$ Mpc in M81 (Bhardwaj et al., 2021; Kirsten et al., 2022). Kirsten et al. (2022) obtained deep persistent flux constraints (6.5μJy at 1.5 GHz) of the source before their reported FRBs, but 1-6 months after previously reported bursts by Bhardwaj et al. (2021). Unfortunately, the low luminosity of the observed FRBs mean that predicted afterglow emission is not observable.

5.6 Conclusions

In this work we have presented results from LOFAR imaging observations of SGR 1935+2154, following the Galactic magnetar burst FRB 200428. We discuss interpretations of the LOFAR results, stressing the importance of simultaneous X-ray/radio observations of active magnetars to constrain both magnetospheric and flare/shock models of FRBs. We also make recommendations of rapid observations on minute-day timescales following Galactic or nearby

5
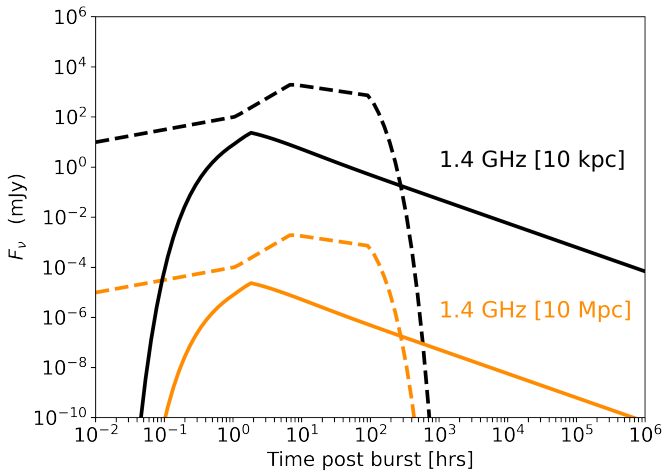
Figure 5.10: Dotted and solid lines denote the thermal and non-thermal components respectively to the afterglow after a typical luminosity FRB, where $\nu_{\rm obs} = 1.4\,{\rm GHz}$. We show two distances representative of a bright Galactic burst (black) and a nearby extragalactic FRB. The non-thermal emission is relatively weak, but allows for late-times monitoring of the lightcurve in the Galactic FRB case. The thermal radio afterglow is tentatively observable ($> \mu{\rm Jy}$) in the hours following a close extragalactic FRB. We assume exponential suppression of non-thermal acceleration before the shock becomes non-relativistic.

extragalactic FRBs. We have analysed optical and radio early time upper limits in the context of models of FRB 200428 that predict a multi-wavelength afterglow, namely the synchrotron maser shock model. We have found that early BOOTES-3 optical observations appear to rule out simple versions of this model, but invoking a wind-like environment close to the FRB emission zone may mitigate the constraints. We also suggest that shock accelerated particle populations should be considered at late times when the shock is non-relativistic, however we find that such non-thermal emission is too faint to be observable, except for future Galactic FRBs.

Acknowledgements

5

Data Availability

The LOFAR visibility data are publicly available at the LOFAR Long Term Archive (https://lta.lofar.eu/) under the relevant project codes. A basic reproduction package providing the scripts and data required to reproduce the figures and tables of this paper will be available upon publication.

Bibliography

Aartsen, M. G., Abbasi, R., Abdou, Y., et al. 2013, *First Observation of PeV-Energy Neutrinos with IceCube*, Physical Review Letters, 111, 021103

Aartsen, M. G., Abbasi, R., Ackermann, M., et al. 2021, *IceCube-Gen2: the window to the extreme Universe*, Journal of Physics G Nuclear Physics, 48, 060501

Aartsen, M. G., Ackermann, M., Adams, J., et al. 2019, *Search for Sources of Astrophysical Neutrinos Using Seven Years of IceCube Cascade Events*, arXiv e-prints, arXiv:1907.06714

Aartsen, M. G., Ackermann, M., Adams, J., et al. 2014, *Observation of High-Energy Astrophysical Neutrinos in Three Years of IceCube Data*, Phys. Rev. Lett., 113, 101101

Aartsen, M. G., Ackermann, M., Adams, J., et al. 2017, *Constraints on Galactic Neutrino Emission with Seven Years of IceCube Data*, ApJ, 849, 67

Abbott, B. P., Abbott, R., Abbott, T. D., et al. 2016, *Observation of Gravitational Waves from a Binary Black Hole Merger*, Phys. Rev. Lett., 116, 061102

Abbott, B. P., Abbott, R., Abbott, T. D., et al. 2017a, *Exploring the sensitivity of next generation gravitational wave detectors*, Classical and Quantum Gravity, 34, 044001

Abbott, B. P., Abbott, R., Abbott, T. D., et al. 2020, *Prospects for observing and localizing gravitational-wave transients with Advanced LIGO, Advanced Virgo and KAGRA*, Living Reviews in Relativity, 23, 3

Abbott, B. P., Abbott, R., Abbott, T. D., et al. 2017b, *GW170817: Observation of Gravitational Waves from a Binary Neutron Star Inspiral*, Phys. Rev. Lett., 119, 161101

Abbott, B. P., Abbott, R., Abbott, T. D., et al. 2017c, *Gravitational Waves and Gamma-Rays from a Binary Neutron Star Merger: GW170817 and GRB 170817A*, ApJ, 848, L13

Abbott, B. P., Abbott, R., Abbott, T. D., et al. 2017d, *Multi-messenger Observations of a Binary Neutron Star Merger*, ApJ, 848, L12

Abbott, B. P., Abbott, R., Abbott, T. D., et al. 2017e, *A gravitational-wave standard siren measurement of the Hubble constant*, Nature, 551, 85

Abbott, B. P., Abbott, R., Abbott, T. D., et al. 2018, *GW170817: Measurements of Neutron Star Radii and Equation of State*, Phys. Rev. Lett., 121, 161101

Abbott, B. P., Abbott, R., Abbott, T. D., et al. 2019, *Tests of General Relativity with GW170817*, Phys. Rev. Lett., 123, 011102

Abbott, B. P., Abbott, R., Adhikari, R., et al. 2009, *LIGO: the Laser Interferometer Gravitational-Wave Observatory*, Reports on Progress in Physics, 72, 076901

Abbott, R., Abbott, T. D., Abraham, S., et al. 2021, *Observation of Gravitational Waves from Two Neutron Star-Black Hole Coalescences*, ApJ, 915, L5

Abdo, A. A., Ackermann, M., Ajello, M., et al. 2009, *A Population of Gamma-Ray Millisecond Pulsars Seen with the Fermi Large Area Telescope*, Science, 325, 848

Abdo, A. A., Ajello, M., Allafort, A., et al. 2013, *The Second Fermi Large Area Telescope Catalog of Gamma-Ray Pulsars*, ApJS, 208, 17

Abramovici, A., Althouse, W. E., Drever, R. W. P., et al. 1992, *LIGO: The Laser Interferometer Gravitational-Wave Observatory*, Science, 256, 325

Achterberg, A., Gallant, Y. A., Kirk, J. G., & Guthmann, A. W. 2001, *Particle acceleration by ultrarelativistic shocks: theory and simulations*, MNRAS, 328, 393

Ackermann, M., Ajello, M., Allafort, A., et al. 2013, *Detection of the Characteristic Pion-Decay Signature in Supernova Remnants*, Science, 339, 807

Adhikari, R. X., Arai, K., Brooks, A. F., et al. 2020, *A cryogenic silicon interferometer for gravitational-wave detection*, Classical and Quantum Gravity, 37, 165003

Adrián-Martínez, S., Ageron, M., Aharonian, F., et al. 2016, *Letter of intent for KM3NeT 2.0*, Journal of Physics G Nuclear Physics, 43, 084001

Aguilar, M., Alberti, G., Alpat, B., et al. 2013, *First Result from the Alpha Magnetic Spectrometer on the International Space Station: Precision Measurement of the Positron Fraction in Primary Cosmic Rays of 0.5-350 GeV*, Phys. Rev. Lett., 110, 141102

Aharonian, F., Akhperjanian, A. G., Bazer-Bachi, A. R., et al. 2006, *Discovery of very-high-energy □-rays from the Galactic Centre ridge*, Nature, 439, 695

Ahnen, M. L., Ansoldi, S., Antonelli, L. A., et al. 2017a, *MAGIC observations of the microquasar V404 Cygni during the 2015 outburst*, MNRAS, 471, 1688

Ahnen, M. L., Ansoldi, S., Antonelli, L. A., et al. 2017b, *A cut-off in the TeV gamma-ray spectrum of the SNR Cassiopeia A*, MNRAS, 472, 2956

Aker, M., Beglarian, A., Behrens, J., et al. 2021, *First direct neutrino-mass measurement with sub-eV sensitivity*, arXiv e-prints, arXiv:2105.08533

Akiyama, K., Alberdi, A., Alef, W., et al. 2022, *First Sagittarius A* Event Horizon Telescope Results. I. The Shadow of the Supermassive Black Hole in the Center of the Milky Way*, ApJ, 930, L12

Aksulu, M. D., Wijers, R. A. M. J., van Eerten, H. J., & van der Horst, A. J. 2022, *Exploring the GRB population: robust afterglow modelling*, MNRAS, 511, 2848

Albert, A., André, M., Anghinolfi, M., et al. 2018, *Joint Constraints on Galactic Diffuse Neutrino Emission from the ANTARES and IceCube Neutrino Telescopes*, ApJ, 868, L20

Albert, A., André, M., Anton, G., et al. 2017, *Time-dependent search for neutrino emission from X-ray binaries with the ANTARES telescope*, Journal of Cosmology and Astroparticle Physics, 2017, 019

Alexander, K. D., Berger, E., Fong, W., et al. 2017, *The Electromagnetic Counterpart of the Binary Neutron Star Merger LIGO/Virgo GW170817. VI. Radio Constraints on a Relativistic Jet and Predictions for Late-time Emission from the Kilonova Ejecta*, ApJ, 848, L21

Amaro-Seoane, P., Audley, H., Babak, S., et al. 2017, *Laser Interferometer Space Antenna*, arXiv e-prints, arXiv:1702.00786

Ambrosi, E., Barthelmy, S. D., D'Ai, A., et al. 2019, *Trigger 933083: Swift detection of SGR 1935+2154*, GRB Coordinates Network, 26153, 1

Amsler, C., Doser, M., Antonelli, M., et al. 2008, *Review of Particle Physics*, Physics Letters B, 667, 1 , review of Particle Physics

Anderson, G. E., Bell, M. E., Stevens, J., et al. 2021a, *Rapid-response radio observations of short GRB 181123B with the Australia Telescope Compact Array*, MNRAS, 503, 4372

Anderson, G. E., Gaensler, B. M., Slane, P. O., et al. 2012, *Multi-wavelength Observations of the Radio Magnetar PSR J1622-4950 and Discovery of Its Possibly Associated Supernova Remnant*, ApJ, 751, 53

Anderson, G. E., Hancock, P. J., Rowlinson, A., et al. 2021b, *Murchison Widefield Array rapid-response observations of the short GRB 180805A*, PASA, 38, e026

Anderson, G. E., Staley, T. D., van der Horst, A. J., et al. 2018, *The Arcminute Microkelvin Imager catalogue of gamma-ray burst afterglows at 15.7 GHz*, MNRAS, 473, 1512

Andreoni, I., Anand, S., Bianco, F. B., et al. 2019, *A Strategy for LSST to Unveil a Population of Kilonovae without Gravitational-wave Triggers*, PASP, 131, 068004

Andreoni, I., Coughlin, M. W., Kool, E. C., et al. 2021a, *Fast-transient Searches in Real Time with ZTFReST: Identification of Three Optically Discovered Gamma-Ray Burst Afterglows and New Constraints on the Kilonova Rate*, ApJ, 918, 63

Andreoni, I., Lu, W., Smith, R. M., et al. 2020, *Zwicky Transient Facility Constraints on the Optical Emission from the Nearby Repeating FRB 180916.J0158+65*, ApJ, 896, L2

B

Andreoni, I., Roestel, J. v., Graham, M., & Sollerman, J. 2021b, *ZTF optical observations of FRB 20200120E in M81*, The Astronomer's Telegram, 14666, 1

Archibald, R. F., Burgay, M., Lyutikov, M., et al. 2017, *Magnetar-like X-Ray Bursts Suppress Pulsar Radio Emission*, ApJ, 849, L20

Arons, J. & Barnard, J. J. 1986, *Wave Propagation in Pulsar Magnetospheres: Dispersion Relations and Normal Modes of Plasmas in Superstrong Magnetic Fields*, ApJ, 302, 120

Arzoumanian, Z., Baker, P. T., Blumer, H., et al. 2020, *The NANOGrav 12.5 yr Data Set: Search for an Isotropic Stochastic Gravitational-wave Background*, ApJ, 905, L34

Arzoumanian, Z., Chernoff, D. F., & Cordes, J. M. 2002, *The Velocity Distribution of Isolated Radio Pulsars*, ApJ, 568, 289

Axford, W. I., Leer, E., & Skadron, G. 1977, *The Acceleration of Cosmic Rays by Shock Waves*, in International Cosmic Ray Conference, Vol. 11, International Cosmic Ray Conference, 132

Baade, W. & Zwicky, F. 1934, *On Super-novae*, Proceedings of the National Academy of Science, 20, 254

Bailes, M., Bassa, C. G., Bernardi, G., et al. 2021, *Multifrequency observations of SGR J1935+2154*, MNRAS, 503, 5367

Bak, P., Tang, C., & Wiesenfeld, K. 1987, *Self-organized criticality: An explanation of the 1/f noise*, Phys. Rev. Lett., 59, 381

Bannister, K. W., Deller, A. T., Phillips, C., et al. 2019, *A single fast radio burst localized to a massive galaxy at cosmological distance*, Science, 365, 565

Bannister, K. W., Murphy, T., Gaensler, B. M., & Reynolds, J. E. 2012, *Limits on Prompt, Dispersed Radio Pulses from Gamma-Ray Bursts*, ApJ, 757, 38

Baring, M. G., Wadiasingh, Z., & Gonthier, P. L. 2011, *Cooling Rates for Relativistic Electrons Undergoing Compton Scattering in Strong Magnetic Fields*, ApJ, 733, 61

Barniol Duran, R. & Giannios, D. 2015, *Radio rebrightening of the GRB afterglow by the accompanying supernova*, MNRAS, 454, 1711

Barthelmy, S. D., Butterworth, P., Cline, T. L., et al. 1998, *The GRB coordinates network (GCN): A status report*, in American Institute of Physics Conference Series, Vol. 428, Gamma-Ray Bursts, 4th Hunstville Symposium, ed. C. A. Meegan, R. D. Preece, & T. M. Koshut, 99–103

Bednarz, J. & Ostrowski, M. 1998, *Energy Spectra of Cosmic Rays Accelerated at Ultrarelativistic Shock Waves*, Phys. Rev. Lett., 80, 3911

Begelman, M. C., Blandford, R. D., & Rees, M. J. 1984, *Theory of extragalactic radio sources*, Reviews of Modern Physics, 56, 255

Belczynski, K., Kalogera, V., Rasio, F. A., et al. 2008, *Compact Object Modeling with the Star-Track Population Synthesis Code*, ApJS, 174, 223

Bell, A. R. 1978a, *The acceleration of cosmic rays in shock fronts - II.*, MNRAS, 182, 443

Bell, A. R. 1978b, *The acceleration of cosmic rays in shock fronts. I*, MNRAS, 182, 147

Bell, A. R. 2004, *Turbulent amplification of magnetic field and diffusive shock acceleration of cosmic rays*, MNRAS, 353, 550

Bellm, E. C., Kulkarni, S. R., Graham, M. J., et al. 2019, *The Zwicky Transient Facility: System Overview, Performance, and First Results*, PASP, 131, 018002

Beloborodov, A. M. 2017, *A Flaring Magnetar in FRB 121102?*, ApJ, 843, L26

Beloborodov, A. M. 2020, *Blast Waves from Magnetar Flares and Fast Radio Bursts*, ApJ, 896, 142

Beloborodov, A. M. 2021, *Emission of Magnetar Bursts and Precursors of Neutron Star Mergers*, ApJ, 921, 92

Benford, G. & Buschauer, R. 1977, *Coherent pulsar radio radiation by antenna mechanisms: general theory.*, MNRAS, 179, 189

Beniamini, P., Hotokezaka, K., van der Horst, A., & Kouveliotou, C. 2019, *Formation rates and evolution histories of magnetars*, MNRAS, 487, 1426

Beniamini, P., Wadiasingh, Z., & Metzger, B. D. 2020, *Periodicity in recurrent fast radio bursts and the origin of ultralong period magnetars*, MNRAS, 496, 3390

Berezinsky, V. S., Bulanov, S. V., Dogiel, V. A., & Ptuskin, V. S. 1990, Astrophysics of cosmic rays, ed. V. L. Ginzburg

Berger, E. 2014, *Short-Duration Gamma-Ray Bursts*, ARA&A, 52, 43

Bessel, F. W. 1838, *On the parallax of 61 Cygni*, MNRAS, 4, 152

Bhandari, S., Bannister, K. W., Lenc, E., et al. 2020a, *Limits on Precursor and Afterglow Radio Emission from a Fast Radio Burst in a Star-forming Galaxy*, ApJ, 901, L20

Bhandari, S., Heintz, K. E., Aggarwal, K., et al. 2022, *Characterizing the Fast Radio Burst Host Galaxy Population and its Connection to Transients in the Local and Extragalactic Universe*, AJ, 163, 69

Bhandari, S., Keane, E. F., Barr, E. D., et al. 2018, *The SUrvey for Pulsars and Extragalactic Radio Bursts - II. New FRB discoveries and their follow-up*, MNRAS, 475, 1427

Bhandari, S., Sadler, E. M., Prochaska, J. X., et al. 2020b, *The Host Galaxies and Progenitors of Fast Radio Bursts Localized with the Australian Square Kilometre Array Pathfinder*, ApJ, 895, L37

Bhardwaj, M., Gaensler, B. M., Kaspi, V. M., et al. 2021, *A Nearby Repeating Fast Radio Burst in the Direction of M81*, ApJ, 910, L18

Bhattacharya, D. & van den Heuvel, E. P. J. 1991, *Formation and evolution of binary and millisecond radio pulsars*, Phys. Rep., 203, 1

Bildsten, L. & Cutler, C. 1992, *Tidal Interactions of Inspiraling Compact Binaries*, ApJ, 400, 175

Bilous, A. V., Watts, A. L., Harding, A. K., et al. 2019, *A NICER View of PSR J0030+0451: Evidence for a Global-scale Multipolar Magnetic Field*, ApJ, 887, L23

Bionta, R. M., Blewitt, G., Bratton, C. B., et al. 1987, *Observation of a neutrino burst in coincidence with supernova 1987A in the Large Magellanic Cloud*, Phys. Rev. Lett., 58, 1494

Blandford, R. D. & Königl, A. 1979, *Relativistic jets as compact radio sources.*, ApJ, 232, 34

Blandford, R. D. & McKee, C. F. 1976, *Fluid dynamics of relativistic blast waves*, Physics of Fluids, 19, 1130

Blandford, R. D. & Ostriker, J. P. 1978, *Particle acceleration by astrophysical shocks*, ApJ, 221, L29

Blandford, R. D. & Payne, D. G. 1982, *Hydromagnetic flows from accretion disks and the production of radio jets.*, MNRAS, 199, 883

Blandford, R. D. & Znajek, R. L. 1977, *Electromagnetic extraction of energy from Kerr black holes*, MNRAS, 179, 433

Blasi, P. 2013, *The Origin of Galactic Cosmic Rays*, Astron. Astrophys. Rev., 21, 70

Blinnikov, S. I., Novikov, I. D., Perevodchikova, T. V., & Polnarev, A. G. 1984, *Exploding Neutron Stars in Close Binaries*, Soviet Astronomy Letters, 10, 177

Bochenek, C. D., McKenna, D. L., Belov, K. V., et al. 2020a, *STARE2: Detecting Fast Radio Bursts in the Milky Way*, PASP, 132, 034202

Bochenek, C. D., Ravi, V., Belov, K. V., et al. 2020b, *A fast radio burst associated with a Galactic magnetar*, Nature, 587, 59

Bodaghee, A., Tomsick, J. A., Pottschmidt, K., et al. 2013, *Gamma-Ray Observations of the Microquasars Cygnus X-1, Cygnus X-3, GRS 1915+105, and GX 339-4 with the Fermi Large Area Telescope*, ApJ, 775, 98

Boersma, O. M. & van Leeuwen, J. 2022, *Investigating the detection rates and inference of gravitational-wave and radio emission from black hole neutron star mergers*, arXiv e-prints, arXiv:2202.02181

Bombaci, I. 1996, *The maximum mass of a neutron star.*, A&A, 305, 871

Bordas, P., Bosch-Ramon, V., Paredes, J. M., & Perucho, M. 2009, *Non-thermal emission from microquasar/ISM interaction*, A&A, 497, 325

Bordas, P., Yang, R., Kafexhiu, E., & Aharonian, F. 2015, *Detection of Persistent Gamma-Ray Emission Toward SS433/W50*, The Astrophysical Journal Letters, 807, L8

Borhanian, S. & Sathyaprakash, B. S. 2022, *Listening to the Universe with Next Generation Ground-Based Gravitational-Wave Detectors*, arXiv e-prints, arXiv:2202.11048

Bosch-Ramon, V., Aharonian, F. A., & Paredes, J. M. 2005, *Electromagnetic radiation initiated by hadronic jets from microquasars in the ISM*, A&A, 432, 609

Bosch-Ramon, V., Romero, G. E., & Paredes, J. M. 2006, *A broadband leptonic model for gamma-ray emitting microquasars*, A&A, 447, 263

Braun, R., Bonaldi, A., Bourke, T., Keane, E., & Wagg, J. 2019, *Anticipated Performance of the Square Kilometre Array – Phase 1 (SKA1)*, arXiv e-prints, arXiv:1912.12699

Buitink, S., Corstanje, A., Falcke, H., et al. 2016, *A large light-mass component of cosmic rays at 10^{17}-$10^{17.5}$ electronvolts from radio observations*, Nature, 531, 70

Bulla, M. 2019, *POSSIS: predicting spectra, light curves, and polarization for multidimensional models of supernovae and kilonovae*, MNRAS, 489, 5037

Burbidge, E. M., Burbidge, G. R., Fowler, W. A., & Hoyle, F. 1957, *Synthesis of the Elements in Stars*, Reviews of Modern Physics, 29, 547

Burgay, M., D'Amico, N., Possenti, A., et al. 2003, *An increased estimate of the merger rate of double neutron stars from observations of a highly relativistic system*, Nature, 426, 531

Burns, E., Connaughton, V., Zhang, B.-B., et al. 2016, *Do the Fermi Gamma-Ray Burst Monitor and Swift Burst Alert Telescope see the Same Short Gamma-Ray Bursts?*, ApJ, 818, 110

Burns, E., Svinkin, D., Hurley, K., et al. 2021, *Identification of a Local Sample of Gamma-Ray Bursts Consistent with a Magnetar Giant Flare Origin*, ApJ, 907, L28

Cai, C., Xiong, S., Lin, L., et al. 2022a, *Insight-HXMT dedicated 33-day observation of SGR J1935+2154 II. Burst Spectral Catalog*, arXiv e-prints, arXiv:2204.07369

Cai, C., Xue, W., Li, C., et al. 2022b, *Insight-HXMT dedicated 33-day observation of SGR J1935+2154 I. Burst Catalog*, arXiv e-prints, arXiv:2203.16855

Caleb, M., Heywood, I., Rajwade, K., et al. 2022, *Discovery of a radio-emitting neutron star with an ultra-long spin period of 76 s*, Nature Astronomy

Callister, T., Dowell, J., Kanner, J., et al. 2017, *LIGO/Virgo G298048: LWA radio observations*, GRB Coordinates Network, 21680, 1

B

Camilo, F., Ransom, S. M., Halpern, J. P., et al. 2006, *Transient pulsed radio emission from a magnetar*, Nature, 442, 892

Camilo, F., Reynolds, J., Johnston, S., et al. 2007, *Polarized Radio Emission from the Magnetar XTE J1810-197*, ApJ, 659, L37

Campana, S., de Ugarte Postigo, A., Thoene, C. C., et al. 2014, *Pre-discovery observations of SGR 1935+2154 in Swift archival data.*, GRB Coordinates Network, 16535, 1

Cao, Z., della Volpe, D., Liu, S., et al. 2019, *The Large High Altitude Air Shower Observatory (LHAASO) Science Book (2021 Edition)*, arXiv e-prints, arXiv:1905.02773

Caprioli, D. & Spitkovsky, A. 2014, *Simulations of Ion Acceleration at Non-relativistic Shocks. I. Acceleration Efficiency*, ApJ, 783, 91

Caraveo, P. A. 2014, *Gamma-Ray Pulsar Revolution*, Annual Review of Astronomy and Astrophysics, 52, 211

Carbone, D., Garsden, H., Spreeuw, H., et al. 2018, *PySE: Software for extracting sources from radio images*, Astronomy and Computing, 23, 92

Caron, B., Dominjon, A., Drezen, C., et al. 1997, *The VIRGO Interferometer For Gravitational Wave Detection*, Nuclear Physics B Proceedings Supplements, 54, 167

Castro-Tirado, A. J., Soldán, J., Bernas, M., et al. 1999, *The Burst Observer and Optical Transient Exploring System (BOOTES)*, A&AS, 138, 583

Chandrasekhar, S. 1931, *The Maximum Mass of Ideal White Dwarfs*, ApJ, 74, 81

Charisi, M., Márka, S., & Bartos, I. 2015, *Catalogue of isolated emission episodes in gamma-ray bursts from Fermi, Swift and BATSE*, MNRAS, 448, 2624

Chatterjee, S., Law, C. J., Wharton, R. S., et al. 2017, *A direct localization of a fast radio burst and its host*, Nature, 541, 58

Chawla, P., Kaspi, V. M., Ransom, S. M., et al. 2022, *Modeling Fast Radio Burst Dispersion and Scattering Properties in the First CHIME/FRB Catalog*, ApJ, 927, 35

Chen, K. & Ruderman, M. 1993, *Pulsar Death Lines and Death Valley*, ApJ, 402, 264

Cheng, A. F. & Ruderman, M. A. 1977, *Bunching mechanism for coherent curvature radiation in pulsar magnetospheres.*, ApJ, 212, 800

Cheng, B., Epstein, R. I., Guyer, R. A., & Young, A. C. 1996, *Earthquake-like behaviour of soft γ-ray repeaters*, Nature, 382, 518

Cheng, K. S., Ho, C., & Ruderman, M. 1986, *Energetic Radiation from Rapidly Spinning Pulsars. I. Outer Magnetosphere Gaps*, ApJ, 300, 500

Cheng, K. S. & Zhang, J. L. 1996, *General Radiation Formulae for a Relativistic Charged Particle Moving in Curved Magnetic Field Lines: The Synchrocurvature Radiation Mechanism*, ApJ, 463, 271

Cherenkov Telescope Array Consortium, Acharya, B. S., Agudo, I., et al. 2019, Science with the Cherenkov Telescope Array

Chevalier, R. A. 1998, *Synchrotron Self-Absorption in Radio Supernovae*, ApJ, 499, 810

CHIME/FRB Collaboration, Amiri, M., Andersen, B. C., et al. 2021, *The First CHIME/FRB Fast Radio Burst Catalog*, ApJS, 257, 59

Chime/Frb Collaboration, Amiri, M., Andersen, B. C., et al. 2020, *Periodic activity from a fast radio burst source*, Nature, 582, 351

CHIME/FRB Collaboration, Amiri, M., Bandura, K., et al. 2018, *The CHIME Fast Radio Burst Project: System Overview*, ApJ, 863, 48

CHIME/FRB Collaboration, Andersen, B. C., Bandura, K. M., et al. 2020, *A bright millisecond-duration radio burst from a Galactic magnetar*, Nature, 587, 54

Chu, Q., Howell, E. J., Rowlinson, A., et al. 2016, *Capturing the electromagnetic counterparts of binary neutron star mergers through low-latency gravitational wave triggers*, MNRAS, 459, 121

Clark, J. P. A. & Eardley, D. M. 1977, *Evolution of close neutron star binaries.*, ApJ, 215, 311

Connor, L., Shila, K. A., Kulkarni, S. R., et al. 2021, *Galactic Radio Explorer: An All-sky Monitor for Bright Radio Bursts*, PASP, 133, 075001

Cooper, A. J. & Wijers, R. A. M. J. 2021, *Coherent curvature radiation: maximum luminosity and high-energy emission*, MNRAS, 508, L32

Coppin, P., de Vries, K. D., & van Eijndhoven, N. 2020, *Identification of gamma-ray burst precursors in Fermi-GBM bursts*, Phys. Rev. D, 102, 103014

Corbel, S., Fender, R. P., Tzioumis, A. K., et al. 2000, *Coupling of the X-ray and radio emission in the black hole candidate and compact jet source GX 339-4*, A&A, 359, 251

Cordes, J. M. & Lazio, T. J. W. 2002, *NE2001.I. A New Model for the Galactic Distribution of Free Electrons and its Fluctuations*, arXiv e-prints, astro

Cordes, J. M. & Wasserman, I. 2016, *Supergiant pulses from extragalactic neutron stars*, MNRAS, 457, 232

Corral-Santana, J. M., Casares, J., Muñoz-Darias, T., et al. 2016, *BlackCAT: A catalogue of stellar-mass black holes in X-ray transients*, A&A, 587, A61

B

Corsi, A., Lloyd-Ronning, N. M., Carbone, D., et al. 2019, *Astro2020 Science White Paper: Radio Counterparts of Compact Object Mergers in the Era of Gravitational-Wave Astronomy*, arXiv e-prints, arXiv:1903.10589

Cowan, C. L., J., Reines, F., Harrison, F. B., Kruse, H. W., & McGuire, A. D. 1956, *Detection of the Free Neutrino: A Confirmation*, Science, 124, 103

Crumley, P., Ceccobello, C., Connors, R. M. T., & Cavecchi, Y. 2017, *The jet-disk symbiosis without maximal jets: 1D hydrodynamical jets revisited*, A&A, 601, A87

Cummings, J. R., Barthelmy, S. D., Chester, M. M., & Page, K. L. 2014, *Newly discovered SGR 1935+2154: Swift observations*, The Astronomer's Telegram, 6294, 1

Curran, P. A., Coriat, M., Miller-Jones, J. C. A., et al. 2014, *The evolving polarized jet of black hole candidate Swift J1745-26*, MNRAS, 437, 3265

Cutler, C. & Flanagan, É. E. 1994, *Gravitational waves from merging compact binaries: How accurately can one extract the binary's parameters from the inspiral waveform\?*, Phys. Rev. D, 49, 2658

Dai, Z. G., Wang, J. S., Wu, X. F., & Huang, Y. F. 2016, *REPEATING FAST RADIO BURSTS FROM HIGHLY MAGNETIZED PULSARS TRAVELING THROUGH ASTEROID BELTS*, The Astrophysical Journal, 829, 27

Daugherty, J. K. & Harding, A. K. 1982, *Electromagnetic cascades in pulsars.*, ApJ, 252, 337

Daugherty, J. K. & Harding, A. K. 1983, *Pair production in superstrong magnetic fields.*, ApJ, 273, 761

Daugherty, J. K. & Harding, A. K. 1986, *Compton Scattering in Strong Magnetic Fields*, ApJ, 309, 362

Daugherty, J. K. & Harding, A. K. 1996, *Gamma-Ray Pulsars: Emission from Extended Polar CAP Cascades*, ApJ, 458, 278

Davis, R., Harmer, D. S., & Hoffman, K. C. 1968, *Search for Neutrinos from the Sun*, Phys. Rev. Lett., 20, 1205

Day, C. K., Deller, A. T., James, C. W., et al. 2021, *Astrometric accuracy of snapshot fast radio burst localisations with ASKAP*, PASA, 38, e050

DeLaunay, J. & Tohuvavohu, A. 2021, *Harvesting BAT-GUANO with NITRATES (Non-Imaging Transient Reconstruction And TEmporal Search): Detecting and localizing the faintest GRBs with a likelihood framework*, arXiv e-prints, arXiv:2111.01769

Dewdney, P. E., Hall, P. J., Schilizzi, R. T., & Lazio, T. J. L. W. 2009, *The Square Kilometre Array*, IEEE Proceedings, 97, 1482

Dewi, J. D. M. & Pols, O. R. 2003, *The late stages of evolution of helium star-neutron star binaries and the formation of double neutron star systems*, MNRAS, 344, 629

Díaz Trigo, M., Migliari, S., Miller-Jones, J. C. A., & Guainazzi, M. 2014, *XMM-Newton observations reveal the disappearance of the wind in 4U 1630-47*, A&A, 571, A76

Díaz Trigo, M., Miller-Jones, J. C. A., Migliari, S., Broderick, J. W., & Tzioumis, T. 2013, *Baryons in the relativistic jets of the stellar-mass black-hole candidate 4U1630-47*, Nature, 504, 260

Dietrich, T., Samajdar, A., Khan, S., et al. 2019, *Improving the NRTidal model for binary neutron star systems*, Phys. Rev. D, 100, 044003

Distefano, C., Guetta, D., Waxman, E., & Levinson, A. 2002, *Neutrino Flux Predictions for Known Galactic Microquasars*, ApJ, 575, 378

Dobie, D., Kaplan, D. L., Murphy, T., et al. 2018, *A Turnover in the Radio Light Curve of GW170817*, ApJ, 858, L15

Dobie, D., Murphy, T., Kaplan, D. L., et al. 2021, *Radio afterglows from compact binary coalescences: prospects for next-generation telescopes*, MNRAS, 505, 2647

Dogiel, V., Chernyshov, D., Koyama, K., Nobukawa, M., & Cheng, K.-S. 2011, *K-Shell Emission of Neutral Iron Line from Sagittarius B2 Excited by Subrelativistic Protons*, PASJ, 63, 535

Drury, L. O. & Voelk, J. H. 1981, *Hydromagnetic shock structure in the presence of cosmic rays*, ApJ, 248, 344

Duchêne, G. & Kraus, A. 2013, *Stellar Multiplicity*, ARA&A, 51, 269

Duncan, R. C. & Thompson, C. 1992, *Formation of Very Strongly Magnetized Neutron Stars: Implications for Gamma-Ray Bursts*, ApJ, 392, L9

Eggleton, P. P. 1983, *Aproximations to the radii of Roche lobes.*, ApJ, 268, 368

Eichler, D., Livio, M., Piran, T., & Schramm, D. N. 1989, *Nucleosynthesis, neutrino bursts and γ-rays from coalescing neutron stars*, Nature, 340, 126

Eilek, J. A. & Hankins, T. H. 2016, *Radio emission physics in the Crab pulsar*, Journal of Plasma Physics, 82, 635820302

Einstein, A. 1916, *Näherungsweise Integration der Feldgleichungen der Gravitation*, Sitzungsberichte der Königlich Preußischen Akademie der Wissenschaften (Berlin, 688

Enoto, T., Terasawa, T., Kisaka, S., et al. 2021, *Enhanced X-ray Emission Coinciding with Giant Radio Pulses from the Crab Pulsar*, arXiv e-prints, arXiv:2104.03492

Erber, T. 1966, *High-Energy Electromagnetic Conversion Processes in Intense Magnetic Fields*, Reviews of Modern Physics, 38, 626

B

Esposito, P., Rea, N., Borghese, A., et al. 2020, *A Very Young Radio-loud Magnetar*, ApJ, 896, L30

Evoli, C., Gaggero, D., Vittino, A., et al. 2017, *Cosmic-ray propagation with DRAGON2: I. numerical solver and astrophysical ingredients*, J. Cosmology Astropart. Phys., 2017, 015

Ezquiaga, J. M. & Zumalacárregui, M. 2017, *Dark Energy After GW170817: Dead Ends and the Road Ahead*, Phys. Rev. Lett., 119, 251304

Falcke, H. & Biermann, P. L. 1995, *The jet-disk symbiosis. I. Radio to X-ray emission models for quasars.*, A&A, 293, 665

Falcke, H., Körding, E., & Markoff, S. 2004a, *A scheme to unify low-power accreting black holes. Jet-dominated accretion flows and the radio/X-ray correlation*, A&A, 414, 895

Falcke, H., Körding, E., & Markoff, S. 2004b, *A scheme to unify low-power accreting black holes. Jet-dominated accretion flows and the radio/X-ray correlation*, A&A, 414, 895

Fang, K., Kotera, K., & Olinto, A. 2013, *High Energy Cosmic Rays and Neutrinos from Newborn Pulsars*, in APS Meeting Abstracts, L14.001

Fender, R. P., Belloni, T. M., & Gallo, E. 2004, *Towards a unified model for black hole X-ray binary jets*, MNRAS, 355, 1105

Fender, R. P., Maccarone, T. J., & van Kesteren, Z. 2005, *Energization of interstellar media and cosmic ray production by jets from X-ray binaries*, MNRAS, 360, 1085

Fermi, E. 1949, *On the Origin of the Cosmic Radiation*, Phys. Rev., 75, 1169

Fong, W. & Berger, E. 2013, *The Locations of Short Gamma-Ray Bursts as Evidence for Compact Object Binary Progenitors*, ApJ, 776, 18

Fong, W., Berger, E., Margutti, R., et al. 2012, *A Jet Break in the X-Ray Light Curve of Short GRB 111020A: Implications for Energetics and Rates*, ApJ, 756, 189

Gabici, S., Gaggero, D., & Zandanel, F. 2016, *Can supernova remnants accelerate protons up to PeV energies?*, ArXiv e-prints

Gaensler, B. M. 2014, *GRB 140705A / SGR 1935+2154: Probable association with supernova remnant G57.2+0.8.*, GRB Coordinates Network, 16533, 1

Gaggero, D., Grasso, D., Marinelli, A., Taoso, M., & Urbano, A. 2017, *Diffuse Cosmic Rays Shining in the Galactic Center: A Novel Interpretation of H.E.S.S. and Fermi-LAT γ -Ray Data*, Phys. Rev. Lett., 119, 031101

Gaisser, T. K., Stanev, T., & Tilav, S. 2013, *Cosmic ray energy spectrum from measurements of air showers*, Frontiers of Physics, 8, 748

Galama, T. J., Vreeswijk, P. M., van Paradijs, J., et al. 1998, *An unusual supernova in the error box of the γ-ray burst of 25 April 1998*, Nature, 395, 670

Gallant, Y. A., Hoshino, M., Langdon, A. B., Arons, J., & Max, C. E. 1992, *Relativistic, Perpendicular Shocks in Electron-Positron Plasmas*, ApJ, 391, 73

Gehrels, N., Chincarini, G., Giommi, P., et al. 2004, *The Swift Gamma-Ray Burst Mission*, ApJ, 611, 1005

Gehrels, N., Sarazin, C. L., O'Brien, P. T., et al. 2005, *A short γ-ray burst apparently associated with an elliptical galaxy at redshift z = 0.225*, Nature, 437, 851

Ghirlanda, G., Salafia, O. S., Paragi, Z., et al. 2019, *Compact radio emission indicates a structured jet was produced by a binary neutron star merger*, Science, 363, 968

Ghirlanda, G., Salvaterra, R., Campana, S., et al. 2015, *Unveiling the population of orphan γ-ray bursts*, A&A, 578, A71

Ghisellini, G. & Locatelli, N. 2018, *Coherent curvature radiation and fast radio bursts*, A&A, 613, A61

Giacinti, G., Kachelrieß, M., & Semikoz, D. V. 2015, *Escape model for Galactic cosmic rays and an early extragalactic transition*, Phys. Rev. D, 91, 083009

Ginzburg, V. L. & Syrovatskii, S. I. 1964, The Origin of Cosmic Rays

Goldreich, P. & Julian, W. H. 1969, *Pulsar Electrodynamics*, ApJ, 157, 869

Goldreich, P. & Keeley, D. A. 1971, *Coherent Synchrotron Radiation*, ApJ, 170, 463

Goldreich, P. & Lynden-Bell, D. 1969, *Io, a jovian unipolar inductor*, ApJ, 156, 59

Goldreich, P. & Reisenegger, A. 1992, *Magnetic Field Decay in Isolated Neutron Stars*, ApJ, 395, 250

Goldstein, A., Veres, P., Burns, E., et al. 2017, *An Ordinary Short Gamma-Ray Burst with Extraordinary Implications: Fermi-GBM Detection of GRB 170817A*, ApJ, 848, L14

Gompertz, B. P., Levan, A. J., & Tanvir, N. R. 2020, *A Search for Neutron Star-Black Hole Binary Mergers in the Short Gamma-Ray Burst Population*, ApJ, 895, 58

Gonthier, P. L. & Harding, A. K. 1994, *General Relativistic Corrections in the Gamma-Ray Emission from Pulsars*, ApJ, 425, 767

Gourdji, K., Michilli, D., Spitler, L. G., et al. 2019, *A Sample of Low-energy Bursts from FRB 121102*, ApJ, 877, L19

Gourdji, K., Rowlinson, A., Wijers, R. A. M. J., et al. 2022, *Searching for low radio-frequency gravitational wave counterparts in wide-field LOFAR data*, MNRAS, 509, 5018

B

Gourdji, K., Rowlinson, A., Wijers, R. A. M. J., & Goldstein, A. 2020, *Constraining a neutron star merger origin for localized fast radio bursts*, MNRAS, 497, 3131

Göğüş , E., Woods, P. M., Kouveliotou, C., et al. 1999, *Statistical Properties of SGR 1900+14 Bursts*, ApJ, 526, L93

Göğüş, E., Woods, P. M., Kouveliotou, C., et al. 2000, *Statistical Properties of SGR 1806-20 Bursts*, ApJ, 532, L121

Green, D. A., Dessenne, C. A. C., Warner, P. J., et al. 1995, *A Search for Prompt Radio Emission from GRBs*, Ap&SS, 231, 281

Hailey, C. J., Mori, K., Bauer, F. E., et al. 2018, *A density cusp of quiescent X-ray binaries in the central parsec of the Galaxy*, Nature, 556, 70

Hallinan, G., Corsi, A., Mooley, K. P., et al. 2017, *A radio counterpart to a neutron star merger*, Science, 358, 1579

Hallinan, G., Ravi, V., Weinreb, S., et al. 2019, *The DSA-2000 — A Radio Survey Camera*, in Bulletin of the American Astronomical Society, Vol. 51, 255

Hancock, P. J., Anderson, G. E., Williams, A., et al. 2019, *A VOEvent-based automatic trigger system for the Murchison Widefield Array*, PASA, 36, e046

Hankins, T. H. & Eilek, J. A. 2007, *Radio Emission Signatures in the Crab Pulsar*, ApJ, 670, 693

Hankins, T. H., Kern, J. S., Weatherall, J. C., & Eilek, J. A. 2003, *Nanosecond radio bursts from strong plasma turbulence in the Crab pulsar*, Nature, 422, 141

Hanlon, W. 2019, *Telescope Array 10 Year Composition*, arXiv e-prints, arXiv:1908.01356

Hansen, B. M. S. & Lyutikov, M. 2001, *Radio and X-ray signatures of merging neutron stars*, MNRAS, 322, 695

Harding, A. K., Baring, M. G., & Gonthier, P. L. 1997, *Photon-Splitting Cascades in Gamma-Ray Pulsars and the Spectrum of PSR 1509-58*, ApJ, 476, 246

Harding, A. K. & Muslimov, A. G. 2011, *Pulsar Pair Cascades in Magnetic Fields with Offset Polar Caps*, ApJ, 743, 181

Hashimoto, T., Goto, T., On, A. Y. L., et al. 2020a, *No redshift evolution of non-repeating fast radio burst rates*, MNRAS, 498, 3927

Hashimoto, T., Goto, T., On, A. Y. L., et al. 2020b, *Fast radio bursts to be detected with the Square Kilometre Array*, MNRAS, 497, 4107

HAWC Collaboration, Abeysekara, A. U., Albert, A., et al. 2018, *Very high energy particle acceleration powered by the jets of the microquasar SS 433*, arXiv e-prints, arXiv:1810.01892

B

HAWC Collaboration, Albert, A., Alfaro, R., et al. 2021, *Evidence that Ultra-High-Energy Gamma Rays are a Universal Feature Near Powerful Pulsars*, arXiv e-prints, arXiv:2101.07895

Heintz, K. E., Prochaska, J. X., Simha, S., et al. 2020, *Host Galaxy Properties and Offset Distributions of Fast Radio Bursts: Implications for Their Progenitors*, ApJ, 903, 152

Heinz, S. & Sunyaev, R. 2002, *Cosmic rays from microquasars: A narrow component to the CR spectrum?*, A&A, 390, 751

Heinz, S. & Sunyaev, R. A. 2003, *The non-linear dependence of flux on black hole mass and accretion rate in core-dominated jets*, MNRAS, 343, L59

Hermsen, W., Hessels, J. W. T., Kuiper, L., et al. 2013, *Synchronous X-ray and Radio Mode Switches: A Rapid Global Transformation of the Pulsar Magnetosphere*, Science, 339, 436

Hermsen, W., Kuiper, L., Basu, R., et al. 2018, *Discovery of synchronous X-ray and radio moding of PSR B0823+26*, MNRAS, 480, 3655

Hess, V. 1928, The electrical conductivity of the atmosphere and its cause, 204

HESS Collaboration, Abramowski, A., Aharonian, F., et al. 2016, *Acceleration of petaelectron-volt protons in the Galactic Centre*, Nature, 531, 476

Hessels, J. W. T., Spitler, L. G., Seymour, A. D., et al. 2019, *FRB 121102 Bursts Show Complex Time-Frequency Structure*, ApJ, 876, L23

Hewish, A., Bell, S. J., Pilkington, J. D. H., Scott, P. F., & Collins, R. A. 1968, *Observation of a Rapidly Pulsating Radio Source*, Nature, 217, 709

Hewitt, D. M., Snelders, M. P., Hessels, J. W. T., et al. 2021, *Arecibo observations of a burst storm from FRB 20121102A in 2016*, arXiv e-prints, arXiv:2111.11282

Hillas, A. M. 1984, *The Origin of Ultra-High-Energy Cosmic Rays*, ARA&A, 22, 425

Hillas, A. M. 2005, *TOPICAL REVIEW: Can diffusive shock acceleration in supernova remnants account for high-energy galactic cosmic rays?*, Journal of Physics G Nuclear Physics, 31, R95

Hirata, K., Kajita, T., Koshiba, M., et al. 1987, *Observation of a neutrino burst from the supernova SN1987A*, Phys. Rev. Lett., 58, 1490

Hirotani, K., Harding, A. K., & Shibata, S. 2003, *Electrodynamics of an Outer Gap Accelerator: Formation of a Soft Power-Law Spectrum between 100 MeV and 3 GeV*, ApJ, 591, 334

Ho, A. Y. Q., Perley, D. A., Beniamini, P., et al. 2020, *ZTF20aajnksq (AT 2020blt): A Fast Optical Transient at z □ 2.9 with No Detected Gamma-Ray Burst Counterpart*, ApJ, 905, 98

Holloway, N. J. 1973, *P-N Junctions in Pulsar Magnetospheres ?*, Nature Physical Science, 246, 6

Hoshino, M., Arons, J., Gallant, Y. A., & Langdon, A. B. 1992, *Relativistic Magnetosonic Shock Waves in Synchrotron Sources: Shock Structure and Nonthermal Acceleration of Positrons*, ApJ, 390, 454

Hulse, R. A. & Taylor, J. H. 1975, *Discovery of a pulsar in a binary system.*, ApJ, 195, L51

Hurley, K., Cline, T., Mazets, E., et al. 1999, *A giant periodic flare from the soft γ-ray repeater SGR1900+14*, Nature, 397, 41

Hurley-Walker, N., Zhang, X., Bahramian, A., et al. 2022, *A radio transient with unusually slow periodic emission*, Nature, 601, 526

IceCube Collaboration, Aartsen, M. G., Ackermann, M., et al. 2018a, *Multimessenger observations of a flaring blazar coincident with high-energy neutrino IceCube-170922A*, Science, 361, eaat1378

IceCube Collaboration, Aartsen, M. G., Ackermann, M., et al. 2018b, *Neutrino emission from the direction of the blazar TXS 0506+056 prior to the IceCube-170922A alert*, Science, 361, 147

IceCube-Gen2 Collaboration, :, Aartsen, M. G., et al. 2014, *IceCube-Gen2: A Vision for the Future of Neutrino Astronomy in Antarctica*, arXiv e-prints, arXiv:1412.5106

Igoshev, A. P., Popov, S. B., & Hollerbach, R. 2021, *Evolution of Neutron Star Magnetic Fields*, Universe, 7, 351

Inui, T., Koyama, K., Matsumoto, H., & Tsuru, T. G. 2009, *Time Variability of the Neutral Iron Lines from the Sagittarius B2 Region and Its Implication of a Past Outburst of Sagittarius A*, PASJ, 61, S241

Ioka, K. 2003, *The Cosmic Dispersion Measure from Gamma-Ray Burst Afterglows: Probing the Reionization History and the Burst Environment*, ApJ, 598, L79

Israel, G. L., Esposito, P., Rea, N., et al. 2016, *The discovery, monitoring and environment of SGR J1935+2154*, MNRAS, 457, 3448

Ivezić, Ž., Kahn, S. M., Tyson, J. A., et al. 2019, *LSST: From Science Drivers to Reference Design and Anticipated Data Products*, ApJ, 873, 111

James, C. W., Anderson, G. E., Wen, L., et al. 2019, *Using negative-latency gravitational wave alerts to detect prompt radio bursts from binary neutron star mergers with the Murchison Widefield Array*, MNRAS, 489, L75

James, C. W., Prochaska, J. X., Macquart, J. P., et al. 2022, *The fast radio burst population evolves, consistent with the star formation rate*, MNRAS, 510, L18

Jansky, K. G. 1933, *Radio Waves from Outside the Solar System*, Nature, 132, 66

Japelj, J., Kann, D. A., de Ugarte Postigo, A., et al. 2019, *GRB 190627A: VLT/FORS2 spectroscopic redshift.*, GRB Coordinates Network, 24916, 1

Jokipii, J. R. & Morfill, G. 1987, *Ultra-high-energy cosmic rays in a galactic wind and its termination shock*, ApJ, 312, 170

Jonas, J. & MeerKAT Team. 2016, *The MeerKAT Radio Telescope*, in MeerKAT Science: On the Pathway to the SKA, 1

Josephy, A., Chawla, P., Curtin, A. P., et al. 2021, *No Evidence for Galactic Latitude Dependence of the Fast Radio Burst Sky Distribution*, ApJ, 923, 2

Jouvin, L., Lemière, A., & Terrier, R. 2017, *Does the SN rate explain the very high energy cosmic rays in the central 200 pc of our Galaxy?*, MNRAS, 467, 4622

KAGRA Collaboration, Abe, H., Adhikari, R. X., et al. 2022, *Performance of the KAGRA detector during the first joint observation with GEO 600 (O3GK)*, arXiv e-prints, arXiv:2203.07011

Kagra Collaboration, Akutsu, T., Ando, M., et al. 2019, *KAGRA: 2.5 generation interferometric gravitational wave detector*, Nature Astronomy, 3, 35

Kalapotharakos, C., Harding, A. K., Kazanas, D., & Wadiasingh, Z. 2019, *A Fundamental Plane for Gamma-Ray Pulsars*, ApJ, 883, L4

Kalapotharakos, C., Wadiasingh, Z., Harding, A. K., & Kazanas, D. 2022, *The Fundamental Plane Relation for Gamma-Ray Pulsars Implied by 4FGL*, arXiv e-prints, arXiv:2203.13276

Kalogera, V. 1998, *Formation of Low-Mass X-Ray Binaries. III. A New Formation Mechanism: Direct Supernova*, ApJ, 493, 368

Kampert, K.-H. & Unger, M. 2012, *Measurements of the cosmic ray composition with air shower experiments*, Astroparticle Physics, 35, 660

Kang, D. 2019, *Latest Results from the KASCADE-Grande Data Analysis*, in International Cosmic Ray Conference, Vol. 36, 36th International Cosmic Ray Conference (ICRC2019), 306

Kantzas, D., Markoff, S., Beuchert, T., et al. 2021, *A new lepto-hadronic model applied to the first simultaneous multiwavelength data set for Cygnus X-1*, MNRAS, 500, 2112

Kardashev, N. S. 2000, *Radio Synchrotron Emission by Protons and Electrons in Pulsars and the Nuclei of Quasars*, Astronomy Reports, 44, 719

Kasen, D., Metzger, B., Barnes, J., Quataert, E., & Ramirez-Ruiz, E. 2017, *Origin of the heavy elements in binary neutron-star mergers from a gravitational-wave event*, Nature, 551, 80

Kaspi, V. M. & Beloborodov, A. M. 2017, *Magnetars*, ARA&A, 55, 261

Katz, J. I. 2014, *Coherent emission in fast radio bursts*, Phys. Rev. D, 89, 103009

Katz, J. I. 2016, *How Soft Gamma Repeaters Might Make Fast Radio Bursts*, ApJ, 826, 226

B

Katz, J. I. 2018, *Coherent plasma-curvature radiation in FRB*, MNRAS, 481, 2946

Keane, E. F., Johnston, S., Bhandari, S., et al. 2016, *The host galaxy of a fast radio burst*, Nature, 530, 453

Keane, E. F., Stappers, B. W., Kramer, M., & Lyne, A. G. 2012, *On the origin of a highly dispersed coherent radio burst*, MNRAS, 425, L71

Kellermann, K. I. & Pauliny-Toth, I. I. K. 1969, *The Spectra of Opaque Radio Sources*, ApJ, 155, L71

Kelner, S. R., Prosekin, A. Y., & Aharonian, F. A. 2015, *Synchro-Curvature Radiation of Charged Particles in the Strong Curved Magnetic Fields*, AJ, 149, 33

Kiel, P. D. & Hurley, J. R. 2006, *Populating the Galaxy with low-mass X-ray binaries*, MNRAS, 369, 1152

Kilpatrick, C. D., Burchett, J. N., Jones, D. O., et al. 2021, *Deep Optical Observations Contemporaneous with Emission from the Periodic FRB 180916.J0158+65*, ApJ, 907, L3

Kirsten, F., Marcote, B., Nimmo, K., et al. 2022, *A repeating fast radio burst source in a globular cluster*, Nature, 602, 585

Kirsten, F., Snelders, M. P., Jenkins, M., et al. 2021, *Detection of two bright radio bursts from magnetar SGR 1935 + 2154*, Nature Astronomy, 5, 414

Klebesadel, R. W., Strong, I. B., & Olson, R. A. 1973, *Observations of Gamma-Ray Bursts of Cosmic Origin*, ApJ, 182, L85

Kothes, R., Sun, X., Gaensler, B., & Reich, W. 2018, *A Radio Continuum and Polarization Study of SNR G57.2+0.8 Associated with Magnetar SGR 1935+2154*, ApJ, 852, 54

Kouveliotou, C., Dieters, S., Strohmayer, T., et al. 1998, *An X-ray pulsar with a superstrong magnetic field in the soft γ-ray repeater SGR1806 - 20*, Nature, 393, 235

Kouveliotou, C., Fishman, G. J., Meegan, C. A., et al. 1993a, *Recurrent burst activity from the soft γ-ray repeater SGR 1900+14*, Nature, 362, 728

Kouveliotou, C., Meegan, C. A., Fishman, G. J., et al. 1993b, *Identification of Two Classes of Gamma-Ray Bursts*, ApJ, 413, L101

Kozlova, A. V., Israel, G. L., Svinkin, D. S., et al. 2016, *The first observation of an intermediate flare from SGR 1935+2154*, MNRAS, 460, 2008

Kramer, M., Stappers, B. W., Jessner, A., Lyne, A. G., & Jordan, C. A. 2007, *Polarized radio emission from a magnetar*, MNRAS, 377, 107

Kroupa, P. 2001, *On the variation of the initial mass function*, MNRAS, 322, 231

B

Krymskii, G. F. 1977, *A regular mechanism for the acceleration of charged particles on the front of a shock wave*, Akademiia Nauk SSSR Doklady, 234, 1306

Kuiack, M., Wijers, R. A. M. J., Rowlinson, A., et al. 2020, *Long-term study of extreme giant pulses from PSR B0950+08 with AARTFAAC*, MNRAS, 497, 846

Kumar, P. & Bošnjak, Ž. 2020, *FRB coherent emission from decay of Alfvén waves*, MNRAS, 494, 2385

Kumar, P., Lu, W., & Bhattacharya, M. 2017, *Fast radio burst source properties and curvature radiation model*, MNRAS, 468, 2726

Kuroda, K. & LCGT Collaboration. 2010, *Status of LCGT*, Classical and Quantum Gravity, 27, 084004

Lai, D. 2012, *DC Circuit Powered by Orbital Motion: Magnetic Interactions in Compact Object Binaries and Exoplanetary Systems*, ApJ, 757, L3

Langdon, A. B., Arons, J., & Max, C. E. 1988, *Structure of relativistic magnetosonic shocks in electron-positron plasmas*, Phys. Rev. Lett., 61, 779

Larroche, O. & Pellat, R. 1987, *Curvature instability of relativistic particle beams*, Phys. Rev. Lett., 59, 1104

Lasky, P. D. 2015, *Gravitational Waves from Neutron Stars: A Review*, PASA, 32, e034

Lasota, J.-P. 2001, *The disc instability model of dwarf novae and low-mass X-ray binary transients*, New A Rev., 45, 449

Lattimer, J. M. 2019, *Neutron Star Mass and Radius Measurements*, Universe, 5, 159

Lattimer, J. M. & Schramm, D. N. 1974, *Black-Hole-Neutron-Star Collisions*, ApJ, 192, L145

Lattimer, J. M. & Schramm, D. N. 1976, *The tidal disruption of neutron stars by black holes in close binaries.*, ApJ, 210, 549

Law, C. J., Gaensler, B. M., Metzger, B. D., Ofek, E. O., & Sironi, L. 2018, *Discovery of the Luminous, Decades-long, Extragalactic Radio Transient FIRST J141918.9+394036*, ApJ, 866, L22

Lazzati, D. 2005, *Precursor activity in bright, long BATSE gamma-ray bursts*, MNRAS, 357, 722

Lazzati, D., Perna, R., Morsony, B. J., et al. 2018, *Late Time Afterglow Observations Reveal a Collimated Relativistic Jet in the Ejecta of the Binary Neutron Star Merger GW170817*, Phys. Rev. Lett., 120, 241103

Lentati, L., Taylor, S. R., Mingarelli, C. M. F., et al. 2015, *European Pulsar Timing Array limits on an isotropic stochastic gravitational-wave background*, MNRAS, 453, 2576

Lerche, I. 1970, *On the Motion of Current Sheets, and the Radio, Optical, and X-Ray Emission from Pulsars*, ApJ, 159, 229

Leung, C., Mena-Parra, J., Masui, K., et al. 2021, *A Synoptic VLBI Technique for Localizing Nonrepeating Fast Radio Bursts with CHIME/FRB*, AJ, 161, 81

Levan, A., Kouveliotou, C., & Fruchter, A. 2018, *Identification of the Infrared Counterpart of SGR 1935+2154 with the Hubble Space Telescope*, ApJ, 854, 161

Levin, L., Bailes, M., Bates, S., et al. 2010, *A Radio-loud Magnetar in X-ray Quiescence*, ApJ, 721, L33

Levinson, A. & Eichler, D. 1993, *Baryon Purity in Cosmological Gamma-Ray Bursts as a Manifestation of Event Horizons*, ApJ, 418, 386

Levinson, A., Ofek, E. O., Waxman, E., & Gal-Yam, A. 2002, *Orphan Gamma-Ray Burst Radio Afterglows: Candidates and Constraints on Beaming*, ApJ, 576, 923

Levinson, A. & Waxman, E. 2001, *Probing Microquasars with TeV Neutrinos*, Phys. Rev. Lett., 87, 171101

Li, C. K., Lin, L., Xiong, S. L., et al. 2021, *HXMT identification of a non-thermal X-ray burst from SGR J1935+2154 and with FRB 200428*, Nature Astronomy

Li, L.-X. & Paczyński, B. 1998, *Transient Events from Neutron Star Mergers*, ApJ, 507, L59

Li, X., Ge, M., Lin, L., et al. 2022, *Quasi-periodic oscillations of the X-ray burst from the magnetar SGR J1935+2154 and associated with the fast radio burst FRB 200428*, arXiv e-prints, arXiv:2204.03253

Lien, A. Y., Barthelmy, S. D., Baumgartner, W. H., et al. 2014, *GRB 140705A: Swift-BAT refined analysis of a possible newly discovered SGR 1935+2154.*, GRB Coordinates Network, 16522, 1

Lieu, R. 2017, *Are Fast Radio Bursts the Birthmark of Magnetars?*, ApJ, 834, 199

Lin, L., Zhang, C. F., Wang, P., et al. 2020, *No pulsed radio emission during a bursting phase of a Galactic magnetar*, Nature, 587, 63

Lipunov, V. M. & Panchenko, I. E. 1996, *Pulsars revived by gravitational waves.*, A&A, 312, 937

Longair, M. S. 2011, High Energy Astrophysics

Lorimer, D. R., Bailes, M., McLaughlin, M. A., Narkevic, D. J., & Crawford, F. 2007, *A Bright Millisecond Radio Burst of Extragalactic Origin*, Science, 318, 777

Lorimer, D. R., Faulkner, A. J., Lyne, A. G., et al. 2006, *The Parkes Multibeam Pulsar Survey - VI. Discovery and timing of 142 pulsars and a Galactic population analysis*, MNRAS, 372, 777

B

Lower, M. E., Shannon, R. M., Johnston, S., & Bailes, M. 2020, *Spectropolarimetric Properties of Swift J1818.0-1607: A 1.4 s Radio Magnetar*, ApJ, 896, L37

Lu, W. & Kumar, P. 2018, *On the radiation mechanism of repeating fast radio bursts*, MNRAS, 477, 2470

Lu, W. & Kumar, P. 2019, *The maximum luminosity of fast radio bursts*, MNRAS, 483, L93

Lu, W., Kumar, P., & Zhang, B. 2020, *A unified picture of Galactic and cosmological fast radio bursts*, MNRAS, 498, 1397

Lu, W. & Piro, A. L. 2019, *Implications from ASKAP Fast Radio Burst Statistics*, ApJ, 883, 40

Lundgren, S. C., Cordes, J. M., Ulmer, M., et al. 1995, *Giant Pulses from the Crab Pulsar: A Joint Radio and Gamma-Ray Study*, ApJ, 453, 433

Luo, R., Wang, B. J., Men, Y. P., et al. 2020, *Diverse polarization angle swings from a repeating fast radio burst source*, Nature, 586, 693

Lyne, A. G., Burgay, M., Kramer, M., et al. 2004, *A Double-Pulsar System: A Rare Laboratory for Relativistic Gravity and Plasma Physics*, Science, 303, 1153

Lyne, A. G., Pritchard, R. S., & Graham Smith, F. 1993, *23 years of Crab pulsar rotational history.*, MNRAS, 265, 1003

Lyubarsky, Y. 2014, *A model for fast extragalactic radio bursts.*, MNRAS, 442, L9

Lyubarsky, Y. 2021, *Emission Mechanisms of Fast Radio Bursts*, Universe, 7, 56

Lyutikov, M. 2019, *Electrodynamics of binary neutron star mergers*, MNRAS, 483, 2766

Lyutikov, M. 2021, *Brightness temperature constraints on coherent processes in magnetospheres of neutron stars*, arXiv e-prints, arXiv:2107.04414

Lyutikov, M. & Popov, S. 2020, *Fast Radio Bursts from reconnection events in magnetar magnetospheres*, arXiv e-prints, arXiv:2005.05093

Maccarone, T. J. 2003, *Do X-ray binary spectral state transition luminosities vary?*, A&A, 409, 697

Macquart, J.-P., Bailes, M., Bhat, N. D. R., et al. 2010, *The Commensal Real-Time ASKAP Fast-Transients (CRAFT) Survey*, PASA, 27, 272

Magee, R. & Borhanian, S. 2022, *Realistic observing scenarios for the next decade of early warning detection of binary neutron stars*, arXiv e-prints, arXiv:2201.11841

MAGIC Collaboration, Ahnen, M. L., Ansoldi, S., et al. 2020, *Statistics of VHE γ-rays in temporal association with radio giant pulses from the Crab pulsar*, A&A, 634, A25

B

MAGIC Collaboration, Ahnen, M. L., Ansoldi, S., et al. 2018, *Constraints on particle acceleration in SS433/W50 from MAGIC and H.E.S.S. observations*, A&A, 612, A14

Malkov, M. A. 1997, *Analytic Solution for Nonlinear Shock Acceleration in the Bohm Limit*, ApJ, 485, 638

Malzac, J. 2014, *The spectral energy distribution of compact jets powered by internal shocks*, MNRAS, 443, 299

Mandel, I. & Broekgaarden, F. S. 2021, *Rates of Compact Object Coalescences*, arXiv e-prints, arXiv:2107.14239

Mannheim, K. & Schlickeiser, R. 1994, *Interactions of cosmic ray nuclei*, A&A, 286, 983

Marcote, B., Nimmo, K., Hessels, J. W. T., et al. 2020, *A repeating fast radio burst source localized to a nearby spiral galaxy*, Nature, 577, 190

Margalit, B., Beniamini, P., Sridhar, N., & Metzger, B. D. 2020a, *Implications of a Fast Radio Burst from a Galactic Magnetar*, ApJ, 899, L27

Margalit, B. & Metzger, B. D. 2018, *A Concordance Picture of FRB 121102 as a Flaring Magnetar Embedded in a Magnetized Ion-Electron Wind Nebula*, ApJ, 868, L4

Margalit, B., Metzger, B. D., & Sironi, L. 2020b, *Constraints on the engines of fast radio bursts*, MNRAS, 494, 4627

Margalit, B. & Quataert, E. 2021, *Thermal Electrons in Mildly Relativistic Synchrotron Blast Waves*, ApJ, 923, L14

Margon, B., Ford, H. C., Grandi, S. A., & Stone, R. P. S. 1979, *Enormous periodic Doppler shifts in SS 433*, ApJ, 233, L63

Markoff, S., Falcke, H., & Fender, R. 2001, *A jet model for the broadband spectrum of XTE J1118+480. Synchrotron emission from radio to X-rays in the Low/Hard spectral state*, A&A, 372, L25

Markoff, S., Nowak, M. A., & Wilms, J. 2005, *Going with the Flow: Can the Base of Jets Subsume the Role of Compact Accretion Disk Coronae?*, ApJ, 635, 1203

Marnoch, L., Ryder, S. D., Bannister, K. W., et al. 2020, *A search for supernova-like optical counterparts to ASKAP-localised fast radio bursts*, A&A, 639, A119

Marsh, T. R., Gänsicke, B. T., Hümmerich, S., et al. 2016, *A radio-pulsing white dwarf binary star*, Nature, 537, 374

Matthews, J. H., Bell, A. R., Blundell, K. M., & Araudo, A. T. 2019, *Ultrahigh energy cosmic rays from shocks in the lobes of powerful radio galaxies*, MNRAS, 482, 4303

Mazets, E. P., Golentskii, S. V., Ilinskii, V. N., Aptekar, R. L., & Guryan, I. A. 1979, *Observations of a flaring X-ray pulsar in Dorado*, Nature, 282, 587

McHardy, I. M., Koerding, E., Knigge, C., Uttley, P., & Fender, R. P. 2006a, *Active galactic nuclei as scaled-up Galactic black holes*, Nature, 444, 730

McHardy, I. M., Koerding, E., Knigge, C., Uttley, P., & Fender, R. P. 2006b, *Active galactic nuclei as scaled-up Galactic black holes*, Nature, 444, 730

McWilliams, S. T. & Levin, J. 2011, *Electromagnetic Extraction of Energy from Black-hole-Neutron-star Binaries*, ApJ, 742, 90

Medvedev, M. V. & Loeb, A. 2013, *On Poynting-flux-driven bubbles and shocks around merging neutron star binaries*, MNRAS, 431, 2737

Meegan, C., Lichti, G., Bhat, P. N., et al. 2009, *The Fermi Gamma-ray Burst Monitor*, ApJ, 702, 791

Meegan, C. A., Fishman, G. J., Wilson, R. B., et al. 1992, *Spatial distribution of γ-ray bursts observed by BATSE*, Nature, 355, 143

Melrose, D. B. 1981, *Maser pulse emission mechanisms*, in Pulsars: 13 Years of Research on Neutron Stars, ed. W. Sieber & R. Wielebinski, Vol. 95, 133–139

Melrose, D. B. 2002, *Coherent Emission in AGN: A Critique*, PASA, 19, 34

Melrose, D. B. 2017, *Coherent emission mechanisms in astrophysical plasmas*, Reviews of Modern Plasma Physics, 1, 5

Melrose, D. B., Rafat, M. Z., & Mastrano, A. 2021, *Pulsar radio emission mechanisms: a critique*, MNRAS, 500, 4530

Mereghetti, S., Savchenko, V., Ferrigno, C., et al. 2020, *INTEGRAL Discovery of a Burst with Associated Radio Emission from the Magnetar SGR 1935+2154*, ApJ, 898, L29

Merloni, A., Heinz, S., & di Matteo, T. 2003, *A Fundamental Plane of black hole activity*, MNRAS, 345, 1057

Mészáros, P., Rees, M. J., & Wijers, R. A. M. J. 1998, *Viewing Angle and Environment Effects in Gamma-Ray Bursts: Sources of Afterglow Diversity*, ApJ, 499, 301

Metzger, B. D. 2019, *Kilonovae*, Living Reviews in Relativity, 23, 1

Metzger, B. D. & Berger, E. 2012, *What is the Most Promising Electromagnetic Counterpart of a Neutron Star Binary Merger?*, ApJ, 746, 48

Metzger, B. D., Margalit, B., & Sironi, L. 2019, *Fast radio bursts as synchrotron maser emission from decelerating relativistic blast waves*, MNRAS, 485, 4091

B

Metzger, B. D. & Zivancev, C. 2016, *Pair fireball precursors of neutron star mergers*, MNRAS, 461, 4435

Michilli, D., Masui, K. W., Mckinven, R., et al. 2021, *An Analysis Pipeline for CHIME/FRB Full-array Baseband Data*, ApJ, 910, 147

Michilli, D., Seymour, A., Hessels, J. W. T., et al. 2018, *An extreme magneto-ionic environment associated with the fast radio burst source FRB 121102*, Nature, 553, 182

Migliari, S., Fender, R., & Méndez, M. 2002, *Iron Emission Lines from Extended X-ray Jets in SS 433: Reheating of Atomic Nuclei*, Science, 297, 1673

Migliari, S. & Fender, R. P. 2006, *Jets in neutron star X-ray binaries: a comparison with black holes*, MNRAS, 366, 79

Miller-Jones, J. C. A., Sivakoff, G. R., Altamirano, D., et al. 2012, *Disc-jet coupling in the 2009 outburst of the black hole candidate H1743-322*, MNRAS, 421, 468

Mirabel, I. F. & Rodríguez, L. F. 1994, *A superluminal source in the Galaxy*, Nature, 371, 46

Mirabel, I. F. & Rodríguez, L. F. 1999, *Sources of Relativistic Jets in the Galaxy*, ARA&A, 37, 409

Mooley, K. P., Nakar, E., Hotokezaka, K., et al. 2018, *A mildly relativistic wide-angle outflow in the neutron-star merger event GW170817*, Nature, 554, 207

Moortgat, J. & Kuijpers, J. 2006, *Scattering of magnetosonic waves in a relativistic and anisotropic magnetized plasma*, MNRAS, 368, 1110

Most, E. R. & Philippov, A. A. 2020, *Electromagnetic Precursors to Gravitational-wave Events: Numerical Simulations of Flaring in Pre-merger Binary Neutron Star Magnetospheres*, ApJ, 893, L6

Most, E. R. & Philippov, A. A. 2022, *Electromagnetic precursor flares from the late inspiral of neutron star binaries*, arXiv e-prints, arXiv:2205.09643

Mulrey, K., Bonardi, A., Buitink, S., et al. 2019, *Extension of the LOFAR Radboud Air Shower Array*, in International Cosmic Ray Conference, Vol. 36, 36th International Cosmic Ray Conference (ICRC2019), 363

Murase, K., Inoue, Y., & Dermer, C. D. 2014, *Diffuse neutrino intensity from the inner jets of active galactic nuclei: Impacts of external photon fields and the blazar sequence*, Phys. Rev. D, 90, 023007

Nan, R. 2006, *Five hundred meter aperture spherical radio telescope (FAST)*, Science in China: Physics, Mechanics and Astronomy, 49, 129

Nimmo, K., Hessels, J. W. T., Kirsten, F., et al. 2021, *Burst timescales and luminosities link young pulsars and fast radio bursts*, arXiv e-prints, arXiv:2105.11446

B

Niu, C. H., Aggarwal, K., Li, D., et al. 2021a, *A repeating fast radio burst associated with a persistent radio source*, arXiv e-prints, arXiv:2110.07418

Niu, C.-H., Li, D., Luo, R., et al. 2021b, *CRAFTS for Fast Radio Bursts: Extending the Dispersion-Fluence Relation with New FRBs Detected by FAST*, ApJ, 909, L8

Núñez, C., Tejos, N., Pignata, G., et al. 2021, *Constraining bright optical counterparts of fast radio bursts*, A&A, 653, A119

Offringa, A. R., McKinley, B., Hurley-Walker, N., et al. 2014, *WSCLEAN: an implementation of a fast, generic wide-field imager for radio astronomy*, MNRAS, 444, 606

Olausen, S. A. & Kaspi, V. M. 2014, *The McGill Magnetar Catalog*, ApJS, 212, 6

Olejak, A., Belczynski, K., Bulik, T., & Sobolewska, M. 2019, *Synthetic catalog of black holes in the Milky Way*, arXiv e-prints, arXiv:1908.08775

Oppenheimer, J. R. & Volkoff, G. M. 1939, *On Massive Neutron Cores*, Physical Review, 55, 374

Paczyński, B. 1986, *Gamma-ray bursters at cosmological distances*, ApJ, 308, L43

Paczyński, B. & Rhoads, J. E. 1993, *Radio Transients from Gamma-Ray Bursters*, ApJ, 418, L5

Palenzuela, C., Lehner, L., Ponce, M., et al. 2013, *Electromagnetic and Gravitational Outputs from Binary-Neutron-Star Coalescence*, Phys. Rev. Lett., 111, 061105

Palmer, D. M. 2020, *A Forest of Bursts from SGR 1935+2154*, The Astronomer's Telegram, 13675, 1

Palmer, D. M., Barthelmy, S., Gehrels, N., et al. 2005, *A giant γ-ray flare from the magnetar SGR 1806 - 20*, Nature, 434, 1107

Pastor-Marazuela, I., Connor, L., van Leeuwen, J., et al. 2021, *Chromatic periodic activity down to 120 megahertz in a fast radio burst*, Nature, 596, 505

Pastor-Marazuela, I., van Leeuwen, J., Bilous, A., et al. 2022, *A fast radio burst with sub-millisecond quasi-periodic structure*, arXiv e-prints, arXiv:2202.08002

Paterson, K., Fong, W., Nugent, A., et al. 2020, *Discovery of the Optical Afterglow and Host Galaxy of Short GRB 181123B at z = 1.754: Implications for Delay Time Distributions*, ApJ, 898, L32

Paxton, B., Bildsten, L., Dotter, A., et al. 2011, *Modules for Experiments in Stellar Astrophysics (MESA)*, ApJS, 192, 3

Péault, M., Malzac, J., Coriat, M., et al. 2019, *Modelling the compact jet in MAXI J1836-194 with disc-driven shocks*, MNRAS, 482, 2447

B

Pepe, C., Vila, G. S., & Romero, G. E. 2015, *Lepto-hadronic model for the broadband emission of Cygnus X-1*, A&A, 584, A95

Peters, B. 1961, *Primary cosmic radiation and extensive air showers*, Il Nuovo Cimento (1955-1965), 22, 800

Peters, P. C. 1964, *Gravitational Radiation and the Motion of Two Point Masses*, Phys. Rev., 136, B1224

Petroff, E., Bailes, M., Barr, E. D., et al. 2015, *A real-time fast radio burst: polarization detection and multiwavelength follow-up*, MNRAS, 447, 246

Petroff, E., Barr, E. D., Jameson, A., et al. 2016, *FRBCAT: The Fast Radio Burst Catalogue*, PASA, 33, e045

Petroff, E., Hessels, J. W. T., & Lorimer, D. R. 2019, *Fast radio bursts*, A&A Rev., 27, 4

Petroff, E., Hessels, J. W. T., & Lorimer, D. R. 2022, *Fast radio bursts at the dawn of the 2020s*, A&A Rev., 30, 2

Pfahl, E., Rappaport, S., & Podsiadlowski, P. 2003, *The Galactic Population of Low- and Intermediate-Mass X-Ray Binaries*, ApJ, 597, 1036

Philippov, A., Timokhin, A., & Spitkovsky, A. 2020, *Origin of Pulsar Radio Emission*, Phys. Rev. Lett., 124, 245101

Pian, E., D'Avanzo, P., Benetti, S., et al. 2017, *Spectroscopic identification of r-process nucleosynthesis in a double neutron-star merger*, Nature, 551, 67

Pierre Auger Collaboration. 2014, *Depth of Maximum of Air-Shower Profiles at the Pierre Auger Observatory: Composition Implications*, arXiv e-prints, arXiv:1409.5083

Pierre Auger Collaboration, Aab, A., Abreu, P., et al. 2017, *Observation of a large-scale anisotropy in the arrival directions of cosmic rays above 8×10^{18} eV*, Science, 357, 1266

Pierre Auger Collaboration, Abraham, J., Abreu, P., et al. 2007, *Correlation of the Highest-Energy Cosmic Rays with Nearby Extragalactic Objects*, Science, 318, 938

Pierre Auger Collaboration, Abraham, J., Abreu, P., et al. 2008, *Correlation of the highest-energy cosmic rays with the positions of nearby active galactic nuclei*, Astroparticle Physics, 29, 188

Pietka, M., Fender, R. P., & Keane, E. F. 2015, *The variability time-scales and brightness temperatures of radio flares from stars to supermassive black holes*, MNRAS, 446, 3687

Piro, A. L. 2012, *Magnetic Interactions in Coalescing Neutron Star Binaries*, ApJ, 755, 80

Platts, E., Weltman, A., Walters, A., et al. 2019, *A living theory catalogue for fast radio bursts*, Phys. Rep., 821, 1

B

Plavec, M. & Kratochvil, P. 1964, *Tables for the Roche model of close binaries*, Bulletin of the Astronomical Institutes of Czechoslovakia, 15, 165

Pleunis, Z., Good, D. C., Kaspi, V. M., et al. 2021a, *Fast Radio Burst Morphology in the First CHIME/FRB Catalog*, ApJ, 923, 1

Pleunis, Z., Michilli, D., Bassa, C. G., et al. 2021b, *LOFAR Detection of 110-188 MHz Emission and Frequency-dependent Activity from FRB 20180916B*, ApJ, 911, L3

Plotkin, R. M., Gallo, E., & Jonker, P. G. 2013, *The X-Ray Spectral Evolution of Galactic Black Hole X-Ray Binaries toward Quiescence*, ApJ, 773, 59

Plotkin, R. M., Markoff, S., Kelly, B. C., Körding, E., & Anderson, S. F. 2012, *Using the Fundamental Plane of black hole activity to distinguish X-ray processes from weakly accreting black holes*, MNRAS, 419, 267

Plotnikov, I. & Sironi, L. 2019, *The synchrotron maser emission from relativistic shocks in Fast Radio Bursts: 1D PIC simulations of cold pair plasmas*, MNRAS, 485, 3816

Popov, S. B. & Postnov, K. A. 2013, *Millisecond extragalactic radio bursts as magnetar flares*, arXiv e-prints, arXiv:1307.4924

Prasad, P., Huizinga, F., Kooistra, E., et al. 2016, *The AARTFAAC All-Sky Monitor: System Design and Implementation*, Journal of Astronomical Instrumentation, 5, 1641008

Punturo, M., Abernathy, M., Acernese, F., et al. 2010, *The Einstein Telescope: a third-generation gravitational wave observatory*, Classical and Quantum Gravity, 27, 194002

Rankin, J. M. 1993, *Toward an Empirical Theory of Pulsar Emission. VI. The Geometry of the Conal Emission Region*, ApJ, 405, 285

Ravi, V. 2019, *The prevalence of repeating fast radio bursts*, Nature Astronomy, 3, 928

Rea, N., Pons, J. A., Torres, D. F., & Turolla, R. 2012, *The Fundamental Plane for Radio Magnetars*, ApJ, 748, L12

Readhead, A. C. S. 1994, *Equipartition brightness temperature and the inverse Compton catastrophe*, ApJ, 426, 51

Rees, M. J. & Meszaros, P. 1992, *Relativistic fireballs - Energy conversion and time-scales.*, MNRAS, 258, 41

Rees, M. J. & Simon, M. 1968, *Evidence for Relativistic Expansion in Variable Radio Sources*, ApJ, 152, L145

Remillard, R. A. & McClintock, J. E. 2006, *X-Ray Properties of Black-Hole Binaries*, ARA&A, 44, 49

B

Ridnaia, A., Svinkin, D., Frederiks, D., et al. 2021, *A peculiar hard X-ray counterpart of a Galactic fast radio burst*, Nature Astronomy, 5, 372

Riley, T. E., Watts, A. L., Bogdanov, S., et al. 2019, *A NICER View of PSR J0030+0451: Millisecond Pulsar Parameter Estimation*, ApJ, 887, L21

Roberts, L. F., Kasen, D., Lee, W. H., & Ramirez-Ruiz, E. 2011, *Electromagnetic Transients Powered by Nuclear Decay in the Tidal Tails of Coalescing Compact Binaries*, ApJ, 736, L21

Romero, G. E. & Vila, G. S. 2008, *The proton low-mass microquasar: high-energy emission*, A&A, 485, 623

Rowlinson, A., Gourdji, K., van der Meulen, K., et al. 2019, *LOFAR early-time search for coherent radio emission from GRB 180706A*, MNRAS, 490, 3483

Rowlinson, A., Meijn, J., Bright, J., et al. 2022, *Search and identification of transient and variable radio sources using MeerKAT observations: a case study on the MAXI J1820+070 field*, arXiv e-prints, arXiv:2203.16918

Rowlinson, A., O'Brien, P. T., Metzger, B. D., Tanvir, N. R., & Levan, A. J. 2013, *Signatures of magnetar central engines in short GRB light curves*, MNRAS, 430, 1061

Rowlinson, A., Starling, R. L. C., Gourdji, K., et al. 2021, *LOFAR early-time search for coherent radio emission from short GRB 181123B*, MNRAS, 506, 5268

Ruderman, M. A. & Sutherland, P. G. 1975, *Theory of pulsars: polar gaps, sparks, and coherent microwave radiation.*, ApJ, 196, 51

Russell, T. D., Soria, R., Miller-Jones, J. C. A., et al. 2014, *The accretion-ejection coupling in the black hole candidate X-ray binary MAXI J1836-194*, MNRAS, 439, 1390

Russell, T. D., Tetarenko, A. J., Miller-Jones, J. C. A., et al. 2019, *Disk–Jet Coupling in the 2017/2018 Outburst of the Galactic Black Hole Candidate X-Ray Binary MAXI J1535–571*, ApJ, 883, 198

Ryan, G., van Eerten, H., Piro, L., & Troja, E. 2020, *Gamma-Ray Burst Afterglows in the Multimessenger Era: Numerical Models and Closure Relations*, ApJ, 896, 166

Ryan, M. J., Ormes, J. F., & Balasubrahmanyan, V. K. 1972, *Cosmic-Ray Proton and Helium Spectra above 50 GeV*, Phys. Rev. Lett., 28, 985

Rybicki, G. B. & Lightman, A. P. 1986, Radiative Processes in Astrophysics

Sadowski, A., Ziółkowski, J., Belczyński, K., & Bulik, T. 2008, *Calculations of the Galactic Population of Black Hole X-Ray Binaries*, in American Institute of Physics Conference Series, Vol. 1010, A Population Explosion: The Nature & Evolution of X-ray Binaries in Diverse Environments, ed. R. M. Bandyopadhyay, S. Wachter, D. Gelino, & C. R. Gelino, 404–406

Sagiv, A. & Waxman, E. 2002, *Collective Processes in Relativistic Plasma and Their Implications for Gamma-Ray Burst Afterglows*, ApJ, 574, 861

Salpeter, E. E. 1955, *The Luminosity Function and Stellar Evolution.*, ApJ, 121, 161

Sanidas, S., Cooper, S., Bassa, C. G., et al. 2019, *The LOFAR Tied-Array All-Sky Survey (LOTAAS): Survey overview and initial pulsar discoveries*, A&A, 626, A104

Sari, R., Piran, T., & Halpern, J. P. 1999, *Jets in Gamma-Ray Bursts*, ApJ, 519, L17

Sari, R., Piran, T., & Narayan, R. 1998, *Spectra and Light Curves of Gamma-Ray Burst Afterglows*, ApJ, 497, L17

Scholz, P., Bogdanov, S., Hessels, J. W. T., et al. 2017, *Simultaneous X-Ray, Gamma-Ray, and Radio Observations of the Repeating Fast Radio Burst FRB 121102*, ApJ, 846, 80

Sedov, L. I. 1959, Similarity and Dimensional Methods in Mechanics

Shakura, N. I. & Sunyaev, R. A. 1976, *A theory of the instability of disk accretion on to black holes and the variability of binary X-ray sources, galactic nuclei and quasars.*, MNRAS, 175, 613

Sironi, L. & Giannios, D. 2013, *A Late-time Flattening of Light Curves in Gamma-Ray Burst Afterglows*, ApJ, 778, 107

Sironi, L., Keshet, U., & Lemoine, M. 2015a, *Relativistic Shocks: Particle Acceleration and Magnetization*, Space Sci. Rev., 191, 519

Sironi, L., Petropoulou, M., & Giannios, D. 2015b, *Relativistic jets shine through shocks or magnetic reconnection?*, MNRAS, 450, 183

Sironi, L., Plotnikov, I., Nättilä, J., & Beloborodov, A. M. 2021, *Coherent Electromagnetic Emission from Relativistic Magnetized Shocks*, Phys. Rev. Lett., 127, 035101

Sironi, L. & Spitkovsky, A. 2009, *Particle Acceleration in Relativistic Magnetized Collisionless Pair Shocks: Dependence of Shock Acceleration on Magnetic Obliquity*, ApJ, 698, 1523

Sironi, L. & Spitkovsky, A. 2011, *Particle Acceleration in Relativistic Magnetized Collisionless Electron-Ion Shocks*, ApJ, 726, 75

Sironi, L., Spitkovsky, A., & Arons, J. 2013, *The Maximum Energy of Accelerated Particles in Relativistic Collisionless Shocks*, ApJ, 771, 54

Slysh, V. I. 1992, *The synchro-Compton limit of the brightness temperature of nonstationary radio sources*, ApJ, 391, 453

Soderberg, A. M., Berger, E., Kasliwal, M., et al. 2006, *The Afterglow, Energetics, and Host Galaxy of the Short-Hard Gamma-Ray Burst 051221a*, ApJ, 650, 261

B

Spera, M., Mapelli, M., & Bressan, A. 2015, *The mass spectrum of compact remnants from the PARSEC stellar evolution tracks*, MNRAS, 451, 4086

Spitkovsky, A. 2008, *Particle Acceleration in Relativistic Collisionless Shocks: Fermi Process at Last?*, ApJ, 682, L5

Spitler, L. G., Cordes, J. M., Hessels, J. W. T., et al. 2014, *Fast Radio Burst Discovered in the Arecibo Pulsar ALFA Survey*, ApJ, 790, 101

Spitler, L. G., Scholz, P., Hessels, J. W. T., et al. 2016, *A repeating fast radio burst*, Nature, 531, 202

Sridhar, N., Metzger, B. D., Beniamini, P., et al. 2021, *Periodic Fast Radio Bursts from Luminous X-ray Binaries*, ApJ, 917, 13

Stein, R., Velzen, S. v., Kowalski, M., et al. 2021, *A tidal disruption event coincident with a high-energy neutrino*, Nature Astronomy, 5, 510

Strong, A. W., Moskalenko, I. V., & Ptuskin, V. S. 2007, *Cosmic-Ray Propagation and Interactions in the Galaxy*, Annual Review of Nuclear and Particle Science, 57, 285

Sturrock, P. A. 1971, *A Model of Pulsars*, ApJ, 164, 529

Sudoh, T., Inoue, Y., & Khangulyan, D. 2019, *Multi-wavelength Emission from Galactic Jets: the Case of the Microquasar SS433*, arXiv e-prints, arXiv:1911.00013

Suvorov, A. G. & Kokkotas, K. D. 2019, *Young magnetars with fracturing crusts as fast radio burst repeaters*, MNRAS, 488, 5887

Suvorov, A. G. & Kokkotas, K. D. 2020, *Precursor flares of short gamma-ray bursts from crust yielding due to tidal resonances in coalescing binaries of rotating, magnetized neutron stars*, Phys. Rev. D, 101, 083002

Suvorov, A. G., Kuan, H.-J., & Kokkotas, K. D. 2022, *Quasi-periodic oscillations in precursor flares via seismic aftershocks from resonant shattering*, arXiv e-prints, arXiv:2205.11112

Swinbank, J. D., Staley, T. D., Molenaar, G. J., et al. 2015, *The LOFAR Transients Pipeline*, Astronomy and Computing, 11, 25

Symbalisty, E. & Schramm, D. N. 1982, *Neutron Star Collisions and the r-Process*, Astrophys. Lett., 22, 143

Takeda, M., Hayashida, N., Honda, K., et al. 1999, *Small-Scale Anisotropy of Cosmic Rays above 10^{19} eV Observed with the Akeno Giant Air Shower Array*, ApJ, 522, 225

Tanaka, Y. T., Terasawa, T., Yoshida, M., Horie, T., & Hayakawa, M. 2008, *Ionospheric disturbances caused by SGR 1900+14 giant gamma ray flare in 1998: Constraints on the energy spectrum of the flare*, Journal of Geophysical Research (Space Physics), 113, A07307

B

Tanvir, N. R., Levan, A. J., González-Fernández, C., et al. 2017, *The Emergence of a Lanthanide-rich Kilonova Following the Merger of Two Neutron Stars*, ApJ, 848, L27

Tauris, T. M., Kramer, M., Freire, P. C. C., et al. 2017, *Formation of Double Neutron Star Systems*, ApJ, 846, 170

Tavani, M., Bulgarelli, A., Piano, G., et al. 2009, *Extreme particle acceleration in the microquasar CygnusX-3*, Nature, 462, 620

Tavani, M., Casentini, C., Ursi, A., et al. 2021, *An X-ray burst from a magnetar enlightening the mechanism of fast radio bursts*, Nature Astronomy, 5, 401

Taylor, G. 1950, *The Formation of a Blast Wave by a Very Intense Explosion. I. Theoretical Discussion*, Proceedings of the Royal Society of London Series A, 201, 159

Taylor, J. H. & Cordes, J. M. 1993, *Pulsar Distances and the Galactic Distribution of Free Electrons*, ApJ, 411, 674

Taylor, J. H. & Weisberg, J. M. 1982, *A new test of general relativity - Gravitational radiation and the binary pulsar PSR 1913+16*, ApJ, 253, 908

ter Veen, S., Enriquez, J. E., Falcke, H., et al. 2019, *The FRATS project: real-time searches for fast radio bursts and other fast transients with LOFAR at 135 MHz*, A&A, 621, A57

Terrier, R., Ponti, G., Bélanger, G., et al. 2010, *Fading Hard X-ray Emission from the Galactic Center Molecular Cloud Sgr B2*, ApJ, 719, 143

Tetarenko, A. J., Sivakoff, G. R., Miller-Jones, J. C. A., et al. 2017, *Extreme jet ejections from the black hole X-ray binary V404 Cygni*, MNRAS, 469, 3141

Tetarenko, B., Sivakoff, G., Heinke, C., & Gladstone, J. 2016a, *WATCHDOG: A Comprehensive All-sky Database of Galactic Black Hole X-ray Binaries*, ApJS, 222, 15

Tetarenko, B. E., Bahramian, A., Arnason, R. M., et al. 2016b, *The First Low-mass Black Hole X-Ray Binary Identified in Quiescence Outside of a Globular Cluster*, ApJ, 825, 10

The CHIME/FRB Collaboration, :, Amiri, M., et al. 2021a, *The First CHIME/FRB Fast Radio Burst Catalog*, arXiv e-prints, arXiv:2106.04352

The CHIME/FRB Collaboration, Andersen, B. C., Bandura, K., et al. 2021b, *Sub-second periodicity in a fast radio burst*, arXiv e-prints, arXiv:2107.08463

The Chime/Frb Collaboration, Andersen, B. Â. C., Band ura, K. Â. M., Bhardwaj, M., et al. 2020, *A bright millisecond-duration radio burst from a Galactic magnetar*, Nature, 587, 54

The Pierre Auger Collaboration, Aab, A., Abreu, P., et al. 2016, *The Pierre Auger Observatory Upgrade - Preliminary Design Report*, arXiv e-prints, arXiv:1604.03637

Thompson, A. R., Clark, B. G., Wade, C. M., & Napier, P. J. 1980, *The Very Large Array.*, ApJS, 44, 151

Thompson, C. & Duncan, R. C. 1995, *The soft gamma repeaters as very strongly magnetized neutron stars - I. Radiative mechanism for outbursts*, MNRAS, 275, 255

Thompson, C. & Duncan, R. C. 1996, *The Soft Gamma Repeaters as Very Strongly Magnetized Neutron Stars. II. Quiescent Neutrino, X-Ray, and Alfven Wave Emission*, ApJ, 473, 322

Thornton, D., Stappers, B., Bailes, M., et al. 2013, *A Population of Fast Radio Bursts at Cosmological Distances*, Science, 341, 53

Thorsett, S. E. 1992, *Identification of the pulsar PSR1509-58 with the 'guest star' of AD 185*, Nature, 356, 690

Thoudam, S., Rachen, J. P., van Vliet, A., et al. 2016, *Cosmic-ray energy spectrum and composition up to the ankle: the case for a second Galactic component*, A&A, 595, A33

Tian, J., Anderson, G. E., Hancock, P. J., et al. 2022, *Early-time searches for coherent radio emission from short GRBs with the Murchison Widefield Array*, PASA, 39, e003

Timokhin, A. N. 2010, *Time-dependent pair cascades in magnetospheres of neutron stars - I. Dynamics of the polar cap cascade with no particle supply from the neutron star surface*, MNRAS, 408, 2092

Timokhin, A. N. & Arons, J. 2013, *Current flow and pair creation at low altitude in rotation-powered pulsars' force-free magnetospheres: space charge limited flow*, MNRAS, 429, 20

Timokhin, A. N. & Harding, A. K. 2015, *On the Polar Cap Cascade Pair Multiplicity of Young Pulsars*, ApJ, 810, 144

Timokhin, A. N. & Harding, A. K. 2019, *On the Maximum Pair Multiplicity of Pulsar Cascades*, ApJ, 871, 12

Tingay, S. J., Goeke, R., Bowman, J. D., et al. 2013, *The Murchison Widefield Array: The Square Kilometre Array Precursor at Low Radio Frequencies*, PASA, 30, e007

Tohuvavohu, A., Kennea, J. A., DeLaunay, J., et al. 2020, *Gamma-Ray Urgent Archiver for Novel Opportunities (GUANO): Swift/BAT Event Data Dumps on Demand to Enable Sensitive Subthreshold GRB Searches*, ApJ, 900, 35

Tominaga, N., Niino, Y., Totani, T., et al. 2018, *Optical follow-up observation of Fast Radio Burst 151230*, PASJ, 70, 103

Torchinsky, S. A., Broderick, J. W., Gunst, A., Faulkner, A. J., & van Cappellen, W. 2016, *SKA Aperture Array Mid Frequency Science Requirements*, arXiv e-prints, arXiv:1610.00683

Totani, T. 2013, *Cosmological Fast Radio Bursts from Binary Neutron Star Mergers*, PASJ, 65, L12

B

Tremblay, S. E., Ord, S. M., Bhat, N. D. R., et al. 2015, *The High Time and Frequency Resolution Capabilities of the Murchison Widefield Array*, PASA, 32, e005

Troja, E., Rosswog, S., & Gehrels, N. 2010, *Precursors of Short Gamma-ray Bursts*, ApJ, 723, 1711

Tsang, D., Read, J. S., Hinderer, T., Piro, A. L., & Bondarescu, R. 2012, *Resonant Shattering of Neutron Star Crusts*, Phys. Rev. Lett., 108, 011102

Tudose, V., Fender, R. P., Kaiser, C. R., et al. 2006, *The large-scale jet-powered radio nebula of Circinus X-1*, MNRAS, 372, 417

Tyson, J. A. 2002, *Large Synoptic Survey Telescope: Overview*, in Society of Photo-Optical Instrumentation Engineers (SPIE) Conference Series, Vol. 4836, Survey and Other Telescope Technologies and Discoveries, ed. J. A. Tyson & S. Wolff, 10–20

Usov, V. V. 1987, *On Two-Stream Instability in Pulsar Magnetospheres*, ApJ, 320, 333

Usov, V. V. & Katz, J. I. 2000, *Low frequency radio pulses from gamma-ray bursts?*, A&A, 364, 655

Vachaspati, T. 2008, *Cosmic Sparks from Superconducting Strings*, Phys. Rev. Lett., 101, 141301

van den Heuvel, E. P. J. 1977, *Evolutionary Processes in X-Ray Binaries and Their Progenitor Systems*, in Eighth Texas Symposium on Relativistic Astrophysics, ed. M. D. Papagiannis, Vol. 302, 14

van der Horst, A. J., Kouveliotou, C., Gorgone, N. M., et al. 2012, *SGR J1550-5418 Bursts Detected with the Fermi Gamma-Ray Burst Monitor during its Most Prolific Activity*, ApJ, 749, 122

van der Laan, H. 1966, *A Model for Variable Extragalactic Radio Sources*, Nature, 211, 1131

van Haarlem, M. P., Wise, M. W., Gunst, A. W., et al. 2013, *LOFAR: The LOw-Frequency ARray*, A&A, 556, A2

van Paradijs, J., Groot, P. J., Galama, T., et al. 1997, *Transient optical emission from the error box of the γ-ray burst of 28 February 1997*, Nature, 386, 686

Vanderlinde, K., Liu, A., Gaensler, B., et al. 2019, *The Canadian Hydrogen Observatory and Radio-transient Detector (CHORD)*, in Canadian Long Range Plan for Astronomy and Astrophysics White Papers, Vol. 2020, 28

Vietri, M. 1996, *Magnetospheric Interactions of Binary Pulsars as a Model for Gamma-Ray Bursts*, ApJ, 471, L95

Vigna-Gómez, A., Neijssel, C. J., Stevenson, S., et al. 2018, *On the formation history of Galactic double neutron stars*, MNRAS, 481, 4009

B

Vila, G. S. & Romero, G. E. 2011, *A model for jets of low-mass microquasars*, ArXiv e-prints

Vink, J. & Laming, J. M. 2003, *On the Magnetic Fields and Particle Acceleration in Cassiopeia A*, ApJ, 584, 758

Voisin, G., Mottez, F., & Zarka, P. 2021, *Periodic activity from fast radio burst FRB180916 explained in the frame of the orbiting asteroid model*, MNRAS, 508, 2079

Voss, R. & Tauris, T. M. 2003, *Galactic distribution of merging neutron stars and black holes - prospects for short gamma-ray burst progenitors and LIGO/VIRGO*, MNRAS, 342, 1169

Wadiasingh, Z., Baring, M. G., Gonthier, P. L., & Harding, A. K. 2018, *Resonant Inverse Compton Scattering Spectra from Highly Magnetized Neutron Stars*, ApJ, 854, 98

Wadiasingh, Z., Beniamini, P., Timokhin, A., et al. 2020, *The Fast Radio Burst Luminosity Function and Death Line in the Low-twist Magnetar Model*, ApJ, 891, 82

Wadiasingh, Z. & Chirenti, C. 2020, *Fast Radio Burst Trains from Magnetar Oscillations*, ApJ, 903, L38

Wadiasingh, Z. & Timokhin, A. 2019, *Repeating Fast Radio Bursts from Magnetars with Low Magnetospheric Twist*, ApJ, 879, 4

Wang, J.-S., Yang, Y.-P., Wu, X.-F., Dai, Z.-G., & Wang, F.-Y. 2016, *Fast Radio Bursts from the Inspiral of Double Neutron Stars*, ApJ, 822, L7

Wang, W., Zhang, B., Chen, X., & Xu, R. 2019, *On the Time-Frequency Downward Drifting of Repeating Fast Radio Bursts*, ApJ, 876, L15

Wang, W.-Y., Yang, Y.-P., Niu, C.-H., Xu, R., & Zhang, B. 2022, *Magnetospheric Curvature Radiation by Bunches as Emission Mechanism for Repeating Fast Radio Bursts*, ApJ, 927, 105

Wasserman, I. & Shapiro, S. L. 1983, *Masses, radii, and magnetic fields of pulsating X-ray sources : is the "standard" model self-consistent ?*, ApJ, 265, 1036

Waxman, E. 1997, *Gamma-Ray–Burst Afterglow: Supporting the Cosmological Fireball Model, Constraining Parameters, and Making Predictions*, ApJ, 485, L5

Weber, J. 1969, *Evidence for Discovery of Gravitational Radiation*, Phys. Rev. Lett., 22, 1320

Weisberg, J. M., Taylor, J. H., & Fowler, L. A. 1981, *Gravitational waves from an orbiting pulsar*, Scientific American, 245, 74

Wijers, R. A. M. J. & Galama, T. J. 1999, *Physical Parameters of GRB 970508 and GRB 971214 from Their Afterglow Synchrotron Emission*, ApJ, 523, 177

Williams, P. K. G. & Berger, E. 2016, *No Precise Localization for FRB 150418: Claimed Radio Transient Is AGN Variability*, ApJ, 821, L22

Williams, R. D. & Seaman, R. 2006, *VOEvent: Information Infrastructure for Real-Time Astronomy*, in Astronomical Society of the Pacific Conference Series, Vol. 351, Astronomical Data Analysis Software and Systems XV, ed. C. Gabriel, C. Arviset, D. Ponz, & S. Enrique, 637

Wood, J., Bissaldi, E., & Fermi GBM Team. 2019, *Fermi/GBM observation of a bright burst from magnetar SGR 1935+2154*, GRB Coordinates Network, 25975, 1

Wright, E. L. 2006, *A Cosmology Calculator for the World Wide Web*, PASP, 118, 1711

Xiao, S., Zhang, Y.-Q., Zhu, Z.-P., et al. 2022, *The quasi-periodically oscillating precursor of a long gamma-ray burst from a binary neutron star merger*, arXiv e-prints, arXiv:2205.02186

Yang, Y.-P. & Zhang, B. 2018, *Bunching Coherent Curvature Radiation in Three-dimensional Magnetic Field Geometry: Application to Pulsars and Fast Radio Bursts*, ApJ, 868, 31

Yang, Y.-P. & Zhang, B. 2021, *Fast Radio Bursts and Their High-energy Counterparts from Magnetar Magnetospheres*, ApJ, 919, 89

Yang, Y.-P., Zhang, B., & Wei, J.-Y. 2019, *How Bright Are Fast Optical Bursts Associated With Fast Radio Bursts?*, ApJ, 878, 89

Yang, Y.-P., Zhu, J.-P., Zhang, B., & Wu, X.-F. 2020, *Pair Separation in Parallel Electric Field in Magnetar Magnetosphere and Narrow Spectra of Fast Radio Bursts*, ApJ, 901, L13

Ye, C. S., Fong, W.-f., Kremer, K., et al. 2020, *On the Rate of Neutron Star Binary Mergers from Globular Clusters*, ApJ, 888, L10

Younes, G., Baring, M. G., Kouveliotou, C., et al. 2020, *A possible polar origin for the FRB associated with a Galactic magnetar*, arXiv e-prints, arXiv:2006.11358

Younes, G., Baring, M. G., Kouveliotou, C., et al. 2021, *Broadband X-ray burst spectroscopy of the fast-radio-burst-emitting Galactic magnetar*, Nature Astronomy

Yuan, Q., Liu, S., Fan, Z., Bi, X., & Fryer, C. L. 2011, *Modeling the Multi-Wavelength Emission of the Shell-type Supernova Remnant RX J1713.7-3946*, ApJ, 735, 120

Yungelson, L. R., Lasota, J. P., Nelemans, G., et al. 2006, *The origin and fate of short-period low-mass black-hole binaries*, A&A, 454, 559

Yushkov, A. 2019, *Mass Composition of Cosmic Rays with Energies above 10(17.2) eV from the Hybrid Data of the Pierre Auger Observatory*, in International Cosmic Ray Conference, Vol. 36, 36th International Cosmic Ray Conference (ICRC2019), 482

Zanin, R., Fernández-Barral, A., de Oña Wilhelmi, E., et al. 2016, *Gamma rays detected from Cygnus X-1 with likely jet origin*, A&A, 596, A55

Zdziarski, A. A., Pjanka, P., Sikora, M., & Stawarz, Ł. 2014, *Jet contributions to the broadband spectrum of Cyg X-1 in the hard state*, MNRAS, 442, 3243

B

Zhang, B. 2014, *A Possible Connection between Fast Radio Bursts and Gamma-Ray Bursts*, ApJ, 780, L21

Zhang, B. 2016, *Mergers of Charged Black Holes: Gravitational-wave Events, Short Gamma-Ray Bursts, and Fast Radio Bursts*, ApJ, 827, L31

Zhang, B. 2020, *The physical mechanisms of fast radio bursts*, Nature, 587, 45

Zhang, S., Hailey, C. J., Mori, K., et al. 2015, *Hard X-Ray Morphological and Spectral Studies of the Galactic Center Molecular Cloud Sgr B2: Constraining Past Sgr A* Flaring Activity*, ApJ, 815, 132

Zhou, P., Zhou, X., Chen, Y., et al. 2020, *Revisiting the Distance, Environment, and Supernova Properties of SNR G57.2+0.8 that Hosts SGR 1935+2154*, ApJ, 905, 99

B

Publications

First-author articles

1. **Cooper, A. J.**, Rowlinson, A., Wijers, R. A. M. J., Bassa, C., Gourdji, K., Hessels, J., van der Horst, A., Kondratiev, V., Michilli, D., Pleunis, Z., Shimwell, T., ter Veen, S. (2022)
Accepted for publication in the *Monthly Notices of the Royal Astronomical Society*. (**Chapter 5**)
Testing afterglow models of FRB 200428 with early post-burst observations of SGR 1935+2154

2. **Cooper, A. J.**, Gupta, O., Wijers, R.A.M.J., Wadiasingh, Z., Boersma, O., Andreoni, I., Rowlinson, A., Gourdji, K. (2022)
Submitted to the *Monthly Notices of the Royal Astronomical Society*. (**Chapter 4**)
Pulsar revival in neutron star mergers: multi-messenger prospects for the discovery of pre-merger coherent radio emission

3. **Cooper, A. J.** & Wijers, R. A. M. J. (2021)
Monthly Notices of the Royal Astronomical Society Letters, 508, 1, L32-L36 (**Chapter 3**)
Coherent curvature radiation: maximum luminosity and high-energy emission

4. **Cooper, A. J.**, Gaggero, D., Markoff, S., Zhang, S. (2020)
Monthly Notices of the Royal Astronomical Society, 493, 3, pp. 3212-3222 (**Chapter 2**)
High-energy cosmic rays from X-ray binary jets

Co-authored articles

1. Bailes, M., Bassa, C. G., Bernardi, G., Buchner, S. , Burgay, M., Caleb, M., **Cooper, A. J.**, Desvignes, G., Groot, P. J., Heywood, I., Jankowski, F., Karuppusamy, R., Kramer, M., Malenta, M., Naldi, G., Pilia, M., Pupillo, G., Rajwade, K. M. , Spitler, L., Surnis, M. Stappers, B. W. , Addis, A., Bloemen, S., Bezuidenhout, M. C., Bianchi, G., Champion, D. J., Chen, W., Driessen, L. N., Geyer, M. , Gourdji, K. , Hessels, J. W. T., Kondratiev, V. I., Klein-Wolt, M., Körding, E., Le Poole, R., Liu, K., Lower, M. E. , Lyne, A. G., Magro, A., McBride, V., Mickaliger, M. B., Morello, V. , Parthasarathy, A. , Paterson, K., Perera, B. B. P. , Pieterse, D. L. A., Pleunis, Z., Possenti, A., Rowlinson, A. , Serylak, M. , Setti, G., Tavani, M., Wijers, R. A. M. J., ter Veen, S., Venkatraman Krishnan, V., Vreeswijk, P., Woudt, P. A. (2021)

Monthly Notices of the Royal Astronomical Society, 503, 4, 5367
Multifrequency observations of SGR J1935+2154

2. Kantzas, D., Markoff, S., **Cooper, A. J.**, Gaggero, D., Petropoulou, M., De La Torre Luque, P. (2022)
To be submitted to the *Monthly Notices of the Royal Astronomical Society*
Exploring neutrino and cosmic ray production in X-ray binary jets using multi-wavelength case studies

Astronomers telegrams

1. Bassa, C., Hessels, J., Kondratiev, V., Michilli, D., Pleunis, Z., **Cooper, A. J.**, Gourdji, K., Rowlinson, A., Wijers, R., (2020)
Astronomer's Telegram, 13707
A LOFAR high time resolution search for radio bursts from SGR 1935+2154

Contribution from co-authors

Here we list bibliographic information of the papers included in this thesis. The relative contribution of every coauthor is represented by their place in the author list. Chapter 2 was executed under the supervision of Sera Markoff, and all other chapters pertain to work done under the supervision of Ralph Wijers and Antonia Rowlinson.

Chapter 2: High-energy cosmic ray production in X-ray binary jets

A. J. Cooper, D. Gaggero, S. Markoff, S. Zhang
Monthly Notices of the Royal Astronomical Society, 2020, 493, 3212

- AJC led the theoretical calculation, analysis and writing of the manuscript. DG provided supervision and contributed extensively to the execution of numerical cosmic ray propagation simulations. SM conceived of the idea for the project and provided supervision and guidance throughout. SZ provided theoretical input for the low-energy constraints on the cosmic ray spectrum.

Chapter 3: Coherent curvature radiation: maximum luminosity and high-energy emission

A. J. Cooper, R. A. M. J. Wijers
Monthly Notices of the Royal Astronomical Society Letters, 2021, 508, L32

- AJC conceived of the idea for the manuscript, and led the theoretical calculation and writing of the manuscript. RAMJW provided extensive supervision, guidance and mentorship throughout.

Chapter 4: Pulsar revival in neutron star mergers: multi-messenger prospects for the discovery of pre-merger coherent radio emission

A. J. Cooper, O. Gupta, R. A. M. J. Wijers, Z. Wadiasingh, O. M. Boersma, I. Andreoni, A. Rowlinson, K. Gourdji
Submitted to the *Monthly Notices of the Royal Astronomical Society*

- AJC conceived of the idea of the manuscript and led the analysis and writing unless otherwise stated. OG led the re-calculation of the corrected electromagnetic conditions of the inspiral and contributed to the overall analysis. RAMJW supervised the project. ZW provided extensive theoretical support pertaining to the pulsar emission mechanism and contributed to the interpretation of the results. OMB led gravitational wave horizon calculations, provided viewing angle dependent gravitational wave horizons and led in part the writing of that section. IA provided the viewing angle dependent kilonovae horizon calculation. AR and KG contributed to the interpretation of our theoretical findings, particularly pertaining to the current & future status of fast radio burst searches and rapid radio observations of gamma-ray bursts and gravitational wave events.

Chapter 5: Testing afterglow models of FRB 200428 with early post-burst observations of SGR 1935+2154

A. J. Cooper, A. Rowlinson, R. A. M. J. Wijers, C. Bassa, K. Gourdji, J. Hessels, A. J. van der Horst, V. Kondratiev, D. Michilli, Z. Pleunis, T. Shimwell, S. ter Veen
Accepted for publication in the *Monthly Notices of the Royal Astronomical Society*

- AJC was principal investigator of two of the observing proposals, co-investigator of the one of the proposals, and led the theoretical interpretation and writing of the manuscript. AR was a co-investigator and led the reduction and calibration of the LOFAR data sets, and wrote the section presenting LOFAR observations. RAMJW and AR supervised the project throughout. CB was the principal investigator for one of the observing proposals, and co-investigators of the others. KG, JH, AvdH, VK, DM, ZP, TS and StV contributed as co-investigators of one or more of the observing proposals.

English summary

Compact objects, neutron stars and black holes (and white dwarfs), are dense, mysterious astronomical sources. They form at the end of stars' lives, or after the merger of two other stellar objects, floating through interstellar space invisible to astronomers searching for them. However, when they are young or in binary systems, they can produce a variety of transient and explosive phenomena visible to us on Earth through a particular wavelength of light or another messenger. This is not an uncommon occurrence, as most stars (particularly more massive ones) are born in binary systems. As they evolve together burning away their hydrogen fuel, eventually one of the pair will undergo a supernova explosion, sometimes producing a young, magnetized neutron star known as a pulsar or a magnetar, or possibly a black hole. These neutron stars can produce a wide range of pulses, bursts and explosions across the electromagnetic spectrum, powered by large magnetic fields and rapid rotations (Chapter 3 & 5).

Occasionally, the star and the newly born compact object can stay together despite the difficulties encountered by the violent supernova. In this case, if the objects are sufficiently close in orbit, the star may begin accreting matter onto the compact object. This can occur either when matter is pulled directly from the stellar surface due to the compact objects' gravitational pull, or due to the stars own powerful stellar winds blowing off material towards its companion. Conservation of angular momentum dictates that this transferred matter forms into a disc around the compact object. This accretion disc shines in X rays and launches powerful outflows of ejected matter and accelerated particles known as jets, which vary on day to year timescales (Chapter 2).

As the compact object and star binary continue to evolve together, the donor star may also eventually explode in a supernova. If, possibly against the odds, the binary pair's orbit stays bound despite this second explosion, a compact object binary forms. These two compact objects are often far apart and initially only interact through due to their motion through space and time. The resulting gravitational radiation, ripples through space-time that propagate across the Universe, is the only signature of their cosmic dance. Eventually, often on timescales nearly as long as the Universe itself, the objects will have radiated sufficient energy such that their orbits decrease to the point of merger. This final, most energetic of transients is detectable across the electromagnetic spectrum, as well as in gravitational waves, as the gravitational chirp ripples through space-time to perturb our own perception of length and time on Earth (Chapter 4).
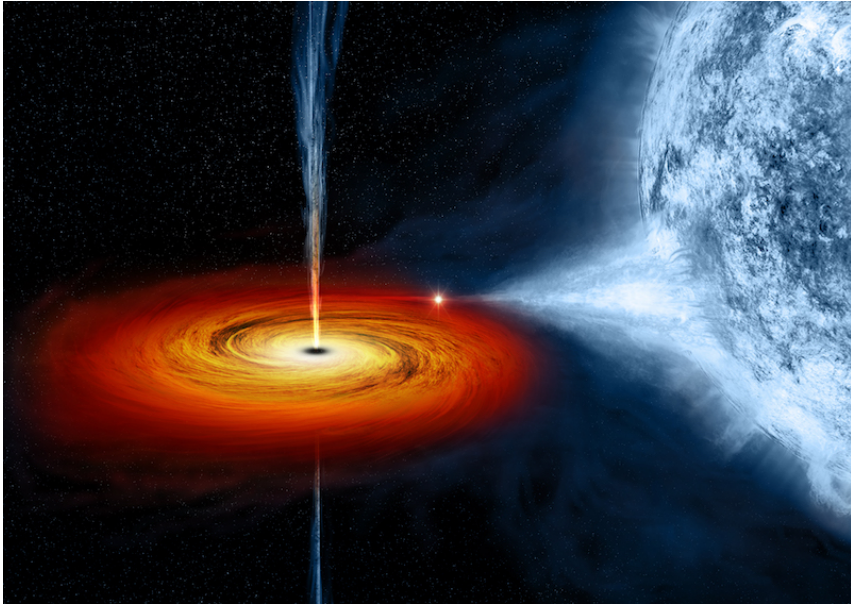
Figure A: An artist's impression of Cygnus X-1, a black hole X-ray Binary (NASA/CXC/M.Weiss)

In the following, I will briefly summarise the research contained within the four science chapters of this thesis.

- **Chapter 2 - High-energy cosmic ray production in X-ray binary jets**

    Chapter 2 examines the jets of X-ray binary systems, a binary system involving a compact object and a star, as particle accelerators. The primary aim of the chapter is to understand how significant is the X-ray binary contribution to the cosmic ray spectrum: an observed flux of astrophysically accelerated protons and ions.

    The chapter is particularly focused on black hole X-ray binaries, sources in which the compact object is a black hole, as astronomical observations conducted thus far across the electromagnetic spectrum indicate these systems are the most efficient particle accelerators. We estimate the Galactic population of X-ray binaries by considering theoretical population synthesis studies rooted in the physics of binary evolution and recent observations of the dense centre of the Galaxy where X-ray binary systems are thought to reside.

    Using observed X-ray and radio properties of black hole X-ray binary systems, an empirical relationship is employed to find the mean jet power. First principles particle acceleration simulations imply a small percentage of the jet energy powers the acceleration hadronic particles (protons, and other heavier ions) during shocks. The total Galactic hadronic acceleration power stemming from shocks within X-ray binary jets is then compared to the known Galactic cosmic ray luminosity.

To gain a fuller understanding of how accelerated particles in jets end up as cosmic rays, we simulate the propagation of these accelerated hadrons from X-ray binaries using the DRAGON code. This allows us to also understand which other messengers are produced from these cosmic rays during their propagation to Earth, along winding paths bent by the interstellar magnetic field. In particular, we calculate the diffuse gamma rays and neutrinos that arise due to the cosmic rays' interactions with the interstellar medium.

We find that up to 10% of Galactic cosmic ray luminosity could be accelerated in X-ray binary jets. Furthermore, jets have the capability to accelerate particles above 1 PeV (10^{15} electron-volts), and possibly to the second knee feature in the observed spectrum at around ~100 PeV. This finding may aid in explaining these peculiar features in the cosmic ray spectrum during the transition from Galactic to extra-Galactic sources. Finally, we find that any second significant Galactic component to the cosmic ray spectrum that has a higher energy cut-off than the primary component (thought to be supernova remnants) should be verifiable through a break in the diffuse Galactic neutrino spectrum in the coming years.

- **Chapter 3 - Coherent curvature radiation: maximum luminosity and high-energy emission**

In this chapter of the thesis, we investigate transient radio bursts from magnetized neutron stars. We consider in detail one radiation mechanism in which very bright *coherent* radio emission can be produced, known as coherent curvature radiation. Coherent emission is a specific type of observed astrophysical radiation in which observed emission is too bright and too short in duration to be explained by the sum of individually emitting particles. Instead, accelerated particles behave and emit in an organised manner similar to a laser beam, boosting the total emitted and observed power.

Particle acceleration close to neutron stars is generally powered by rotation-induced steady electric fields, or transient electric fields arising due to a change in magnetospheric properties. Accelerated particles are directed along magnetic field lines, as strong electromagnetic forces radiate away motion perpendicular to the field lines. The curvature of field lines results in an acceleration component perpendicular to the particles' momenta resulting in radiation, similar to centripetal acceleration during uniform circular motion. Coherence is invoked due to the particles' proximities to each other both spatially and in momentum space. In this way, bunches of particles confined to one emission wavelength in the observer frame and having well-aligned momenta, effectively radiate as one large clump of charge equal to the sum of all charges in the clump.

We find that the accelerated particles themselves perturb the magnetic field lines along which they propagate. The net effect is that instead of moving along the slowly curving neutron star magnetic field lines, individual particles move along helical curves, similar to a bent spring. This has two important consequences. Firstly, there is a maximum coherent luminosity for each bunch of particles, that depends on the properties of the

Figure B: An artist's impression of a magnetar, a highly magnetized neutron star (Maciej Rebisz/Quanta Magazine)

bunch and therefore the properties of the neutron star itself. This stems from the fact that if the magnetic field lines are too tightly wound, individual particles will not longer have their directions of motion well-aligned, which breaks the coherence. Secondly, the perturbations to the particles' paths leads to a small-scale acceleration transverse to the guiding neutron star magnetic field lines. This results in an additional, subdominant, *incoherent* component to the bunches' radiation at high frequencies. It is found that this component is nominally emitted in the X-ray or gamma-ray band for sources of interest, and may be detectable for the brightest radio bursts in some conditions.

These consequences are compared to the observed properties of transient radio bursts from the Crab Pulsar, the bright FRB 200428 observed from the Galactic magnetar SGR 1935+2154, and extra-Galactic fast radio bursts of unknown origin. We show that the maximum luminosity condition means that the brightest pulses from the Crab pulsar must come from close to the surface of the star. Furthermore, it limits the progenitors of fast radio bursts to only high magnetic field neutron stars within the context of this radiation mechanism. The high-energy component of the emission may be able to explain (a part) of the high-energy burst observed coincidentally with FRB 200428.

- **Chapter 4 - Pulsar revival in neutron star mergers: multi-messenger prospects for the discovery of pre-merger coherent radio emission**

Chapter 4 investigates the possibilities for the detection of emission from neutron star mergers produced before the merger event itself. The magnetospheric interaction between two neutron stars is considered, where one neutron star has a negligible mag-
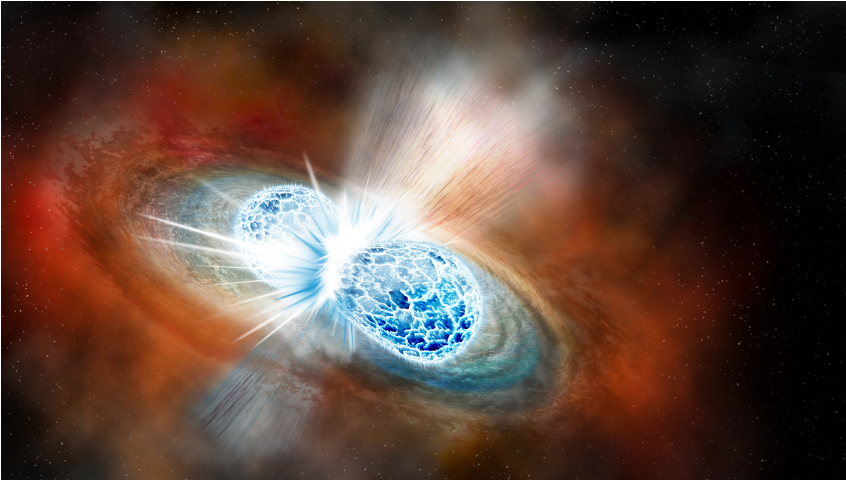
Figure C: An artist's impression of a neutron star merger (Robin Dienel/The Carnegie Institution for Science)

netic field. Such properties are generally expected for typical binary evolutionary chan-
nels, and have been observed for double neutron star systems in our Galaxy.

The first half of the chapter investigates the manner in which particle acceleration and
radiation could occur. We correct calculations in the literature for the electromagnetic
response of a perfect conductor (i.e. the less magnetized neutron star) moving through
a uniform magnetic field, which here represents the magnetosphere of the magnetized
neutron star. Using this, we identify regions in which a strong electric field is present
parallel to local magnetic field lines, conductive to particle acceleration. We estimate
the coherent luminosity of these regions by calculating the height of a vacuum gap that
forms due to high-energy curvature photons interacting with the magnetic field. In this
interaction, photons can produce pairs that screen screen the electric field, similar to
theories of pulsar emission.

Using a semi-analytical framework, we can map this electric field and the perturbed
magnetic field lines as a function of time to understand the direction of particle accel-
eration and radiation. In this way we are able to, for the first time, predict pre-merger
emission in a viewing-angle dependent manner and produce simulated observer-dependent
lightcurves. The emission profile of coherent radio radiation depends on a few key pa-
rameters: the radiative efficiency, the surface magnetic field of the primary magnetized
neutron star, the inclination angle of the system, the magnetic obliquity of the system,
and distance to the merger.

In the second half of the paper, we investigate five possibilities for the discovery of
this pre-merger emission using multi-messenger and multi-wavelength observing tech-
niques. Firstly, the radio bursts may be discovered a fast radio burst without a multi-
messenger or multi-wavelength counterpart. We suggest these pre-merger bursts could

make up a fraction of one-off bursts observed by wide-field instruments, and may be identifiable due to their characteristic temporal structure. Secondly, the pre-merger emission may be detected by rapid observations of gamma-ray bursts performed by low-frequency instruments. The most optimistic parameters (high magnetic field neutron stars with well-aligned systems) have already been probed by low-frequency radio telescopes, where the dispersion delay of radio waves as compared to the prompt gamma-rays allows these instruments to effectively observe before the merger. Thirdly, similar rapid observations may be performed for gravitational-wave events involving a neutron star, particularly important for the upcoming ground-based gravitational-wave detector runs. Fourthly, a gamma-ray burst afterglow may be detectable following a coherent burst without an initial counterpart, to confirm a merger origin of the coherent burst. Finally, a kilonova, a short-lived optical afterglow of a neutron star merger, may be verifiable after a coherent burst in a similar manner.

- **Chapter 5 - Testing afterglow models of FRB 200428 with early post-burst observations of SGR 1935+2154**

Around 14.30 UTC on the 28th of April 2020, an extremely bright radio burst was observed from within our Galaxy from a magnetar SGR 1935+2154. The burst was many orders of magnitude brighter than typical giant pulses previously observed from neutron stars. The properties of this burst were similar to the recently discovered fast radio bursts of unknown origin that originate from other galaxies. Despite being less luminous that typical fast radio bursts, it provided strong evidence that magnetars may be progenitors of fast radio bursts, as had already been proposed in the literature.

The radio burst, also known as FRB 200428, was observed during a highly active period of the magnetar where many transient X-ray bursts were also observed. Of particular note is that one X-ray burst was observed by four separate instruments almost simultaneously to the radio burst. It has a peculiar spectrum as compared to the hundreds of other radio bursts. This represented the first time such a bright radio burst was observed with a multi-wavelength counterpart, providing a unique opportunity to constrain and develop the emission mechanisms proposed to power fast radio bursts. One popular theory of fast radio bursts, the synchrotron maser shock model, is the primary focus for the theoretical part of the paper. In this model, a synchrotron maser powers the fast radio burst, that forms due to shocks as a relativistic blast-wave impacts the surrounding medium. This model can be constrained by post-burst observations, as a multi-wavelength afterglow is predicted as the blast-wave propagates away from the neutron star, similar to the afterglow of a gamma-ray burst.

In this Chapter we present observations of the magnetar taken after FRB 200428 with the Low Frequency Array (LOFAR), an international radio telescope based in the Netherlands. We do not find any emission at the location of the magnetar during deep images across three observing epochs, nor during snapshot imaging on shorter timescales. We first discuss the implications of our LOFAR non-detection. Some magnetars are radio-loud, emitting radio pulsations modulated by their spin period. The

fact that this magnetar does not, and produced an FRB, may suggest that the FRB production mechanism is completely separate from pulsar like mechanism.

We discuss the coincident X-ray detection and multi-wavelength non-detections, both with LOFAR and other reported limits in radio and optical, in the context of the multi-wavelength afterglow predicted by the maser shock model. We find that earlier observations hours to days after the burst are crucial to detect the radio afterglow. Based on these findings we make recommendations for the possibility of automatic triggering of rapid response telescopes in the event of another Galactic FRB. We further discuss a very early optical observation reported in the literature to begin just one second after the burst. By modelling the optical afterglow we suggest that, at least for the most simple shock model with a uniform density circumburst medium, the non-detection rules out the synchrotron maser shock model. We further find that if the blast wave instead interacts with a non-uniform density medium, these constraints may be mitigated with certain parameter choices. We further suggest that the non-thermal acceleration of particles should be incorporated within the model after the shock is not longer relativistic. We show that if non-thermal acceleration is accounted for, afterglows from the brightest radio bursts could be detectable for much longer periods of time.
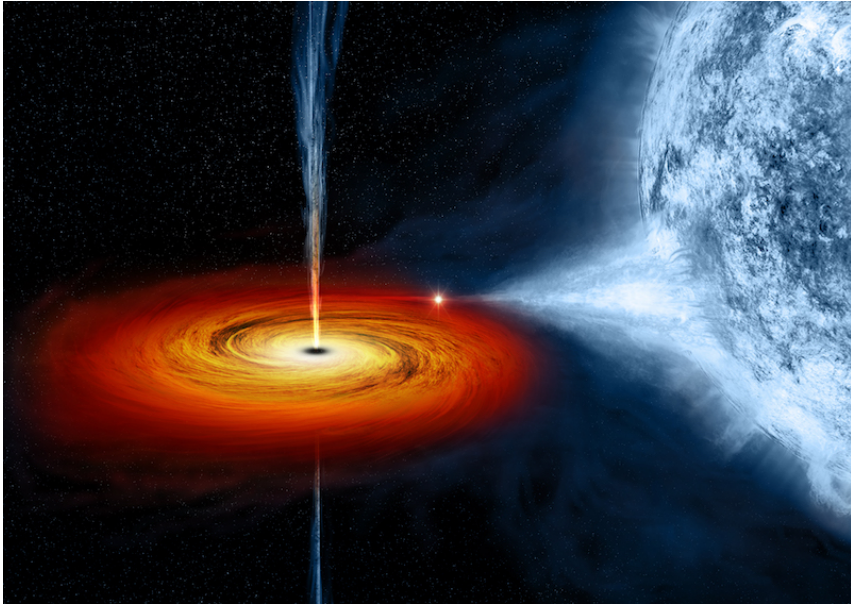
E

Nederlandse samenvatting

Compacte objecten, d.w.z. neutronensterren en zwarte gaten (en witte dwergen), zijn mysterieuze astronomische bronnen met een hoge dichtheid. Ze ontstaan aan het eind van het leven van sterren, of na de fusie van twee andere stellaire objecten, en zweven door de interstellaire ruimte, onzichtbaar voor astronomen die ernaar zoeken. Als ze echter jong zijn of in dubbelstersystemen zitten, kunnen ze allerlei kortdurende en explosieve verschijnselen voortbrengen die voor ons op aarde zichtbaar zijn door licht van een bepaalde golflengte of een andere boodschapper. Dit is geen ongewoon verschijnsel, aangezien de meeste sterren (vooral de zwaardere) geboren worden in dubbelsterren. Naarmate ze samen evolueren en hun waterstof opbranden, ondergaat een van de twee uiteindelijk een supernova-explosie, waarbij soms een jonge, gemagnetiseerde neutronenster ontstaat die bekend staat als een pulsar of een magnetar, of mogelijk een zwart gat. Deze neutronensterren kunnen een breed scala aan pulsen, uitbarstingen en explosies in het elektromagnetische spectrum produceren, aangedreven door grote magnetische velden en snelle rotaties (Hoofdstuk 3 & 5).

Soms kunnen de ster en het pasgeboren compacte object bij elkaar blijven, ondanks de gewelddadige supernova. In dat geval kan de ster, als de objecten dicht genoeg bij elkaar in een baan zijn, materie gaan afgeven aan het compacte object. Dit kan gebeuren doordat materie rechtstreeks van het oppervlak van de ster wordt getrokken door de zwaartekracht van het compacte object, of doordat de krachtige wind van de ster zelf materiaal naar zijn begeleider blaast. Behoud van impulsmoment dicteert dat deze overgedragen materie een schijf vormt rond het compacte object. Deze zogeheten accretieschijf schittert in röntgenstraling en lanceert krachtige stromen van materie en versnelde deeltjes, jets genaamd, die variëren op tijdschalen van dagen tot jaren (Hoofdstuk 2).

Als het compacte object en de ster samen verder evolueren, kan de donorster uiteindelijk ook exploderen in een supernova. Als, mogelijk tegen de verwachting in, de baan van de dubbelster ondanks deze tweede explosie gebonden blijft, ontstaat een dubbel compact object. Daarin zijn de compacte objecten aanvankelijk vaak ver van elkaar verwijderd en hebben daardoor alleen interactie door hun beweging door ruimte en tijd. De resulterende zwaartekrachtstraling, rimpelingen door de ruimtetijd die zich door het heelal voortplanten, zijn de enige signatuur van hun kosmische dans. Uiteindelijk, vaak op tijdschalen bijna zo lang als de leeftijd van het heelal zelf, zullen de objecten voldoende energie hebben uitgestraald dat hun banen krimpen tot het punt van samensmelting. Dat veroorzaakt een laatste, meest energieke transiënt die waarneembaar is in het elektromagnetische spectrum en in

Figuur A: Een artistieke impressie van Cygnus X-1, een zwart gat met röntgenstraling. (NASA/CXC/M.Weiss)

gravitatiegolven, die door de ruimte-tijd rimpelen en onze eigen perceptie van lengte en tijd op aarde verstoren (Hoofdstuk 4).

Hieronder zal ik het onderzoek in de vier wetenschappelijke hoofdstukken van dit proefschrift kort samenvatten.

- **Hoofdstuk 2 - High-energy cosmic ray production in X-ray binary jets**

  Hoofdstuk 2 onderzoekt de jets van röntgendubbelsterren, een dubbelster met een compact object en een gewone ster, als deeltjesversnellers. Het voornaamste doel van het hoofdstuk is te begrijpen hoe belangrijk de bijdrage van röntgendubbelsterren aan kosmische straling is: een waargenomen flux van astrofysisch versnelde protonen en ionen.

  Dit hoofdstuk is vooral gericht op röntgendubbelsterren waarin het compacte object een zwart gat is, aangezien astronomische waarnemingen over het hele elektromagnetische spectrum erop wijzen dat deze systemen de meest efficiënte deeltjesversnellers zijn. We schatten de Galactische populatie van röntgendubbelsterren met behulp van theoretische studies van populatiesynthese, gebaseerd op de fysica van de evolutie van dubbelsterren, en recente waarnemingen van het dichte centrum van onze Melkweg, waar vermoedelijk veel röntgendubbelsterren verblijven.

  Met behulp van waargenomen röntgen- en radio-eigenschappen van röntgendubbelsterren met zwarte gaten vinden we een empirische relatie voor het gemiddelde ver-

mogen van jets. Uit nauwkeurige simulaties van deeltjesversnelling blijkt dat een klein percentage van de energie van de jet de versnelling van hadronen (protonen en andere zwaardere ionen) tijdens schokken aandrijft. Het totale Galactische hadronische versnellingsvermogen als gevolg van schokken in deze jets wordt vervolgens vergeleken met de bekende totale hoeveelheid Galactische kosmische straling.

Om beter te begrijpen hoe versnelde deeltjes in jets eindigen als kosmische straling, simuleren we de voortplanting van deze versnelde hadronen uit röntgendubbelsterren met behulp van de DRAGON code. Hierdoor kunnen we ook begrijpen welke andere boodschappers uit deze kosmische stralen worden geproduceerd op hun weg naar de aarde, langs kronkelige paden die door het interstellaire magnetische veld worden afgebogen. In het bijzonder berekenen we de diffuse gammastraling en neutrino's die ontstaan door de interactie van de kosmische straling met het interstellaire medium.

Wij vinden dat tot 10% van de Galactische kosmische straling kan worden versneld in jets van röntgendubbelsterren. Bovendien kunnen jets deeltjes versnellen tot boven 1 PeV (10^{15} elektronvolt), en mogelijk tot het tweede kniepunt in het waargenomen spectrum rond $\sim$100 PeV. Deze bevinding kan bijdragen aann de verklaring van deze eigenaardigheden in het kosmische-stralingsspectrum rondom de overgang van Galactische naar extra-galactische bronnen. Ten slotte vinden wij dat een tweede significante Galactische component in het kosmische stralingsspectrum met een hogere grensenergie dan de primaire component (vermoedelijk supernovaresten) in de komende jaren moet kunnen worden geverifieerd via een knik in het diffuse Galactische neutrinospectrum.

- **Hoofdstuk 3 - Coherent curvature radiation: maximum luminosity and high-energy emission**

In dit hoofdstuk van het proefschrift onderzoeken we radio-uitbarstingen van gemagnetiseerde neutronensterren. We onderzoeken in detail één stralingsmechanisme waarbij zeer heldere coherente radio-emissie kan worden geproduceerd, bekend als *coherente* krommingsstraling. Coherente emissie is een specifiek type waargenomen astrofysische straling waarbij de waargenomen emissie te helder en te kort van duur is om te worden verklaard door de som van individueel uitstralende deeltjes. In plaats daarvan gedragen de versnelde deeltjes zich op een georganiseerde manier en zenden ze gezamenlijk straling uti, vergelijkbaar met een laserstraal, waardoor het totale uitgezonden en waargenomen vermogen toeneemt.

Deeltjesversnelling in de buurt van neutronensterren wordt over het algemeen aangedreven door langdurig bestaande rotatie-geïnduceerde elektrische velden, of door elektrische velden die tijdelijk ontstaan door een verandering in de eigenschappen van de magnetosfeer. Versnelde deeltjes worden langs magnetische veldlijnen geleid, aangezien beweging loodrecht op de veldlijnen snel door straling gedempt wordt. De kromming van de veldlijnen resulteert in een versnellingscomponent loodrecht op de impulsen van de deeltjes, vergelijkbaar met centripetale versnelling bij uniforme cirkelbeweging; die resulteert in straling. Coherentie wordt veroorzaakt doordat de deeltjes zich

Figuur B: Een artistieke impressie van een magnetar, een sterk gemagnetiseerde neutronenster. (Maciej Rebisz/Quanta Magazine)

zowel ruimtelijk als in de impulsruimte dicht bij elkaar bevinden. Op deze manier stralen bundels deeltjes die zich binnen tot één emissiegolflengte van elkaar bevinden en goed op elkaar afgestemde impulsen hebben, effectief als één grote lading die gelijk is aan de som van alle ladingen in de klomp.

We vinden dat de versnelde deeltjes zelf de magnetische veldlijnen waarlangs ze zich voortbewegen verstoren. Het netto effect is dat in plaats van langs de langzaam krommende magnetische veldlijnen van de neutronenster te bewegen, individuele deeltjes langs spiraalvormige krommingen bewegen, vergelijkbaar met een gebogen veer. Dit heeft twee belangrijke gevolgen. Ten eerste is er een maximale coherente helderheid voor elke bundel deeltjes, die afhangt van de eigenschappen van de bundel en dus van de eigenschappen van de neutronenster zelf: als de magnetische veldlijnen te strak gewikkeld zijn bewegen de afzonderlijke deeltjes niet meer voldoende in dezelfde richting, waardoor de coherentie uitblijft. Ten tweede leiden de verstoringen van de banen van de deeltjes tot een kleinschalige versnelling dwars op de leidende magnetische veldlijnen van de neutronenster. Dit resulteert in een extra, subdominante, *incoherente* component in de straling van de bundels bij hoge frequenties. Het blijkt dat deze component nominaal wordt uitgezonden in de röntgen- of gammaband voor interessante bronnen, en onder bepaalde omstandigheden detecteerbaar kan zijn voor de helderste radio-uitbarstingen.

Deze gevolgen worden vergeleken met de waargenomen eigenschappen van voorbijgaande radio-uitbarstingen van de Krabpulsar, de heldere FRB 200428 van de Galac-

tische magnetar SGR 1935+2154, en buiten-Galactische snelle radio-uitbarstingen van onbekende oorsprong. Wij laten zien dat de voorwaarde van maximale helderheid betekent dat de helderste pulsen van de Krabpulsar afkomstig moeten zijn van dicht bij het oppervlak van de ster. Bovendien beperkt het de voorlopers van snelle radio-uitbarstingen tot alleen neutronensterren met een hoog magnetisch veld in de context van dit stralingsmechanisme. De hoogenergetische component van de emissie kan wellicht (een deel) van de hoogenergetische uitbarsting verklaren die samen met FRB 200428 is waargenomen.

- **Hoofdstuk 4 - Pulsar revival in neutron star mergers: multi-messenger prospects for the discovery of pre-merger coherent radio emission**

Hoofdstuk 4 onderzoekt de mogelijkheden voor de detectie van straling van samensmeltende neutronensterren voorafgaand aan de samensmelting zelf (zgn. pre-merger emissie). De magnetosferische interactie tussen twee neutronensterren wordt beschouwd, waarbij één neutronenster een verwaarloosbaar magnetisch veld heeft. Dergelijke eigenschappen worden algemeen verwacht voor typische evolutiekanalen van dubbelsterren, en zijn waargenomen voor dubbele neutronenstersystemen in onze Melkweg.

De eerste helft van het hoofdstuk onderzoekt de manier waarop deeltjesversnelling en straling zouden kunnen optreden. We corrigeren berekeningen in de literatuur voor de elektromagnetische respons van een perfecte geleider (d.w.z. de minder gemagnetiseerde neutronenster) die door een uniform magneetveld beweegt, wat hier de magnetosfeer van de gemagnetiseerde neutronenster voorstelt. Aan de hand hiervan identificeren we gebieden waarin een sterk elektrisch veld aanwezig is parallel aan lokale magnetische veldlijnen, wat gunstig is voor deeltjesversnelling. We schatten de coherente helderheid van deze gebieden door de hoogte te berekenen van een vacuüm spleet die ontstaat doordat hoogenergetische fotonen wisselwerken met het magnetische veld. Daarbij kunnen fotonen deeltjesparen produceren die het elektrische veld afschermen, vergelijkbaar met theorieën over pulsaremissie.

Met behulp van een semi-analytisch kader kunnen wij dit elektrisch veld en de verstoorde magnetische veldlijnen in kaart brengen als functie van de tijd om de richting van deeltjesversnelling en straling te begrijpen. Op deze manier zijn wij voor het eerst in staat om de straling voor de samensmelting te voorspellen voor verschillende waarneemrichtingen en gesimuleerde waarnemer-afhankelijke lichtkrommen te produceren. Het emissieprofiel van coherente radiostraling hangt af van enkele belangrijke parameters: het stralingsrendement, het magnetisch veld van de neutronenster, de inclinatiehoek van het systeem, de hoek tussen magneetveld en baan, en de afstand tot het moment van samensmelting.

In de tweede helft van het hoofdstuk onderzoeken we vijf mogelijkheden voor de ontdekking van deze pre-merger emissie met behulp van multi-messenger en multi-golflengte waarneemtechnieken. Ten eerste kan het gaan om de ontdekking van een snelle radio-uitbarsting zonder een multi-messenger of multi-golflengte tegenhanger. Wij suggereren dat deze pre-merger uitbarstingen een fractie kunnen vormen van

N
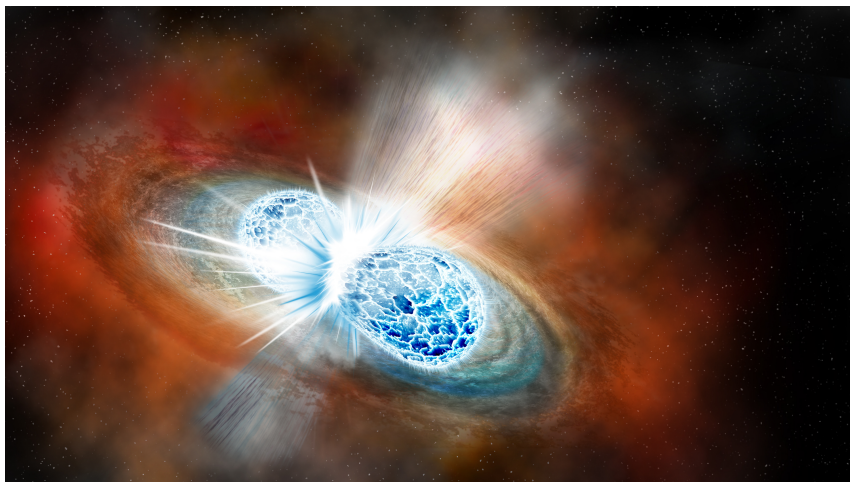
Figuur C: Een artistieke impressie van een neutronensterfusie (Robin Dienel/The Carnegie Institution for Science)

de eenmalige uitbarstingen die door instrumenten met een groot beeldveld worden waargenomen, en dat zij identificeerbaar zijn door hun karakteristieke tijdsstructuur. Ten tweede kan de pre-merger emissie worden gedetecteerd door snelle waarnemingen van gammaflitsen door radiotelescopen. De meest optimistische parameters (neutronensterren met een hoog magnetisch veld en goed uitgelijnde systemen) zijn reeds onderzocht met laagfrequente radiotelescopen, waar de dispersievertraging van radiogolven in vergelijking met de snelle gammastraling deze instrumenten in staat stelt effectief waar te nemen vóór de fusie. Ten derde kunnen soortgelijke snelle waarnemingen worden gedaan voor uitbarstingen van zwaartekrachtgolven waarbij een neutronenster betrokken is, wat bijzonder belangrijk is voor de komende waarneemperioden van detectoren voor zwaartekrachtgolven op de grond. Ten vierde kan na een coherente uitbarsting zonder aanvankelijke tegenhanger een nagloeier van een gammaflits worden waargenomen om te bevestigen dat de coherente uitbarsting zijn oorsprong vindt in een fusie. Ten slotte kan een kilonova, een kortstondige optische nagloeier van een fusie van neutronensterren, na een coherente uitbarsting op soortgelijke wijze worden gecontroleerd.

- **Hoofdstuk 5 - Testing afterglow models of FRB 200428 with early post-burst observations of SGR 1935+2154**

Rond 14.30 UTC op 28 april 2020 is een extreem heldere radio-uitbarsting waargenomen van een magnetar SGR 1935+2154 in onze Melkweg. De uitbarsting was vele orden van grootte helderder dan de typische reuzenpulsen die eerder van neutronensterren zijn waargenomen. De eigenschappen van deze uitbarsting waren vergelijkbaar met de onlangs ontdekte snelle radio-uitbarstingen van onbekende oorsprong die afkomstig zijn van andere melkwegstelsels. Hoewel hij minder helder was dan typische snelle

radio-uitbarstingen, leverde hij sterk bewijs dat magnetars de voorlopers kunnen zijn van snelle radio-uitbarstingen, zoals reeds in de literatuur was voorgesteld.

De radio-uitbarsting, ook bekend als FRB 200428, werd waargenomen tijdens een zeer actieve periode van de magnetar waarin ook veel kortdurende röntgenuitbarstingen werden waargenomen. Van bijzonder belang is dat één röntgenuitbarsting door vier afzonderlijke instrumenten vrijwel gelijktijdig met de radio-uitbarsting werd waargenomen. Deze heeft een eigenaardig spectrum in vergelijking met de honderden andere radio-uitbarstingen. Dit was de eerste keer dat zo'n heldere radio-uitbarsting werd waargenomen met een tegenhanger op meerdere golflengten, wat een unieke gelegenheid biedt om de emissiemechanismen die worden voorgesteld om snelle radio-uitbarstingen aan te drijven te testen en verder te ontwikkelen. Een populaire theorie over snelle radio-uitbarstingen, het synchrotron-maserschokmodel, staat centraal in het theoretische deel van dit artikel. In dit model drijft een synchrotron-maser de snelle radio-uitbarsting aan, die ontstaat door schokken als een relativistische drukgolf op het omringende medium inslaat. Dit model kan worden gecontroleerd aan de hand van waarnemingen na de uitbarsting, aangezien een nagloeier met meerdere golflengten wordt voorspeld naarmate de schokgolf zich van de neutronenster verwijdert, vergelijkbaar met de nagloeier van een gammaflits.

In dit Hoofdstuk presenteren we waarnemingen van de magnetar na FRB 200428 met de Low Frequency Array (LOFAR), een internationale radiotelescoop in Nederland. We vinden geen emissie op de locatie van de magnetar tijdens diepe beelden over drie waarnemingsepochen, noch tijdens momentopnamen op kortere tijdschalen. We bespreken eerst de implicaties van deze non-detectie. Sommige magnetars zijn radio-luid en zenden radiopulsen uit die gemoduleerd worden door hun rotatieperiode. Het feit dat deze magnetar dat niet doet, en een FRB produceerde, kan erop wijzen dat het FRB-productiemechanisme volledig losstaat van het pulsar-achtige mechanisme.

Wij bespreken de samenvallende röntgendetectie en multi-golflengte non-detecties (zowel met LOFAR als met andere instrumenten in radio en optisch) in de context van de multi-golflengte nagloeier voorspeld door het maser-schokmodel. Wij vinden dat eerdere waarnemingen uren tot dagen na de uitbarsting cruciaal zijn om de radio-nagloeier te detecteren. Op basis van deze bevindingen doen wij aanbevelingen voor de mogelijkheid van automatische activering van snelle-reactietelescopen in geval van een nieuwe Galactische FRB. Verder bespreken wij een zeer vroege optische waarneming die volgens de literatuur slechts één seconde na de uitbarsting begint. Door de optische nagloeier te modelleren suggereren wij dat, althans voor het meest eenvoudige schokmodel met een circulerend medium met uniforme dichtheid, de non-detectie het synchrotron-maserschokmodel uitsluit. Verder blijkt dat als de schokgolf in wisselwerking staat met een medium met een niet-uniforme dichtheid, deze beperkingen met bepaalde parameterkeuzes kunnen worden verzacht. Verder stellen wij voor de niet-thermische versnelling van deeltjes in het model op te nemen nadat de schok niet langer relativistisch is. Wij laten zien dat, als rekening wordt gehouden met niet-

thermische versnelling, de nagloeier van de helderste radio-uitbarstingen veel langer waarneembaar zou kunnen zijn.

N

Acknowledgements

Believe in myself but I also know that I don't know everything
So I don't take things too seriously and I like to play the fool
I understand the best things in life
Aren't things at all
- Beans on Toast

When I first arrived in Amsterdam in 2016 I struggled for the first few months wondering whether I had made a good decision to move here to pursue a masters degree. 6 years on, it is clear that it was the best decision I could have made. These years spent during my masters and then PhD in Amsterdam have been the best of my life, wholly attributable to my colleagues, friends and family.

Ralph, you have been an excellent supervisor and I would like to thank you for guiding me on my PhD journey. I especially appreciate the freedom you gave me to work on what I was interested in. This flexibility allowed me to follow my curiosities, and I hope you have also enjoyed the winding path that led to this thesis. I always enjoyed our meetings, and your ability to provide insight on almost any topic, astrophysical or not, made for very interesting discussions. Thank you also for narrowing my focus when needed, particularly in the last year of the PhD (maybe someday I'll write something about the Schwinger pairs). Thank you also for your diligent service to the community, ranging from directing the institute, moderating the ArXiv, spearheading the ASPIRE project, and the vital moderation of Astronomy cartoons Facebook page.

Antonia, thank you for guiding me through many of the projects of this thesis. I am particularly grateful for all your hard work in these last few months with the final chapter of this thesis, which helped me finish on time and for sharing your rapid radio transient enthusiasm.

I'd like to thank my MSc supervisor Sera, without whom I would not have even considered applying for a PhD (and definitely wouldn't have got one). Thanks for taking me on for such an interesting project, and for seeing it through to its conclusion. I'd also like to thank Daniele who helped me immensely with the X-ray binary project, including long after my MSc had finished and you had moved on from Amsterdam. Thank you also to Phil whose accretion course was my first proper experience of high-energy astronomy which piqued my interest to work in this field.

My greatest thanks go to my two paranymphs and my two paranymphs-in-lieu, Deniz, Oli, Vatsal and Dimitris. Deniz, my vice-manager, thank you for always being there for me in all aspects of my life in Amsterdam. You have always been my go-to person for any issues and hardships I encounter both in and out of astronomy, and I value your advice above all. You are a beacon of optimism and positivity, particularly when listening to other peoples problems, which you always have time for no matter what. You helped me immensely both during the pandemic with many a cheeky pint after work and during the PhD helping diagnose my many python problems. Oli, thank you for being there to laugh at academia (and everything else) with me. It's been so much fun to get to know you in these last few years, and even more fun to work with you a little. I especially appreciate your proud sharing of Dutch culture over the years, which I have enjoyed immensely ("Well, in the Netherlands we..."). You are a great friend and the first person I come to when I need to poke fun at something/someone; I am so happy that I got to know you. Vatsal, I don't know where to start. There is never a boring moment with you, and your neverending knowledge about almost anything is admirable. Thanks for being part of my pandemic bubble, for cooking amazing food for us, and for always being up for anything. I am so incredibly happy that you and Elspeth are continuing life in the UK and cannot wait to spend time with you both in the future. Need I remind you, if all else fails, a samosa/coffee truck on the leafy streets of Coventry is a cracking back-up plan. Dimitris, thanks for showing me the ropes during my first year of research, and for sharing my love for neutrinos. You are the smiliest person in the office, and I greatly miss poking my head into your office to annoy you about whatever is on my mind; you always make me feel better. It was so much fun being your paranymph and meeting your family. I will never forget that emotional day, sorry for making you drink the milk. I already miss you so much, and I can't wait to come visit you in Annecy!

I'd also like to thank my academic siblings, the members of the radio transient group that I have been part of for these last 4 years. We may not be the most prolific transient discoverers, but we sure had fun doing it. Aleksander, thanks for your time as the tsar of the group which always livened up Friday afternoons. Your unique viewpoints on all things always led to interesting discussions to say the very least. Mark, thanks for being our glorious leader for 3ish years, helping us reach the luminous scientific summits. Thanks for sharing your endless wisdom about all things, but mostly about the ever-impending global societal and financial collapse. Thanks also for reminding us that there are more important things than Astronomy. Also, thanks for giving me Covid. Kelly, I miss you! Thanks for always answering my naive questions about our observations of FRBs and NS-NS mergers, you were a huge help at various points throughout the last 4 years. I'm glad you and Fen are enjoying life down under. David, thank you for educating us on a weekly basis on how noise can turn into frogs (and vice versa?). Iris, you are an amazing scientist and I look forward to reading about all your low-frequency transient discoveries soon. Thanks for being an amazing group-mate, and for appreciating the absurdity of all things. Ibrahim, thanks for being around for a chat and teaching me a lot about Turkey, and of course for keeping AARTFAAC running! Thanks also to the amazing masters students we have had in the group: Stefanie, Angana and Jelle for doing amazing science. I am sure that Ruggero and Annika will keep up the trend! Also to Rhaana, Adam, and Alexander who always provided useful insights across the little and

big ponds, it was great to hear all about your interesting work. I'd also like to say thank you to the members of the JetSet group from my time there, especially Dimitris, Matteo, Koushik, Atul and Doosoo, who gave me my first experiences of collaborative research, and helped turn my shitty presentations into less shitty presentations.

I'd also like to those who have acted as mentors to me outside of my research group. Firstly, Martin. Thanks for always being the person to order the last beer; often one can learn much more from a night at the Oerknal than a day in the office, and have a lot more fun too. I aim to one day understand what 'the point' is, and to know all the rules. Secondly, thank you to Alexander. It was so much fun to meet you in DC after so many discussions online, and to see how you have kept the API vibes going at George Washington. I particularly appreciate your kind advice over the years, and your introducing me to many amazing and fun astronomers. Third, to Zorawar, it was great to meet you in DC and begin collaborating. Thank you for your time and effort towards Chapter 3, and for being the only person to enable me (kind of) understand pulsar emission mechanisms and the politics behind science. Finally thank you to Om for being the ideal student, I loved working with you. Your work on the ASPIRE project and later on neutron star mergers was truly exceptional and was a highlight of my PhD. Enjoy your PhD years in Austin and don't work too hard. I look forward to seeing what I know you will uncover about the true nature and utility of fast radio bursts.

Many of the friends I have met in Amsterdam have been through GRAPPA and API. Most people reading this will know that API is a special place to work, and it is so because of the people that form the community. Firstly, thanks to Milena, Susan and Renee, who always ensure API is a welcoming place to come and work (as well as a functional one). Thank you to those API PhDs who make the institute as friendly and exciting as it is, in no particular order. Ben, thanks for taking us all on exceptional adventures. Thanks for guiding us to the Deltaworks, the source of the Amstel, the Baambrugse Zuwe and through the Biesbosch mangroves (you really do love water eh?). Safe to say I wouldn't have seen half of the countryside I have without you. David, thank you for playing, organising and watching all the sports with me. Ines, thank you for being the life of the party. Arkadip, thanks for always having a cold beer ready for me when I come over to watch Man United lose. Frank, you spidermonkey, thanks for bringing the weird. Kenzie, thanks for always answering my questions about FRBs. Vladimir, you are the glue of the institute and you still hold it together from afar. Mitchell, thanks for being in all the committees. Also thanks to the many other masters, Phds and Postdocs that have been and gone in the last 6 years, its been a lot of fun. Ariane, Julien, Mart, Jordan, Aiden, Jasper and Dora, thanks for struggling through the perils of a physics masters degree with me.

Thank you to all the people who have played in various football teams over the last four years, especially Bram, Theo, Ruud, Jasper, Gullo, Juan, David, Jakob at the DVVA and Uddipta, Kelly, Eva, Floris x2, Dion, Bart, Sancho, Antoine, Emmanuele, Akif, Fedde and Ruggero at Science Park. In particular thanks two people in particular. To our renowned player-manager Uddipta for taking over all the responsibility and turning our lack of success around around. Was a great joy to be promoted after (4?) seasons without many wins, the pregame beers must have had something to do with it. Emmanuele, the ice-cream advocate, thanks for

A

taking over API Sports from us, amongst many other things. Also thanks to all the Monk fiends who have laughed at me falling off the wall: Elspeth, Vatsal, Claire, Johannes, Morgan, David & Frank. Finally thanks to all the API members past and present I have got to know over the years who I didn't get to mention already: Lorenzo, Sam, Dante, Wanga, Kate and Anwesh.

I'd also like to thank the people in Amsterdam outside of astronomy that made my time here so fun. Nalin, thanks for showing me the wonders of the Amsterdam clubs and being a great roommate and Fortnite companion back in the day. Elspeth, thanks for having such an amazing boyfriend... thanks also for your unadulterated enthusiasm about mushrooms, birds, bargins (I say bargins, I mean crap people have thrown out) and crisps. Sinem, I am so glad you managed to move to Amsterdam, its been so fun getting to know you properly! Alicia & Milan, thanks for having the cutest pets and for introducing me to so many new people over the years, its been great fun! Can't wait to come and visit you in Barcelona.

Thanks also to my friends back home who always provided a place where astrophysics was the last thing on my mind. Will, thanks for lending me Tommy's bed and catching me up on everything whenever I was in London. Also to all the other members of Qua for all the good times. Thank you to KAB for being the people I feel most myself around, I love you both. The time we spend in Amsterdam (and London/Cardiff/Bosham/Nottingham) together in the magical mystery forests, singing around a fire and BBQing in the park are the highlights of my time my last 6 years. Beth, thanks for reminding me of my love of music on a regular basis and always forcing me to be creative. Kieran, I have no words. I miss you every single day. You were (are) the brightest of lights and made everyone around you a better, happier person. Keep rolling with the good times.

To my family, thanks for supporting me so much in the last 6 years. Thank you to Penny and Grant for always welcoming me on the best island when I needed time away from work, and of course for having the most amazing grandchildren. Chris & Karolina, thanks for driving me around when I'm in the UK, I can't wait for August!!! Jenny & Kieran, thanks for catsitting in our time of need, and for being there when I get to come home.

To my Grandparents: Thank you for always being interested in what I am doing and always giving me the best advice. Thank you for inspiring me with many old stories and tales of my roots, and continuing to inspire me with new gadgets, magic tricks and hydrid steam-internal combustion engine patents. I am always amazed, and I cherish my time with you all.

To my parents, you do not understand how much I appreciate your unwavering support over the last 6 (28) years. It means the world to me, I wouldn't be here without it. Mum, thanks for always being there for me no matter what. Dad, thank you for inspiring my interest in maths and science from a very young age. Also thank you to both Amanda and Andrew, thank you for your constant support and for all the great trips, Christmases and meals over the years.

To my family in Amsterdam. Luna, thanks for being the cutest baby and reminding me that everything is edible if you really try. Freddie, thanks for being the snuggliest, grumpiest ball

of fluff there ever was. Alicia, Ali, my love. I wouldn't have finished a year of the masters without you, let alone anything else. My life in Amsterdam is my life with you in it and it has been the best time of my life because of you. Words cannot describe how grateful I am for your unwavering support and love over these 6 years together. Thank you for making me a better version of myself when I am with you, for your unending utterly selfless actions of kindness, for your amazing cakes, for being the only person I want spend 5 hours bouncing a ping pong ball to, for enabling me to make it through the final stretch of the PhD with my sanity mostly intact and for always being you. I am so proud of how far you have come in the last 6 years & I can't wait for our future together. I know that even when it seems scary it will be okay as you'll be by my side. The universe is mostly empty space, without you.

Alex Cooper,
Amsterdam, 2022

A